Soft X-ray Spectroscopy of Metal Nitrides and Oxides: Uncovering Structure-property Relationships in Phosphors for pc-LEDs

A Thesis Submitted to the
College of Graduate and Postdoctoral Studies
in Partial Fulfillment of the Requirements
for the Degree of Doctor of Philosophy
in the Department of Physics and Engineering Physics
University of Saskatchewan
Saskatoon

By

Thomas M. Tolhurst

Permission To Use

Head of the Department of Physics and Engineering Physics
163 Physics Building
116 Science Place
University of Saskatchewan
Saskatoon, Saskatchewan
Canada
S7N 5E2

Abstract

This thesis engages a problem that is seemingly a little incongruous: to develop an understanding of, and link together, the structure-property relationships of LED-phosphors and frontier polymorphs of vanadium oxides using the same experimental and theoretical framework. Soft x-ray spectroscopy and density functional theory calculations are used as the probe of, and interpretive tool for, the electronic structures of these materials. By comparing and contrasting the observed electronic structures to those of other, similar systems, changes in electronic structure are linked to changes in crystal structure and atomic composition. From this vantage point the LED-phosphors, which are essentially metal nitrides, and vanadium oxides are not as disparate as they would seem at first glance. Their properties lie on a continuum, allowing them to be readily understood within a single framework. At the same time, there are significant insights to be gained about each group, by studying the other.

In both groups the interplay between localization and delocalization of metal d-states is seen to be key to their functional properties, both as a result of and in conjunction with, the influence of their ligands. The effects of the ligands are seen to stem directly from their local charge densities, as well as their separation from and arrangement around the metal sites. In addition the interaction of non-metal sites is seen to be critical in many cases.

Structure-property relationships are outlined for this suite of materials. Critical material properties, such as the band gaps, and the location of metal states in the band gaps, are determined experimentally. Several analysis techniques are developed that prove critical for the analyses of these compounds. Included in this is a thorough analysis of x-ray self-absorption in vanadium oxides, which is too often ignored. Ultimately a coherent framework for understanding the properties of these compounds is developed and it is hoped that this will serve as the basis of further refinement of their useful properties.

Acknowledgements

There is no doubt that the work presented here could not have been done alone. The very nature of the experimental techniques used, based on synchrotron radiation, requires the effort of countless individuals. There are also many people to whom I am indebted for their assistance in learning the experimental and theoretical aspects of this work. And of course, no one works in a vacuum. My colleagues, supervisor, and friends have formed a large part of the stable, productive and vibrant environment, in which I have been privileged enough to work.

It is an understatement to say that this work could not have been done without the support of my supervisor, Professor Alexander Moewes. He has provided an exceptional work environment, access to the tools needed for this work, generous financial support, and exposure to the broader research community, far beyond what I would have asked for. The addition of sincere encouragement and interest in the success of his students has truly earned my lasting grattitude.

I have also had the privilege of working directly with several members of the technical staff at the synchrotron facilities where the experimental work presented in this thesis was conducted. I extend my sincerest thanks to Dr. Wanli Yang, Dr. David Muir, Dr. Teak Boyko and Dr. Tom Regier for their there technical support and for the wealth of information that they have shared.

I have also had the fortune to be part of a research group replete with knowledgeable and friendly colleagues. The knowledge and time they have shared has made my time at the University of Saskatchewan truly meaningful both academically and personally. I thank them all heartily for the colour they have added to my studies. I must also thank my family, both nuclear and extended, which I am truly blessed to have.

Dedicated to my fiancée Sarah, whose love and support have been invaluable.

Contents

List of Figures

List of Tables

List of Abbreviations

XES	x-ray emission spectroscopy
XAS	x-ray absorption spectroscopy
NXES	normal x-ray emission spectroscopy
RXES	resonant x-ray absorption spectroscopy
RIXS	resonant inelastic x-ray scattering
XEOL	x-ray excited optical luminescence
TFY	total fluorescence yield
TEY	total electron yield
PFY	partial fluorescence yield
IPFY	inverse partial fluorescence yield
DFT	density functional theory
pc-LED	phosphor-converted light emitting diode
UV	ultraviolet
CRI	color rendering index
BB	black body
LAPW	linearized augmented plane wave
LO	local orbital
VB	valence band
CB	conduction band
LCAO	linear combination of atomic orbitals
RE	rare earth
AE	alkaline earth
REIXS	resonant elastic and inelastic x-ray scattering
SGM	spherical grating monochromator
FWHM	full width at half maximum
SDD	silicon drift detector

Chapter 1

Introduction

If you start from nothing, it is very difficult to get anywhere.

–Gerhard Herzberg

1.1 pc-LEDs and Luminescent Materials

Electroluminescence was first reported in 1906 by Henery Joseph Round, who had observed it in his experiments with corundum SiC. [1] An expanse of over thirty years followed until the creation of the first near infra-red LEDs. [2] This was accomplished at Texas Instruments using InGaP chips. These early LEDs remained unappealing for lighting as a result of their fragility, inefficiency and the absence of any blue-emitting diodes. [3] In 1974, Akasaki and Amano began adapting metal-organic vapour phase epitaxy for growing device quality layers of GaN, which they achieved in 1986. [2] The growth of high quality GaN, AlGaN and GaInN set the stage for the final steps in the development of efficient blue-emitting LEDs. The subsequent development of low-resistvity Mg-doped GaN and AlGaN by Nakamura in the early 1990s, lead to his successful demonstration of InGaN as an effective blue-emitting LED material in 1993. [1,3] The developments of these three preceding scientists have made the rise of solid state lighting possible, and led to their receipt of the Nobel prize in physics in late 2014. At the time of writing, it is expected that the continued introduction of solid state lighting will reduce energy consumption in the lighting sector by 15% by 2020 and 40% by 2030. [2] This is dramatic, given that lighting currently accounts for roughly 10% of global electricity consumption. [4] In order to produce the white light that is needed for solid state lighting a full, black body-like spectrum is needed in the visible portion of the electromagnetic spectrum. This means that the emissions of a single LED alone are not enough and a more elaborate device is needed.

LED chips based on InGaN can be tuned from the UV to green spectral regions by varying their In content, but efficiency is lost at the same time. [3] Therefore, although green to yellow LEDs may be produced there is a loss in efficiency. At least in principle, tuneable, efficient white light can be generated with different LEDs. However, the complex circuitry and different driving currents required, as well as the variable aging and temperature dependence of the LEDs make such a device less appealing. [1, 3] Thus, although highly tuneable, the development of different hues over time, and subsequent poor colour rendering make an all-LED device ineffective. [1] It is clear that another method of generating white light is needed, if high efficiency and quality solid state lighting is to be realized. Phosphor-converted LEDs–where part of the blue light of a GaN-based LED is converted to longer wavelengths by a thin layer of phosphors covering the LED chip–have consequently become the front runners in the search for efficient solid state lighting.

The pc-LED has already proven itself a leading candidate for the next-generation of high-quality lighting. Traditional incandescents and fluorescents have large energy losses through their high operating temperatures and Stokes shifts. [5] The Stokes shift is given by the difference in the emission and excitation energies. [6] Solid state lighting offers higher energy efficiency, longevity, compact devices, high luminous efficiency and environmentally friendly construction. Whereas fluorescents have reached their peak efficiency, LEDs can be further improved by reducing non-radiative recombination and improving the external quantum efficiency of devices. [5] It is anticipated that LED lighting will reach luminous efficiencies of 200 lm/W by 2020, while their production costs are forecast to decrease continually. [5] The pc-LED has already proven itself so successful that it is poised to dominate the lighting market in the near future. [2]

The list of properties that is needed for an LED-phosphor is lengthy and demanding. The material's excitation spectrum must overlap the emission range of the blue LED (≈ 450 nm for GaN), it must emit in a desirable region visible spectrum, have a high quantum efficiency, have an optimized grain size, be chemically stable at the LED operating temperature (at least 200°C), should have emissions that do not vary in wavelength with temperature, have a high emission efficiency up to this temperature, and having a low production cost is ideal. [1] A short decay time is also ideal in order to avoid saturation. This last point explains why the most popular phosphors are those doped with Eu^{2+} or Ce^{3+}. The visible emissions from these dopants are due to the $4f^{n-1}d^1 \rightarrow 4f^n$ transition. As an allowed transition the decay time is on the order of a μs. [6] These rare earth elements can emit throughout the visible spectrum, depending on the host lattice. This tunability is important as it allows the creation of a variety of spectra with a pc-LED, when multiple phosphors are used. Finding the right host lattices for the rare earth ions allows the creation of pc-LEDs with varying efficiencies and quality of spectra. The former is best measured by the luminous efficacy and the latter the colour rendering index (CRI).

The luminous efficacy measures the efficiency of a light source as seen by the human eye. Measured in lm/W, a light source that converts 100% of its electrical power into 555 nm (green) light defines the maximum possible luminous efficacy of 683 lm/W. [2] Another important measure of the quality of a spectrum for lighting is the correlated colour temperature, which is defined by the emission spectrum of a black body at that temperature. The collection of corresponding chromatic points on the chromaticity diagram form the black body locus, and serves as a principal reference for other light sources. Related to this, the CRI is a dimensionless measure of how well colours are rendered by a light source when compared to a black body of the same correlated colour temperature. A maximum CRI of 100 would indicate that all test colours appear identically under the test light source and the reference black body source. [2] The problem of matching the black body spectrum with the emissions from a solid state device is visualized in Figure 1.1.

Interestingly, there is a loss in luminous efficacy in going from an all-LED device to a two phosphor pc-LED due to the energy loss associated with the Stokes shift of the phosphors. The blue LED with a single phosphor can achieve a CRI in the 70-80 range. It may therefore have lower energy losses than a multi-phosphor device, potentially leading to a higher luminous efficacy. One historically successful, and inexpensive, way of generating white light in this way is the use of Ce^{3+}-doped YAG ($Y_3Al_5O_{21}$). The YAG:Ce^{3+} emits a broad yellow band, which combines with the transmitted blue light from the LED to produce

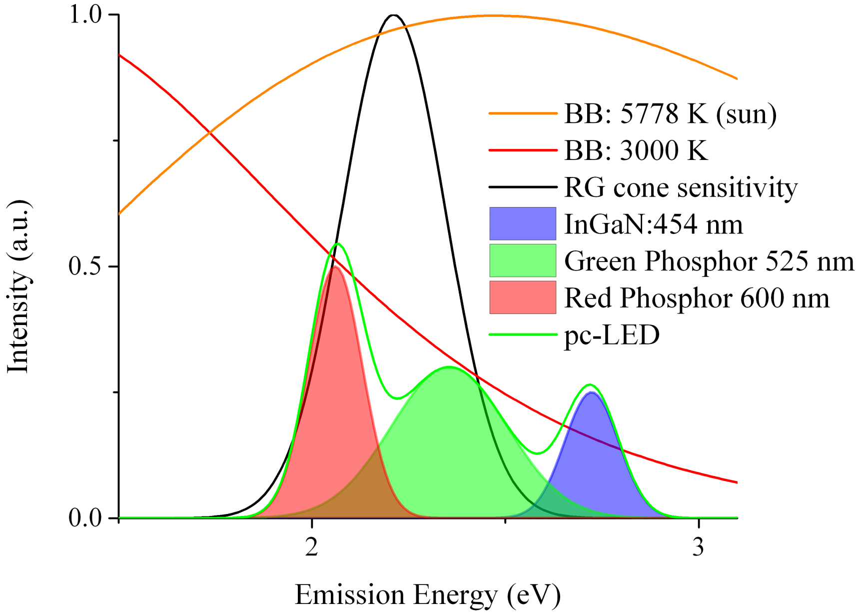

Figure 1.1: The replication of the black body (BB) spectrum with a pc-LED. The high and low temperature spectra indicate what the pc-LED must match to form what is perceived as daylight and warm white light, respectively. Hypothetical LED-chip and phosphor spectra are given as shaded curves, while their sum representing the pc-LED output is given as a solid green line. The sensitivity curve for the red and green cones in the human eye is given as a solid black line, based on a fit to the data in [13].

white light. Generally a single phosphor device has a CRI that is too low for general lighting. This is certainly the case for YAG:Ce^{3+}, which also tends to have a colour temperature that is dependent on the device driving conditions. [3] The combination of a UV LED with blue, green and red phosphors is also possible, and although it can give a high CRI, the quantum losses are higher and lead to a lower luminous efficacy. [1] This brings the discussion to the current state of the art in solid state lighting.

The creation of white light with a blue LED chip and two or three phosphors are the configurations greatest current interest. [2,7] Using multiple phosphors to create a spectrum that is closer to that of a black body also allows for the tuning of the correlated colour temperature. Combining red luminescent materials $Sr_{1-x}Ca_xS{:}Eu^{2+}$ or $(Sr_{1-x}Ca_x)_2Si_5N_8{:}Eu^{2+}$ with YAG:Ce^{3+} has made CRIs above 90 accessible for low colour temperatures within the last decade. [3] Such devices are approaching such high efficiencies that gains are largely to be made through changes in the device packaging. [3]

Nitrides have become prominent as LED phosphors, replacing oxides, due to their higher stability, resulting from greater bond covalency. Phosphors such as the orange $Sr_2Si_5N_8$:Eu^{2+} allow high colour rendering, efficiency and device lifetimes. [3] Another major improvement is to be found in the use of narrow red-emitting phosphors in place of the rather broad-band-emitting $Sr_2Si_5N_8$:Eu^{2+}. [3] This last improvement can help increase the lumen equivalent of the devices. Further improvement can be made though applying new phosphors to more closely match the black body spectrum.

With an eye to the next generation of LED phosphors, application of the breakthrough material SLA ($Sr[LiAl_3N_4]$:Eu^{2+}) has already shown a 14% increase in luminous efficacy with respect to currently available high CRI LEDs. [8] This is achieved through its long emission wavelength (650 nm), narrow emission band ($\approx$ 50 nm), and exceptional thermal stability (QE $>$ 95% at 473 K). [8] It is key to have narrow emissions in the red region so as to limit light output outside of the sensitivity range of the human eye. In addition SLA has a strong, broad absorption band peaking at $\approx$ 466 nm, which is ideal for excitation by blue GaN-based LEDs. SLA and other phosphors, which will be constituting the main body of work here, follow this pattern. They are narrow, red-emitting phosphors, as well as related materials. [9–11]

1.2 Metal Oxides for Frontier Electronics

Transition metal compounds are some of the most important for technological applications. They have diverse properties, including high strength and stability. [12] This is in large part a result of their partially filled 3d shells, which despite having energies close to those of the valence 3s electrons, are more confined to the transition metal atom, as can be seen in Figure 1.2. The radial confinement of the 3d electrons of the is a consequence their large angular momenta. Consequently they exhibit minimal overlap with the orbitals of neighbouring atoms and can have properties that are dominated by interconfigurational interactions, as will be discussed in subsequent sections. At the same time the degree of localization of the 3d electrons varies considerably with the nuclear charge of the transition metal atom. Localization generally increases as one moves towards higher nuclear charges. Highly localized electrons lead to strong correlation effects and the magnetic properties that make many transition metals technologically important. On the other hand the interplay of localization and delocalization in the early transition metals gives rise to new mechanisms for switching between the conducting and insulating states. [15,16] Key materials for the current and next generation of Li, and beyond-Li, ion battery cathodes are metal oxides. [17,18] Many high temperature superconductors are found in this class of materials as well, including the high critical temperature cuprates. [12] Their importance can scarcely be overstated.

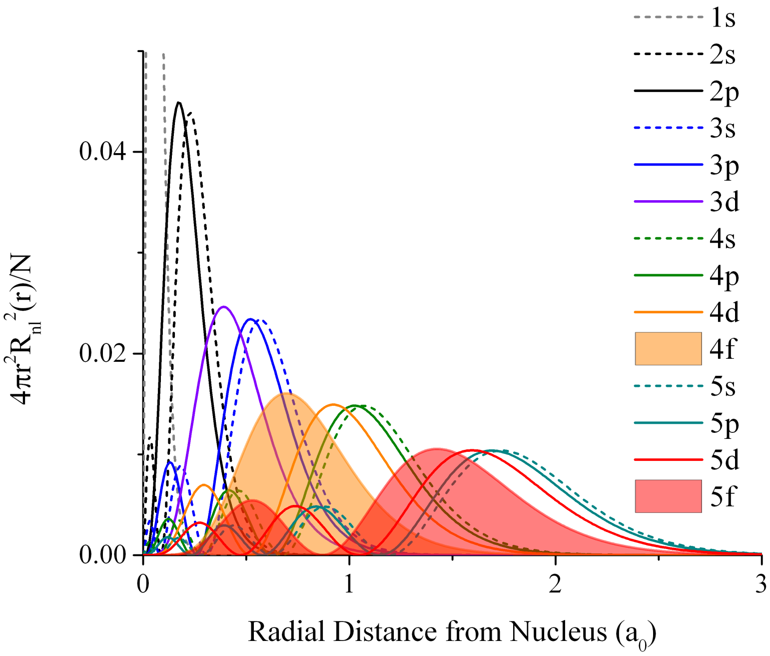

Figure 1.2: Radial probability distributions for atomic V, from solutions to the radial Schrödinger equation assuming an unperturbed Coulomb potential. [14] The functions are normalized to unit area.

1.3 Solids

Throughout this work the primary concern will be arrangements of atoms in the solid state. It is characteristic of such systems in thermal equilibrium that they will take up a regular arrangement, they must be crystalline. [19] Unless otherwise stated all solids referred to in this work are crystalline. However, thermodynamically metastable amorphous solids also exist in nature and will be of occassional interest in this work. They feature atoms vibrating about randomly arranged points, and have relaxation times that are sufficiently long that they can be considered stable.

1.3.1 Symmetry of Crystals

The thoughtful discussion of symmetry in reference [19] is followed here. Symmetry is a key concept in any physical system, and given that in general the concern here is crystalline systems, it can be expected to play a key role in determining their properties. At the same time the nuclei and electrons in a crystal do not occupy well defined locations. Their positions are given probabalistically by a density function $\rho(\mathbf{r})$. The coordinate transformations, that leave the $\rho(\mathbf{r})$ unchanged define the symmetry properties of a crystalline system. The set of all symmetry transformations for a given crystal define its *symmetry group*.

Gasses, liquids and amorphous solids are examples of isotropic materials, and therefore have have the highest symmetry possible. Crystalline solids are examples of anisotropic materials and the density function will have sharp maxima at lattice points. Any two lattice points that can be brought into coincidence through application of symmetry transformations are physically equivalent.

The possible symmetry elements of a crystal are translations, axes of symmetry, planes of symmetry, rotary-reflection axes, screw axes and glide planes. The latter two are a combination of a translation and rotation about a parallel axis, and a translation followed by a reflection in a parallel plane. Translations paired with perpendicular reflection or rotation axes do not form new symmetry operations. These symmetry elements serve as a useful means of classification, about which some discussion is merited.

The Bravais Lattice

The translational symmetries of a crystal can be described by vectors in the direction of the translation and of a magnitude equal to the translational period. Although there are an infinite number of different lattice vectors they are not all independent. They can always be reduced to a set of three basic lattice vectors $\mathbf{a}_i$ ($i = 1, 2, 3$), not all lying in a plane. An arbitrary lattice vector $\mathbf{a}$ can then be described by a linear combination of the basic vectors with integer coefficients n_i

$$\mathbf{a} = n_1\mathbf{a}_1 + n_2\mathbf{a}_2 + n_3\mathbf{a}_3$$

The three basic vectors, which are not unique, form a parallelepiped which defines the *unit cell* of the crystal lattice. The crystal in its entirety is then an assembly of these identical unit cells. The corners of all of these parallelepipeds are equivalent through the translational symmetry of the crystal. The set of all lattice points that are equivalent under translations form the *Bravais lattice* of the crystal. This does not include all lattice points in general, nor all of the equivalent points, since it does not consider rotations or reflections. Since a new Bravais lattice can be constructed from every lattice point, it follows that all possible unit cells in the crystal will have the same volume. Each unit cell must contain one Bravais lattice point, and there are as many such points as there are atoms in the crystal. The number of unit cells in a crystal is therefore independent of the basic vectors.

Crystal Systems

The possible symmetries of a Bravais lattice under rotations and reflections form a corresponding *crystal system.* Each crystal system is composed of a set of axes of symmetry and planes of symmetry and therefore forms a point group. There is a strong restriction on the order of axes of symmetry that can occur for any Bravais lattice. Simple geometric arguments show quickly that only axes of order 2, 3, 4 and 6 are possible. [19] Similarly the translational symmetry of the Bravais lattice implies that every point therein is a centre of symmetry. With this knowledge it is possible to specify the fourteen Bravais lattices and seven crystal systems. The possible crystal systems are, from lowest to highest symmetry: the triclinic system, which only has inversion symmetry, the monoclinic, orthorhombic, tetragonal, rhombohedral, hexagonal, and highest-symmetry cubic system. Each system in this list contains the symmetries of the system preceding it in the list. In keeping with this, less information is needed to specify each system moving along the list. Six quantities are needed to specify a triclinic system, and only one for cubic systems. Examples of most of these are encountered in the analysis presented here.

Crystal Classes

When considering the macroscopic properties of a crystal, which amounts to the equivalence of different directions therein, only symmetry axes and planes contribute. No new equivalencies are added by considering translations, screw axis, or glide planes. The set of such symmetry axes and planes defines the *crystal class.* This is in general different from a crystal's system. Since more points in the crystal are included here, the class will have at most the same number of symmetry elements as the system. Crystal classes are assigned to the systems of lowest symmetry that contain all the elements of the class. This follows naturally from the physically reasonable idea that the atoms in a crystal's Bravais lattice are unlikely to arrange themselves in such a way that they have higher symmetry than required by its class. In light of this, a total of 32 crystal classes can be found corresponding to the various crystal systems. [19]

Space Groups

The set of actual symmetry elements of a crystal, the microscopic symmetry in opposition to the macroscopic symmetry of the crystal class, defines its *space group.* The space group of a crystal can be found by combing the translational symmetries that define its Bravais lattice with the rotation and reflection symmetry elements. There are 230 different space groups possible, each of which can be assigned to a crystal class that contains the same axes and planes of symmetry. There are two groups within this set of 230 space groups between which it is useful to distinguish. Those space groups that contain no glide planes or screw axes form the 73 *symmorphic* space groups. The 157 remaining, or non-symmorphic, space groups contain glide planes or screw axes. These must also therefore contain at least two of the same atom in each unit cell. The lattice of such systems must consist of at least two interpenetrating Bravais lattices. This is necessary to accommodate the fractional translations effected by the screw axis and glide plane symmetry elements.

1.3.2 The Reciprocal Lattice

The reciprocal lattice is fundamental to the analysis of crystalline solids. Its basic properties can be developed in a very natural way by starting with another fundamental concept: that physical quantities associated with a crystal must have the same symmetries as the crystal itself. Then, any property $U(\mathbf{r})$ must be such that

$$U(\mathbf{r} + n_1\mathbf{a_1} + n_2\mathbf{a_2} + n_3\mathbf{a_3}) = U(\mathbf{r}) \tag{1.1}$$

and if one then considers the Fourier series expansion of this quantity

$$U = \sum_b U_b e^{i\mathbf{b}\cdot\mathbf{r}} \tag{1.2}$$

where $\mathbf{b}$ are a set of vectors over which the summation runs. The two preceding equations imply that the addition of any displacement $\mathbf{r} \rightarrow \mathbf{r}+\mathbf{a}$ must leave the exponential in Equation 1.2 unchanged. This implies the following

$$\mathbf{a} \cdot \mathbf{b} = 2\pi \tag{1.3}$$
$$\mathbf{a_1} \cdot \mathbf{b} = 2\pi p_1 \tag{1.4}$$
$$\mathbf{a_2} \cdot \mathbf{b} = 2\pi p_2 \tag{1.5}$$
$$\mathbf{a_3} \cdot \mathbf{b} = 2\pi p_3 \tag{1.6}$$

for $p_1, p_2, p_3 \in I$, which have a solution of the form

$$\mathbf{b} = p_1\mathbf{b_1} + p_2\mathbf{b_2} + p_3\mathbf{b_3} \tag{1.7}$$

and the b_i are related to the a_i by the relations

$$b_i = 2\pi\epsilon_{ijk}a_j a_k/v \tag{1.8}$$
$$v = \mathbf{a_1} \cdot \mathbf{a_2} \times \mathbf{a_3} \tag{1.9}$$

which imply that

$$\begin{aligned} \mathbf{a_i} \cdot \mathbf{b_k} &= 0 \text{ if } i \neq k \\ &= 2\pi \text{ if } i = k \end{aligned}$$

The lattice constructed from the basis set of the three b_i is the reciprocal lattice.

1.3.3 Irreducible Representations of Space Groups

In order to apply the theory of symmetry to a physical situation it is generally necessary to pick a particular representation of the symmetry groups concerned. It follows from the preceding discussion that any element of the space group can be represented in terms of translations (determined by the Bravais Lattice) or rotation-type elements (point group forming the crystal class). Whereas the set of translations and rotation-type elements each form a subgroup of the space group, the glide planes and screw axis do not, as their repeated application leads to lattice translations. There can be many representations of a particular group, however it is most useful to consider the irreducible representations of space groups.

The irreducible representations of the space groups can be constructed by considering the functions

$$\phi_{k\alpha} = u_{k\alpha} e^{i\mathbf{k}\cdot\mathbf{r}} \tag{1.10}$$

where the **k** are constant wave vectors and the $u_{k\alpha}$ have translational invariance with α indexing functions with the same **k**. It follows readily that for any two vectors **k** that differ from one another by a reciprocal lattice vector **b** will have the same transformation properties under translations. Any two such reciprocal lattice vectors are therefore said to be equivalent. This has the consequence that only those wave vectors lying within the unit cell are nonequivalent.

The set of all nonequivalent wave vectors that can be obtained by applying the rotation-type symmetry elements to a **k** constitutes the *star* of **k**. As translations do not bring about changes to **k**, there must be functions $\phi_{k\alpha}$ corresponding to all wave vectors in the star of **k** in any irreducible representation. That set of symmetry elements that may be applied to **k** without effecting any change, that is to say transform it into an equivalent vector, form the proper symmetry group of **k**. The proper symmetry group of a wave vector will be one of the regular point groups. [19] One of the great virtues of the group theoretical treatment of a system is the reduction in the size of the computation that is required to describe the system. Calculations are necessary for only those **k** which are nonequivalent.

1.4 Symmetry of isolated systems

1.4.1 Crystal Field Theory

Here a brief account is made of the treatment of Crystal Field Theory given by Ballhausen. [20] This serves as an effective platform for analyzing transition metal and rare earth metal d-states, which are integral to the work herein. To varying degrees, particularly as one moves towards heavier nuclei in the 3d transition metals, or 5d lathanides, the d-states become more and more localized. This often allows for the treatments of the metal d-states as though the metal ion were part of an ionic complex, and its ligands serving as a source of electric potential of a certain symmetry, and nothing more. This is the basis of crystal field theory; the spherical symmetry of the free atom is broken by the arrangement of ligand ions. The symmetry of the ligands, in concert with their charges, determines the properties of the metal d-states.

The Hamiltonian for the system will be of the form

$$H = H_F + V \tag{1.11}$$

$$H_F = -\frac{h^2}{2m_e}\sum_i \nabla_i^2 - \sum_i \frac{Ze^2}{r_i} + \frac{1}{2}\sum_{i\neq j}\frac{e^2}{r_{ij}} + \sum_i \xi_i(r)\mathbf{l}_i \cdot \mathbf{s}_i \tag{1.12}$$

where H_F is the free ion Hamiltonian and V is the potential of the ligands. The other terms retain their usual meanings: Z and r_i are the number of protons in the central ion's nucleus and the position of electron i with respect to it; e is the elementary charge; r_{ij} is the separation of electrons i and j; the last term in this free ion Hamiltonian describes the spin-orbit interaction between spin and orbital magnetic moments s_i and l_i; m_e is the mass of an electron and h Planck's constant.

The potential V is treated as a perturbation on H_F. It is important to note the size of V with respect to the electron-electron Coulomb interaction and the spin-orbit terms. This consideration suggests three regimes of interest: where $V < \xi(r)\mathbf{l}\cdot\mathbf{s}$, as in rare earths; where $\xi(r)\mathbf{l}\cdot\mathbf{s} < V < \frac{e^2}{r_{ij}}$, as in the first row of transition metals; where $\frac{e^2}{r_{ij}} < V$, as in covalent complexes. These groups pass analytically into one another, but they serve as a good base for understanding the interactions in a given compound.

The Hamiltonian must be symmetric in the symmetry group of the ligand field V. Fields of octahedral, trigonal pyramidal and cubic symmetry are of interest here, and they are depicted in Figure 1.3. Octahedral fields will be discussed in some detail as an example of what to expect in general. The ligand potential can be expanded in spherical harmonics having the form

$$\sum_i \sum_l \sum_m Y_L^m(\hat{\mathbf{r}})R_{nl}(r_i) \tag{1.13}$$

where the leading $l = 0$ term is spherically symmetric and only has the effect of adding a spherical potential around the metal ion. The $R_{nl}(r_i)$ are solutions to the radial Schrödinger equation. To analyze the splitting of the d-states it is therefore useful to split the potential into two terms, the spherically symmetric V_R and the non-symmetric V_0. The splitting of the d-states will be determined by the latter, where the former simply leads to a constant shift in their energies. This constant energy shift is of some interest here for its impact of the position of the barycenter of the ion's d-states. However it is the form of V_0 that is of most interest. Under the operation of octahedral symmetry transformations the d-states are described by the irreducible representations a_{1g}, e_g, t_{1g}, and t_{2g}. Choosing the C_4 axis as the direction of the z-axis the potential can then be seen to take on the form

$$V_0 = x^4 + y^4 + z^4 - \frac{3}{5}r^4 \tag{1.14}$$

which will remove the degeneracy of the d-states, as metal d-electrons seek regions of lower ligand charge density.

The reducible representation spanned by the five d-orbitals contain the irreducible representations e_g and t_{2g}. One therefore needs to find linear combinations of d-orbitals that transform according to these irreducible representations in O_h. Starting with the functions $d_{m_l} = Y_2^{m_l}$ of the form

$$d_{\pm 2} = \sqrt{3/8}(x \pm iy)^2 \tag{1.15}$$
$$d_1 = -\sqrt{3/2}(x + iy)z \tag{1.16}$$
$$d_0 = \frac{1}{2}(3z^2 - r^2) \tag{1.17}$$
$$d_{-1} = \sqrt{3/2}(x - iy)z \tag{1.18}$$

Applying the symmetry elements of O_h it is seen that these orbitals must be grouped in the following linear combinations

$$t_{2g}^0 = \frac{1}{\sqrt{2}}(d_2 - d_{-2}) \qquad t_{2g}^- = d_{-1} \qquad t_{2g}^+ = d_1$$
$$e_g^a = d_0 \qquad e_g^b = \frac{1}{\sqrt{2}}(d_2 + d_{-2})$$

These then can be written as

$$e_g = \left\{ \begin{array}{r} d_{x^2-y^2} = \frac{\sqrt{3}}{2}(x^2 - y^2) \\ d_{z^2} = \frac{1}{2}(3z^2 - r^2) \end{array} \right. \quad t_{2g} = \left\{ \begin{array}{r} d_{xy} = \sqrt{3}xy \\ d_{xz} = \sqrt{3}xz \\ d_{yz} = \sqrt{3}yz \end{array} \right.$$

which are energetically split as shown in Figure 1.3. The symmetries and associated crystal field splitting of d-states shown in the figure will be relevant throughout this work, as will the labelling introduced here. It is both interesting and relevant to note that the energetic separation of the states, 10Dq, is found to vary with known spectrochemical series. They have the form $I^- < Br^- < Cl^- < OH^- < F^- \ldots$, where each successive ion is more electronegative.

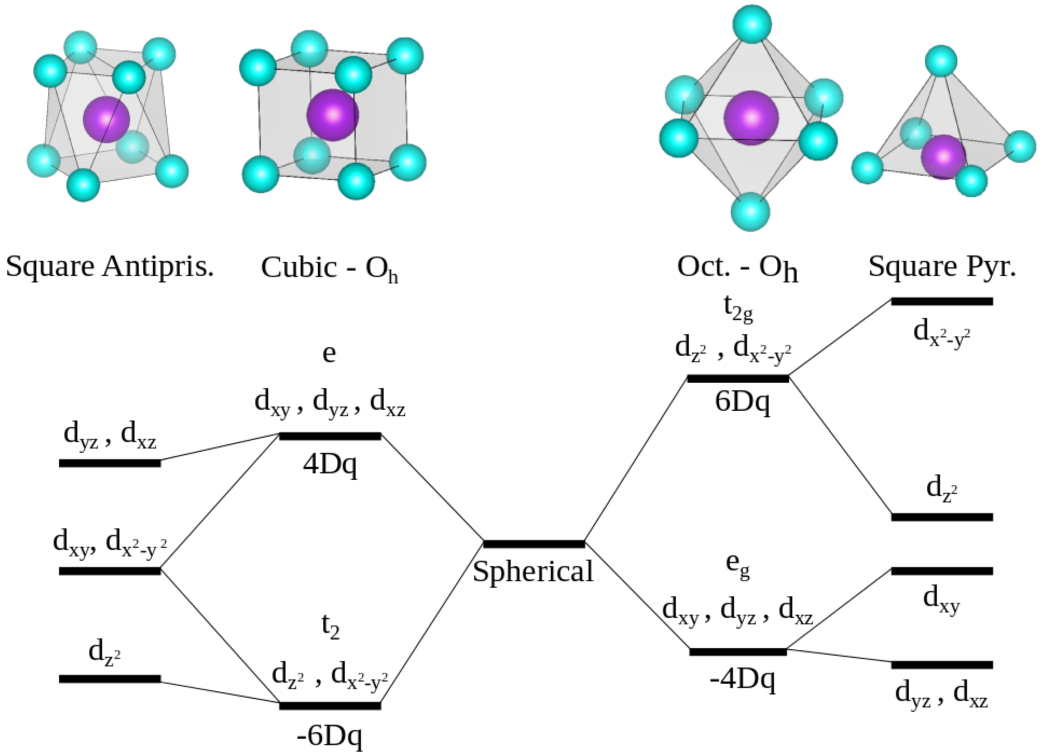

Figure 1.3: Crystal field splitting for relevant geometries.

1.5 The Quantum Mechanical Many Body Problem

The development of solutions to the quantum many-body problem of R. H. Landau are followed here. [21] In order to make theoretical predictions of properties of a quantum system, wavefunctions are needed. If we wish to know the properties of electrons in a material, that is their wavefunctions, the time independent Schrödinger equation for the system must be solved. It is instructive to look at the case of a single atom with N bound electrons, before considering the $\sim 10^{23}$ atoms in a typical solid. The potential experienced by the ith electron will be [21]

$$V_i = \sum_{j=1, j\neq i}^{N} \frac{e^2}{\mathbf{r}_i - \mathbf{r}_j} - Z\frac{e^2}{r_i} \tag{1.19}$$

which immediately takes one outside of the simple case of a spherical potential. The heart of the problem is that the position $(\mathbf{r}_i)$ of electron i is dependent on that of all the other electrons, and the nucleus, which yields the time independent Schrödinger equation

$$\left[\sum_{i}^{N} K_i + V_i(\mathbf{r_1}, \mathbf{r_2}, \ldots)\right]\Psi(\mathbf{r_1}, \mathbf{r_2}, \ldots) = E\Psi(\mathbf{r_1}, \mathbf{r_2}, \ldots) \tag{1.20}$$

where $\Psi(\mathbf{r_1}, \mathbf{r_2}, \ldots)$ denotes the many-electron wavefunction.

Since the above potential is not a sum of single-particle operators, the wavefunction Ψ will not be a product of single particle wavefunctions. [21] At the same time, Ψ must be totally antisymmetric with the interchange of any two coordinates, making the solution for any one electron the solution for all. Any attempt to write the solution of Equation 1.20 as a product of such states is therefore only an approximation.

1.5.1 Hartree Approximation

A useful approximation allowing solutions to the many body problem was proposed by Hartree in 1928. [21] The central idea is that one should be able to describe the system in terms of single-particle, bound-state wavefunctions $\phi_a(\mathbf{r})$, for electron i in state a. This follows from the fact that bound states exist in nature, and that the electrons in the system should be in Eigenstates thereof. There must therefore be a corresponding effective single-particle potential $V_a(\mathbf{r})$ defining the single particle state $\phi_a(\mathbf{r})$, through the single-body Schrödinger equation

$$\left[\frac{-\nabla^2}{2m} + V_a(\mathbf{r})\right]\phi_a(\mathbf{r}) = \epsilon_a\phi_a(\mathbf{r}) \tag{1.21}$$

where a ranges over all single-particle states with energy Eigenvalues ϵ_a. There is still a technical problem that needs to be overcome, which is that the single-particle potential depends on the yet-to-be-determined eigenstates for the other single particle states. Hartree made the approximation that

$$V_a(\mathbf{a}) \simeq \int d^3r' \frac{e^2}{\mathbf{r} - \mathbf{r}'} \sum_{b\neq a}^{N} |\phi_b(\mathbf{r}')|^2 - Z\frac{e^2}{r} \tag{1.22}$$

where $\mathbf{r}'$ is the dummy variable for the coordinates of the other particles. Equation 1.21 represents N integro-differential equations, with the potential depending on the solutions thereof. Such a system can be solved numerically through self-consistent iteration. A guess for the form of the single-particle wavefunctions must first be made, the equations 1.21 can then be solved for a new set of $\phi_a(\mathbf{r})$, which can be used to find new eigenvalues and so on. This process is simply repeated until there is negligible change in the wavefunctions. The solution is then said to have converged. In this approximation the total wavefunction of the sytem is taken to be the simple product of these resulting wavefunctions

$$\Psi(1, 2, \ldots, N) = \phi_a(1)\phi_a(2)\ldots\phi_{A_N}(N) \tag{1.23}$$

A natural first guess for the problem being considered here would be the hydrogenic wavefunctions

$$\phi_a(\mathbf{r}) = \frac{R_{nl}(r)}{r} Y_{lm}(\Omega) \tag{1.24}$$

Although the form of basis states will change considerably, most of these approximations carry over into the solution of large systems with DFT.

1.5.2 Hartree-Fock Equations

The many-fermion wavefunction in Equation 1.23 does not capture an important aspect of such a system, that is the fact that since all of the fermions are identical, their wavefunction must be anitsymmetric under the interchange of particles. This imposes a correlation on the coordinates of any two particles, which leads to the application of the Pauli exclusion principle, or exchange correlations between the electrons. Whereas dynamical correlations might be attractive or repulsive and of limited range, the exchange correlations are typically repulsive and range over the extent of the system itself.

The above many-fermion wavefunction is therefore improved if the exchange correlations are included, which is accomplished by using a Slater determinant for the many-fermion wavefunction [21]

$$\Psi = \frac{1}{\sqrt{N!}} \sum_P (-1)^P \prod_{i=1}^{N} \phi_{PA_i}(i) \tag{1.25}$$

where the sum is over all permutation, P, of the states. Orthogonality must be imposed on the single particle wavefunctions, which is accomplished with a linear combination of the states that result from a self-consistent calculation. This does not alter Ψ, the system energy, nor the dynamical equations for the correlated system, which are the Hartree-Fock equations. Following the variational principle of Rayleigh and Ritz, [21] it can be shown that the Hartree-Fock equation can be written as

$$\epsilon_a \phi_a(\mathbf{r}) = T_a \phi_a(\mathbf{r}) + V_a(\mathbf{r})\phi_a(\mathbf{r}) + \int d^3 r' W(\mathbf{r}, \mathbf{r}')\phi_a(\mathbf{r}') \tag{1.26}$$

$$W(\mathbf{r}, \mathbf{r}') = v(\mathbf{r} - \mathbf{r}')\delta_{sa,sb}\rho(\mathbf{r}, \mathbf{r}') \tag{1.27}$$

$$V_a(\mathbf{r}) = \Phi(r) + U(r) \tag{1.28}$$

$$U(\mathbf{r}) = -e^2 \sum_{b=1}^{N} \int d^3 r' \frac{|\phi_b(r')|^2}{\mathbf{r} - \mathbf{r}'} \tag{1.29}$$

where $v(\mathbf{r} - \mathbf{r}')$ is the electron-electron Coulomb interaction, $\delta_{sa,sb}$ ensures that correlation effects only occur for electrons of the same spin, $\rho(\mathbf{r}, \mathbf{r}')$ is the probability of finding electrons at $\mathbf{r}$ and $\mathbf{r}'$, while $W(\mathbf{r}, \mathbf{r}')$ as a whole represents the effective potential for the electron-electron interactions. $W(\mathbf{r}, \mathbf{r}')$ is inherently non-local as a result of the exchange correlations. The above system of equations reduces to the Hartree equations as the exchange correlation effects are neglected.

For small systems where exchange correlation effects are strong the Hartree-Fock equations are an accurate and effective means for determining the electronic properties of a system. The computational cost becomes prohibitive as the number of particles in the system is increased. As systems reach a size of about 100 particles, other, less accurate, theories are needed. [21] It is in this regime of large fermion systems that modern Density Functional Theories become important. These *models* can be very effective in predicting properties of large fermion systems, but are not without their limitations.

1.5.3 Density Functional Theory

One of the forerunners of density functional theory (hereafter DFT) was the Thomas-Fermi Theory, where the electron density $\rho(\mathbf{r})$ becomes the fundamental variable, as opposed to the wavefunctions. [21] Combining aspects of this theory and the Hartree-Fock theory leads to DFT. The particle density is the basic dynamical variable, but unlike in the Thomas-Fermi Theory which assumes a uniform electron gas, DFT does not. Where the Hartree-Fock theory treats exchange exactly while ignoring other correlations, DFT treats both approximately.

There are clear trade-offs and gains in moving from one theory to another, but for large systems DFT can be highly accurate, while being computationally efficient.

In what follows the account of the basis of DFT and its solutions to the quantum many body problem will follow the discussion in Reference [22]. With DFT the aim is to move beyond the isolated atomic systems just discussed and determine the electronic properties of crystalline solids. In essence one needs solutions to the Schrödinger equation with the many body Hamiltonian for the solid

$$\begin{aligned} H = -\frac{\hbar^2}{2}\sum_i \frac{\nabla^2_{\mathbf{R_i}}}{M_i} - \frac{\hbar^2}{2}\sum_i \frac{\nabla^2_{\mathbf{r_i}}}{m_e} - \frac{1}{4\pi\epsilon_0}\sum_{i,j}\frac{e^2 Z_i}{|\mathbf{R_i}-\mathbf{r_j}|} \\ +\frac{1}{8\pi\epsilon_0}\sum_{i\neq j}\frac{e^2}{|\mathbf{r_i}-\mathbf{r_j}|} + \frac{1}{8\pi\epsilon_0}\sum_{i\neq j}\frac{e^2 Z_i Z_j}{|\mathbf{R_i}-\mathbf{R_j}|} \end{aligned} \tag{1.30}$$

where the nuclei of mass M_i at $\mathbf{R_i}$ interact with the electrons at locations $\mathbf{r_i}$, all of wich interact with each other through the Coulomb potential. DFT addresses the solution to this otherwise intractable problem through three levels of approximation.

First, the Born-Oppenheimer approximation is made, wherein the nuclei are considered to be stationary and in instantateous equilibrium with the much lighter electrons in the system. This reduces the influence of the nuclei to that of an external potential and simplifies Equation 1.30 considerably. All that remains is the electron kinetic energy, electron-electron interactions and this external potential, which is simply expressed as

$$H = T + V + V_{ext} \tag{1.31}$$

This has the interesting effect of dividing the Hamiltonian into a universal electron-electron interaction term, and the system-specific external potential. The preceding Hamiltonian is not a hallmark of DFT, which is founded on two theorems delivered in 1964 by Hohenberg and Kohn. [22]

***Theorem* 1** *There is a one-to-one correspondence between the ground state density* $\rho(\mathbf{r})$ *of a many-electron system (atom, molecule, solid) and the external potential* V_{ext}*. An immediate consequence is that the ground-state expectation value of any observable* $\hat{O}$ *is a unique functional of the exact ground-state electron density:* $< \Psi|\hat{O}|\Psi >= O[\rho]$.

***Theorem* 2** *For $\hat{O}$ being the Hamiltonian $\hat{H}$, the ground-state total energy functional $H[\rho] \equiv E_{V_{ext}}[\rho]$ is of the form*

$$E_{V_{ext}}[\rho] =< \Psi|T+V|\Psi > + < \Psi|V_{ext}[\rho]|\Psi > \tag{1.32}$$

$$= F_{HK}[\rho] + \int \rho(\mathbf{r})V_{ext}(\mathbf{r})d\mathbf{r} \tag{1.33}$$

where the Hohenberg-Kohn density functional $F_{HK}[\rho]$ is universal for any many-electron system. $E_{V_{ext}}[\rho]$ reaches its mimimal value (equal to the ground-state total energy) for the ground-state density corresponding to V_{ext}

There are a few important implications of these theorems. It follows that there is not a loss of information if the electron density is used in place of the unique many-particle wavefunction that would result from solving the Schrödinger equation with the Hamiltonian unique to a system. The second theorem makes the determintation of the ground state electron density possible through application of the Rayleigh-Ritz variational principle. Only that density which minimizes $E_{V_{ext}}[\rho]$ is the ground state density corresponding to the external potential.

A meaningful solution to the Schrödinger equation for the many body problem is within reach. What is needed is a useful form for the Hamiltonian as well as a set of basis functions. Effective basis functions for the materials studied here will be discussed the next section. To address the first point one can start by defining the correlation energy as the energy difference between the exact and Hartree-Fock solutions. It also follows from the preceding discussion that the exchange contribution can be comfortably defined as that part of the energy that is present in the Hartree-Fock solution, but not the Hartree solution. With these definitions a form can now be given to the Hohenberg-Kohn functional in Equation 1.32. Let T, T_0, V and V_H be the exact kinetic energy functional, kinetic energy functional of a non-interacting electron gas, exact electron-electron potential energy functional and Hartree potential energy functional, respectively. The exchange energy and correlation energy are written as

$$V_x = V - V_H \tag{1.34}$$

$$V_c = T - T_0 \tag{1.35}$$

which gives the following form to the sought after functional:

$$F_{HK} = T + V + T_0 - T_0 = T_0 + V_H + (V_x + V_c) = T_0 + V_H + V_{xc} \tag{1.36}$$

If one then interprets the energy functional $E_{V_{ext}}[\rho]$ as that of a non-interacting electron gas subject to the external nuclear and exhange correlation potentials the corresponding Hamiltonian is

$$H_{KS} = T_0 + V_H + V_{xc} + V_{ext} \tag{1.37}$$

giving rise to the Kohn-Sham equation

$$H_{KS}\phi_i = \epsilon_i \phi_i \tag{1.38}$$

which can be solved for the single particle wavefunctions ϕ_i. The exact ground state density for the system under consideration is then

$$\rho(\mathbf{r}) = \sum_{i=1}^{N} \phi_i^*(\mathbf{r})\phi_i(\mathbf{r})$$

Since several operators depend on the electron density itself, the solutions of the Kohn-Sham equation need to be determined numerically through self-consistent iteration.

Choosing the Exchange Correlation Functional

The last detail that needs to be addressed before the Kohn-Sham Hamiltonian can be determined is to choose an approximate form for the exchange-correlation potential. Until this point the only other approximation made was the Born-Oppenheimer approximation. A widely used and theoretically satisfying choice is to use the Local Density Approximation (LDA), where the exchange-correlation energy fucntional is postulated to be

$$E_{xc}^{LDA} = \int \rho(\mathbf{r})\epsilon_{xc}(\rho(\mathbf{r}))d\mathbf{r} \tag{1.39}$$

with $\epsilon_{xc}(\rho)$ is the function describing the exchange-correlation energy of a homogeneous electron gas of a given density. This functional is expected to be accurate for slowly varying densities, but generally outperforms this expectation.

A natural next step is to let the exchange-correlation energy depend on the density at neighbouring points in space, in addtion to the density at the point being considered. This in effect makes it dependent on the gradient of the density and gives rise to another popular approximation, the Generalized Gradient Approximation (GGA). Although accurate for many cases the GGA is empirical and many forms exist. [23] The LDA has the advantage of having a unique form. In the work presented here the GGA of Perdew, Berke and Ernzerhof (GGA-PBE) which takes the rather typical form

$$E_C^{GGA} = \int d^3r \ n[\epsilon_C^{unif}(r_s, \zeta) + H(r_s, \zeta, t)] \tag{1.40}$$

where r_s is the local Seitz radius, ζ the relative spin polarization and t a dimensionless density gradient. In addition to the first term in the integrand, which is common to the LDA, there is a second term $H(r_s, \xi, t)$, which depends on the density gradient. [24]

Choice of Basis Set

At this point one is left with an infinite set of single particle (sp) dynamical equations

$$H_{sp}\phi_m(\mathbf{r}) = \epsilon_m \phi_m(\mathbf{r}) \tag{1.41}$$

which for the case at hand is the Kohn-Sham equation, but this form is common to the Hartree-Fock approximation as well, for example. The difference in the two approaches is, as mentioned, the treatement of exchange and correlation energies. In either case the method of solution is the same.

The final step is to choose a basis set for the solution of Equation 1.41. Choosing functions of the form

$$\phi_m(\mathbf{r}) = \sum_{p=1}^{P} c_p^m \phi_p^b \tag{1.42}$$

solution of Equation 1.41 ammounts to determining the coefficients c_p^m required to express $\phi_m(\mathbf{r})$ in terms of the ϕ_p^b. This amounts to diagonalizing a PxP matrix, where P is infinite in the case of an exact solution. Use of a finite basis and a particular form of basis function are the last approximations needed to solve the equations governing the many-body system.

A Brief Account of (L)APW Methods

There are many choices of basis set available and each will have its own advantages and disadvantages. To develop a picture of what will be most effective, it is worth considering a few common and historically relevant basis sets. A natural guess for solving the periodic hamiltonian of crystal systems is to use a plane wave basis, leading to Eigenfunctions of the form

$$\psi_{\mathbf{k}}^n(\mathbf{r}) = \sum_{\mathbf{K}} c_{\mathbf{K}}^{n,\mathbf{k}} e^{i(\mathbf{k}+\mathbf{K})\cdot\mathbf{r}} \tag{1.43}$$

where it can be seen that the index m of Equation 1.42 corresponds to the pair $(n, \mathbf{k})$. Some maximum value of K at which to cut off the basis set must be selected. This will define a sphere of radius K_{max} in reciprocal space, which can also be expressed as an energy

$$E_{cut} = \hbar \frac{K_{max}^2}{2m_e}$$

A solution to Equation 1.41 will be needed at a number of different $\mathbf{k}$ in order to provide a sufficiently dense sample of the frist briollouin zone. The solutions at each point in reciprocal space will yield P energy Eigenvalues, each of which corresponds to another band index.

The principle problem with a planwave-only basis is that of describing the rapid changes in the wavefunctions near the nucleus of an atom. An intractable number of plane waves is needed. This problem lead to the development of *psuedopotential* methods where the exact nuclear potential is replaced by a smooth pseudopotential that approximates the exact potential near the atom's exterior, while yielding a slowly varying tail to the wavefucntion in its interior. Such an approximation does not allow calculation of properties involving the core states of a material, and for the studies conducted here is insufficient.

In order to avoid the use of pseudopotentials, a basis set that is more efficient in the vicinity of the nuclei is needed. A natural choice is a set of spherical harmonics, paired with radial solutions to the free atom Schrödinger equation. At the same time this is likely to be an inefficient basis far from the nuclei. Both situations are addressed if the space within the crystal is divided into two regions: a collection of spherical regions S_α composed spheres of radius R_α surrounding each atom, and the remaining interstitial space, I. Spherical harmoncis and plane waves can be used in the regions where they will be most efficient yielding the, now outdated, but conceptually relevant Augmented Plan Wave (APW) basis

$$\phi_{\mathbf{K}}^{\mathbf{k}}(\mathbf{r}, E) = \begin{cases} \frac{1}{\sqrt{V}} e^{i(\mathbf{k}+\mathbf{K})\cdot\mathbf{r}} & \mathbf{r} \in I \\ \sum_{l,m} A_{lm}^{\alpha,\mathbf{k}+\mathbf{K}} u_l^\alpha(r', E) Y_m^l(\hat{r}') & \mathbf{r} \in S_\alpha \end{cases} \tag{1.44}$$

There are a few important consequences that result from this choice of basis and bifurcation of space into 'muffin tin spheres' and an interstitial region. Wavefunctions must be continuous across the interface between the muffin tins and the interstitial region. This determines the form of the coefficients $A_{lm}^{\alpha,\mathbf{k}+\mathbf{K}}$. A perfect match between the plane waves and spherical harmonics would require an infinite sum over l, which again means that a truncation must occur at a maximal value of l that is deemed good enough, l_{max}. The matching criterion is that the number of nodes of the function within and outside of the muffin tin spheres should be about the same. For a sphere of radius R_α and a plane wave cut off K_{max}, this occurs when $R_\alpha K_{max} = l_{max}$. This provides the additional guiding principle that the values of R_α in a given calculation should be kept roughly similar, so that they all require the same l_{max}. Although the APW method is no longer in use, the ideas presented here carry forward to the important Linearized Augmented Plane Wave (LAPW) and local orbital (LO) basies that are used in the calculations given here.

To overcome the dependence of Equation 1.44 on the yet-to-be determined energy $E = \epsilon^n_{\mathbf{k}}$, a Taylor series expansion of $u^\alpha_l(r', E)$ can be made about the fixed energy $E^\alpha_{1,l}$. Including only the first and second order terms of the exapansion givs the LAPW basis functions

$$\phi^{\mathbf{k}}_{\mathbf{K}}(\mathbf{r}) = \begin{cases} \frac{1}{\sqrt{V}} e^{i(\mathbf{k}+\mathbf{K})\cdot\mathbf{r}} & \mathbf{r} \in I \\ \sum_{l,m} \big(A^{\alpha,\mathbf{k}+\mathbf{K}}_{lm} u^\alpha_l(r', E^\alpha_{1,l}) + & \\ B^{\alpha,\mathbf{k}+\mathbf{K}}_{lm} \dot{u}^\alpha_l(r', E^\alpha_{1,l}) \big) Y^l_m(\hat{r}') & \mathbf{r} \in S_\alpha \end{cases}$$

To address the technical problem encountered when two states with the same l , but different principle quantum number, *local orbitals* (LO) are used and have the following form

$$\phi^{lm}_{\alpha,LO}(\mathbf{r}) = \begin{cases} 0 & \mathbf{r} \notin S_\alpha \\ \big(A^{\alpha,LO}_{lm} u^\alpha_l(r', E^\alpha_{1,l}) + B^{\alpha,LO}_{lm} \dot{u}^\alpha_l(r', E^\alpha_{1,l}) & \\ + C^{\alpha,LO}_{lm} u^\alpha_l(r', E^\alpha_{2,l}) \big) Y^l_m(\hat{r}') & \mathbf{r} \in S_\alpha \end{cases}$$

The use of local orbitals mitigates the problem of choosing a single energy value for semi-core and valence states with the same l. The local orbital is defined for a particular atom (α), l and m. Further, the LO is normalized, in addition to having zero value and slope at the muffin tin boundary.

In a similar vein to the above LAPW+LO basis, local orbitals can be added to an APW basis, leading to an APW+lo basis set. Such a basis is usually more effective in treating d- and f-states, as well as states with relatively small muffin tin sphere radii, than is the LAPW+LO basis. At the same time, like the LAPW+LO basis, all energy eigenvalues are obtained in a single diagonalization. In light of this WIEN2k, which is used for all of the DFT calculations presented herein, uses a mixed LAPW+LO/APW+lo basis. [23]

1.6 An Intuitive Approach to Band Structures

The following is based on the acount of electronic structure given by W. A. Harrison. [12] A useful conceptual picture of the electronic structure of a solid can be formed by first considering bond formation in simple, molecular systems. As many atoms are brought together in the formation of a crystalline solid, the number of electronic states is still conserved, as with simple molecules, though now the number of states is on the order of 10^{23}. As a consequence, as the atoms are drawn together, they do not form sharply defined bond and anti-bond states, but rather bands between these limits. [12] The formation of the bands, which consist of many states of slightly differing energies as the crystal momentum is varied, is a necessity of the Pauli exclusion princliple in the periodic lattice.

How atomic states can be transformed into the bands seen in solids is intuitively demonstrated in the *linear combination of atomic orbitals* (LCAO) model of electronic structure. As opposed to using the quite general basis functions shown in the last section, a basis of atomic oritals is used to describe the electron wavefunctions. For example, the states of the low-lying, valence s-band of CsCl, a highly ionic system, can be taken as

$$|\psi >= \sum_i u_i |s_i > \tag{1.45}$$

where i ranges over all Cl atoms. Due to the high polarity of the bonding in this crystal, the Cs valence electrons will spend most of their time at the Cl sites. The Cl s- and p-states can therefore be taken as the basis for the occupied states and the Cs s-states a basis for the unoccupied states. Equation 1.45 leads to the systems of dynamical equations

$$\sum_i H_{ij} u_i - E u_j = 0 \tag{1.46}$$

Making the simple approximation of interactions between nearest neighbour Cl atoms, and periodic boundary conditions, leads to solutions of the form

$$E(\mathbf{k}) = \epsilon_s - V_2 \sum_{i=1}^{6} e^{i\mathbf{k}\cdot\mathbf{r}_i} \tag{1.47}$$

where $V_2 = H_{ij} =< s_j|H|s_i >$ and $\epsilon_s = H_{ii}$. The sum in Equation 1.47 suns over the nearest neighbour Cl ions in the close packed CsCl structure. The p-states of the crystal can be determined similarly. In either case the atomic orbitals form periodic bands of states in the crystal. The natural energetic separation of the Cl p- and s-states will give rise to energetically separated bands. If the atomic potential is reduced, for example by moving vertically downwards in a column of the periodic table, this separation decreases. In the limit of free electrons, the separate bands become those of free electrons, appropriate for describing states in metals. [12]

A discussion of different solid types also follows naturally from the preceding ideas. The different characteristics of metallic and semiconducting solids, as well as polar and nonpolar solids, can be understood by considering the changes in electronic structure that occur in bringing various atoms together, at various interatomic spacings. If for example one considers a collection of Si atoms being drawn together, as the atomic orbitals begin to overlap, a filled s-band and half-filled p-band will form, as shown in Figure 1.4. This will give rise to a metallic system. As the atoms are brought closer together and the bands become broader, they will eventually reach one another. When this occurs, a gap will open with four bonding states below and four antibonding states above. With further decreases in interatomic distance the bond-anitbond splitting will simply increase in the now semiconducting silicon crystal. It is interesting to note that this crossing of bands will only occur if the symmetry of the systems is such that there are no matrix elements between the p- and s-states. If there are non-zero matrix elements between the states the bands will not cross, leaving the system metallic. The crossing of bands is associated with covalent bonding.

The effect of interatomic distances is well displayed by considering the homopolar series of semiconductors formed be C, Si, Ge, Sn. Diamond has the smallest interatomic distance and the largest band gap, and this decreases along this series until a zero band gap is attained in Sn. Another important concept in this vein is the 'metallicity' of an atom, which will be rigorously defined below, and increases along the C → Sn series. The metallicity will be seen to increase along this series as the energetic separation of the s- and p-states decreases, with the decreasing atomic potential felt by the valence electrons.

The preceding effect is shown in Figure 1.4, along with the effects of varying polarization in the crystal, which will now be briefly discussed. The effects of polarization are clearly demonstrated by considering the isoelectronic series of tetrahedral, polar semiconductors:

Ge, GaAs, ZnSe, CuBr. As one moves along this series one nuclear charge is added to the non-metallic atom, and one removed from the metallic atom. They can at this point be considered the anion and cation, repectively, since a disproportionate amount of negative charge will reside on the non-metal. As the system becomes more polar, the valence and conduction bands will separate into increasingly narrow s- and p-bands, while the band gap will increase.

To further tie these trends together, it is interesting to consider the stability of different crystal structures as the polarity or metallicity of the atoms in a tetrahedral solid are varied. As the polarity increases, or the metallicity increases, the angular forces stabalizing the tetrahedral arrangement of atoms weaken. Polar solids will eventually collapse into an insulating compound in the rocksalt structure, as in CsCl. In such a case the electronic structure is well-described in terms of the states of isolated ions, as above. As the metallicity of a compound increases, there will again be a collapse into a close-packed structure, which will now be conducting and the states free-electron-like.

Before moving on to discuss a few important special cases, it is worth looking at a general trend that was found by Harrison and Ciraci in 1974. [12] It was found that the interatomic matrix elements between atoms in solids tend to scale as the inverse square of the interatomic distance, d. This was solidified whith the derivation of the general relation

$$V_{ll'm} = \eta_{ll'm}\hbar^2/(m_e d^2) \tag{1.48}$$

which results from the comparison of LCAO and free-electron bands. Here, $\eta_{ll'm}$ is a structure-dependent constant for interaction between orbitals of character l/l' and orientation designated by m.

1.6.1 Tetrahedral Solids

Tetrahedral solids are of central importance here, and their structure and properties can be better understood by considering the LCAO description of their electronic structrues. Most of the relevant characteristics can be seen by looking at simple, monoatomic, tetrahedral solids. The generalization to mixed tetrahedral solids is relatively straight forward thereafter.

The two simplest crystals containing tetrahedrally coordinated atoms are the zinc blende and wurtzite structures. The former can be constructed by starting with a cubic close-packed

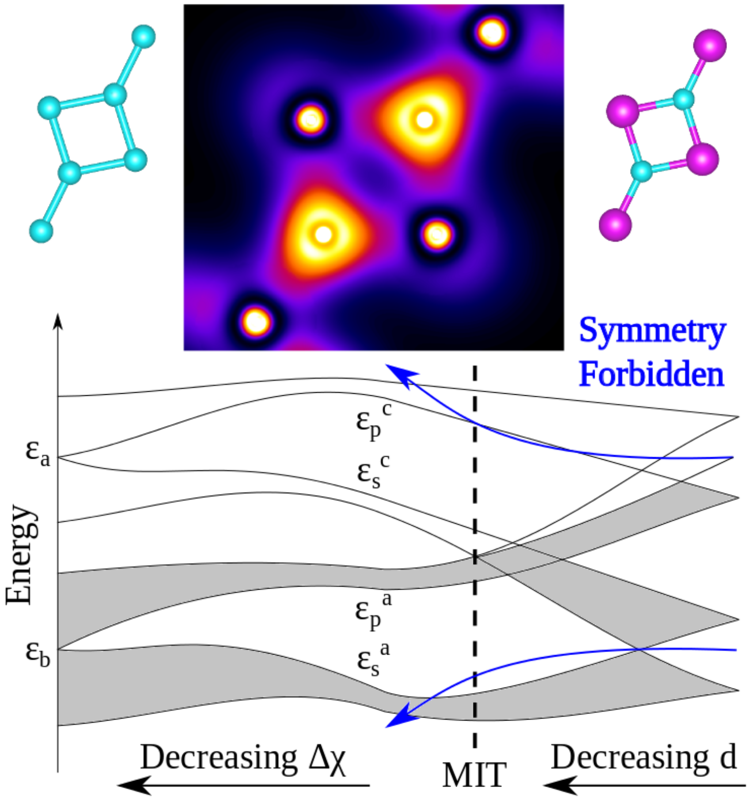

Figure 1.4: Visualization of the effects of changing crystal symmetry, interatomic spacing and bond polarity, adapted from [12]. The left of the bottom shows the band structure of a homopolar solid. The center shows a covalent polar solid, with the electron density of trigonally coordinated N atoms in P_3N_5 as an example. Adjacent to the electron density are simple ball and stick models of the atomic configuration, with N atoms in cyan and phosphorus in magenta. Filled bands are shaded grey, making the band structure at the left and right of the figure insulating and metalic, respectively.

structure of one type of atom (stacking is ABCABCABC) and then adding a second type of atom directly above the atoms in each layer, three quarters of the way to the upper layer. The wurtzite structure is formed in the same way with by starting with stacking ABABAB. An appropriate basis set for a LCAO description of such structure is one of sp^3 hybrid orbitals.

Starting with the normalized p- and s-orbitals $|p_i>$ and $|s>$, the sp^3 hybrid states are given by the linear combinations

$$|h_1 >= \frac{1}{2}[|s > +|p_x > +|p_y > +|p_z >]$$
$$|h_2 >= \frac{1}{2}[|s > +|p_x > -|p_y > -|p_z >]$$
$$|h_3 >= \frac{1}{2}[|s > -|p_x > +|p_y > -|p_z >]$$
$$|h_4 >= \frac{1}{2}[|s > -|p_x > -|p_y > +|p_z >]$$

which are orriented in the [111], [$1\overline{1}\overline{1}$], [$\overline{1}1\overline{1}$], and [$\overline{1}\overline{1}1$] directions respectively, with axis being cubic and pointing to nearest neighbour atoms of one species. The expectation value of the energy of these states is the average of $\epsilon_s =< s|H|s >$ and $\epsilon_p =< p_x|H|p_x >=< p_y|H|p_y >=< p_z|H|p_z >$, called the *hybridization energy* with value

$$\epsilon_h = (\epsilon_s + \epsilon_p)/4 \tag{1.49}$$

This construction is also relevant for mixed tetrahedral solids. The sp^3 hybrids can be constructed in the same way for each atomic species, which will have hybrid energies ϵ_h^1 and ϵ_h^2. It is useful to construct a hybrid polar energy

$$V_3^h = (\epsilon_h^1 + \epsilon_h^2)/2 \tag{1.50}$$

which gives rise to bond polarity in the crystal. The hybrid covalent energy is the matrix element between hybrid orbitals that are directed towards one another. It gives rise to the bond-antibond splitting and can be given as

$$V_2^h =< h^1|H|h^2 >= (-V_{ss\sigma} + 2\sqrt{3}V_{sp\sigma} + 3V_{pp\sigma}) \tag{1.51}$$

A schematic of the hybrid energy levels is given in Figure 1.5.

It is also informative to consider the matrix elements that exist between the hybrid orbitals of one site. These give rise to the *metallic energy*, which is simply proportional to the energetic separation of the atomic s and p orbitals, in keeping with the usual notion of metallicity. The matrix element has the form

$$< h_i|H|h_j >= -\frac{1}{4}(\epsilon_p - \epsilon_s) = -V_1 \tag{1.52}$$

These matrix elements in relation to the atomic term values are also shown in Figure 1.5.

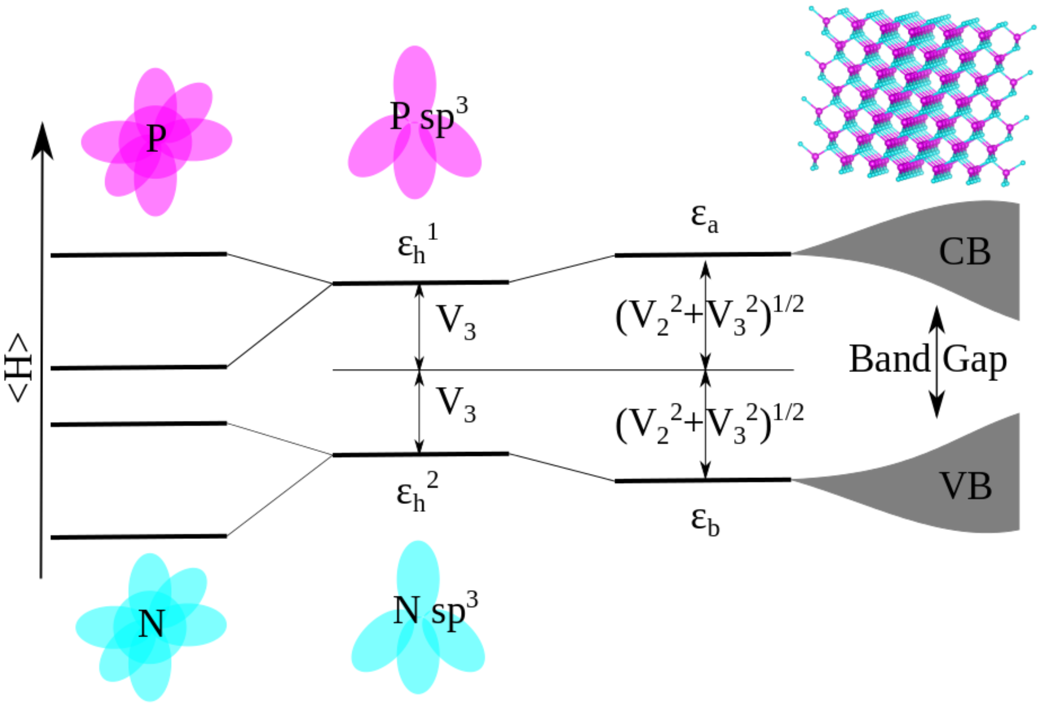

Figure 1.5: Hybridization and splitting of states in a polar, covalent solid. P_3N_5 is used as an example. Matrix elements are as defined in the text. Adapted from [12].

The use of the above hybrid orbitals as a basis set for the solution of the time independent Schrödinger equation leads to several informative results. One is to find an analytic form for the bond-antibond splitting, which can be found to be

$$\epsilon_b = \bar{\epsilon} - \sqrt{V_2^2 + V_3^2} \tag{1.53}$$

$$\epsilon_a = \bar{\epsilon} + \sqrt{V_2^2 + V_3^2} \tag{1.54}$$

where $\bar{\epsilon}$ is the average hybrid energy. Using the matrix elements defined above it is also possible to define a bond polarity with the form $\alpha_p = V_3/(V_2^2+V_3^2)^{1/2}$. The development this far already serves as a useful tool for predicting material properties in a semi-quantitative fashion.

A more detailed description of tetrahedral semiconductors, based on the same ideas, requires the use of Bloch sums, which can make use of hybrid orbitals as just discussed, or simple atomic orbitals. As it happens the latter leads to particularly simple and illuminating results. The sums will have the form

$$|\chi_\alpha(\mathbf{k})>=\sum_i e^{i\mathbf{k}\cdot\mathbf{r_i}}|\phi_\alpha(\mathbf{r}-\mathbf{r_i})>/\sqrt{N_i} \tag{1.55}$$

and lead to eigenstates for a given wavenumber

$$|\psi_\mathbf{k}>=\sum_\alpha u_\alpha|\chi_\alpha(\mathbf{k})> \tag{1.56}$$

As per usual the dynamical equations

$$\sum_\beta H_{\alpha\beta}(\mathbf{k})u_\beta = E_\mathbf{k}u_\alpha \tag{1.57}$$

$$H_{\alpha\beta} =< \chi_\alpha(\mathbf{k})|H|\chi_\alpha(\mathbf{k})> \tag{1.58}$$

need to be solved. With the atomic p- and s-states chosen as the basis the Hamiltonian can be written in terms of the composite matrix elements

$$\begin{aligned}
E_{ss} &= V_{ss\sigma}\\
E_{sp} &= -V_{sp\sigma}/\sqrt{3}\\
E_{xx} &= \frac{1}{3}V_{pp\sigma}+\frac{2}{3}V_{pp\pi}\\
E_{xy} &= \frac{1}{3}V_{pp\sigma}-\frac{1}{3}V_{pp\pi}
\end{aligned}$$

The solutions of these equations will need to be done numerically in general but the result at the Γ point is easily evaluted to give state energies

$$E=\frac{\epsilon_s^c+\epsilon_s^a}{2}\pm\sqrt{\left(\frac{\epsilon_s^c-\epsilon_s^a}{2}\right)^2+(4E_{ss})^2} \tag{1.59}$$

$$E=\frac{\epsilon_p^c+\epsilon_p^a}{2}\pm\sqrt{\left(\frac{\epsilon_p^c-\epsilon_p^a}{2}\right)^2+(4E_{xx})^2} \tag{1.60}$$

This result gives exact energies for states at the Γ point in tetrahedral solids and a means to evaluate the band separations. The band gap is a result of the dominance of bond-antibond splitting over the breadth of the bands. As the splitting is decreased a transition to the metallic state is approached.

1.6.2 d-block Metals

The d-states of d-block elements have similar energies to their valence s-states. However, due to their large angular momentum they have a radial distribution that is drawn closer to the atom's nucleus, as shown earlier in Figure 1.1. The greater radial extent of the s-states holds atoms far enough apart that the d-states do not overlap greatly. As a result the d-electrons tend to behave in a way that is more atomic, than itenerant in nature. Consequently, the intra-atomic Coulomb interaction of the d-electrons tends to dominate the matrix elements that would otherwise lead to band formation. The degree to which this is the case varies from metal to metal across the 3d transition metal series. As the nuclear charge and electronegativity increase, the d-states become more and more localized. The early transition metals have well developed d-bands, whereas the late transition metals are better described by the multiplet physics of isolated d-electrons. Structure will also play a role in determining the exact nature of these states. The f-states of the lathanides are quite similar to the transition metal 3d-states, though their localization is even more extreme.

The d-states are unique because of the two competing energies in materials that contain them. The relative magnitude of the matrix elements between d-states and the Coulomb interaction energy U are highly influential in determining the properties of such compounds. In the latter case, the energy U is required to move an electron from one site to another. It is only when the coupling between states on neighbouring atoms excedes U that a description in terms of itinerant electrons is most appropriate. Where the balance lies for a given compound will clearly be influential for its conduction properties. [25]

A few additional characteristics of transition metals can be briefly considered. As the potential well at the metal sites deepens, the s-states decrease in energy more rapidly than the p-states, leading an increase in V_1 and a general improbability of tetrahedral complexes forming. The spins of the electrons in the partially filled d-shells tend to be aligned as a result of Hund's rule. This is the source of the interesting magnetic properties of many transition metals. When the coupling between the spin moments on different sites is small, a large paramagnetic susceptibility results. However some coupling always exists, even though the magnetic interaction between sites may be small. There are nonmagnetic interactions through which the spins can be aligned. [12] Of the utmost importance are the trends of decreasing localization as one moves to lighter nuclei in a row of metals, and as one moves down a column of the periodic table. The radial extend of d-states becomes more like s-states for the 4d and 5d orbitals. Even the 5f states at the far left of the actinides form bands. [12] This emphasizes the importance of geometry if localized 4d or 5d states are to exist in a given lattice. It is worthwhile to close this section by considering two instructive, and common, transition metal compound types.

Monoxides

The transition metal monoxides are held together by ionic forces, much as discussed for CsCl above, and the associated electronic structure can be described in the same way. They consequently all take on the rock salt structure and most are insulators. Their more interesting properties stem from the electronic structure of their d-states. In this picture the metal ions have n-2 electrons and are surrounded by six O^{2-} ions. If the d-states are temporarily ignored, the electronic structure will be of the form shown in Figure 1.6 for MnO. The valence band is composed of O 2p-states and the conduction band is a band of Mn s-states. To a first approximation the Mn^{2+} d-states can be overlain with the bands to give a fuller picture of the electronic structure, with the ^6S ground state of the Mn d-electrons lying a few eV below the s-band. The d-states will be further modified by crystal field splitting in cases where the ground state is not spherically symmetric. The splitting will tend to quench the orbital angular momentum. This was briefly introduced in Section 1.4.1. As the strength of the crystal field splitting increases a qualitative change in the state of the system may occur, in which the differences in orbital energy would exceed the exchange energy that leads to Hund's rules. There would then be a tendency for the electrons to form pairs and reduce the system's spin. In such a case the band picture becomes useful again. A classic example of systems where this occurs is the perovskites.

Perovskites

It is typical of the perovskites, such as $SrTiO_3$, to have a conduction band that is composed of the metal, here Ti, d states. They may be conducting or not, depending on the number of electrons in the system. In cases where there are many d-electrons per metal ion, a multiplet

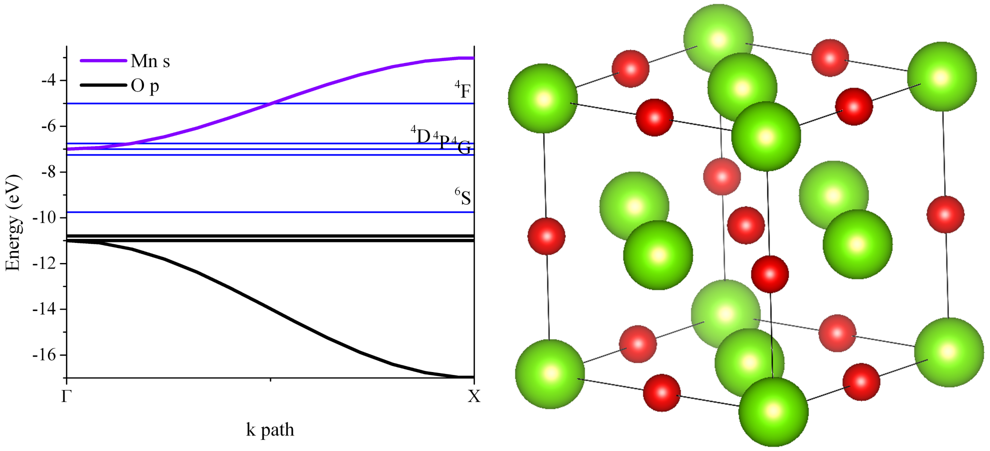

Figure 1.6: A conceptual band structure plot of MnO, based on nearest neighbour orbital overlap as described above for CsCl, and d-state multiplet energies (blue bands) given in [12]. The Mn d-states are assumed to be isolated from their environment as a first approximation. Such a scheme will become a better approximation in the case of 4f multiplets that are of some concern here. Right: rock salt MnO structure with Mn in green and O in red.

structure may still form. Of principle interest here is a description of systems in terms of bands of states. This discussion will be seen to be of considerable utility in the analysis of V_2O_5 compounds and the rare earth phosphors presented here.

A treatment similar to what was outlined above for the band structure of tetrahedral solids can also be carried out for the perovskite structure. [12] For a simple model of $SrTiO_3$ the Eigenvalues at the Γ point are found to have the form

$$\Gamma_{15} = \epsilon_p \pm 4\sqrt{2}E_{xx}$$
$$\Gamma_1 = \epsilon_s$$
$$\Gamma_{12} = \frac{\epsilon_s + \epsilon_d}{2}\sqrt{\left(\frac{\epsilon_s - \epsilon_d}{2}\right)^2 + 6V_{sd\sigma}^2}$$
$$\Gamma'_{25} = \epsilon_d$$
$$\Gamma_{25} = \epsilon_p$$

where the subscripts of Γ denote the irreducible representations to which the atomic orbitals belong. Only those orbitals transforming as the same irreducible representation will mix. Again, this emphasizes the importance of crystal structure in determining properties. It is a significant result that an excellent description of the valence and conduction bands is formed by considering only the O s-, O p-, and Ti d-states. This leads to the conclusion that the role of the body-centred ion in the perovskite, here Sr, has little role beoyond the contribution of the electrons to the system. The Sr s- and d-states are at sufficiently high energies in comparison to the others that they have little influence on the band structure around the gap. Again, this will be seen to be highly relevant in the studies of vanadium oxides pursued in the work presented here. The matrix elements appearing in the above equations are well described by the relation

$$V_{ldm} = \eta_{ldm} \frac{\hbar^2}{m} \frac{r_d^{3/2}}{d^{7/2}} \tag{1.61}$$

which can be derived from transition-metal psuedopotential theory. [12] The parameter r_d is the atom-specific d-state radius and as before d is the interatomic distance.

This section can be closed by discussing a few general features of the transition metals and their mathematical description. The lion's share of these compounds can be analyzed by starting with an ionic picture and applying the interatomic matrix elements (covalency) as a perturbation. This holds even for tetrahedral compounds. It is also generally possible to consider those d-electrons that do not participate in bonding as existing in multiplets, which remain distinct from the other bands in the electronic structure. [12]

Crystal Momentum

At several points in this thesis a discussion of the dynamics of electrons or other charged particles within crystals will be needed. It is therefore useful to briefly touch on the subject at this point. The dynmanic properties of electrons in a crystal can be described using a linear combination of energy Eigenstates, which form a wave packet. One can be formed by considering states with wave numbers near some k_0 in the first Brillouin zone such that

$$\psi(\mathbf{r}, t) \propto e^{-|\mathbf{k}-\mathbf{k_0}|^2} \psi(\mathbf{r}, 0) e^{-iE(\mathbf{k})t/\hbar} \tag{1.62}$$

wich corresponds to a wavefunction ψ_{k_0} modulated by a Gaussian profile, so long as $|\mathbf{k} - \mathbf{k_0}|$ is small. This wave packet will move with a velocity

$$\dot{\mathbf{r}} = \frac{1}{\hbar} \frac{\partial E(\mathbf{k})}{\partial \mathbf{k}} \tag{1.63}$$

which is consistent with the expectation value for the current operator on a state ψ_{k_0}. Under the influence of a slowly varying potential $V(\mathbf{r})$ one has that

$$\hbar \frac{d\mathbf{k}}{dt} = -\frac{dV}{d\mathbf{r}} \tag{1.64}$$

The two preceding equations completely describe the dynamics of electrons in a band. At the same time it is found that $\hbar\mathbf{k}$ corresponds to the classical momentum $\mathbf{p}$. It can also be seen that the electron velocities will be dependent on the energetic breadth of the bands. Narrow bands will correspond to slow moving, massive, electrons, while broad bands will correspond to lighter electrons with correspondingly greater speeds. Narrow bands are characteristic of the upper valence band states in insulators, for example, while broader bands are seen in metals.

1.7 Soft X-ray Spectroscopy

1.7.1 Basics of X-ray Interactions With Matter

Before considering finer details of the interaction of x-rays with matter, the general properties of materials with respect to the absorption and emission of x-rays will be considered. Essentially this will amount to considering the rate at which a particular atom in a solid absorbs and emits electromagnetic radiation of particular energies. Although much of the analysis herein focuses on the finer details of photon-matter interactions, the general development in this section will be very important for understanding a few special cases. In particular a relation is derived for the expected photon emission intensity from an irradiated material, which is essential to the following studies of VO compounds.

The probability that a photon interacts with an atom is given by the atomic interaction cross section, μ_{at}, which is dependent on the atom involved (Z), as well as the energy of the incident x-ray. The total atomic cross section can be specified in terms of its constituent processes

$$\mu_{at} = \tau_{at} + \sigma_{at,coh} + \sigma_{at,incoh} \tag{1.65}$$

where τ_{at} is the photo-absorption cross section, and $\sigma_{at,coh}$, $\sigma_{at,incoh}$ are the coherent (elastic) and incoherent (inelastic) scattering cross section. [26] For the photon energies of interest here these are the only interactions that need to be considered. [27] Since it is quite instructive for understanding trends in matter-xay interactions, the quantum field theoretical derivation of τ_{at} is outlined below in Section 1.7.3.

The probability of a photon interacting with an atom in a material, p_{at}, will be related to the probability of interaction with one of n atoms as follows: $p_n = 1 - (1 - p_{at}) \approx e^{-np_{at}}$. The approximation is valid for $p_{at} \ll 1$ or n large. It is clear the $1 - p_{at}$ will be equal to the ratio of the number of x-rays leaving a thin sample (N) to the total number incident (N_0), leading to the expression

$$\frac{N}{N_0} = e^{-np_{at}} = e^{-\hat{n}\mu_{at}} \tag{1.66}$$

where in the last step the equivalence of np_{at} and $\hat{n}\mu_{at}$ is used, with $\hat{n}$ the areal density of the atoms.

It is more common to use the mass or linear attenuation coefficients, than it is to use μ_{at}. With units of $[cm^2/g]$ the mass attenuation coefficient is defined as $\mu_{mass} \equiv \mu = \mu_{at}\frac{N_{av}}{W_Z}$, where N_{av} and W_Z are Avogadro's number and the atomic weight of element Z. The linear attenuation coefficient–the probability of interaction per unit length traversed by the x-rays–, $\bar{\mu}$, is then easily defined as

$$\bar{\mu} = \rho\mu = \mu_{at}\rho\frac{N_{av}}{W_Z} \tag{1.67}$$

giving rise to the useful relation

$$\frac{N}{N_0} = e^{-l\bar{\mu}} \tag{1.68}$$

for describing the attenuation of the x-ray beam over some path length l. This is of course the well-known Beer-Lambert Law, known for visible light attenuation well before the discovery of x-rays.

The last step before deriving the desired equation is to enumerate a few of the other quantities that are needed to describe the absorption and emission processes of atoms in a material. Since compounds are of interest the relation between the total attenuation coefficient and those of the constituent atoms (j) is needed, and has the following form:

$$\mu_{at} = \sum_j C_{at,j}\mu_{at,j}$$

where the coefficients $C_{at,j}$ are the atomic concentrations in the material. The equation that will be made use of here is the analogue of the preceding equation for mass attenuation coefficients

$$\mu = \sum_j C_j\mu_j \tag{1.69}$$

where C_j is the mass fraction of each atom in the material. Photoabsorption in particular subshells is of interest, which is described by the *edge jump ratios*–the fraction of photons absorbed by a subshell of interest–S_K, S_{L1}, …, and so on. Once photo-absorption has occured the probability of emission of a photon of a particular energy becomes relevant. The atom may de-excite to fill the emptied core state through either Auger electron emission, or emission of a fluorescence photon. The probabilities of the two events consequently add to unity. Only fluorescence photon emission, with *fluorscence yield w*, is of interest here.

An equation for the fluorescent photon intensity expected from a particular atomic species in a sample following *direct* excitation can now quickly be derived. In reality there is the possibility for secondary, tertiary, and so on, absorption events, but the related equations can be derived using the same ideas as the following derivation. The approximation of direct excitation only is sufficient for the analysis herein.

One can first consider how many photons will be absorbed by an infinitesimal slice of the material under consideration, when irradiated with some incident photon intensity I_0:

$$dI_i = I_0 \hat{\mu}_i e^{-l\mu_{\hat{M},0}/\sin\theta} \frac{dl}{\sin\theta} \tag{1.70}$$

as shown in Figure 1.7. In order to obtain the number of detected photons emitted from that slice, the emission probability, the detector solid angle ($\Delta\Omega/4\pi$), and attenuation by the matrix need to be considered and give the following relationship for the number of photons detected from the infinitesimal slice being excited:

$$\begin{aligned} dI_i &= I_0 w_i S_i e^{-l\mu_{\hat{M},i}/\sin\phi} \hat{\mu} e^{-l\mu_{\hat{M},0}/\sin\theta} \frac{\Delta\Omega}{4\pi} \frac{dl}{\sin\theta} \\ &= I_0 w_i S_i \hat{\mu} e^{-l\left(\frac{\mu_{\hat{M},0}}{\sin\theta} + \frac{\mu_{\hat{M},i}}{\sin\phi}\right)} \frac{\Delta\Omega}{4\pi} \frac{dl}{\sin\theta} \end{aligned} \tag{1.71}$$

All that remains is to integrate over the thickness of the sample. What is most relevant for the soft x-ray analysis here is to assume an infinitely thick sample. The result of the integration is then

$$I_i = I_0 C_i w_i \frac{S_i - 1}{S_i} \mu_{\hat{i},0} p_i \left(\frac{\mu_{\hat{M},0}}{\sin\theta} + \frac{\mu_{\hat{M},i}}{\sin\phi} \right)^{-1} \frac{\Delta\Omega}{4\pi \sin\theta} \tag{1.72}$$

which will be relevant for several analysis herein, but is also of interest for a wide range of problems in x-ray spectroscopy. [28]

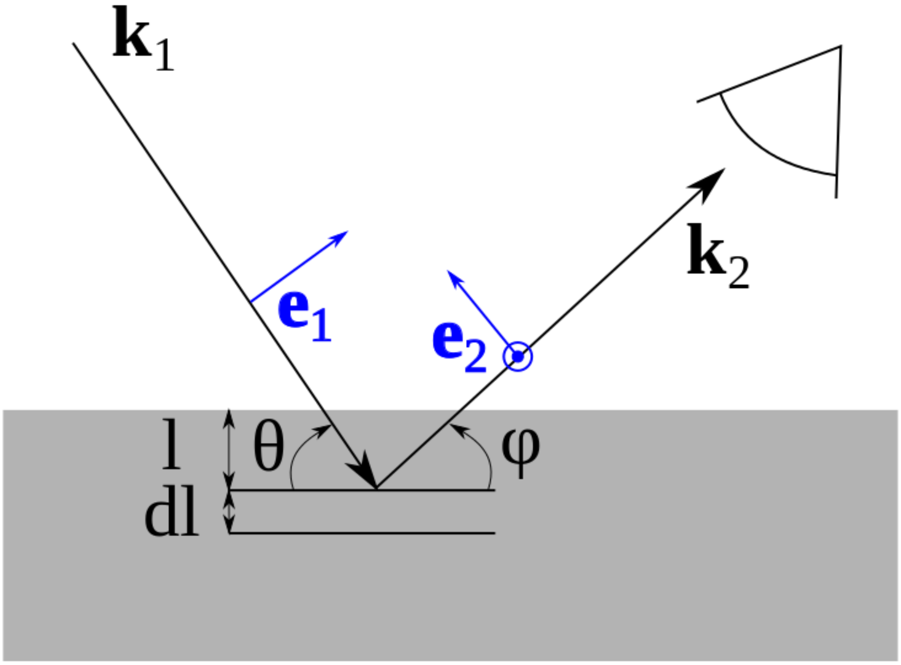

Figure 1.7: Typical experimental geometry for the measurements presented here, as seen from within the scattering plane. All measurements were conducted using the displayed π-polarization configuration, where the photon polarization vector $\mathbf{e}_1$ is in the scattering plane and $\theta + \phi = 90°$. All quantities are as defined in the text.

Angular Momentum and Spin Selection

Electric dipole transitions are of principal interest in this work. The electric dipole transition probability between two states is dependent on the integral $\int \psi_f \mathbf{r} \psi_i d\mathbf{r}$. [20] This immediately gives rise to a constraint on the character of the states that can take part in the transition, namely the Laporte selection rule: electric dipole transitions can only occur between states of different parity. In order to be independent of the coordinates used the preceding integral must be an even function, since $\mathbf{r}$ has odd parity the wavefunctions must have different parity, otherwise the integral will vanish. Further, looking at the determinantal wavefunctions Ψ described above, matrix elements $< \Psi_f | \mathbf{r} | \Psi_i >$ will be nonzero only if the total wavefunctions differ by at most one orbital, and the S and M_S quantum number are the same.

Transitions between states of the same parity and different spin quantum numbers are possible through the magnetic dipole operator $\mathbf{r} \times \mathbf{p}$, which is an even operator. [20] This would allow transitions between d-states, for example, subject to the spin selection rules

$\Delta M_J = \{0, \pm 1\}$. Magnetic dipole transtions are not considered here, as they are much weaker in general and are not usually observed where dipole transitions are possible.

1.7.2 Interaction of X-rays with Matter

Before a detailed discussion of the experimental techniques used herein can be had, the quantum mechanical description of the photon-matter interaction needs to be considered. The description of interactions will be in terms of the second quantization of the matter and electromagnetic fields. Detailed accounts are found in many classic works, [29–31] where it can be seen that the total interaction Hamiltonian for the electron-photon interactions is

$$H = H_{rad} + H_{atom} + H_{int} \tag{1.73}$$

where H_{rad} and H_{atom} are the Hamiltonians of the radiation field and atomic electrons, respectively. In the Coulomb gauge one has the first and second order terms

$$H_{int,1} = \frac{e}{m_e c} \sum_i \mathbf{p_i} \cdot \mathbf{A}(\mathbf{r}_i) + \frac{e}{2m_e c} \sum_i \sigma_i \cdot \nabla \times \mathbf{A}(\mathbf{r}_i) \tag{1.74}$$

$$H_{int,2} = \frac{e^2}{2m_e c^2} \sum_i \mathbf{A}(\mathbf{r}_i)^2 \tag{1.75}$$

where $\mathbf{p_i}$ is the electron momentum operator, $\mathbf{A}(\mathbf{r}_i)$ the second quantized vector potential and σ_i gives the electron spin.

With the above form of the interaction Hamiltonian, the transition rates can be addressed. The transition rate is given by Fermi's Golden Rule, which states that

$$W_{fi} = \frac{2\pi}{\hbar} | < \Phi_f | T | \Phi_i > |^2 \delta(E_f - E_i - \hbar\Omega) \tag{1.76}$$

for the transition rate W between initial state Φ_i and final state Φ_f, with energies E and a photon of energy $\hbar\Omega$. The transition operator T is related to the interaction Hamiltonian through the Lippmann-Schwinger equation

$$T = H_{int} + H_{int} \frac{1}{E_i - H + i\Gamma/2} T \tag{1.77}$$

where Γ is the lifetime broadening of the excited state. In the first order it describes single photon processes: x-ray absorption, emission and photoemission. In the second order

Equation 1.77 describes two photon processes, and takes the form

$$T_2 = H_{int,2} + H_{int,1}\frac{1}{E_i - H + i\Gamma/2}H_{int,1} \tag{1.78}$$

and warrants further explanation. The term $H_{int,2}$ describes x-ray diffraction and small angle scattering, while the second term in Equation 1.78 describes resonant x-ray scattering. In addition to the single photon processes, this last process is of considerable interest in the studies presented here.

It is well worth unfurling the above expressions a little further. The transition operator for the single photon processes can be obtained by inserting the second quantized vector potential into the interaction Hamiltonian, $\mathbf{p}\cdot\mathbf{A}$. The resulting form of the operator is

$$T_1 = \sum_{\mathbf{k},\lambda}\frac{e}{m_e c}A_0[b_{\mathbf{k}\lambda}(\mathbf{e}_{\mathbf{k}\lambda}\cdot\mathbf{p})e^{i\mathbf{kr}} + \frac{\hbar}{2}b_{\mathbf{k}\lambda}(\mathbf{e}_{\mathbf{k}\lambda}\cdot\sigma\times\mathbf{k})e^{i\mathbf{kr}}] \tag{1.79}$$

where the first and last terms on the right hand side of the equation represent the electric and magnetic transitions respectively. The $\mathbf{e}_{\mathbf{k}\lambda}$ are the polarization vectors of photons of wavevector $\mathbf{k}$ and polarization λ (λ=1,2), while the $b_{\mathbf{k}\lambda}$ are the associated annihilation operators. In the limit of small $\mathbf{kr}$ the first term reduces to the electric dipole transition operator

$$T_{1,dipole} = \sum_{\mathbf{k},\lambda}\frac{A_0 e}{m_e c}b_{\mathbf{k}\lambda}(\mathbf{e}_{\mathbf{k}\lambda}\cdot\mathbf{p}) \tag{1.80}$$

In order to link this to the preceding discussion and for completeness the transition rate can be linked to the cross section. The cross section is given by the ratio of the interaction rate to the incident flux, F_p, and therefore has the form

$$\sigma = \frac{W_{fi}}{F_p} \tag{1.81}$$

For typical soft x-ray energies the attenuation length of x-rays in a material is usually less than a micrometer. This leads to a rather small volume of the sample absorbing all of the incident photons. At typical photon fluxes at synchrotron facilities, this leads to the excitation of every strongly absorbing atom in the material, roughly, each second.

1.7.3 Photoelectric Effect

Prior to discussing the finer details of x-ray absorption experiments that will be of primary interest here, it is well worth looking at the derivation of the photoelectric absorption cross section. [29] The theoretical cross section gives a means to understanding many key concepts in x-ray absorption spectroscopy, from the unique absorption energies of each atom, to the absorption process' polarization dependence. A summary derivation is given here following the work in [29].

Photoelectric absorption may occur once the incident photon energy exceeds the ionization energy of the atom, as described by Einstein's famous equation

$$T = \hbar v - I \tag{1.82}$$

for final electron kinetic energy T, ionization energy I and photon energy $\hbar v$. Once the ionization threshold has been breached, the absorption is continuous. Therefore, even at energies high above the absorption edge the photoeffect can still have a relevant cross section.

Assuming a tightly bound electron, that is a K-electron, and a photon energy that is much greater than the ionization energy, the problem can be solved for the case where

$$T = \frac{p^2}{2m_e c^2} \gg I = \frac{Z^2 m_e c^2}{2 \times 137^2} \tag{1.83}$$

which is equivalent to the Born approximation, allowing the final state electrons to be described as plane waves. At the same time the final state electron is assumed to be nonrelativistic.

The relevant matrix element will be given by the first order term in the transition operator

$$H' = -\frac{e}{m_e c^2}\sqrt{\frac{2\pi\hbar^2 c^2}{k}} \int \psi^* p_e e^{-i\mathbf{kr}} \psi_b d\mathbf{r} \tag{1.84}$$

where p_e is the electron momentum in the direction of the incident photon of wave vector $\mathbf{k}$. Using wavefunctions of the form

$$\psi_a = \frac{1}{\sqrt{\pi (a_0/Z)^3}} e^{-rZ/a_0} \psi_b = e^{i\mathbf{pr}/\hbar c} \tag{1.85}$$

which can then be used in Equation 1.84 to find the differential cross section. Assuming $\frac{\hbar c Z}{a_0}$ (a_0 the Bohr radius) small compared to the electron momentum p it can be shown that

$$\frac{d\sigma}{d\Omega} = r_0^2 \frac{Z^5}{137^4}\left(\frac{\mu}{k}\right) \frac{4\sqrt{2}\sin^2\theta\cos^2\phi}{(1-\beta\cos\theta)^4} d\Omega \tag{1.86}$$

where, $\mu = m_e c^2$, $\beta = v/c$, θ is the angle between $\mathbf{k}$ and $\mathbf{p}$, and ϕ is the angle between the photon polarization vector and the plane formed by the preceding vectors. Of most interest here is the total cross section, which can be obtained by integrating over all solid angles and polarizations, yielding

$$\sigma = \phi_0 \frac{Z^5}{137^4} 4\sqrt{2} \left(\frac{\mu}{k} \right)^{7/2} \tag{1.87}$$

where ϕ_0 is the Thompson scattering cross section. The key features to note in Equation 1.87 are the strong dependence on the nuclear charge, and the 7/2 power decay with the photon energy.

1.7.4 X-ray Absorption Spectroscopy

The principal experimental probe of material properties in this thesis is a beam of monochromatic x-rays. As mentioned above, there are several processes that are possible as the x-rays interact with the sample. They may be scattered, either elastically or inelastically, or they may be absorbed. The absorption events lead to the promotion of electrons from inner atomic levels to the conduction bands, or even expulsion from the material. The empty state, or core hole, that is left behind in the atom has a role to play in all the phenomena of interest here, and so can be considered in a little more depth before moving on to other aspects. The basic cross section for the creation of a core hole, is the photoabsorption cross section just discussed. [29, 31] A core hole will generally have a lifetime of about 10^{-15} s, which leads to a lifetime broadening of the state of about 0.1 eV. [30] As already mentioned, Auger and Fluorescence decay are the means of de-excitation following photo-absorption.

Useful starting points for the interpretation of x-ray absorption spectra are the approximations that: the ground state density of states can be used to describe the system under study, and that this density of states is not modified by the core hole. [30] These points are not expected to be generally true, but rather to serve as a basis for analysis and more accurate approximations.

As the incident x-ray energy is increased, there will come a point at which the number of x-rays absorbed by the sample increases sharply. This will occur at the minimum photon energy needed to promote a core state electron into the unoccupied states of the material. This defines an absorption edge of some atom in the material. This absorption edge energy will be characteristic of the atom and cannot only be used for speciation, but for probing the chemistry of a material. The absorption edges for N and O are shown in Figure 1.8.

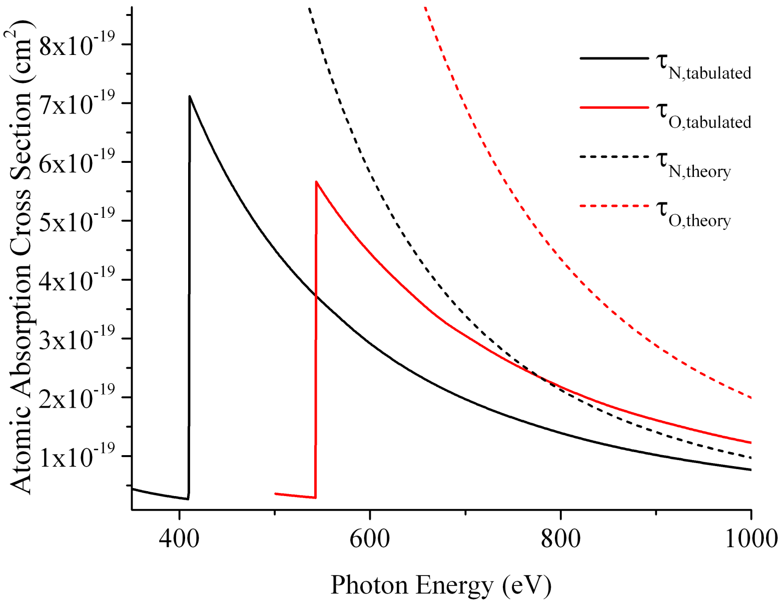

Figure 1.8: Comparison of tabulated CXRO cross sections and theoretical cross sections based Equation 1.87. [27] The theoretical curves use tabulated binding energies in the equation. The comparison shows that the theoretical curve has the correct energy dependence to match the tabulated vaules as $k \gg I$.

The ability of the XAS to give chemical information is based on the proportionality of the absorption intensity to the density of unoccupied states, which is implied by the delta function in Fermi's Golden Rule. For example at the O K-edge, where a 1s electron is promoted to the conduction band, the O p-projected density of states is measured. The photon absorption and emission events will always be indicative of the projected density of states as a result of the dipole selection rules. It will be found in general that the shape of the absorption spectrum will not quite match the theoretical density of states of the material. It will be more closely matched by this density in the presence of a core hole, convoluted by the ≈ 0.1 eV lifetime broadening of the core state, and the width of the incident x-ray beam, with its roughly Gaussian energy spread. [30] The calculated spectra given herein apply this last, more detailed, view of the x-ray absorption spectral shape.

It is clear from the preceding discussion that soft x-rays will only be transmitted in relevant numbers from very thin samples. Most studies, and indeed all those presented here, work with powder samples with $\sim \mu m$ particle size. Further, the samples are measured on thick metal substrates. Clearly true absorption measurements based on the transmission of the incident beam are not possible. However, the emission of photons or electrons with every absorption event provides another means of measuring the absorption intensity. The two types of absorption measurement that will be used here are the fluorescence yield and electron yield. In most cases the fluorescence photons and electrons are emitted from the sample in proportion to the number of absorption events. This can be seen in Equation 1.72 above.

Most of the absorption spectra presented here are of the fluorscence yield type. Two types of fluorescence yield are possible, depending on the style of detector that is used for the measurement. If a simple counting dector is used a total fluorescence yield (TFY) measurement results. If on the other hand an energy-discriminating detector is used, and emissions from only the element and edge of interest being counted, a partial fluorescence yield (PFY) measurement results. The PFY spectra are used almost exclusively here. An important feature of this style of absorption measurement is that since the fluorescence x-rays have similar attenuation lengths, or perhaps even greater attenuation lengths, than the incident x-rays, a measure of the absorption intensity from within the excited volume as a whole is measured. That is to say the TFY/PFY are bulk-sensitive measurement techniques. There is a cautionary point, which should be drawn from Equation 1.72. As the absorption cross section increases the denominator of Equation 1.72 grows as well, decreasing the excitation volume and the number of fluorescence photons emitted. This effect tends to damp strong spectral features, and is usually referred to as the 'self-absorption' or 'saturation' effect. There are ways around this: one can use dilute samples, or in select cases *inverse partial fluorescence yield* can be used. [28, 32]

Electron yield methods form an interesting case, though they will not be exploited at length here. To collect a total electron yield (TEY) spectrum devices such as a pico-ameter or channeltron can be used to measure the number of electrons ejected from the sample. Electron escape depths range from 1-10 nm for most samples implying that: this method measures the absorption intensity at the surface of the sample only; if the x-ray attenuation length is much greater than that of the electrons, self absorption should be negligible. It is found that

$$I_{TEY}(\Omega) \propto \frac{\lambda_e}{\lambda_e + \lambda_p(\Omega)\sin\phi} \tag{1.88}$$

for electron and photon attenuation lengths λ_e and λ_p. [30]

1.7.5 X-ray Emission Spectroscopy

There is a tremendous amount of information that can be accessed through the various x-ray emission processes that are observed in x-ray emission spectroscopy (XES) measurements. Of particular interest here are normal x-ray emission spectroscopy (NXES)–constant energy emissions that are seen when exciting far above the absorption threshold–and resonant x-ray emission spectroscopy (RXES), where the excitation energy is in the neighbourhood of the absorption edge. Under the blanket classification of RXES is also contained resonant inelastic x-ray scattering (RIXS)–energy loss features that linearly track the excitation energy, and are described by the Kramers-Heisenberg formula–, resonant elastic scattering, as well as resonant fluorescence, where although the emission energy is constant there are fluctuations in spectral shape due to the excitation of nonequivalent lattice sites. These are typical definitions, [30] but they are not too convenient here, as it is necessary to consider RIXS and resonant fluorescence spearately. Therefore the convention here will be to use RIXS with the above definition and use RXES to refer only to nonequivalent site excitation.

A cursory description of the RIXS process was given above, but it is interesting to discuss it in greater depth, and will be invaluable for understanding the analysis presented later on. The differential cross section for photon scattering is

$$\frac{d^2\sigma}{d\Omega_{k_2} d(\hbar\omega)} = \frac{\omega^2 V_s}{\hbar c^4}\left(\frac{1}{2\pi}\right)^3 W_{12} \tag{1.89}$$

for incident photons with k_1, λ_1, ω, and a subscript 2 denoting quatities for the outgoing photon. [29] The relevant form of the transition rate W_{12} is found by including the first order term of $\mathbf{A}^2$-type and second order term of $\mathbf{p} \cdot \mathbf{A}$-type from the interaction hamiltonian. The result, which describes the transitions of interst here, is

$$W_{12} = \frac{2\pi}{\hbar} \sum_j \frac{(2\pi)^2}{\Omega\omega} \left(\frac{e^2\hbar}{m_e V_s}\right)^2 \delta(E_g + \hbar\Omega - E_j - \hbar\Omega)$$
$$\times \Bigg| \Bigg[< j|\rho_{k_1 - k_2}|g > (\mathbf{e}_1 \cdot \mathbf{e}_2) + \frac{1}{m_e} \sum_i \Bigg(\frac{< j|\mathbf{p}(\mathbf{k}_2) \cdot \mathbf{e}_2|i >< i|\mathbf{p}(-\mathbf{k}_1) \cdot \mathbf{e}_1|g >}{E_i - E_g - \hbar\Omega}$$
$$+ \frac{< j|\mathbf{p}(\mathbf{k}_1) \cdot \mathbf{e}_1|i >< i|\mathbf{p}(-\mathbf{k}_2) \cdot \mathbf{e}_2|g >}{E_i - E_g + \hbar\Omega} \Bigg) \Bigg] \Bigg|^2 \tag{1.90}$$

where $|g >$, $|j >$, and $|i >$ are the initial, final and intermediate states. [30] Other quantities are as described above. The terms are represented pictorially in Figure 1.9. The three terms have straight forward interpretations. The first A^2-type term is an elastic scattering term that describes Thompson scattering. Resonant elastic scattering is described by the second terms when $|g >= |j >$. The second two terms are of greatest interest, and they become large as the resonance condition is met, when $E_i - E_g - \hbar\Omega$ vanishes. The most essential part of the RIXS spectrum can be expressed as

$$F(\Omega, \omega) = \sum_j \left| \sum_i \frac{< j|T_2|i >< i|T_1|g >}{E_g + \hbar\Omega - E_i + i\Gamma_i} \right|^2 \delta(E_g + \hbar\Omega - E_j - \hbar\omega) \tag{1.91}$$

for transition operators T_1 and T_2. It is noteworthy that the RIXS term in Equation 1.90, for excitation energies well above resonance, can be shown to reduce to an expression describing NXES with a spectrum proportional to the occupied DOS broadened by the core state lifetime Γ_i. [30, 33]

Typical experimental setups should be considered moving into more detailed discussions of RXES and RIXS. All experimental data presented here were collected in the 'depolarized' configuration. As shown in Figure 1.7 this configuration has the electric field vector of the incident radiation in the scattering plane, and perpendicular to the polarization vector of the outgoing radiation. This configuration, also called π-polarization, minimizes the contribution of the Thompson scattering term in the scattering cross section just considered, which is useful for removing background from the x-ray spectra. The polarized, or σ-polarized, configuration is also popular, but is not used here as it can be seen to allow a considerable contribution from Thompson scattering.

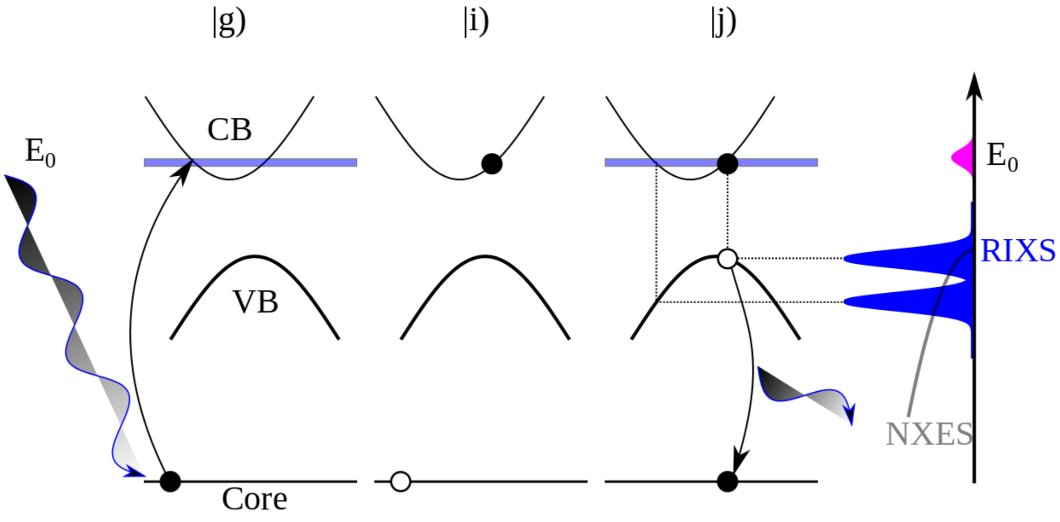

Figure 1.9: RIXS in wide band solids and other materials. The case of a wide band solid is shown, but that of isolated states, such as transition metal 3d-states, is obtained naturally as the bands flatten.

1.7.6 RXES

Nonequivalent site excitation has a dramatic influence on the XES spectral shape as the excitation energy is varied near the conduction band onset. The reason for this is straight forward. Looking at the theoretical cross section for photoabsorption, [29,31] there is a clear dependence on the core level energy. Since the core level energy varies considerably with the chemical environment of the atom, it follows simply that the photoabsorption cross section will not be identical for the same element at nonequivalent lattice sites. Therefore as the incident x-ray energy is varied the atoms at nonequivalent lattice sites will be preferentially excited. The core holes at these sites will be selectively filled by the occupied states in the vicinity, leading to an x-ray emission spectrum that reflects the occupied DOS of specific lattice sites. This form of resonant emission provides an exceptional means for testing the validity of DFT calculations, which can be readily used to determine site-specific densities of states and emission spectra.

1.7.7 RIXS

The Kramers-Heisenberg equation provides an accurate theoretical description of RIXS. It must be borne in mind that the exact phenomena that are observed are highly dependent on the material under study and the absorption edge at which one is exciting. With this in mind, there are a few special cases that need to be considered for the interpretation of RIXS spectra. There are three cases that are relevant here: RIXS in broad band solids, RIXS at metal L-edges, RIXS at ligand K-edges. In evey case different material properties are probed, making RIXS a truly powerful tool for understanding them.

RIXS in Semiconductors

A full account of RIXS in broad band solids is given by Eisebitt et al. and the most important details are summarized here. [33] The electronic states in a single-crystalline solid are completely characterized by the four quantum numbers $E(\mathbf{k})$. That is to say, the band structure of the solid. Band structure information was first observed using RIXS in diamond, [34] and later in graphite, Si, BN, SiC and other compounds. The proper theoretical description of RIXS in these cases follows from assuming that the electrons in the system can be described by Bloch waves. The RIXS process in such a system is depicted in Figure 1.9.

The interesting, and distinguishing, result for RIXS in this picture is that the coherent absorption and emission of a photon via intermediate states leads to **k**-conservation between the electron-hole pair created in the process. This is quite natural since the absence of a core hole in the final state leads to the maintenance of translational symmetry. [33] This conservation rule can follow from a description where the core states are treated as atomic wavefunctions, and the core hole is only present in the transient intermediate states. Because of this, it is impossible to tell at which atomic site within the coherent x-ray field was excited, making the summation over intermediate states include all non-equivalent sites therein. [33]

Since **k**-conserving RIXS will be rellevant for several analyses herein it is worthwhile to show the development of the mathematical description of the phenomenon in this context. Starting with the factorized wavefunctions

$$|g>=|full\ core\ levels>|full\ VB> \tag{1.92}$$
$$|i>=|core\ hole\ at\ n_c,\mathbf{R_m}>|full\ VB>|n'\mathbf{k}'> \tag{1.93}$$
$$|j>=|full\ core\ levels>|hole\ at\ n''\mathbf{k}''>|n'\mathbf{k}'> \tag{1.94}$$

where $|n'\mathbf{k}'>=e^{i\mathbf{k}'\mathbf{r}}u_{n'\mathbf{k}'}(\mathbf{r})$, $\psi_{n_c}(\mathbf{r}-\mathbf{R}_m)=|n_c\mathbf{R}_m>$, and similarly for the other states. The absorption term in the dipole approximation is

$$\begin{aligned} M_A &\equiv <i|\mathbf{p}_1\cdot\mathbf{A}_1|g> \\ &=<n'\mathbf{k}'|\mathbf{p}_1\cdot\mathbf{A}_1|n_c\mathbf{R}_m> \\ &=e^{i\mathbf{k}'\mathbf{R}_j}e^{i\mathbf{q}_1\mathbf{R}_m}\int d^3x'\mathbf{p}_1\mathbf{e}_{\alpha_1}u_{n'\mathbf{k}'}(\mathbf{r}')\psi_c(\mathbf{r}') \end{aligned} \tag{1.95}$$

and similarly for the emission matrix element. The photon quantum numbers are denoted at α_1 for brevity. It is also convenient to define $M_1=\int d^3x'\mathbf{p}_1\mathbf{e}_{\alpha_1}u_{n'\mathbf{k}'}(\mathbf{r}')\psi_c(\mathbf{r}')$. The sum over all intermediate states includes all $(n'\mathbf{k}')$, all core levels n_c, and all equivalent lattice positions within the x-ray field. This leads to a differential cross section

$$\frac{d\sigma}{d\omega_2 d\Omega}\propto\sum_m\left|\Delta_{\mathbf{k}+\mathbf{q}_1-\mathbf{k}''-\mathbf{q}_2}\sum_{n_c}\frac{M_1(n'',\mathbf{k}'',\alpha_1)M_2(n,\mathbf{k},\alpha_2)}{E_i-E_g-\hbar\omega-i\Gamma_i/2}\right|^2\times\delta(\omega_1-\omega_2-\omega_{gj}) \tag{1.96}$$

where Δ is a delta function that is periodic in the reciprocal lattice. The energies appearing in Equation 1.96 are

$$\begin{aligned} &E_g\equiv 0 \\ &E_i=\tilde{E}_{n'\mathbf{k}'}-\tilde{E}_{n_c}+E_g=\tilde{E}_{n''\mathbf{k}''}-\tilde{E}_{n_c}+E_g \end{aligned}$$

with $\tilde{E}$ single particle energies with respect to the Fermi energy. The Δ ensures that only **k**-conserving processes affect the cross section. With the minimal momentum transfer of soft x-rays this enforces the CB electron and VB hole to have the same wave vector. The **k**-conservation here is analagous to the parity conservation in molecular RIXS. Choosing the excitation energy $\hbar\omega_1$ allows control of the energy of the CB electron in the intermediate states, and this is the mechanism that allows for experimental band mapping. This picture is only valid in the case where correlation effects are negligible between the core state and the excited electron. This implies that excitation to and from narrow bands will not be well described. It is also very important to realize that other momentum transfer events, such as electron-phonon or electron-electron scattering, will destroy the **k**-selectivity of RIXS. Such interactions will have a randomizing effect on the CB electron momentum. Therefore with a scattering rate $\Lambda \gg \hbar\Gamma_0$ the emission spectrum contains information for the entire Brillouin zone. This leads to a **k**-unselective contribution to the RIXS spectrum that often appears in tandem with the **k**-selective portion. The effect is shown in Figure 1.9.

In closing this section it is instructive to consider scattering in the lattice and the induced **k**-unselective contribution to the RIXS spectrum. The selective and unselective contributions to the RIXS spectrum vary with the sample. From one perspective the latter is an inconvenience, but from another it can also be used to understand the scattering processes of electrons in the CB. Contributions from electron-electron scattering are only expected for electrons excited to energies $\sim$ 1 eV (the band gap energy) above the conduction band minimum. Below this energy it is electron-phonon interactions that dominate. [33] The **k**-selective fraction in the spectrum will be given by

$$f = \frac{R_c}{R_c + R_{ph}} \tag{1.97}$$

for the core hole decay rate R_c and phonon scattering rate R_{ph}. For Si it has been shown that within the first 0.1 eV of the CB minimum, while R_{ph} increases rapidly, it is similar to or less than R_c. [33] This result was both theoretically derived and experimentally measured, and holds for other systems studied. [33]

RIXS in Metal Oxides

A relatively complete description of RIXS in wide band materials is given in the preceding section. Although the ideas therein are invaluable for analysis to be presented here, RIXS in wide band materials plays a relatively small role in the x-ray spectroscopy field. The lion's share of research is done at metal L-edges, where correlation effects are large. RIXS at these edges measures primarily intra-atomic excitations. [35] Incidently, the theory of RIXS corresponding to this situation is also applicable to inter-atomic transitions at ligand edges. It is this theory which will be covered in this section, and plays a significant role in the analysis that follows.

The basic idea is the same as discussed above, where a core electron is excited into the valence band (unoccupied states) and the highly excited system subsequenly decays to fill the core hole. As opposed to exciting into thoroughly delocalized states as in the preceding section, here the excitation is into rather localized metal d- or f-states. The energy and momentum of the incident photon may change by two different loss mechanisms, deemed *direct* and *indirect* RIXS. Only the former is of interest here, the latter being largely relevant at hard x-ray energies and is due to shake-up excitations incited in the intermediate state. It is a second order effect at lower x-ray energies where direct RIXS occurs.

Direct RIXS refers to the excitation of an electron to the unoccupied states followed by the decay of an occupied state to fill the core hole. The result is the creation of an electron hole pair which can propogate through the lattice with $\hbar\mathbf{q} = \hbar(\mathbf{k}' - \mathbf{k})$ and $\hbar\omega = \hbar(\omega_{\mathbf{k}} - \omega_{\mathbf{k}'})$, where $(\omega_{\mathbf{k}}, \mathbf{k})$ and $(\omega_{\mathbf{k}'}, \mathbf{k}')$ refer to the incoming and outgoing photons, respectively. These are the same type of transitions discussed above for wide band insulators, only the nature of the states involved is different. In either case the valence and conduction states are probed directly. The intermediate states in the RIXS process affect the spectral weight of different energy loss features in the spectra. Direct RIXS will simply be referred to as RIXS hereafter.

The remainder of this section will look at the quasiparticles that can be excited, with RIXS. The energy scales for different excitations are shown in Figure 1.10. Excitations from phonons at energies of a few meV, to d-d and charge transfer excitations of a few eV are possible. Both the energies and dispersion of quasiparticles can be measured in principle, though their energies are the main concern here.

The transport of electrons is determined by the energies required to move them from one lattice site to another. The charge transfer energy in a system is that required to move and electron from the ligand to the metal site, and is defined as $\Delta = E(d^{n+1}\underline{L}) - E(d^n)$. Another relevant energy is the energy needed to move d-electrons between metal sites. This is described by the Coulomb repulsion energy $U = E(d^{n+1} - 2E(d^n))$. Charge tranport in a material will be controlled by whichever of these two energies is the lowest. [25, 35] When $\Delta > U$ the material is said to be a Mott-Hubbard insulator, whereas for $U > \Delta$ the material is said to have an energy gap of the charge-transfer type. Many important metal oxides, such as the cuprates, manganates and nickelates are of the charge-tranfer type. However, Mott-Hubbard insulators are also relevant here.

Another very important class of excitations that can be excited with RIXS are crystal-field and orbital excitations. These occur when an electron may occupy several different sets of orbitals. The nature of these orbital degrees of freedom, their ground state and their excitations can be very influential in the properties of strongly correlated materials. There are two cases to consider, which are the cases of a strong and a weak crystal field. This is the theme that has appeared time and again since its introduction in Section 1.4.1. In the former case the physics is governed by the crystal field. In this regime RIXS may excite electrons between crystal field levels. Referred to as d-d excitations these transtions are well described in terms of transitions within a single lattice site. The ability to measure these transitions with relative ease is a stark contrast to optical spectroscopy, where these interconfigurational transitions are forbidden. The transitions to and from the intermediate states are allowed in RIXS, making for relativlely strong contributions from these excitations in spectra. The $|\underline{c}d^{n+1} >$ ($\underline{c}$ a core hole) intermediate state forms a local exciton, implying the excited electron does not easily move to neighbouring sites. Only local excitations are probed. In the latter case, where the splitting of levels is small, a quasi-degeneracy of states is possible in the ground state. Superexchange–exchange of electrons between metal sites intermediated by a shared ligand–allows the coupling of orbital degrees of freedom on neighbouring metal sites, and hence the emergence of collective orbital excitations. The quanta of these collective orbital excitations are known as orbitons, and are analagous to the more commonly observed magnon quasi-particles. The energy scales for d-d excitations and orbitons/magnons are $\sim$ 1 eV and $\sim$ 0.1 eV respectively.

The phenomena just discussed, with the exception of orbitons and magnons, are well established in RIXS experiments. Orbitons in particular have been difficult to measure, [35] and given their relevance to some studies herein, should be discussed in greater depth. When the crystal field splitting of states is low, superexchange becomes dominant and gives rise to the interaction of orbital degrees of freedom. This allows the propagation of orbital excitations through the lattice with considerable dispersion.

There are two interactions between orbitals that need to be considered: cooperative Jahn-Teller lattice distortions accompanied by lattice distortions of the same symmetry, and superexchange. The interaction of the orbital degrees of freedom leads to ground states with orbital order. The RIXS scattering off of orbitons takes the form of excitation to an

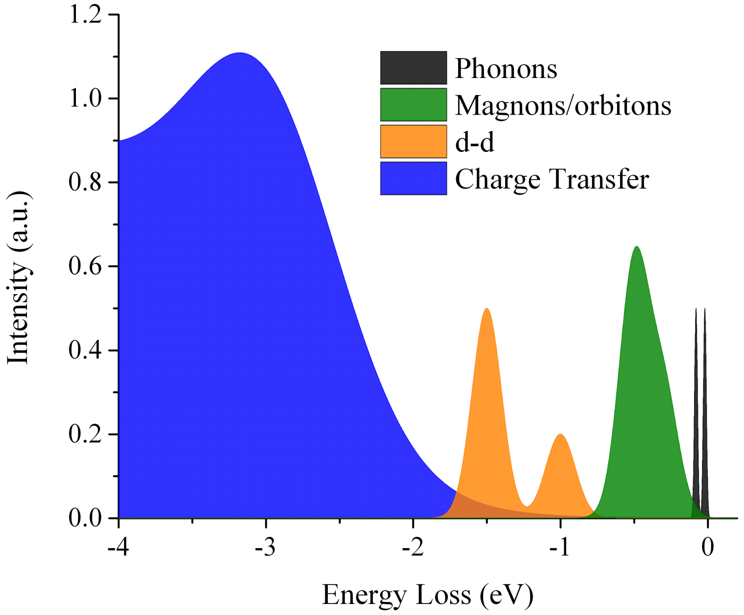

Figure 1.10: Overview of elementary excitations that can be probed with RIXS, as well as their energy scale relative to the incident x-ray beam energy (observed energy loss). [35]

empty d-state at a lattice site and the core hole being filled by another electron from that site's occupied d-states. Importantly, excitations can also be seen at ligand edges as a result of orbital hybridizaton. [35] Since one is then dealing with delocalized states, inter-atomic excitations can be probed. [36–38]

Excitation of phonons–vibrational quanta of the lattice–by RIXS are of some interest. As was discussed above they can be influential in RIXS spectra, even when they are not themselves the phenomenon of interest. Phonons have energies below a tenth of an eV in general, and are only barely resolved in state-of-the-art RIXS experiments. Resolving these features of spectra promises quantitative analysis of the electron-phonon interaction in materials. However, in the studies pursued here, only their collective influence will need to be considered.

1.7.8 X-ray Excited Optical Luminescence

X-ray excited optical luminescence (XEOL) is a technique that is somewhat underexploited. It will therefore be introduced here by looking at how it relates to what has already been discussed, while citing a few interesting examples from the literature. The starting point in a XEOL experiment is an x-ray absorption measurement, of the kind that have already been discussed. Instead of looking at the emitted x-rays as in XES, which lead to a state with an electron in the conduction band and a hole in the valence band, the subsequent transitions are studied through optical light emissions that result from electron-hole recombination. [39] This gives information on any energy levels lying in the band gap of the material, provided the transitions between states are radiative. Included in this is everything from the luminescing levels in rare-earth ions, to other defect states in the same crystals, to the band gap energy itself. [40, 41] Importantly, the distinction between TEY and PFY measurements retains its usefulness in XEOL measurements. Monitoring the variations in intensity of luminescence from particular defects, creates a partial luminescence yield (PLY) spectrum concurrently with the TEY and PFY. The PLY will have a spectral shape that matches the TEY or PFY, depeding on whether the defects are in the surface or bulk of the sample. [40, 41] To summarize, XEOL leverages the large electron-hole density in a crystal during an XAS measurement to monitor optical transitions in a material, while retaining the site specificity and surface-bulk differentiation of XAS.

1.8 Rare Earth Elements

Transition metals have been discussed to a considerable extent at this point, with particular emphasis on the intriguing properties that they confer with their semi-local 3d-states. It was seen that they are well described by the moderate to strong crystal field cases where interconfiguration interactions play a smaller role. The 3d states of α-V_2O_5 are relatively itinerant and therefore fall into the strong crystal field group. The weak field case becomes highly relevant when discussing another block of the periodic table, the Lanthanides. Members of a class generally refered to as the *rare earth elements*, they are a group of tremendous industrial relevance, and like the 3d-transition metals deserve special consideration. Their 4f electrons are even more localized than the transition metal 3d-states, for the reasons discussed above. It is for the 4f states that these metals are usually revered, but the often ignored 5d states will also be relevant to the studies herein. One can expect that the 5d-states will exhibit properties somewhat similar to the 3d-states of the early transition metals, such as vanadium. There is therefore little new to discuss to understand the lanthanide 5d-states, leaving a detailed discussion of the 4f states as a matter of great import for the role they play in the rare earth-doped phosphors that form the focus of this thesis.

With orbital quantum number $l = 3$ there are seven 4f-orbitals that can be filled with up to 14 electrons. The ground state configurations will maximize the total spin S, which is combined with the total orbital angular momentum L such that: $J = L - S$ if $n < 7$, and $J = L + S$ is $n > 7$. States are therefore indicated as ${}^{2S+1}L_J$, but it should be noted that in general 4f states of the rare-earths are described by a combination of these states mixed through the spin-orbit interaction, especially for highly excited states. [42] The atomic-like 4f-states have been well characterized for the lanthanides in various oxidation states. [42]

The 4f states are singular for the dearth of influence that the rare earth ion's environment seems to hold over them. Therefore the 4f levels of the lanthanides follow the same patterns in relative energy across their row of the periodic table regardless of the surrounding lattice. This implies that crystal field splitting is also negligible, in stark contrast to the 3d states, which are heavily influenced by their surroundings. The interconfigurational 4f transitions therefore give approximately the same luminescence spectra in all crystals. Most light emitting levels in lanthanides are separated from the next lowest level by at least 2x10^3 cm^{-1}. [42] This is because the rate of phonon emission varies exponentially with the ratio of this separation to the maximum phonon energy coupling to the states. [42] This type of transition is dipole forbidden, and therefore has a long lifetime, on the order of milliseconds. For those transitions that are spin allowed, shorter lifetimes occur. This is a sharp contrast to transitions that occur between the 5d and 4f states of some lanthanides.

The excitation of an electron from a 4f level to the 5d leads to the formation of $4f^{n-1}5d^1$ states. Direct luminescence from the $4f^{n-1}5d^1$ states decaying to low-lying 4f states result when the $4f^{n-1}5d^1$ levels are energetically well-above the 4f states. Without this separation there can be other interactions with 4f levels that lead to 4f-4f emissions. There is therefore a need for the correct crystal field splitting and spectroscopic red-shift of the 5d states in order to create conditions where strong $4f^{n-1}5d^1 \rightarrow 4f^n$ luminescence can occur. The systematics of this transition for different lathanides have been studied at length. [43–45]

Chapter 2

Experimental Methods and Data Analysis

The experimental work in this thesis was conducted at the REIXS and SGM beamlines of the Canadian Light Source in Saskatoon, Saskatchewan, and beamline 8.0.1.1 at the Advanced Light Source in Berkeley, California. [46–49] The standard experimental setup that has been used in the analysis in this thesis is shown in Figure 1.7. In all cases the incident x-rays are generated by undulator insertion devices. Beamline optics make the x-ray beam quasi-monochromatic, with a FWHM of less than 0.1 eV. In all cases a π-polarized incident beam is used in order to minimize the number of elastically scattered x-rays entering the emission spectrometer. The REIXS beamline and Beamline 8.0.1.1 have high-resolution emission spectrometers in the Rowland circle geometry. Detectors used for collecting the final x-ray emission spectra were either multichannel plate or CCD detectors. The SGM beamline has traditional TEY capabilities, but also an array of silicon drift detectors (SDDs), which allow the rapid collection of high-quality PFY spectra. The beamline also has an Ocean Optics QU 65000 spectrophotometer for collecting XEOL data. [39]

Methods for processing the detector images recorded with the emission spectrometers have been outlined in ealier works. [50] There have been a few developments in the processing of absorption spectra that have been utilized in the analysis presented here. These methods will be outlined in detail in the following sections. They address three data analysis problems: the need to consistently remove background from the x-ray emission spectra collected with the SDDs, the need to resolve the x-ray emission peaks in the SDDs for accurate band gap determinations in vanadium oxide compounds, accounting for the spectral distortions of high-resolution O K-edge emission spectra.

2.1 Processing Emission and Absorption Data

In this section the methods used here for calibrating and removing background from emission and absorption spectra are outlined. The emission spectra, after image correction, [50] typically exhibit a smoothly varying background count rate. It is therefore reasonable to apply a linear, or in some cases quadratic, polynomial fit to the extreme edges of the spectra in order to remove this contribution from the spectral shape. Background functions of higher order are not used here for two reasons: higher order polynomials will influence the spectral second derivatives used to determine band edges; the edges of the spectra give essentially two locally linear regions of data amounting to two slope values and two data points, which would leave higher order polynomials underdetermined. A typical result is shown in Figure 2.1.

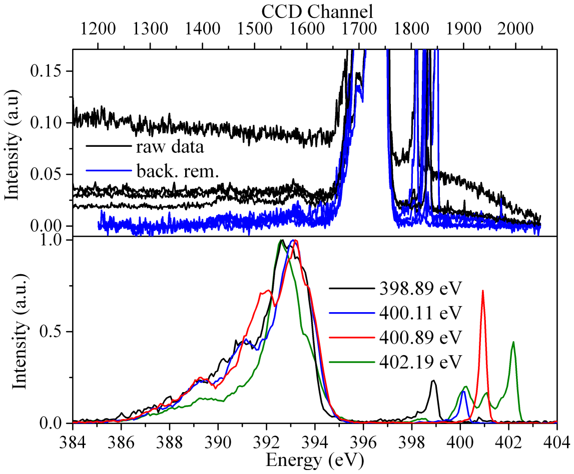

Figure 2.1: Processing of emission spectra collected at various excitation energies for CLMS. These spectra are used in analysis in a subsequent chapter. Top: removal of background from raw data by fitting a quadratic function to, then subtracting it from the data. Bottom: resulting spectra after having fit all of the elastic scattering peaks with Gaussian distributions, then shifting their centers to the known monochromator excitation energy. The monochromator in this instance was calibrated using the absorption spectrum of hBN.

With the background of the spectra removed, the spectra can then be calibrated. In general the energy dispersion across the detector face is nonlinear, the resulting distortion of the spectrum needs to be removed. Traditionally this was accomplished with reference spectra, where reference peak energies were used to shift and stretch the emission spectra. However, a different approach is preferred here. Wherever possible the stretching of spectra exploits the linearity of the incident x-ray energy from the beamline monochromator for calibration. This is done by fitting Gaussian distributions to several elastic scattering peaks on the face of the emission detector, and using the known monochromator energy to shift the appropriately stretched spectrum. This has the added advantage of making the XES spectra as consistent as possible with the absorption spectra, as they are now both calibrated with the same reference absorption spectrum. This consistency is critical for band gap studies. This process is shown summarily in Figure 2.1

Absorption spectra in general will also have a locally linear background that should be removed after normalization to the incident x-ray beam intensity. This is done for all TEY spectra shown here, however, these are the minority of absorption spectra. Most abosoprtion spectra will be PFY spectra determined with SDDs. Since these spectra only measure the emissions from one edge of a single element, they should have no background to remove. There may be detector noise, which at high count rates in the SDD may introduce additional background to the collected emission spectrum. Ideally one only wants to count the roughly Gaussian emission peak from the element of interest, which should be proportional to the absorption intensity. To circumvent any influence of this effect a background removal algorithm is used to remove the background from the SDD spectra, prior to fitting the remaining Gaussian-like peaks to determine the emission intensity at each step in the absorption scan.

Each incident energy in the absorption scan has a corresponding SDD emission spectrum, as shown in Figure 2.2. The background of the SDD spectra is not well represented by a simple mathematical function in general, and will also vary with the sample being studied. It is therefore most effective to use an algorithm to estimate the background. Here the SNIP algorithm as implemented in the ROOT data analysis software was used. [51, 52] The principle idea of the algorithm is to use the following iterative approximation to the background at each bin i in the spectrum

$$v_p(i) = min\left\{ v_{p-1}, \frac{v_{p-1}(i+p) + v_{p-1}(i-p)}{2} \right\} \tag{2.1}$$

where p indexes the iteration. The range of p is fixed and determines the degree of smoothing that the algorithm performs. The effect of the algorithm is to smooth, or clip, the peaks from the spectrum, which should render the background signal. This can then be removed and the peaks fit with Gaussian or other distributions. The final point to consider is the challenges posed by spectral peaks that fall within about 50 eV of each other, for then they are not resolved by the SDD. One of the main classes of compounds studied here is vanadium oxides, which perhaps have the most poorly resolved peaks of any pair of elements, with a difference in emission energy of only about 15 eV between the O K-edge and V L-edge. The method used here to address this is outlined in the next section.

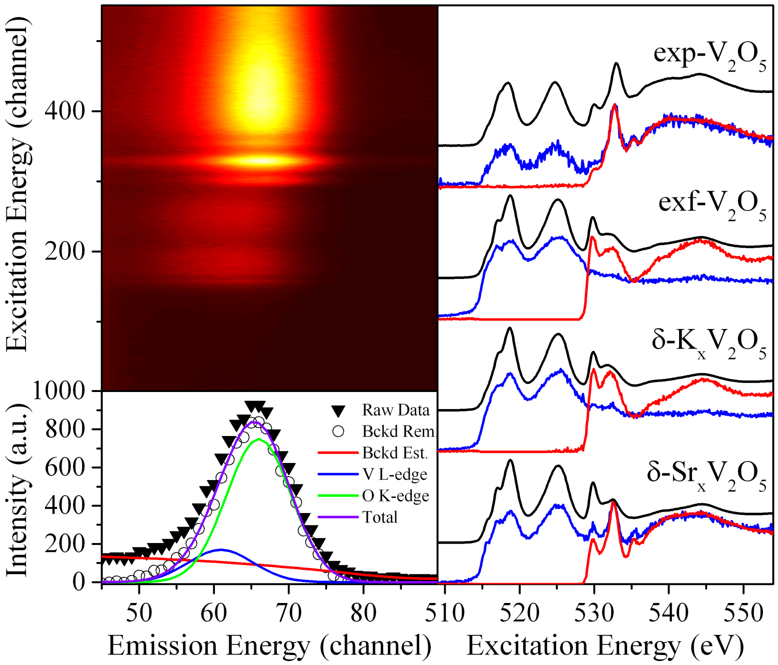

Figure 2.2: Top left: raw 2D colour map of emission intensity as a function of excitation energy and SDD channel for a VO compound. A horizontal slice renders the SDD emission spectrum seen in the bottom left. This emission spectrum is plotted with the estimated background and fit of constrained Gaussian distributions to the data. A vertical cut of the contour plot renders an absorption spectrum. Those shown on the right of the figure are TEY (black) and the PFY spectra obtained from the fitting shown to the left of the figure. O K-edge spectra are in red and V L-edge spectra are in blue.

2.2 Separation of the V L- and O K-Edges

With a FWHM of about 50 eV the SDD will clearly not resolve the emission peaks of V and O in a VO compound, which are separated by about 15 eV. This poses a problem if one needs isolated O K-edge and V L-edge spectra, as is the case here for determining the band gaps of these compounds. The bottom left graph of Figure 2.2 shows an SDD spectrum from a V_2O_5 compound prior to any processing. The O K-edge and V L-edge emissions are so close as to form a single Gaussian peak in the detector.

In order to separate the two PFY spectra, the Gaussian distributions that are being fit to the data need to be sufficiently constrained, such that the peak areas associated with each spectrum are not correlated. First, the background is removed from the total spectrum as described above. The energy of each emission line can be fixed. The absorption onset of the V L-edge is about 30 eV lower in energy than the O K-edge. This energetic separation is easily resolved by the 0.1 eV resolution of the incident x-ray beam. Prior to the onset of the O spectrum the V L-edge emission peaks can be fit to determine their mean position. This parameter can then be fixed in the same way for the O K-edge emission lines. A further constraint can be introduced by exploiting the fact that the emission lines from any two elements will have about the same width when measured with the SDD. Although the natural line widths may differ by a few eV, the instrumental broadening of the SDD will be an order of magnitude larger. The SDD itself controls the peak widths. The widths of the V L-edge and O K-edge emission lines can therefore be constrained to be equal. Using the fitting function

$$f(E) = I_V e^{-\frac{(E-E_V)^2}{2\sigma_{SDD}^2}} + I_O e^{-\frac{(E-E_O)^2}{2\sigma_{SDD}^2}} \tag{2.2}$$

where I_V, I_O, and σ_{SDD} are the only free parameters. Applying this fitting function leads to the spectral deconvolution shown in Figure 2.2. The deconvolution of theV L-edge and O K-edge PFY spectra in this fashion is very successful, although it will not account for the conversion of O K-edge emissions to V L-edge emissions through self-absorption and re-emission. It is conceivable that this could be addressed by an algorithm based on the theory in Section 1.7, but this has not been pursued for lack of necessity in the current studies.

2.3 Accounting for the Unusual Self-Absorption in V_2O_5

Although the effects of the self-absorption of the O K-edge emissions by V need not be considered for its effects on the PFY spectra, the same cannot be said of high-resolution O K-edge XES spectra. The exact spectral shape is strongly influenced by this effect and proper interpretation of data is not possible if it is not considered. The close proximity of these absorption edges means that the V L-edge absorbs strongly over the breadth of the O K-edge, leading to absorption of up to 50% in regions of the O emission spectrum. That this occurs only in certain regions is also important. Uniform absorption would not alter the spectral shape, and although it would affect the count times needed to collect spectra, it would not affect the interpretation of data. That the V L-edge absorption intensity varies strongly overy the energetic breadth of the O spectrum leads to strong distortions, which must be modelled for the accurate interpretation of spectra.

A quantitative analysis of this self-absorption is critical. This can in fact be accomplished in first order by the application of Equation 1.72. The experimental geometry is of course known, making the absorption coefficients the only parameters that need to be determined. First and foremost the magnitude of the edge-jumps of all elements in the sample must be known. Tabulated values can be obtained from the Center for X-ray Optics. [27] One needs the absorption coefficients of the matrix for the constant energy incident radiation, as well as for the O emissions. The latter is a function of emission energy and the only term in this approximation that leads to distortions. Further the V L-edge is the only significant term contributing to it. Once a functional form for the V L-edge is found, the problem is solved. The edge-jump is insufficient as it does not describe the varying absorption in the near edge region of the spectrum, which is the most important effect. The measured V spectrum cannot convincingly be used as it includes instrumental broadening effects than are certainly not seen by the O K-edge emissions. Only the core state lifetime broadening is relevant.

The solution adopted here is to use calculated Anderson Impurity Model V absorption spectra that have been fit to the experimental data. Applying only modest ≈ 0.1 eV lifetime broadening to the spectra, and scaling them so that the L_2 and L_3 edges contribute one and two thirds to the edge jump respectivey, [30] the required absorption coefficient is attained. Each edge jump is modelled by an arctan(E) function. The DFT-calculated emission spectra ($I_{calc}(E)$) are then scaled in accordance with the following equation:

$$I_{det,i}(E) = A' \frac{I_{calc}(E)}{\mu_{M,I_0} \csc\theta + \mu_{M,i}(E) \csc\phi} \tag{2.3}$$

which simulates the self-absorption in the actual sample, giving a model spectrum $I_{det,i}(E)$. A' is an arbitrary scaling factor and all other quantities are as defined elsewhere. This approach has proven very successful in accounting for the spectral shape of O K-edge emission in VO compounds, as shown in Figure 2.3.

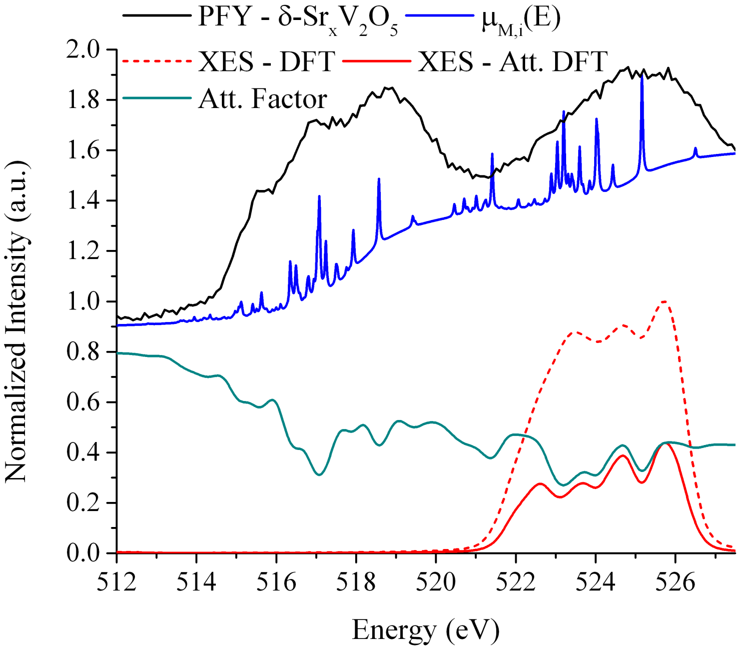

Figure 2.3: Determining the attenuation of V_2O_5 emissions from the O K-edge, by the V L_2-edge in δ-$Sr_xV_2O_5$. The measured PFY is shown along with $\mu_{M,i}(E)$, which is the term of interest in 9.1. Although $\mu_{M,i}(E)$ is scaled to 1 here, in application it is scaled to the edge jump of the V $L_{2,3}$-edge, [27] and then used to produce the attenuation factor shown in cyan. The convolution of the cyan and dashed red curves yields a DFT-derived XES spectrum that accounts for the attenuation seen in experimental measurements of the O K-edge.

Chapter 3

P_3N_5 and the Electronic Structure of Nitrides

3.1 Introduction

In this chapter the problem of understanding the electronic structure of insulators, and in particular nitrides, is addressed in full force with a study of crystalline α-P_3N_5. The applicability of the preceding discussion on the use of a LCAO model for understanding a material's band structure becomes clear, and the utilization of simple hybridization schemes to form a first approximation for the ordering of bands is put on a firm footing. In addition to expounding the structure-property relationships defining this material, several key material properties are quantitatively measured, including the all-important band gap. This study forms the foundation on which the analysis of other materials central to this thesis, such as $Sr[LiAl_3N_4]:Eu^{2+}$, $Li_2Ca_2[Mg_2Si_2N_6]:Eu^{2+}$ and ζ-V_2O_5, are analyzed.

This study, published in *Chem. Eur. J.*, [53] is also of interest for the predictive power that the results confer. The methods therein can be applied to other polymorphs of P_3N_5, and their derivatives, as well as chemically similar materials that have been newly synthesized or studied theoretically. [53] My contributions to this manuscript range from the processing the data, to the DFT calculations, data analysis, and its writing. Thanks are always due to the other authors who have collected data, provided feedback, or facilitated the work in one way or another.

3.2 The Publication

Experiment-driven modeling of crystalline phosphorus nitride P_3N_5: wide ranging implications from a unique structure

Thomas M. Tolhurst[a], Cordula Braun[b][b′], Teak D. Boyko[a], Wolfgang Schnick[c],
Alexander Moewes[a]*

[a] T. M. Tolhurst, Dr. T. D. Boyko, Prof. Dr. A. Moewes, Department of Physics and Engineering Physics, University of Saskatchewan, 116 Science Place, Saskatoon Saskatchewan S7N 5E2 , Canada. E-mail: alex.moewes@usask.ca, Fax: 1-306-966-6431.

[b] Dr. C. Braun, Karlsruher Institut für Technologie (KIT Karlsruhe), Institut für Angewandte Materialien-Energiespeichersysteme (IAM-ESS), Hermann-von-Helmholtz-Platz 1, 76344 Eggenstein-Leopoldshafen, Germany.

[b'] TU Darmstadt, Fachbereich Material- und Geowissenschaften Fachgebiet Strukturforschung, Alarich-Weiss-Straße 2, 64287 Darmstadt, Germany.

[c] Prof. Dr. W. Schnick, Department of Chemistry, University of Munich (LMU), Butenandtstrasse 5-13, 81377 Munich, Germany.

3.3 Abstract

Nitridophosphates have emerged as advanced materials due to their structural variability and broad technical applicability. Their binary parent compound P_3N_5, a polymeric network of corner- and edge-sharing PN_4 tetrahedra with N[2] and N[3] sites, is a particularly interesting example. We present a study of the band gap and electronic structure of α-P_3N_5 using soft X-ray spectroscopy measurements and density functional theory calculations. The band gap, which is crucial for all applications, is measured to be 5.87 ± 0.20 eV. This agrees well with the calculated, indirect band gap of 5.21 eV. The density of states are found to show dramatic variation between the nonequivalent N sites and a high degree of covalency. Coupled to these results is what is, to our knowledge, the largest core hole shift reported to date for a soft X-ray absorption spectrum. We propose an intuitive bonding scheme for α-P_3N_5 that explains the observed band gap and unique density of states, while providing a framework for predicting

these properties in known and yet to be discovered PN compounds. We briefly consider the implications of these results for new low-dimensional P and PN materials, which alongside graphene, could become important materials for nanoelectronics.

3.4 Introduction

Nitridophosphates and oxonitrido-phosphates, and in particular ambient-stable, crystalline α-P_3N_5 (see Figure 3.1), have a long history and a bright future as advanced materials. They offer tremendous structural variability and consequently, broad technical applicability. Compounds with tetrahedral framework structures, which are well known from silicates and related compounds such as alumosilicates or alumophosphates, are of great interest both from a scientific point of view as well as for industrial applications. Owing to their framework structure of PN_4 tetrahedra, most nitridophosphates are closely related to silicates but offer a broader structural diversity because of the possibility of triply bridging N[3] atoms resulting in highly cross-linked structures. [54–73] The incorporation of nitrogen into a tetrahedral network has a significant impact on its properties. It leads to high stability and more covalent bonding, as well as higher network charges, giving PN compounds excellent materials properties. [74]

Investigations of dielectric and optical properties of thin films of phosphorus nitrides started in the 1970s, [75, 76] building the basis of future electronic applications of P_3N_5. High performance enhancement mode InP MISFETs were successfully fabricated with photo-CVD grown P_3N_5 gate insulators. The photo-CVD grown P_3N_5 gate insulators provide a phosphorus-rich ambience during the film deposition, preventing phosphorus volatilization from the InP substrate. [77, 78] Accordingly fabricated MISFETs exhibit excellent pinch-off behavior, superior stability of the drain current and superior thermal stability. [79] Although amorphous P_3N_5 (a-P_3N_5) was used in these applications, the rich coordination chemistry of the P_3N_5 system was already apparent, paving the way for studies of crystalline P_3N_5. [55, 56, 80]

High-pressure investigations of P_3N_5 led to the synthesis of γ-P_3N_5. [81, 82] Its crystal structure is shown in Figure 3.1 alongside that of α-P_3N_5, but unlike the normal-pressure phase, it is not exclusively built from PN_4 tetrahedra but from both PN_4 tetrahedra and square PN_5 pyramids. This structural feature had not been observed in nitridophosphates before. An even denser, high pressure modification was predicted by Kroll and Schnick: a hypothetical δ-P_3N_5 with the kyanite structure type where even PN_6 octahedra are present (see Figure 3.1). [83] To obtain a deeper understanding of (oxo)nitridophosphates at very high pressures (e.g. Stishovite analogous compounds), HP-/HT-investigations have been made and revealed that in this pressure region a coesite-analogous coes PON is accessible. [59, 84] PON is the ternary parent compound of oxonitrido phosphates and is isoelectronic to SiO_2. More recently the potential of lower-dimensional, crystalline PN systems have come to the fore, [85–88] reprising the early electronics applications of P_3N_5.

Multifaceted research on graphene and its intriguing properties prompted the quest for a broader range of low-dimensional structures or even single layer two-dimensional (2D) materials. [85–87] Many 2D layered compounds have been predicted, showing diverse properties and band gaps ranging from zero gap semi-metals to wide gap semiconductors. Group V-V monolayers are predicted to have great potential in future nanoelectronics, as shown by two recent theoretical works investigating two-dimensional PN and arsenic monolayer sheets, [88, 89] namely α-, β-, and γ-PN were recently investigated for the first time. [88] They are all predicted to be indirect band gap semiconductors with low-buckled honeycomb structures, with tunable band gaps ranging from 1.80 eV (monolayer) to 0.24 eV (N=8).

Phosphorus nitrides have even found application in $Ba_3P_5N_{10}X{:}Eu^{2+}$(X=Br,I,Cl), novel nitridophosphates with a zeolite structure, underlining the high potential of this compound class as high-performance luminescence materials. [68,69] $MP_2N_4{:}Eu^{2+}$ (M = Ca, Sr, Ba) and $BaSr_2P_6N_{12}{:}Eu^{2+}$ point towards an expansion of Eu^{2+}-doped ternary nitridophosphates as a new class of luminescent materials for solid-state lighting. [90] Fundamental for the synthesis of each of these phosphors is P_3N_5.

With each form of P_3N_5 and each PN compound comes the potential for new and enhanced applications. Critical to all applications and of primary theoretical interest are the band gap, and more generally the electronic structure. Investigations of the band gap of phosphorus nitride compounds have been made in the past, but a unifying study is missing. As α-P_3N_5 is the parent compound of all nitrido- and oxonitridophosphates and a key ingredient of future high performance materials, a detailed investigation of its band gap and electronic

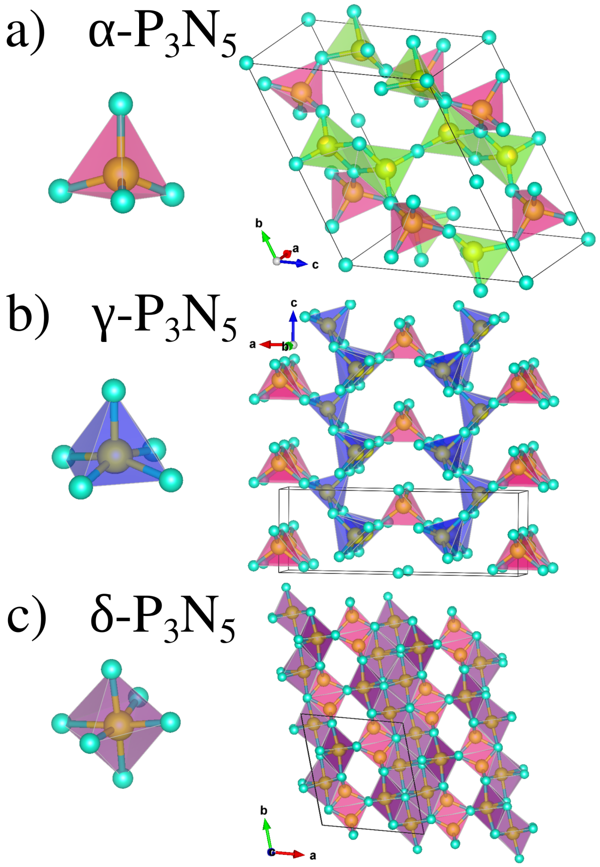

Figure 3.1: Comparison of a) α-P_3N_5 which is based on corner-sharing (magenta) and edge-sharing (green) PN_4 tetrahedra; b) γ-P_3N_5 which additionally contains tetragonal PN_5 pyramids (blue); c) δ-P_3N_5 which contains PN_6 octahedra (violet). Phosphorus and nitrogen atoms are shown in yellow and cyan respectively.

structure is indispensable. In this study soft X-ray spectroscopy measurements combined with first principles density functional theory (DFT) calculations are applied to α-P_3N_5 in order to elucidate its chemical bonding and electronic behavior. This approach gives important insight into a material's electronic structure by providing an accurate measurement of the band gap, as well as element- and orbital-specific information on the electronic density of states (DOS). In addition, we put forward an intuitive model that allows the prediction of major features of the electronic structure of α-P_3N_5, which will be seen to be generally applicable, allowing the prediction of the electronic structures of other and yet to be discovered PN compounds. With this work we close the gap between the electronic structures of different PN compounds, based on an extensive investigation of the band gap and electronic structure of α-P_3N_5, setting a foundation for better a understanding and enhanced application of PN compounds.

3.5 Results and Discussion

3.5.1 Structural Model and Density of States

Using the crystal structure of α-P_3N_5 derived from the X-ray diffraction data, density functional theory (DFT) calculations were performed. The calculated partial density of states (pDOS) of all nonequivalent atoms are shown in Figure 3.2 b). The total density of states, which includes the calculated interstitial DOS, is not shown in the figure, but shows no new features when compared to the pDOS. There are four distinct regions in the valence band (VB) DOS, labeled with Latin characters. They can be very well understood by considering the atomic term energies of P and N, their coordination in α-P_3N_5, and the expected hybridization of states. [12, 91] A qualitative schematic of the expected orbital mixing is shown in Figure 3.2 a), alongside the pDOS.

From their tetrahedral coordination it can be anticipated that the P orbitals will be sp^3 hybridized. The nonequivalent N sites show three distinct coordinations: trigonal (N3 (8f)), linear (N1 (4a)) and 'bent' two-coordination (N2 (8f)); the N sites are then expected to exhibit sp^2, sp and sp hybridization, respectively. The need for sp^2 hybridization of the N3 site has been pointed out previously, where it was also noted that the N-P bond lengths exclude the presence of double bonds. [59] Importantly, this implies the presence of unhybridized p states associated with the N sites. This leads to the final set of N states shown in Figure 3.2 a). The mixing of these N states with the hybrid P states leads to the presence of four distinct regions in the DOS. At the highest levels of the VB, labeled **a**, we find the nonbonding N p states. It follows that the contributions to this region should decrease in the series N1, N2, N3. In region **b** states associated with the bonding between N sp^2, and P sp^3 states occur. One expects p states to still be dominant, but hybridized with s states, and contributed to in descending order by N3, N2 and N1. In region **c** the states associated with the mixing of N sp and P states are predicted, increasing the prominence of s states, leading to contributions in descending strength from N1, N2 and N3. In region d states of varied character resulting from mixing of N s and P states should occur. Looking at the DOS plots accompanying the bonding scheme, it can be seen that all of these characteristics are born out in the calculation. The DOS are labeled with Latin characters to match those in the bonding scheme. The strong presence of N p states at the upper edge of the VB and lower edge of the conduction band (CB) supports the use of the N K-edge measurements for determining the band gap of this material, which will be covered in detail in subsequent sections. The energetic ordering of states is consistent with the proposed bonding scheme, but it also implies a particular spacial distribution of these states, which will be discussed below with plots of the calculated electron density.

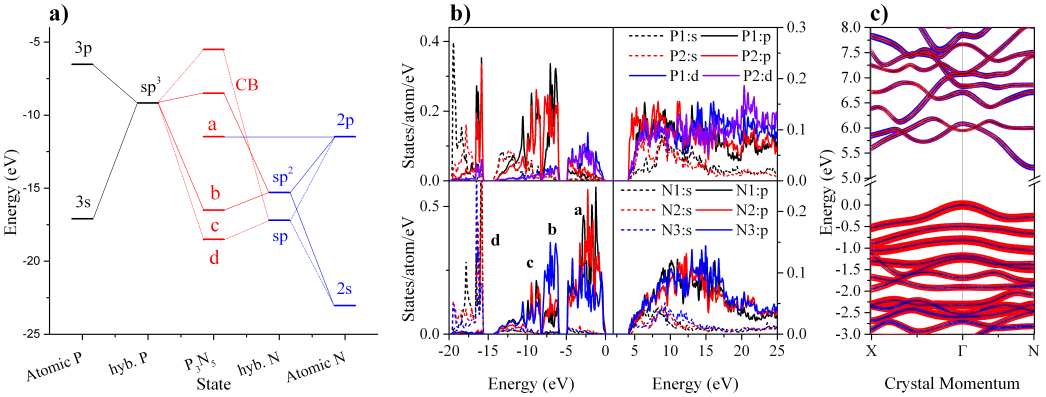

Figure 3.2: a) A qualitative schematic of the states and their energetic ordering, expected from the atomic term energies and coordination environments in α-P_3N_5. Latin letters label the states expected to give rise to the bands carrying the same labels in the DOS. b) The calculated DOS for the nonequivalent atoms of α-P_3N_5. The upper panel shows the DOS of P1 (4e) and P2 (8f). The lower panel shows the DOS of their coordinating N atoms. c) The calculated band structure and characters of α-P_3N_5, using the mBJ potential. The P p states are shown in blue and the N p states in red. The line thickness is proportional to the atom's relative contributions to the states.

3.5.2 Band Structure and Character

The band structure of α-P_3N_5 was calculated using the mBJ exchange-correlation potential, [92] and is shown in Figure 3.2 c), along with the determined band characters. The band gap is predicted to be indirect, with the CB minimum at the N point and the VB maximum at the Γ point. The character of the bands is in keeping with what is predicted by the bonding scheme in Figure 3.2 a) and the analysis given elsewhere on similar systems. [12] It is expected that the majority of upper VB states will be N p states, and the lower CB states will be P p states. This is what is seen in the character plots. However, at this finer level of detail the extreme prominence of N p states at the upper edge of the VB is apparent. Modest levels of N-P bonding appear as the gradual increase in the contribution of P p states with decreasing state energy.

That the band gap of α-P_3N_5 is indirect has implications for optical measurements of the band gap. It is typical for optical measurements to be most sensitive to direct transitions in the band structure of a material, due to the negligible momentum of optical photons. Therefore, to compare our results to optical measurements it is desirable to determine the smallest direct transition that is possible, based on the X-ray spectroscopy measurements and calculations. The calculated band structure predicts that the smallest direct transition is 0.28 eV greater than the indirect band gap. This allows us to use our measured indirect band gap, which is presented below with the relevant X-ray spectroscopy measurements, to predict the optical gap for α-P_3N_5.

3.5.3 Electron Density

To verify the nature of the bonding in α-P_3N_5 and the accuracy of the bonding scheme given above, the calculated electron density should be considered. The valence electron densities along several cuts of the α-P_3N_5 unit cell are shown in Figure 3.3. With the high electron density lying along the bond axes, the covalent character and orbital hybridization outlined above is strongly supported. Figure 3.3 b) offers a clear example, but also shows the maxima of the electron density drawn towards the N3 site, indicating that the bond is polar, as would be expected. Further support for the bonding scheme outlined above is found by considering the electron density of only those states lying within 5 eV of the VB maximum (region **a** in Figure 3.2). As noted above these are expected to be non-bonding N p states. From Figure 3.3 d) it is immediately clear that these upper-valence states are directed away from the bond axis, localized at the N sites, and have p-symmetry. They are non-bonding N p states. The bonding scheme outlined in Figure 3.2 a) appears to offer a convenient and accurate explanation for the unique, layered VB structure and electron density of α-P_3N_5.

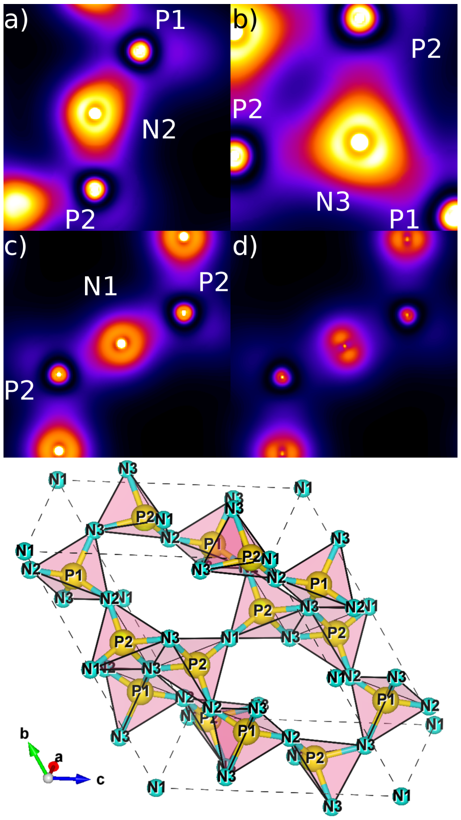

Figure 3.3: The calculated electron density of α-P_3N_5 along several cuts of its unit cell. The color coding runs from black to white for low to high densities respectively. a) Valence electron density centered on the N2 site, showing orbitals directed at P1 and P2. b) Valence electron density centered on N3, which is trigonally coordinated. The electron density is clearly concentrated between the P and N atoms, with maxima drawn towards the N atoms, showing polar bonds. c) Valence electron density around linearly coordinated N1, still showing the electron density residing along the bond axis. d) Upper-valence electron density (region a of Figure 3.2) of the same cut shown in c), showing clear p-symmetry orbits directed away from the bond axis and confined to the N sites. The lower panel shows the crystal structure of α-P_3N_5 with nonequivalent atoms labeled.

3.6 Nitrogen K-edge and the Band Gap

The strong accord between the proposed bonding model and the results of the DFT calculations has been demonstrated, but a thorough experimental characterization is also needed. X-ray spectroscopy is a powerful probe of many material properties, including the electronic DOS, which is the primary concern in this study. X-ray emission (XES), resonant X-ray emission (RXES), and X-ray absorption spectroscopy (XAS) measurements were collected on a powder sample of α-P_3N_5. They are shown alongside calculated spectra, which are derived from the calculated pDOS, in Figure 3.4. The XAS spectrum gives a measure of the CB pDOS by measuring the energy-dependent cross section for the promotion of core electrons to the CB. Similarly, the XES spectra show the spectrum of X-rays emitted as VB electrons decay to the emptied core states. [30] In the present case transitions to and from the N 1s core states are used. Conservation of angular momentum dictates that the transitions will be to or from N p states, hence the pDOS is measured. By probing the occupied states (XES) and unoccupied states (XAS), and also resonantly exciting nonequivalent sites (RXES), a very complete picture of the outermost DOS of a material is obtained. The spectra in Figure 3.4 were calibrated using peaks in the emission and absorption spectra of hBN. The main emission peaks were taken to lie at 392.75 and 396.60 eV, while the leading absorption peak was taken to occur at 402.1 eV.

To model the experimental X-ray spectra, DFT calculations were performed for the ground and excited states of the material. The latter is necessary due to the effect of the N 1s core hole on the observed shape of the absorption spectrum. [93–95] There is excellent agreement between the measured and calculated, excited-state absorption spectra. Excellent agreement is also obtained between the non-resonant emission spectrum (NXES), excited at 422.14 eV, and the calculated non-resonant spectrum. This outstanding match strongly supports the accuracy of the calculated N pDOS and the structure used for the calculations. The calculations can be tested further through the resonant emission measurements, which selectively measure emissions from nonequivalent N sites. Whereas the XES and XAS spectra measure the total N pDOS, the RXES spectra test the calculation's predictions for individual crystallographic sites. This can be done because of the dependence of the RXES spectral shape on the CB and VB pDOS of the nonequivalent sites. There is some change in the shape of the RXES spectra as the excitation energy is increased from 400.84 to 405.54 eV. Once the latter excitation energy is reached, there is little change. Although several higher energy excitation spectra were collected (grey arrows), they have been omitted. The largest deviation from the shape of the NXES spectrum is seen with an excitation energy of 400.84 eV; a concavity forms in the location of a prominent peak of the NXES spectrum. Looking at the location of this excitation on the XAS spectrum, while considering the contributions of the nonequivalent N sites, points to the origin of this change in spectral shape. In Figure

3.4 the calculated XAS spectra for the non-equivalent N sites are shown in violet. The total calculated spectrum is a linear combination of these spectra. It is clear that exciting at 400.84 eV will almost exclusively excite the N2 site, which implies that the resonant emission spectrum should also be due predominantly to that site. Appropriate increase in the contribution of N2 to the calculated emission spectrum gives the calculated resonant spectrum in the figure, which is an excellent match to the experimental spectrum. The level of agreement between the calculated XAS, XES and RXES spectra and the measurements underscores the accuracy of our DFT calculations. It gives very strong support for the calculated electronic structure, as well as the predicted contributions of the nonequivalent N sites to the measured spectra.

The XES and XAS spectra probe respectively the occupied and unoccupied density of states of the system. The band gap of α-P_3N_5 can therefore be determined using the second derivative of the X-ray emission and absorption spectra. [93] Selecting the first peaks in the second derivative above the noise level, as shown in the central panel of Figure 3.4, a gap of 2.36 ± 0.20 eV is obtained. This result must be adjusted for two effects to give an accurate measure of the band gap. The effect of the core hole on the CB density of states (DOS) must be considered, along with the variation in binding energy between nonequivalent N sites. Comparison of the calculated ground state and excited state absorption spectra supports a shift in the CB edge of 2.17 eV. A binding energy correction of 1.34 eV must also be added to account for its effect on the location of the upper edge of the NXES spectrum. The final band gap estimate for α-P_3N_5 is therefore 5.87 ± 0.20 eV. Drawing on the band structure results presented above we then predict a direct gap of 6.15 ± 0.20 eV. The extreme core hole shift seen in these spectra is unprecedented. To our knowledge the next largest core hole shift to have been reported is 1.40 eV, seen in N K-edge absorption spectra in a study of manganese carbodiimide ($MnCN_2$), [96] a system which also features doubly-coordinated N sites. Interestingly, it has been identified elsewhere that the two-connected N sites of α-P_3N_5 are easily distorted, due to a shallow potential energy surface associated with their bending modes. [83] This phenomenon has also been seen for doubly coordinated nitrogen atoms in carbodiimides. [97] The large shift in the measured edge of the CB is due to strong relaxation at the N2 site. Although the calculated 1s binding energies of the N1 and N2 sites are very similar, they differ sharply from that of the N3 site, leading to another large correction. It is well known that DFT predicts absolute binding energies rather poorly; however, differences in binding energies tend to match experiment rather well. [98] It should further be noted that the agreement between the calculated and measured spectra, which is excellent, is entirely dependent on the accuracy of the calculated differences in binding energy. The N3 site exhibits substantially different orbital hybridization from what is seen at the other sites, making a substantial shift in the N 1s binding energy reasonable. Ultimately, the large core hole shift is the result of the strong variations in local coordination of the nonequivalent N sites in α-P_3N_5. All together this provides strong support for the calculated corrections to the band gap. Further support follows from the calculated band gap of α-P_3N_5, as well as a comparison to previous experimental studies of a-P_3N_5.

The binding energy correction that is used above is put on a very solid foundation after considering XPS data collected in an earlier study of a-P_3N_5. [80] The authors note the presence of two distinct N 1s peaks in their XPS spectra, which when fit with Gaussian profiles give a peak separation of 1.6 eV. This is in good agreement with the 1.34 eV binding energy difference calculated here between the N2 and N3 sites. As noted the N1 and N2 sites have calculated binding energies which differ by only a tenth of an eV, well below the 1.7 eV resolution of the XPS spectra. The authors of the XPS study also took care to conduct angle dependent measurements to determine if the split in the N 1s peak was a surface or bulk property, concluding that it was a bulk property. This result is unequivocally confirmed by the calculations presented here.

Our DFT calculations using the GGA-PBE exchange correlation potential predict a band gap of 3.69 eV. Using a modified Becke Johnson (mBJ) potential gives a band gap of 5.21 eV, in good agreement with the measured value. The mBJ potential is generally accurate to within about 10%. [92] The determined band gap of 5.87 ± 0.20 eV is also in keeping with previous work specifying α-P_3N_5 as a wide band gap material, and the white body color which is often reported. [59] Several previous studies have reported optical gaps in the range of 5.1 to 5.7 eV for a-P_3N_5, [80, 99, 100] though much lower values have been obtained as well. [75, 101] Some of the lowest energies can be assigned to optical absorption by states in the band gap, due to the band tailing that invariably occurs in an amorphous material. Significantly the 5.7 eV gap was found after the authors annealed their original sample. There may be a conflict with a beige body color reported previously, or the similar light orange color of the crystalline sample studied here, if it is assumed that the coloration is not due to other color centers in the crystal. [59] Red coloration has been seen to be due to N deficiency in P_3N_5, where the red emissions may be associated with localized lattice defects. [75] The sample used in this study was orange in color; however, the excellent match between the measured and calculated spectra implies the measurements presented here are representative of crystalline α-P_3N_5. The calculations assume an undisturbed crystalline lattice. Previous work has shown that N deficiency simply leads to localized defect states formed by otherwise absent P-P bonds. [80] The element specificity of XES and XAS leaves the N K-edge measurements completely unaffected by such states. To address the influence of the surface of the material it should be noted that the XAS spectra were collected using both total fluorescence yield (TFY), which is shown in Figure 3.4, and total electron yield (TEY). The former is bulk sensitive, and the latter surface sensitive, due to the relative escape depths of X-rays and electrons respectively. The TFY and TEY are found to match very well, indicating that both the surface and bulk of the material are well represented by the results given here.

It is worth considering whether it is reasonable for the band gap of α-P_3N_5 to be much larger than that measured for the amorphous material. Indeed, the measurement presented here stands as an asymptotic value to the spread of gaps measured previously, as shown in the lower panel of Figure 3.4. It is generally expected that amorphous materials should exhibit a smaller band gap than crystalline phases, but there are a few subtleties to keep in mind. Different types of disorder can be found in amorphous materials. Simple topological disorder, where a material's tetrahedral subunits are strictly maintained, has been seen not only to maintain the presence of a band gap, but even to result in systems with larger band gaps. [102] Such a topologically disordered system is perhaps a good first approximation for a-P_3N_5, given that the same coordination environments identified in the crystalline system have been seen in the amorphous material. However, once bond lengths and angles are allowed to vary, as in a revealing study on α-quartz and a-SiO_2, [103] small reductions in band gap are seen in the amorphous phases of the material. This was seen to be true of topologically disordered a-SiO_2 where variations in bond parameters of a few percent were present, as well as an a-SiO_2 structure created through molecular dynamics modeling. The latter results in a much more random network and greater variation in the bonding parameters. The comparison of the calculated band gaps for α-quartz and the two amorphous systems showed reductions in the band gaps of 0.9 eV and 1.1 eV respectively for the topologically disordered and molecular dynamical models. On top of this one also would expect to see band tailing and other effects. [102, 103] This is in keeping with the expectation that the statistical variation of bond lengths and angles will lead to a concomitant variation in bond strength at different lattice sites, including those responsible for the location of the band edges. The increase in the band gap in passing from a-P_3N_5 to α-P_3N_5 seen here is very much in keeping with this idea and previous results. The lower panel of Figure 3.4 offers a striking visualization that the band gap of the crystalline phase represents the upper limit of the observed band gaps.

3.7 Discussion

The results of studies comparing the electronic structure of crystalline and amorphous materials suggest that a material's electronic structure is more generally determined by short range structure, with only small scale details resulting from long range order. In SiO_2 the tetrahedral subunits of the material are the determining structural detail. [102,103] This also follows from the strong accord between the results found here for α-P_3N_5 and those of previous studies of a-P_3N_5. With this in mind, and the success of the structural model in Figure 3.2, we are in a position to forecast the resulting electronic structure of new PN compounds such as mono-layers, novel structure types, or solid solutions.

First, the effects of elemental substitutions and structural changes on the band gap and electronic structure of α-P_3N_5 can be considered briefly. There is only a ≈2.4 eV separation of the nominal P sp^3 and N p states, which implies that the band gap in a-P_3N_5 is large as a result of the splitting induced by the σ bonds between the P sp^3 states with the N sp^2 states. It is the associated antibonding states and the nonbonding N p states that define the band edges. Stronger overlap between the N sp^2 and P sp^3 states, as might be seen in high pressure phases, should increase the band gap. A large band gap can generally be expected for a range of PN compounds, making them ideal as gate insulators in MISFETs,

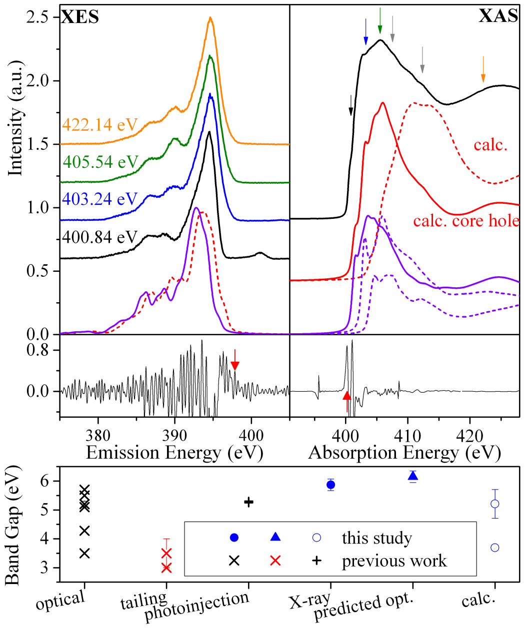

Figure 3.4: Comparison of XES, RXES and XAS spectra from the powder α-P_3N_5 sample. Calculated ground state spectra are given as dashed, red lines. The calculated excited-state absorption spectrum is in solid red. Calculated, excited-state absorption spectra for the non-equivalent N sites are in violet, with that of the N2 site given as a solid line. The calculated RXES spectrum, where the N2 site is preferentially excited is given as a solid, violet line. Second derivatives of the measured spectra used to determine the band gap of α-P_3N_5 are shown in the central panel, with arrows indicating the peaks chosen as the band onsets. Arrows along the absorption spectrum indicate energies for RXES excitations. The grey arrows indicate measurements not shown for brevity. The lower panel shows a comparison of our measured and predicted band gaps alongside several results from the literature, noting the method used for each determination. [75,80,99–101] Error bars are shown where available.

an application that has been the focus of several previous studies. [75, 99, 100] Replacement of N by atoms with deeper p states, or replacing P with atoms having shallower sp^3 states will lead to a larger band gap. SiO_2 would be an extreme example. Relative positions of impurity or defect states can be similarly inferred. It is now natural to ask what band gap should be found in other P or PN systems, particularly for novel two-dimensional materials such as the recently reported few-layer black phosphorus (BP) and monolayer PN. [85, 88]

Black phosphorus has shown tremendous promise as a result of a narrow band gap of 0.3 eV, which puts it on the same footing as graphene for many novel electronics applications. Although containing no N, it is still worth considering it within the framework of Figure 3.2

a). It not only shows the applicability of the model, but serves to highlight the effect of introducing N into the lattice, as in monolayer PN. The three-coordination and buckled structure of BP, are in keeping with the tendency of P to form sp^3 hybridized orbitals. The problem is then to consider the orbitals expected for a system of interacting sp^3 hybridized P atoms. It is clear from the three-coordination that each P atom will form three σ bonds, leaving an orbital left over to be either non-bonding, or form part of a network of π bonds, as in graphene. The structure of black phosphorus does allow for overlap of the remaining sp^3 states to form π bonds, which due to their relatively weak overlap one expects only a small gap, if any, to exist. The states formed by the sigma bonding sp^3 states will have comparatively large splitting, leaving the p states to form the CB minimum and VB maximum. This predicts a small gap, in keeping with the 0.3 eV gap reported elsewhere. [85] Lastly, the presence of five valence electrons per atom implies the system may be metallic if an uninterrupted network of π bonds were to form. The presence of non-bonding orbitals as in α-P_3N_5, or defects, would be necessary for the π^* states to be unoccupied. At the same time this will leave BP vulnerable to oxidation and functionalization generally, as with the facile incorporation of H into P_3N_5. [80,99] This known characteristic of the analogous materials silicene and graphene will also be true of low-dimensional PN and related compounds. [104–107]

Monolayer PN compounds with all N and P atoms triply coordinated were explored in a recent theoretical work, where the N and P atoms are proposed to be sp^2 and sp^3 hybridized, respectively. [88] Reported band gaps are on the order of 2 eV. As the authors note, the tendency of P to take on sp^3 hybridization will lead to a buckled structure, as in silicene. [104,105] It is inevitable that the N atoms will take on a hybridization that is more complex than sp^2 in order to accommodate the buckling. The same can be said of the sp hybridization of the N2 site in α-P_3N_5. From the start we can propose that these materials should have a large band gap, just by virtue of the minimal separation of 2.4 eV of the P and N states in Figure 2 a). The fact that the bond lengths in the hypothetical PN compounds are about 0.2 Å larger than those in α-P_3N_5, implies that the energy level splitting will be reduced. [12] It is also likely that extensive π bonds will be introduced in the buckled PN structures, which will lead to only weak level splitting, as in BP. If the π^* states form the CB minimum, as is likely, a band gap on the order of 2.4 eV should result. The inevitability of a large band gap in PN compounds makes them ideal for gate insulators or as an alternative to the popular transition metal dichalcogenides. Smaller band gaps could however be achieved if the P sites take on a mixed hybridization, or where extensive P-P or N-N bonding occurs, as in BP.

Some insight can also be gained from looking at the recent use of P_3N_5 as a precursor in the synthesis of new rare earth (RE)-doped phosphorus nitride, as new luminescent materials (phosphors) for pc-LEDs. [68,69,90] The electronic structure of the RE's host lattice is very important for its emission characteristics. For example, if narrow Eu^{2+} 5d→4f emissions are to occur, the density of states surrounding the N atoms (or the species coordinating with the RE ion) should be as similar as possible, which is not uncommon in some other nitrides. [108] It can be seen readily that there is a stark lack of uniformity in the DOS of nonequivalent N sites in α-P_3N_5. If a PN-based crystal is to be used as a rare earth host, this is a characteristic that must be changed, unless broad-band emissions are sought. The width of the band of p states in α-P_3N_5 is quite large in comparison to what is seen in other phosphor systems and is manifest in the width of the measured XES spectra. [108] It is due to a greater degree of covalency and varied coordination environments in α-P_3N_5 in comparison to many other nitrides. The high degree of covalency of this system was pointed to previously. [59] In many phosphors, for example $Sr[LiAl_3N_4]:Eu^{2+}$, the bonding is much more ionic, as indicated by the narrow band of N p states at the upper edge of the VB and narrow band of s states at the bottom of the VB. [108] A highly covalent lattice is generally seen as favorable for a small Stokes shift and narrow emissions from a RE-doped phosphor. [109]

3.8 Conclusions

The DOS of α-P_3N_5 is well described by considering the P atoms, N1, N2 and N3 atoms as sp^3, sp, sp, and sp^2 hybridized respectively, in accordance with the crystallographic data. The calculated DOS also suggest a higher degree of covalency than is seen in many other nitrides. These points are reinforced by the calculated electron density for this system, which in concert with the band structure, supports the outlined bonding scheme and a band gap controlled by the non-bonding N p states of the upper VB and P sp^3 -N sp^2 hybrid states at the CB minimum. The band gap of α-P_3N_5 is supported to be 5.87 ± 0.20 eV, which is in good agreement the 5.21 eV gap predicted by our calculations and stands as the upper limit of the previously reported band gaps of a-P_3N_5. Our DFT calculations predict that the band gap is indirect, with the direct (optical) gap being 6.15 ± 0.20 eV. With its large band gap and unique electronic structure α-P_3N_5, and related compounds, are ideal for device applications ranging from gate insulators in MISFETs, to nanoelectronics, to pc-LEDs, to protective coatings. These diverse applications demand a diverse set of possible electronic properties, which have been seen to be accessible and predictable to a first approximation with the bonding scheme proposed in this study.

3.9 Methods

Synthesis of phosphorus(V) nitride Partially crystalline phosphorus(V) nitride was obtained by the reaction of gaseous ammonia with hexachlorocyclotriphosphazene $(PNCl_2)_3$ (Merck, p.a.) according to the literature. [110] $(PNCl_2)_3$ (ca. 2 g, Merck, p.a.) were placed into an corundum boat, which had previously been dried in vacuo (5×10^{-4} mbar) at 950°C. The starting material was then heated to 100°C at a rate of $0.8°\mathrm{C\,min}^{-1}$ in a light flow of NH_3 (Messer Griesheim, 3.8), which was dried through a column of KOH. The temperature was maintained for 10 h. After cooling to room temperature, the NH_3 was expelled by a flow of argon, and the sample was ground to a powder in a mortar. It was placed into the crucible again, and the procedure was repeated at 130°C (5h), 190°C (3h), and 300°C (4h). Further heating to 600°C (2h) in vacuo is to remove NH_4Cl and start condensation reactions. In the last step, the sample was heated to 900°C for 2 h to complete condensation. The thus obtained partially crystalline α-P_3N_5 has a light orange color.

3.10 Experimental

X-ray absorption spectroscopy measurements were conducted at the Canadian light source's Spherical Grating Monochromator (SGM) Beamline. [46, 47] They were carried out under a high vacuum of 10^{-7} Torr or better and monochromator resolving power ($E/\Delta E$) of about 5000. The absorption spectra were collected using the total fluorescence yield (TFY). Beamline 8.0.1 of the Advanced Light Source was used for the collection of the nitrogen K-edge emission spectra. [48] This beamline has a monochromator resolving power of about 4000 and spectrometer resolving power of about 800. Beamline 8.0.1 uses a Rowland circle spectrometer equipped with an area sensitive multichannel plate detector. The powder samples were prepared for the measurements by simply pressing a small quantity of the powder into clean In foil.

The X-ray diffraction measurements of α-P_3N_5 were performed on a STOE STADI P powder diffractometer in Debye-Scherrer geometry with Ge(111)-monochromatized Mo-Kα1 radiation (λ=0.709026Å). The samples were enclosed in glass capillaries with 0.5 mm diameter.

3.11 Calculations

The DFT calculations presented in this work were performed with the WIEN2k software package, using the (C2/c) structure model for P_3N_5. [83] The code uses a full potential and linearized-augmented-planewaves with local orbitals (LAPW + lo) to self-consistently solve the Kohn-Sham equations. [112] The generalized gradient approximation of Perdew, Burke and Ernzerhof (GGA-PBE) was used for most calculations. [112] Calculations were also performed using the modified Becke-Johnson (mBJ) potential to predict the band gap and structure. [92] The effect of core holes at the nonequivalent N sites in the final states of the system during the X-ray absorption measurements were modeled using 2x2x2 supercells. [93, 94] An electron is removed from the relevant core orbital, while an additional background charge is added to the supercell. One such calculation was performed for each nonequivalent N site. The resultant spectra were then combined according to the multiplicity of the nonequivalent sites, and aligned with the core level energy eigenvalues, to provide a model of the experimental XAS spectrum. The ground state calculation is used for describing the XES spectra and the DOS. Muffin tin sphere sizes of 1.70 Å for P and 1.09 Å for N where used in all cases. A k-mesh of dimensions 12x6x12 was used for the ground state calculations, which was then scaled to a 4x3x5 mesh for the excited state, supercell calculations.

3.12 Acknowledgements

We would like to acknowledge the support of the Natural Sciences and Engineering Research Council of Canada (NSERC) and the Canada Research Chair program. The authors also acknowledge Compute Canada, as well as financial support by the Fonds der Chemischen Industrie (FCI). The calculations presented in this work were performed on the Grex high-performance computing cluster, which is part of the Westgrid network (www.westgrid.ca) and Compute Canada Calcul Canada (www.computecanada.ca). Research described in this paper was performed at the Canadian Light Source, which is funded by the Canada Foundation for Innovation, the Natural Sciences and Engineering Research Council of Canada, the National Research Council Canada, the Canadian Institutes of Health Research, the Government of Saskatchewan, Western Economic Diversification Canada, and the University of Saskatchewan. The Advanced Light Source is supported by the Director, Office of Science, Office of Basic Energy Sciences, of the U.S. Department of Energy under Contract No. DE-AC02-05CH11231.

Chapter 4

An Ultra-Efficient, Narrow-Emitting LED-Phosphor: Sr[LiAl$_3$N$_4$]:Eu^{2+}

4.1 Introduction

The LED-phosphor Sr[LiAl$_3$N$_4$]:Eu^{2+} is one of the greatest discoveries in the pc-LED field in recent years, and is considered to have been a breakthrough. [2, 8] It exhibits the thermal stability and narrow, red emissions that have been widely sought after. It has cuboidally-coordinated Sr sites, which are ultimately to house the Eu^{2+} dopants. This coordination, shown in Figure 1.3, is largely seen to correlated with efficient and narrow emissions. The large, negative energy offset that is induced by the CFS in this configuration makes this little surprise. However, there are other materials, one of which is studied below, [131] that have this same structure, but inefficient emissions. As always the problem is not one dimensional.

The following paper focusing on SLA was published in *Adv. Opt. Mater.*, [108] and is based on a determination of key material properties that are needed for efficient, narrow emissions. This study builds on the understanding of electronic structure gained from the preceding work on P$_3$N$_5$, and forms a natural bridge to studies of other phosphors. My contribution ranges from data collection, to data processing and analysis, to the writing of the manuscript.

4.2 The Publication

Investigations of the Electronic Structure and Band Gap of the Next-generation LED-phosphor $Sr[LiAl_3N_4]:Eu^{2+}$ - Experiment and Calculations

Thomas M. Tolhurst, Teak D. Boyko, Philipp Pust, Neil W. Johnson, Wolfgang Schnick, Alexander Moewes*

T. M. Tolhurst, Dr. T. D. Boyko, N. W. Johnson, Dr. A. Moewes

Department of Physics and Engineering Physics, University of Saskatchewan, 116 Science Place, Saskatoon, Saskatchewan, Canada S7N 5E2, alex.moewes@usask.ca

P. Pust, Dr. W. Schnick

Department of Chemistry, University of Munich (LMU), Butenandtstrasse 5-13, 81377 Munich, Germany

Introduction

The research on novel, suitable materials for phosphor-converted light-emitting diodes (pc-LEDs) has attracted a lot of attention in recent years, due to their dramatically increased energy efficiency compared to conventional light sources. The replacement of conventional sources, such as incandescent lamps, is considered a fundamental step toward reducing worldwide electrical energy consumption. [4] LED efficiency can be captured by the *luminous efficacy* of the LED, which relates power input to emitted intensity, weighted by the sensitivity of the human eye. [8], [113] The dispersion of the emitted light is therefore of the utmost importance. This will also affect the perceived color of illuminated objects, and is captured by the *color rendering index* (CRI). [8] The luminous efficacy is at odds with the CRI and a balance between the two must be struck. The appropriate combination of luminescent materials (phosphors) and excitation method must be selected in order to achieve the desired CRI and luminous efficacy. The resulting pc-LED can be tailored to a variety of lighting needs. On this front, the recently reported nitridolithoaluminate $Sr[LiAl_3N_4]:Eu^{2+}$ (SLA) can be considered a breakthrough material. [8] With its high emission intensity in the red region of the electromagnetic spectrum and its uniquely narrow bandwidth for an Eu^{2+}-doped phosphor, this material shows great potential for use in illumination-grade pc-LEDs. To fully understand the complex structure-property relationships and to enable further optimization of the material properties of $Sr[LiAl_3N_4]:Eu^{2+}$, an in-depth presentation of the electronic structure determined through experimental soft X-ray spectroscopy measurements and density functional theory calculations is presented here. SLA is found to have an indirect band gap of (4.56 ± 0.25) eV, highly similar local electronic structure at nonequivalent Sr sites, and the necessary characteristics for a uniform shift in the centroid of the Eu^{2+} 5d states. This clarifies why, with two sites which can be occupied by the activator ion Eu^{2+}, such a narrow emission band is still observed and re-enforces the importance of SLA as a phosphor for LED applications.

Efficient pc-LEDs are typically fabricated using UV to blue emitting InGaN semiconductor LED chips to excite other phosphors. [114] The additive mixture of emissions creates white light. [115] Blue-LED chips coated with broadband yellow emitting Ce^{3+}-doped garnet materials have been commercialized, but suffer from variations in color output with applied current and undesirable, low CRI values. [115], [116] An alternative for generating illumination-grade light is the combination of several different phosphor materials on the chip surface (e.g. a yellow-green and red emitting material). [117], [118] This style gives a high CRI, fair luminous efficacy and stable emissions, but has often suffered from the inefficiency of the available red phosphors. [115] The ultimate goal is to produce an efficient illumination-grade white light, as measured by the correlated color temperature (CCT). Here, a CCT in the range of 2700 K to 4000 K is desired, which combines a brilliant CRI with optimized luminous efficacy values. [8], [9], [119], [9] The spectral position and width of the red-emitting component has the greatest influence on CRI as well as on the luminous efficacy. [120] Many red emitters in commercial use produce a significant portion of their light outside of the visible range, limiting their luminous efficacy. [8] These infrared emissions result in wasted power input and undesirable heating in the device. Therefore, the discovery of a narrow-band red-emitting phosphor material would be a breakthrough in LED technology.

Results

The synthesis and the determination of the crystal structure of SLA are described elsewhere. [8] The crystal structure of SLA is shown in Figure 4.1, where the XN_4 (X = Li, Al) tetrahedra can be seen surrounding the Sr sites. The labelling in this figure will be used throughout. The Eu^{2+} ions are assumed to occupy the Sr sites due to their similar ionic radii. X-ray emission spectroscopy (XES) and X-ray absorption spectroscopy (XAS) measurements for the undoped and doped (0.4% Eu^{2+}) samples are shown in Figure 4.2, where they are compared to the calculated spectra. The measured spectra for the doped and undoped sample are largely identical. This is expected for the low dopant concentrations dealt with here, because it is the N sites being probed and the RE ions are expected to be largely atomic in nature, having little influence on the bonding in the crystal. It can be safely assumed that the calculation results for the undoped sample are largely applicable to the doped sample. In the XES spectra the same peaks (*a*, *b*, *c* and *d* as marked on the non-resonant spectrum) are observed throughout. The high-energy shoulder *d* becomes suppressed at the lowest excitation energy. This same feature is augmented under 401.30 eV excitation. Feature *a* increases in intensity under 404.30 eV excitation. These slight changes in the emission spectra are attributed to the preferential excitation of nonequivalent N sites. By comparing the calculated density of states (DOS) of the nonequivalent N sites, the variations can be accounted for, supporting the calculated electronic structure of SLA.

Using the second derivative method on the non-resonant (439.50 eV excitation) XES and XAS spectra, an initial estimate of the band gaps for the undoped and doped samples is found to be (4.30 ± 0.25) eV and (4.31 ± 0.25) eV respectively. The peaks in the second derivatives of the spectra used to determine the band gaps, [93] are shown in Figure 4.2. It is the band gap of the material in its ground state that is desired, making it necessary to account for the core-hole effect. [93] In this vein the Density Functional Theory (DFT) calculations suggest a 0.26 eV increase in energy for each of these values, leading to final, experimental band gaps of (4.56 ± 0.25) eV and (4.57 ± 0.25) eV respectively for the undoped and doped samples. These constitute an upper limit for the band gap, due to the inevitable overestimation of the core hole effect. This stems from differences in the shielding of the effective charge of the

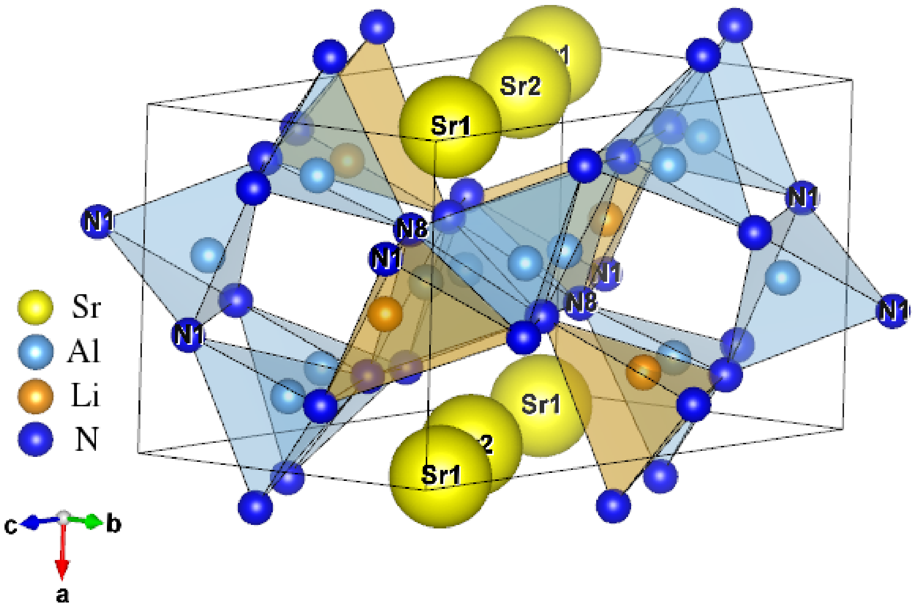

Figure 4.1: Crystal structure of SLA.

core hole in the modelled system, when compared to the actual system during collection of the XAS spectra. The band gap determined through the GGA-PBE (Generalized Gradient Approximation of Perdew, Burke and Ernzerhof) calculations is 2.90 eV, which as expected is much smaller than the experimental value. For accurate results a LDA-mBJ (Local Density Approximation with modified Becke-Johnson potential) calculation was performed, which yielded a band gap of 4.14 eV. There is near agreement between the shifted, measured band gaps and the mBJ value. Considering the uncertainty in the measured band gaps and a 10% error margin for the mBJ calculation, [92] the results agree. The final experimental band gap of SLA is (4.56 ± 0.25) eV. A summary of the band gap results is shown in Table 4.1. This result compares well with the estimated optical band gap of ∼ 4.7 eV and what is seen in sphalerite Li_3AlN_2, a 4.4 eV band gap. [8], [121]

SLA Band Gap			
Experimental	GGA-PBE	LDA-mBJ	Literature [8]
$4.56\ eV \pm 0.25\ eV$	$2.90\ eV$	$4.14\ eV$	$\sim 4.7eV$

Table 4.1: Determined experimental and theoretical band gaps for SLA.

The band structure as determined by the GGA-PBE calculation can be seen in Figure 4.3. The band gap is predicted to be indirect, with the valence band (VB) maximum between

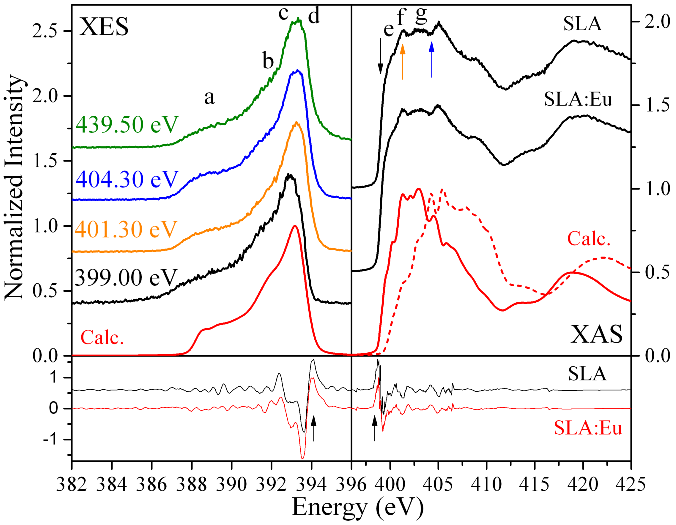

Figure 4.2: Comparison of XES and XAS spectra from SLA. The XAS spectra for the doped and undoped material are shown. The XES spectra for the doped and undoped sample are identical, therefore only those from the undoped sample are shown. The excitation energy for each XES spectrum is as indicated. Colored arrows on the undoped SLA XAS spectrum indicate excitation energy locations. The red curves are the calculated spectra. The calculated XAS for the ground (dashed line) and excited (solid line) states are shown. Second derivatives of the non-resonant spectra, used to determine the band gap, are in the lower window. Arrows indicate the maxima selected for the onset of the VB and CB. Prominent features are labelled with lower case Latin letters. The calculated spectra are shifted in energy and slightly broadened to facilitate comparison.

the Γ and M points and the conduction band (CB) minimum at the R point. The energy needed for direct transitions from the VB to the CB will therefore be a few tenths of an eV greater than the band separation determined through the XAS and XES measurements. This result is somewhat dissimilar to that of Li_3AlN_2, a direct band gap analogue of AlN. [121] Were the host lattice itself expected to emit light this would be a disadvantageous result, but its purpose is to provide an appropriate environment for the Eu^{2+} states. [122], [123] It should also be noted that the high density of bands inhibits the measurement of RIXS features, [173], [33], [124] leading to the interpretation of the variations in the XES spectra with excitation energy in terms of the variation in the DOS of the nonequivalent N sites.

The DOS for the VB and CB, as determined by the ground-state GGA-PBE calculation, are shown in Figure 4.3. The DOS of N1 (2i), N8 (2i), atoms with which they coordinate, and atomic totals are shown alongside non-resonant XES and XAS spectra. The nonequivalent N sites are similarly coordinated and between N1 and N8 the principal features of the N sites are represented. Most of these sites can be distinguished by their behavior in regions α and δ.

From Figure 4.3 it can be seen that the N:p states dominate the VB. In addition, the variations in the N DOS are mirrored in the DOS of the coordinating atoms. This not only suggests covalent bonding with the N sites, but a degree of sp-hybridization in Li and Al, as well as pd-hybridization in Sr. Strong peaks are observed in Al:s states corresponding to α in the N:p DOS of the lower VB, implying this region is characterized by Al:s - N:p covalent bonds. This is a trend seen in other materials based on XN_4 tetrahedra. [123], [125], [126] The Sr:d states dominate the lower CB, although N:p states are also present. The N states largely mirror the Sr:d states in this region, suggesting that the Sr:d states determine the lower CB as N:p states do the VB. Coincident peaks suggesting shared Al:s - N:p states are present at feature θ, similar to what was seen in the lower VB. The presence of N:p states in the lower CB and upper VB supports the use of N XES and XAS to determine the band gap. The DOS show contributions from all elements in the VB and CB, including strong participation of the N states, suggesting a rigid lattice with pervasive covalent bonding.

It can be seen in the XES spectra that excitation to e, f and g results in variations in the size of regions d and a. These preferential excitations can be explained in terms of the calculated DOS for nonequivalent N sites in the regions α through θ, supporting the varied contributions of nonequivalent N sites to the upper VB and lower CB as predicted in the DOS. The nearly unvarying shape of the XES spectra with changes in excitation energy and that the subtle changes can be explained in terms of the preferential excitation of nonequivalent N sites, points to the purity of the samples used. The presence of leftover reactants or contaminants can often be detected through such selective excitations. [127] The calculated density of states accounts for the variations in the XES spectra with excitation energy and suggests the influence of impurities is negligible. That these variations are subtle also reflects a general similarity in the DOS of nonequivalent N sites.

The calculated CB and VB DOS in Figure 4.3 show considerable similarity between the DOS of the nonequivalent Sr sites, Sr1 (2i) and Sr2 (2i). There is some variation observable in the height of a few peaks in the CB, but it is slight. In the VB the DOS are again very similar. However, there are some notable fluctuations at the upper edge of the VB at features γ and δ. These fluctuations link directly to what is seen in the coordinating N DOS. In Sr2 feature δ is suppressed, a trait seen in the associated N states. In contrast, this feature is present in Sr1 and its coordinating N atoms. For instance, δ is most prominent in N1 and N5 (2i), which coordinate solely with Sr1. In N2 (2i) and N7 (2i), which coordinate with Sr2 only, this feature is absent. N sites that coordinate with both Sr sites show the presence of δ to varying degrees. This lends further support to the Sr:pd - N:p covalent bonding in the VB. Overall the DOS suggests a similar degree of covalency between the non-equivalent Sr sites and their coordinating N sites, with slight site-specific variations. This will have an impact on the centroid shift of the Eu^{2+} ions occupying the Sr sites, which will strongly influences the material's luminescence properties.

Discussion

General features of SLA's electronic structure, such as the nature of the bonding in the XN_4 tetrahedra, are shared by other phosphor materials, which in turn do not have the same luminescence properties as SLA. [123], [125], [126] These general features are clearly insufficient for efficient visible light emissions. The band gap must be large enough as to be transparent to the the RE ion's emissions or house the relevant ground and excited states of the RE ion. [123], [125] For efficient luminescence in the desired spectral range, the crystal field splitting (CFS), centroid shift and Stokes shift are also key considerations for phosphor design. [8], [122], [128], [44]

A reoccurring theme for narrow-band emissions is a small Stokes shift. The covalent nature of N bonding in SLA suggests it should exhibit considerable rigidity and as a result, a limited Stokes shift. The principal factor for determining the CFS experienced by metal cations is the geometry of the ligands, as opposed to the ligands themselves. [44] The two nonequivalent Sr sites in SLA have a very similar cuboidal coordination. [8] The similarity in the crystal fields experienced at the Sr sites in SLA is further supported by their highly similar DOS. Elsewhere, substantial variation in the DOS of nonequivalent metal sites is seen, [127] alongside broader emissions. [125] The uniformity of the crystal field experienced by the two nonequivalent Sr sites in SLA is supported by the similarity in their DOS.

The nephelauxetic effect is largely accredited with introducing the appropriate centroid shift in the RE cation d-orbitals and can be attributed to the covalency between the RE cation and the surrounding anions, as well as their polarizability. [122], [128], [129] The anion polarizability is similarly influenced by its own coordination environment. [128], [44] The centroid shift occurs independently of the CFS, [44], [128] therefore both must be considered to engineer phosphor emissions. The calculated DOS for SLA show covalent interaction between the nonequivalent Sr and surrounding N sites, in conjunction with a high degree of similarity in that interaction. The coordination of the N sites is known to be similar from X-ray diffraction measurements. [8] As with Sr, the N DOS reflect this. Despite the slight variations pointed to, the N DOS and the implied interactions with coordinating atoms are quite uniform across nonequivalent sites. Therefore, the centroid shift for the Eu^{2+} ions occupying either of the Sr sites can be anticipated to be similar. Since the CFS is largely determined by the ligand geometry, similar CFS at the nonequivalent sites demands similar centroid shifts if a narrow emission bandwidth is to result. To that end the information from the DOS overwhelmingly supports that conditions in SLA are highly favourable for narrow band emissions.

The band structure and DOS for the promising new LED-phosphor SLA have been calculated and related to the observed luminescence properties of the material. The calculated XAS and XES spectra reproduce those observed experimentally. The site-selective XES spectra also lend strong support to the predicted DOS. The experimentally determined band gaps of undoped and doped SLA are (4.56 ± 0.25) eV and (4.57 ± 0.25) eV, respectively. The band gap is predicted to be indirect by the GGA-PBE calculations. The VB of SLA is characterized by Al:s - N:p covalent bonds at lower energies and N:p - Sr:pd covalent bonds towards higher energies. The CB is characterized by N:p and Sr:d states in the lower CB, with a notable N:p - Al:s contribution. The strongly covalent nature of the bonding in SLA, the interaction of the N:p and Sr:pd states and high degree of similarity in the DOS of the two nonequivalent Sr sites all re-enforce its importance as a phosphor for LED applications. These results help in understanding the structure-property relations in $Sr[LiAl_3N_4]:Eu^{2+}$ and explain the narrow-band emission despite the presence of two crystallographically independent Sr-sites. These studies should inform further advances in the development of phosphors for illumination-grade pc-LEDs.

Experimental

XES and XAS measurements were performed at Beamline 8.0.1 of the Advanced Light Source (Berkeley, California, USA) [48] and the Spherical Grating Monochromator (SGM) beamline at the Canadian Light Source (Saskatoon, Saskatchewan, Canada), [46], [47] respectively. Beamline 8.0.1 is equipped with a Rowland circle X-ray spectrometer, spherical gratings and area sensitive multichannel detector. [48] The XAS spectra were measured through the partial fluorescence yield (PFY), detected with silicon drift X-ray fluorescence detectors. The resolving power for the XES measurements, given in terms of the photon energy E as $\frac{E}{\Delta E}$, is approximately 800. The XAS measurements have approximate resolving powers of 4000 and 2000 at Beamline 8.0.1 and the SGM beamline, respectively.

The powdered samples were stored and prepared for measurement under dry N_2 or Ar atmospheres to avoid possible oxidation or hydrolysis. Samples were pressed into freshly exposed indium foil before being placed into the sample transfer chambers, which were initially filled with dry N_2, then evacuated. No other treatment of the samples was carried out. Measurements were conducted under a high vacuum of 5×10^{-7} torr or better. The XES and XAS energy scales were calibrated using the XES and XAS spectra of hexagonal boron nitride (h-BN) powder (99.5% purity, Alfa Aesar). The peaks used for XES calibration are the two dominant peaks in the h-BN non-resonant emissions, positioned at 392.75 eV and 394.60 eV. The lowest energy peak in the XAS spectrum of h-BN is taken to lie at 402.1 eV.

Calculations

DFT calculations were performed using the WIEN2k software package. This software uses the full potential (linearized) augmented plane waves with local orbitals (LAPW + LO) to self consistently solve the Kohn-Sham equations. [112] The generalized gradient approximation of Perdew, Burke and Ernzerhof (GGA-PBE) is used for the exchange and correlation energies. [112], [22] Additional calculations were performed using the local density approximation

(LDA) with a modified Becke-Johnson (LDA-mBJ) potential to predict the band gap of the material. [92] Core hole calculations with a 2×2×2 supercell were performed to model the experimental XAS as necessitated by the final state rule. [94], [130] The ground state calculation is sufficient for describing the XES spectra and in addition to the DOS, is used to provide the predicted band structure of SLA.

Acknowledgements

Research described in this paper was performed at the Canadian Light Source, which is funded by the Canada Foundation for Innovation, the Natural Sciences and Engineering Research Council of Canada, the National Research Council Canada, the Canadian Institutes of Health Research, the Government of Saskatchewan, Western Economic Diversification Canada, and the University of Saskatchewan. The Advanced Light Source is supported by the Director, Office of Science, Office of Basic Energy Sciences, of the U.S. Department of Energy under Contract No. DE-AC02-05CH11231. We would also like to acknowledge the support of the Natural Sciences and Engineering Research Council of Canada (NSERC) and the Canada Research Chair program. The authors also acknowledge Compute Canada. The calculations presented in this work were performed on the Grex high-performance computing cluster, which is part of the Westgrid network (www.westgrid.ca) and Compute Canada Calcul Canada (www.computecanada.ca).

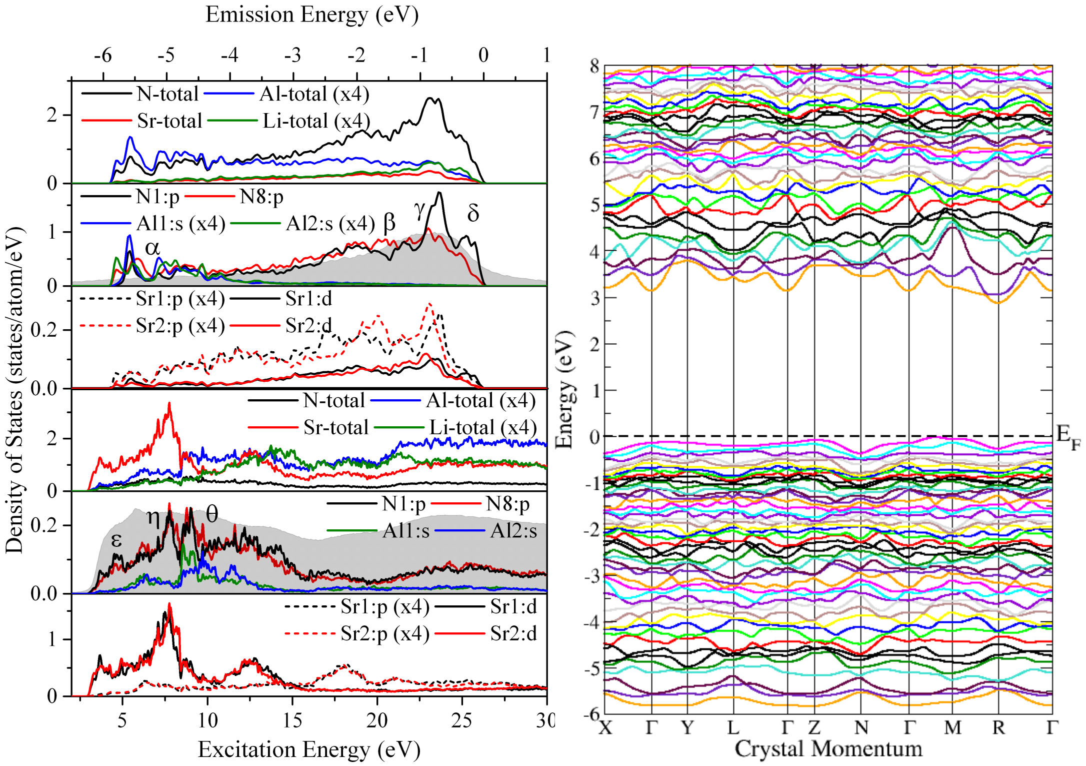

(a) (b)

Figure 4.3: (a) Calculated DOS in the VB (upper half) and CB (lower half) of SLA. The DOS of nonequivalent N sites and several coordinating atoms are given (all with Wyckoff position 2i), along with atomic totals in the unit cell. Normalized, measured spectra are included for comparison and are shaded grey. To aid comparison, measured and calculated band edges are aligned and select DOS are scaled by the factors indicated. Greek letters denote prominent features in the DOS. (b) The band structure of SLA based on ground state GGA-PBE calculations. The band gap is indirect. The CB minimum is at the R-point and the VB maximum between the Γ and M points. The energy scales are set with respect to the Fermi energy.

Chapter 5

An Inefficient, Ultra Narrow-Emitting LED-Phosphor: Sr[Mg_3SiN_4]:Eu^{2+}

5.1 Introduction

In close timing with the discovery of SLA, was the discovery of Sr[Mg_3SiN_4]:Eu^{2+}. [9] This phosphor is structurally similar to, and isoelectronic with SLA. It has a lone site that can be occupied by the Eu^{2+} dopant, cuboidal ligand coordination, and the narrowest emissions observed to date for a red-emitting Eu^{2+}-doped phosphor. However, it shows poor efficiency and thermal quenching behaviour, making it of as little applicability in pc-LEDs as it is great in utility for understanding SLA and other phosphors.

The publication given here compares SMS and SLA to derive a deeper understanding of their structure-property relationships, again building on the foundation established with the study of α-P_3N_5. My contribution to the manuscript, published in *Adv. Opt. Mater.*, [131] was the same as for the preceding manuscript on SLA.

5.2 The Publication

Electronic Structure, Band Gap, and Thermal Quenching of $Sr[Mg_3SiN_4]:Eu^{2+}$ in Comparison to $Sr[LiAl_3N_4]:Eu^{2+}$

Thomas M. Tolhurst, Sebastian Schmiechen, Philipp Pust, Peter J. Schmidt, Wolfgang Schnick, Alexander Moewes*

Thomas M. Tolhurst, Alexander Moewes

Department of Physics and Engineering Physics, University of Saskatchewan, 116 Science Place Saskatoon, Saskatchewan S7N 5E2, 1-306-966-6431, alex.moewes@usask.ca

Sebastian Schmiechen, Philipp Pust, Wolfgang Schnick

Department of Chemistry, University of Munich (LMU), Butenandtstrasse 5-13, 81377 Munich, Germany.

Peter J. Schmidt

Lumileds Development Center Aachen, Lumileds Germany GmbH, Philipsstrasse 8, 52068 Aachen, Germany.

5.3 Abstract

In this study the band gap and electronic structure of the next-generation, red phosphor $Sr[Mg_3SiN_4]:Eu^{2+}$ (SMS), are explored through a combination of soft X-ray spectroscopy, density functional theory calculations and thermal quenching data for the Eu^{2+} 5d → 4f emissions. The results will be compared to those for the high-efficiency phosphor $Sr[LiAl_3N_4]:Eu^{2+}$ (SLA), which shows different, yet exceptional emission characteristics in the red-spectral region. It is found that SMS has an indirect band gap of 3.28 ± 0.20 eV, strong uniformity in the density of states of its nonequivalent nitrogen sites and an estimated energetic separation between the lowest Eu^{2+} 5d state and the conduction band of ~ 0.13 eV. The Eu^{2+} 5d - conduction band separation in SLA is found to be ~ 0.28 eV, which points to why the visible emissions of SLA, and not SMS, show outstanding thermal stability. A bonding scheme explaining the band gap difference of SMS and SLA is proposed based on the density of states of SMS. Modifications to each lattice are put forward for achieving optimized phosphor characteristics for use in pc-LEDs.

5.4 Introduction

With a significant portion of global energy consumption going towards lighting, it is important to develop efficient, illumination-grade lighting technologies. [4] One of the most promising technologies in this regard is the phosphor-converted light emitting diode (pc-LED). Several designs have been proposed for efficient pc-LEDs, each with its own advantages and limitations [4]. Blue LED-chips with YAG:Ce are low cost, but have poor color stability with input current and poor color rendering from a lack of emissions in the red-spectral region. Other designs are therefore preferable for high-quality illumination. [7] If pc-LEDs are to be used in general lighting they must be efficient, have high color rendering and temperature-stable emission spectra. Two promising designs meeting these requirements are UV and blue LED chips, using three and two phosphors, respectively. Even these designs have encountered challenges, such as the inefficiency of the available red phosphors. [4] The discovery of new, efficient red phosphors is therefore of the utmost importance. With constantly improving efficiency and color rendition, along with dropping production costs, pc-LEDs can be expected to replace traditional lighting methods in the near future. [5]

Rare earth (RE)-doped nitride phosphors based on condensed tetrahedral networks, with their tendency to exhibit highly efficient and stable emissions, are promising candidates for the next generation of phosphors for pc-LEDs. [5, 7] However, not all nitride matrices are equal. The polarizability of the ligands, covalency and crystal field splitting (CFS) experienced by the RE dopants are all key parameters. [5]

Recently the promising, red phosphors $Sr[Mg_3SiN_4]:Eu^{2+}$ (SMS) and $Sr[LiAl_3N_4]:Eu^{2+}$ (SLA) have been reported [8,9]. These highly condensed nitrides show narrow-band emissions in the red-spectral region. SMS shows $\lambda_{em} = 615$ nm with a FWHM of 43 nm, while SLA shows $\lambda_{em} = 650$ nm with a FWHM of 50 nm. Narrow emissions in this region are of interest because they are more likely to fall within the sensitivity range of the human eye. Emissions outside of this range, which often occur with a large FWHM in the red-spectral region, lead to wasted energy input and additional heating in the device.

This work will focus on characterizing the electronic structure of SMS, which exhibits the narrowest emissions to date for a red-emitting, Eu^{2+}-doped phosphor [9]. A combination of X-ray spectroscopy and density functional theory (DFT) calculations are used in this characterization. The thermal quenching data for the visible, Eu^{2+} 5d → 4f emissions of SMS and SLA are also modelled and compared. Where SMS shows poor emission stability with increases in temperature, SLA shows exceptional stability. However, SMS emits at a shorter wavelength, which may be more useful for certain applications. Between these phosphors many ideal characteristics for use in pc-LEDs are present. Their comparison leads to several suggestions for directing the search for the ideal red-emitting LED-phosphor.

5.5 Results

5.5.1 X-ray Emission and Absorption

Nitrogen K-edge

Resonant (RXES) and normal (NXES) X-ray emission and X-ray absorption (XAS) spectra were collected at the nitrogen K-edge and the silicon L-edge, and are shown in Figure 5.1 alongside our calculated spectra. Due to the presence of a core hole in the final state of the X-ray absorption process, calculated absorption spectra for the ground and excited states of the system are shown. The latter case is needed to estimate the influence of the nitrogen core hole on the measured spectrum [93–95]. Largely there is excellent agreement between the calculated and measured spectra, supporting the structure and space group determined through X-ray diffraction [9]. This agreement also provides strong experimental support for calculated properties of SMS, such as the density of states (DOS) and band structure, from which the spectra are derived. There is better agreement between the ground state XAS calculation and the experimental spectrum, than with the excited state calculation. This suggests that the screening of the 1s core hole in the excited state calculation is somewhat less than that in the actual material during the measurement, as well as a slight overestimation of the core hole concentration.

There are a few differences between the calculated and measured spectra that should be noted. It is apparent that the peak at 401.30 eV in the measured XAS spectrum is absent from the calculation. At the same time the 401.30 eV resonant emission spectrum clearly deviates from the general shape of the other resonant and non-resonant emission spectra. There is evident vibrational fine structure in the 401.30 eV absorption peak, which corresponds to what is expected for the $1\pi_g^*$ absorption of N_2 [133]. It can then be immediately recognized that the dominant contribution to the 401.30 eV emission spectrum is the N_2 $3\sigma_g^{-1}$ line expected when exciting to the $1\pi_g^*$ [134]. This is a common sign of mild radiation damage in nitride materials [135]. The otherwise normal emission of the sample can be seen alongside the N_2 emissions. It is inevitable that the emission spectra excited at energies at, or above, the N_2 $1\pi_g^*$ feature will contain emissions from N_2. However, the emission spectrum excited at 399.00 eV shows no sign of N_2 emissions. Given the absence of absorption from the N_2 $1\pi_g^*$ at this energy, this is to be expected. Further, the match between this emission spectrum and the calculation is outstanding, suggesting no resonant, or contaminant, effects are present and that it is representative of the valence band (VB) partial density of states (pDOS) of SMS. Although emission spectra excited well above the absorption edge, here at 439.50 eV, are usually taken as the best representation of the partial density of states, the normal emissions of N_2 will be present in this case. The normal N_2 emissions are expected to approach the upper edge of the 439.50 eV emission spectrum, [134] which would normally be considered the onset of the VB. In this case the 399.00 eV excitation will be the best representation of the VB pDOS. It should be pointed out that although the N_2 absorption peak increases in intensity as a function of exposure time, no shift is seen in the onset of the XAS spectrum, which corresponds to the conduction band (CB) edge.

Resonant effects also appear in the emission spectrum with the lowest excitation energy. At this energy no effect from the N_2 is possible. A shift in the band edge is seen along with the deformation of the spectrum and a new peak at 393 eV. These are the effects expected for the k-conserving resonant inelastic X-ray scattering (RIXS) process in the vicinity of the band edge [33]. The shift of the measured VB edge to a lower energy upon excitation to the CB edge is indicative of an indirect band gap.

Silicon L-edge

The NXES and XAS at the silicon L-edge, with corresponding calculations, are shown in Figure 5.1. Since the initial and final states of the XES and XAS transitions at this edge are p states, it is expected that the measured spectra should be due to transitions to and from s and d states. Once again there is excellent agreement between the calculated and measured spectra, aside from a slight difference in peak heights at lower energies in the VB. The calculated s and d pDOS are included in the figure, and account for the observed emission and absorption peaks. Once again, the calculated ground state absorption spectrum is the best match to the experimental data.

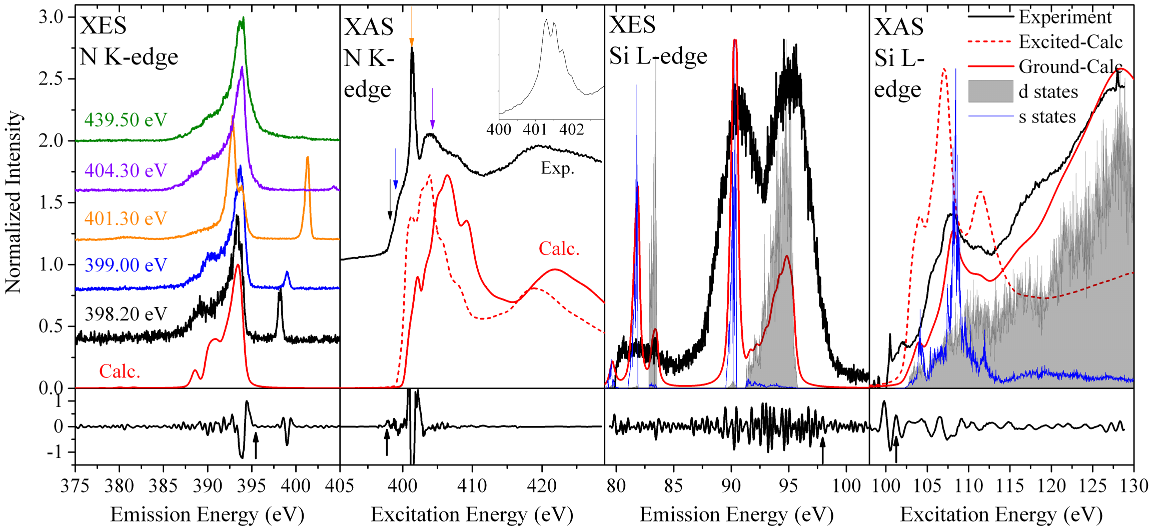

Figure 5.1: Left: Nitrogen K-edge emission and absorption spectra, alongside those calculated with DFT. The 398.20 eV resonantly excited emission spectrum shows a band edge shift and change in spectral shape. The spectrum excited at 401.30 eV shows characteristic N_2 RIXS. The inset is a magnification of the 401.30 eV absorption peak, which shows the characteristic vibrational fine structure of N_2. Right: Silicon L-edge emission and absorption spectra, alongside the calculated spectra and selected silicon pDOS. The varying contributions of the s and d states to the the spectra can be clearly seen. Second derivatives of the relevant spectra, which are used to determine the band gap, are shown in the lower panels. The peaks selected for the band gap determination are indicated with arrows.

5.5.2 Band Gap

The band gap for this sample is determined using the nitrogen K-edge data, through the second derivative of the 399.00 eV RXES spectrum and the XAS spectrum, as shown in Figure 5.1 [93]. As per the discussion above, the NXES from excitations above the N_2 absorption edge cannot be used to determine the VB edge. The calculated band structure in Figure 5.3 supports that the full range of crystal momenta is excited at 399.00 eV, and therefore that the upper edge of the XES spectrum at this energy represents the true edge of the VB. Taking the first peak in the second derivative that lies above the noise level, on either side of the gap, a band gap of 3.03 ± 0.20 eV is obtained. However, this value must be corrected for the effect of the core hole [93]. The calculated spectra for the ground and excited states suggest a 0.25 eV shift, which leads to a supported band gap of 3.28 ± 0.20 eV. Given that the spectra from the ground state calculation match the experimental spectra more closely than those from the excited state calculation, this constitutes an upper limit for the band gap of SMS.

An estimate of the band gap may also be taken from the silicon L-edge spectra in Figure 5.1. Once again applying the second derivative method a measured band gap of 3.31 ± 0.20 eV is found. The silicon L-edge calculations suggest a shift of 0.11 eV due to the core hole effect, which leads to a final gap of 3.42 ± 0.20 eV, which is in agreement with the value obtained from the nitrogen K-edge. However, due to the poor definition of the absorption onset at the silicon L-edge, it is most prudent to use the nitrogen K-edge result as the final estimate. This is especially the case since, unlike at the nitrogen K-edge, the effect of any radiation damage to the measured band edge is unknown at the silicon L-edge.

Two separate calculations were performed for this system, one using the generalized gradient approximation (GGA), and another using the local density approximation with a modified Becke-Johnson potential (LDA-mBJ) [92]. The former gives a band gap of 2.694 eV and the latter a 4.124 eV band gap. The underestimation of the band gap by the GGA calculation is typical, whereas the mBJ potential is expected to be accurate to within about 10% [92]. The measured value for SMS lies between these two values. With the good agreement between the calculated and measured spectra, the calculation can be taken as a good representation of the other aspects of the system. The results of the experimental and calculated band gap estimations are summarized in Table 5.1, alongside an optical measurement from the literature [9]. The difference between our measured band gap and the measured optical gap will be discussed below, with the band structure of SMS.

Table 5.1: Determined experimental and theoretical band gaps for SMS.

SMS Band Gap			
Experimental	GGA-PBE	LDA-mBJ	Literature (optical) [9]
$3.28\ eV \pm 0.20\ eV$	$2.694\ eV$	$4.124\ eV$	$\sim 3.9\ eV$

5.5.3 Density of States

The density of states of SMS, shown in Figure 5.2, has many features in common with those of other nitrides and phosphors based on XN_4 (X = Al, Ga, P, Si ...) tetrahedra [108, 136]. The nitrogen p states dominate the VB, while the strontium d states dominate the CB. There is strong mixing of silicon s and nitrogen p states in the lower VB (α), as well as in the mid CB (ϵ). The strontium states show marked pd hybridization and mixing with the nitrogen p states in the upper VB (γ) and lower CB (δ). The contributions of magnesium are quite modest and show a degree of sp hybridization (α and β), and mixing with the nitrogen p states (α - γ). The bonding seen here between nitrogen, silicon and magnesium is very similar to that between nitrogen, aluminum and lithium in SLA [108], as is the high uniformity of pDOS from nonequivalent nitrogen sites. From the agreement between the calculated nitrogen and silicon spectra, it can be expected that the DOS given here are an accurate representation of those in SMS. However, these calculations do not include the Eu^{2+} atoms found in the doped matrix, whose properties are of great interest and can be addressed through data on the thermal quenching of the visible 5d → 4f emissions.

5.5.4 Band Structure and RXES Spectra

Using the mBJ potential, the predicted band structure of SMS was determined and is shown in Figure 5.3. Using this potential has previously led to improved agreement with experiment [92]. The band gap is predicted to be indirect, with its minimum at the Γ-point. In addition to the band structure, RXES spectra were calculated and the excitation corresponding to the 398.20 eV experimental spectrum is also shown as a band across the relevant E-k diagram in Figure 5.3. As can be seen, the excited states surround the gamma point. The predicted shift in the VB edge from the calculated RXES spectrum of about 0.1 eV matches reasonably well with the observed shift of 0.2 eV. This provides experimental support for an indirect

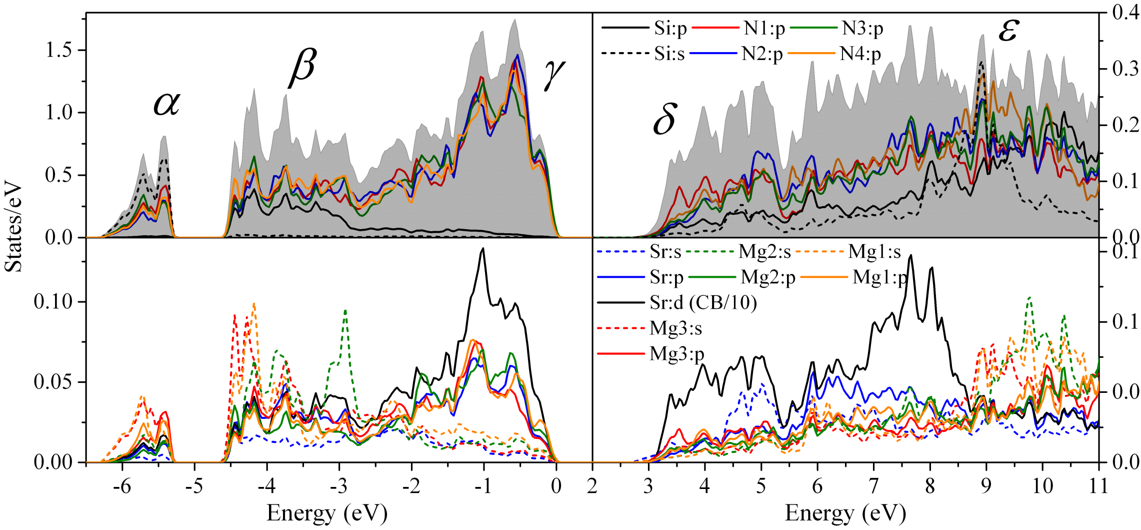

Figure 5.2: Calculated density of states of SMS. The total DOS is shaded grey, and scaled to facilitate comparison with the pDOS. Select pDOS are given for several non-equivalent sites. Characteristic regions of the DOS are labelled with Greek characters.

band gap in accordance with what has been calculated. The discrepancy between the X-ray and optical band gaps can also be explained by the calculated band structure. Energetically the smallest direct transition from the VB to the CB is 0.31 eV larger than the indirect gap. Combining this with the measured X-ray band gap, the predicted optical gap is 3.58 ± 0.20 eV, which agrees rather well with the optical gap measured elsewhere [9]. All of this strongly supports that the band gap of SMS is indirect, and the accuracy of the calculated band structure.

It is also worth considering the character of the calculated bands in the context of the observed difference in the band gaps of SMS and SLA. The band structure of SLA using a standard GGA-PBE calculation has been presented elsewhere [108]. For comparison with SMS this band structure was recalculated using the mBJ potential and the resulting character plot is shown with that of SMS in Figure 5.3. It should be noted that the VB maximum has the same energetic location in SMS and SLA, making the difference in band gaps due entirely to the positioning of the CB.

The overarching trends that can be seen are a VB dominated by nitrogen p states, a CB dominated by strontium d-states, and the appearance of s states in the lowest CB energy band. This lowest energy band has its minimum at the Γ point, as would be expected [12]. Although this band does form the minimum in SMS, the strontium d-states at R in SLA drop below the s-band to form the CB minimum.

This arrangement of states and the related difference in the band gaps of these materials can be understood in terms of the relative positioning of the atomic term values and bond formation of their constituents [12]. Such a picture has been used to great effect elsewhere in the description of band characters of mixed III-V tetrahedral compounds [91].

Focusing on SMS, the state energies for the atomic constituents in order of decreasing energy will be the strontium 3d, strontium 3s (-5.00 eV), magnesium 2s (-6.86 eV), 3sp^3-hybridized Si states (-8.29 eV) and the nitrogen 2p states [12]. Taking the nitrogen p states as the approximate location of the valence band, the mixing of these states with the others forms a consistent picture of the observed band structure and density of states. The mixing of the nitrogen p and strontium d states will be minimal on account of their separation in energy. With such a small perturbation the nitrogen p - strontium d hybrid states can be expected to be present at the uppermost levels of the VB and in the higher levels of the CB. The bonding between magnesium and nitrogen will tend to be polar, but a larger degree of mixing should be seen than with the strontium d states. The largely emptied magnesium s states should be expected to form the bands near the base of the CB and the levels below the nitrogen p - strontium d states in the VB, which is what is observed in the DOS and band character plots. Finally one expects the stronger mixing of the silicon hybrid states with the nitrogen p states to form the lower levels of the VB and states more centrally located in the CB, which is observed. The associated strong splitting of these states ensures the magnesium s states form the bottom of the CB. The strontium s states can be expected to be largely ionized and contribute at energies above those of magnesium. This orbital mixing scheme is consistent with that suggested by the tetrahedral coordination of silicon and magnesium in SMS, as well as the octahedral coordination of the nitrogen atoms.

With the structural similarities between SLA and SMS, the same general description, just given for SMS, applies to SLA. A few key differences come about from the different atomic composition of the two materials. The root cause for the difference in the band gaps of these materials becomes apparent when considering the relative positioning of the cation energy levels in SLA as compared to those in SMS. The atomic lithium s states are expected at -5.48 eV and the Al sp^3 states at -6.17 eV [12]. With the largely ionized lithium s states again forming the bottom of the CB a difference in the the band gaps of the two materials of about 1 eV would be expected. Indeed, this is what is observed when comparing to the reported band gap of SLA [108]. One also expects that the emptied strontium s states will start affecting the CB minimum, due to their similarity in energy to those of lithium.

A few more details can be considered to finish the discussion of the differences between the SMS and SLA band structures. The degree of splitting of the energy levels subject to hybridization is expected to scale roughly as the inverse square of the inter-atomic separation [12]. The trends in the cation-anion bond distances in these materials are what would be expected from the ionic radii in both cases. This leads to the SLA Al-N and Li-N distances being larger than the SMS Si-N and Mg-N distances respectively. Associated with this is a smaller Sr-N distance in SLA than in SMS. One therefore expects a slight increase in the energy of the pd states associated with the N-Sr bonds in the CB of SLA. This has important implications for the effects of any elemental substitutions on the thermal quenching behaviour of these materials, because it will influence the character and energy of the lowest lying CB states [139].

This last effect was discussed by Dorenbos [139], where he specifies two material types. Type I materials are those whose CB minimum changes with the type of alkaline earth cation being replaced by the RE ion (strontium in the present cases). Type II materials are those whose CB minimum is independent of such substitutions [139]. The difference lies in whether the alkaline earth cation states form the CB minimum or not. Where they do, the thermal quenching behaviour can be expected to vary considerably with the substitution of different alkaline earth cations. The determined band characters of SMS place it squarely as a type II material, with the tetrahedral cation states forming the CB minimum. It would seem that SLA is a borderline case, where the CB minimum follows the same trends as SMS, with the exception of the states around R, where the strontium d states form the true CB minimum. As well, the strontium s states begin to contribute to the CB minimum in SLA.

The effect of cation substitutions on the CB minimum of SLA can then be expected to depend on two competing trends. It is clear that replacement of lithium with heavier cations of the same row will increase the energy of the low-lying s states, and potentially increase the band gap. An overall increase will not occur if the strontium states remain fixed energetically. However, the introduction of larger cations into the tetrahedral sites can be expected to decrease the N-Sr separation with a concomitant increase in the energy of the antibonding pd (ps) states which form the CB minimum. This is the same trend seen in moving from SMS, with its small N-Mg/Si and large N-Sr separation, to SLA. An overall increase in the band gap of SLA should therefore follow from the substitution of larger tetrahedral cations on the lithium site.

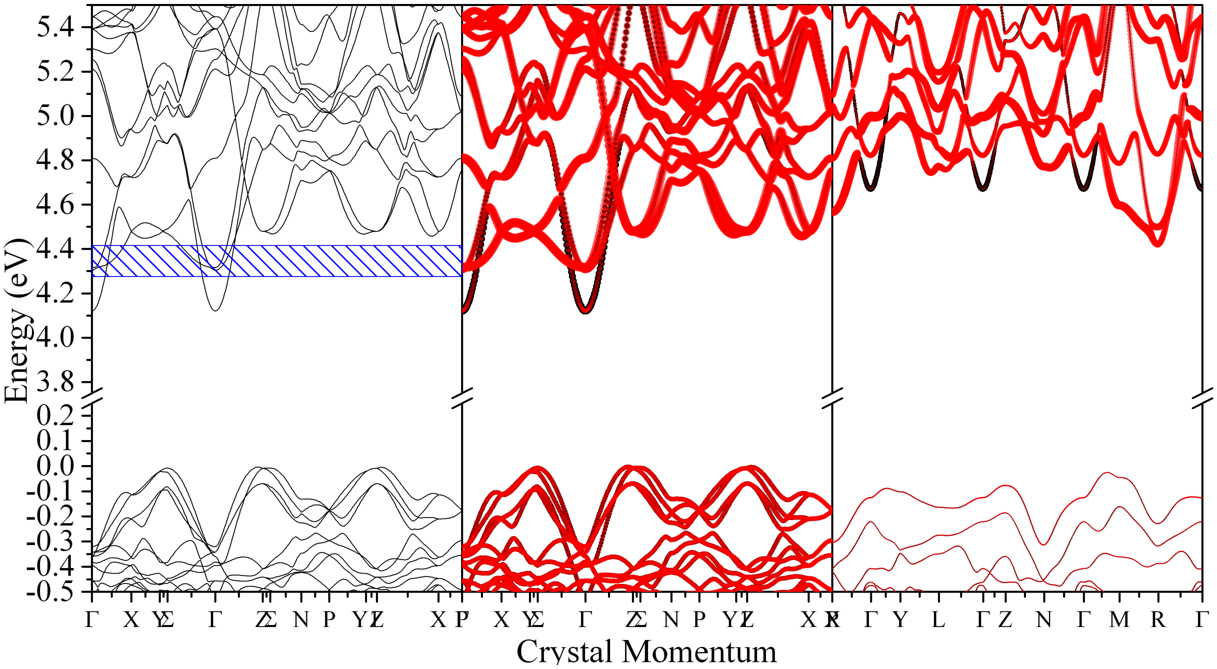

Figure 5.3: Left: the band structure of SMS calculated using the mBJ potential. The hatched energy region identifies the area summed over to obtain k-weighted RXES spectra. Center: the mBJ band character plot of SMS with nitrogen s states in black and strontium d states in red. The line thickness is proportional to the fractional composition of the states. Right: the mBJ band character plot of SLA with nitrogen s states in black and strontium d states in red.

5.6 Position of the Eu^{2+} 5d States in the Band Gap

The DFT calculations suggest a considerable degree of covalency between the atomic species in SMS. However, the Eu^{2+} orbitals responsible for the optical fluorescence of the doped material are localized. Their energetic position is critical for the stability and color of fluorescence produced by the phosphor. A degree of interaction between the 5d states and their surroundings is expected, and shifts the centroid of the orbitals. Also key to the energetic positions of the 5d states are the polarizability of the ligands and the crystal field splitting (CFS) they induce [44, 128, 137, 138]. A simple analysis of the variation in the 5d → 4f emission intensity as a function of temperature for SMS and SLA, can offer some insight into which matrix characteristics are the most influential in determining the positions of the RE 5d states. The thermal quenching data of SLA and low temperature emission spectra of SMS are published elsewhere [8, 9]. The emission intensities of SMS and SLA as functions of temperature are shown in Figure 5.4, along with fits to the data.

The data can be modelled by assuming that non-radiative decay of the 5d states follows thermal excitation from the lowest 5d state into the CB or another low-lying state. The rate of non-radiative decay will then be given by a term $\Gamma_0 e^{-\Delta E/kT}$ [139], where Γ_0 is the attempt rate for surpassing the energy barrier ΔE, the separation of the 5d state from the next-lowest-lying level, here assumed to be the CB. The use of Boltzmann statistics is justified by the expected separation of the 5d and CB states from the Fermi energy, as well as the high density of states in the CB. With a radiative decay rate Γ_v it can then be expected that the emission intensity as a function of temperature can be described by a function of the form [139]:

$$I(T) = I(0)/\left(1 + \frac{\Gamma_0}{\Gamma_v} e^{-\Delta E/kT}\right) \tag{5.1}$$

which gives the fit results displayed in Figure 5.4. The ΔE values obtained for SMS and SLA are respectively 0.13 eV and 0.28 eV. Systematic uncertainties in these values are difficult to quantify and therefore, these values should be considered approximate. It is important to note that the thermal quenching of phosphors is strongly influenced by concentration quenching and the presence of defects [141–144]. The modified Arrhenius equation does not account for these additional effects and its results are therefore very sensitive towards defects, impurities and the Eu^{2+} concentration. Other methods for determining the 5d-CB separation, such as using the charge transfer to a trivalent RE ion, can be more accurate [139, 140]. However, the fits to the thermal quenching data give the qualitative indication that the 5d states of SLA are further separated from the CB than those of SMS. The source of SLA's temperature stability seems clear, the 5d states are well separated from the edge of the conduction band. The question then becomes whether the difference between the 5d positions in SLA and SMS should be attributed to the CFS or the centroid shift in the respective cases. This can be addressed through a brief, qualitative discussion drawing on this and other work.

The centroid shift and CFS can be treated separately [128]. The CFS will be influenced by the RE ion's coordination geometry and the RE-ligand separation. The magnitude of the centroid shift can be related to the polarizability of the anions coordinating with the Eu^{2+} [128]. This polarizability is in turn affected by the electronegativity of the anion's own coordinating cations. Looking at the averaged, Pauling electronegativities of the tetrahedrally coordinated cations for SMS and SLA, values of 1.46 and 1.45 are obtained respectively. This implies the polarizability of the nitrogen anions in both cases should be similar, although perhaps marginally greater in SLA. Although the centroid shift in SLA should be greater than in SMS, it likely cannot account for the difference in the positions of their respective Eu^{2+} 5d states. The CFS is the only alternative explanation.

The Eu^{2+} ions are coordinated by eight nitrogen anions in similar cuboidal coordination in both SMS and SLA, leaving only the bond lengths as the cause of any difference in CFS [128]. Indeed the difference between the Eu^{2+} sites is notable in these materials. The mean Eu-N separation in SLA is 2.80 ± 0.10 $\AA$ for both lattice sites that can be occupied, whereas in SMS the mean Eu-N separation is 2.86 ± 0.20 $\AA$. It has been shown elsewhere that the variation in CFS with RE-ligand separation goes as the inverse square of this separation, which is a large effect [128]. This suggests the CFS is the dominant factor giving rise to the varying emission properties in SMS and SLA. The CFS should then also be a means to alter the emission characteristics of these materials.

It is known that variation in the RE-ligand separation is an effective means of varying the CFS and thus the emission wavelength in RE-doped phosphors [145]. An increase in the RE-ligand distance will lead to a decrease in the CFS and thus an increase in the emission energy. Given that both SLA and SMS exhibit similar, small Stokes shifts, [8, 9] it is worth noting that the emissions of SLA are at a longer wavelength than those of SMS. This further suggests that the relative depth of the Eu^{2+} states in the band gap of SLA can be attributed to increased CFS.

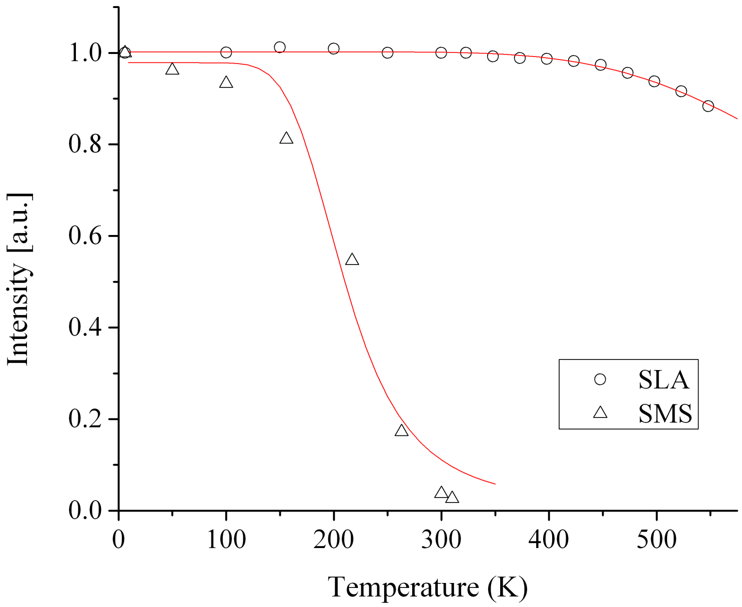

Figure 5.4: Measured intensity of 5d → 4f emissions as a function of temperature, along with the fit of equation 5.1 to the data. The fits of a single activation energy to the data are shown as solid, red lines. Thermal quenching data for SLA and low temperature emission spectra for SMS are published elsewhere. [8, 23]

5.7 Discussion

For certain applications it may be desirable to alter the band gap or emission wavelengths of SLA or SMS. Shorter wavelength emissions might readily be achieved through a lattice with slightly lowered CFS. This would lead to a higher energetic position of the 5d states in the band gap, and a related decrease in thermal stability. However, in the case of SLA there may be room to spare. Similarly, narrow and efficient emissions in the right portion of the red-spectral region might be accessible through variations of the SMS lattice. As an example, variations in the crystal field of RE sites have been successfully brought about by variations in the material's lattice constant through a solid solution series [145], where larger ions are introduced into the lattice. The larger ions lead to an expansion of the unit cell, a concomitant increase in the RE-ligand separation, and reduced CFS. Such solid solutions are typically carried out through substitution at the cation site which is also occupied by the

Eu^{2+} ion. The case of SMS and SLA suggest that the effect of substitution on the tetrahedral cation sites will be slightly different. The increase in size of the tetrahedral cations in going from SMS to SLA leads to an increase in the CFS. Although the larger cations may lead to an expansion of the unit cell, at the same time there will be a decrease in the N-Sr separation associated with this same substitution. Coupled to the effects on the band gap discussed above, the general effect of larger tetrahedral cations can be expected to be larger CFS and a larger band gap.

Another interesting feature of SMS is its narrow emission band. It has been pointed out elsewhere that this can be attributed to the rigid lattice and lone site occupied by the Eu^{2+} ions [9]. Also important is a lack of statistical variation in the occupation of the tetrahedrally coordinated cation sites [146]. The notable covalent bonding suggested here by the calculated DOS supports the idea of a rigid lattice. The bonding between strontium and its coordinating nitrogen ligands is also clear, suggesting some degree of covalency between these ligands and the Eu ions should also occur. This suggests that the centroid shift of the Eu 5d states must be due in part to covalency with the ligands and the nephelauxetic effect [138]. Of course, anion polarizability must also be considered, but is expected to have a limited effect in highly covalent lattices, as seen in condensed borates, which have a small spectroscopic polarizability and centroid shift [128]. In general there is a tendency for the CFS to be the dominant contributor to the red shift [128]. At the same time, changes in the electronegativity of the cations surrounding the nitrogen anions should be kept in mind, although their influence will be secondary.

Ultimately, it would be desirable to shift the 5d positions in SMS to lower energies, which will also red-shift the emissions and to shift those of SLA to higher energies, simultaneously blue-shifting the emissions. For SMS this could be attempted through the incorporation of larger isoelectronic, tetrahedrally-coordinated ions into the lattice. This modification is essentially represented by SLA. It may also be desirable to pursue the substitution of larger isoelectronic, tetrahedrally-coordinated ions into SLA. Although this will increase the CFS, a simultaneous band gap increase may lead to highly efficient emissions at a desirable wavelength. The associated changes in the average cation electronegativity may, in some cases, tend to counter the changes brought about by the CFS. Further, statistical distribution of the cations in the lattice may broaden emissions. With this in mind, complete replacement of one cation for another may be the best option if narrow emissions are to be maintained. Replacement of the tetrahedrally-coordinated cations with others possessing larger ionic radii, while leading to the smallest possible shift in average cation electronegativity, should allow for a systematic increase in the CFS. Ion replacement along these lines could lead to interesting solid-solution series, with the potential for achieving ideal luminescence properties.

5.8 Conclusions

Several key properties of SMS have been determined. The band gap is supported to be $3.28 \pm 0.20\ eV$. Both DFT calculations and X-ray scattering measurements indicate that this band gap is indirect. Calculations suggest covalent bonding between the nitrogen and other species, similar to what is seen in other materials based on XN_4 (X = Al, Ga, P, Si ...) tetrahedra. The DOS of the nonequivalent nitrogen sites are also seen to be highly similar. The narrow emissions in the red-spectral region shown by SMS are very desirable for a phosphor for use in pc-LEDs. However, the low temperature stability of its emissions leaves room for improvement. Evidence has been given here that the reason for this lower stability is the proximity of the Eu^{2+} states to the edge of the CB. Comparison to SLA points to a possible solution. Modulation of the CFS and band gap through cation substitution represent an effective means to shift emission peak positions and band gaps, as well as improve thermal stability. A solid solution involving the tetrahedraly-coordinated cations in these systems may be one method of achieving this.

Experimental

The powder SMS sample was stored and prepared for the X-ray measurements under N_2 or Ar atmospheres. Sample preparation consisted solely of pressing the powder into clean indium foil. Both of these steps were to protect against the hydrolysis of this mildly hygroscopic sample. Measurements were carried out under a high vacuum of 10^{-7} Torr or better. Absorption measurements at the nitrogen K-edge were made at the Spherical Grating Monochromator (SGM) Beamline at the Canadian light source [46,47], with a monochromator resolving power

($E/\Delta E$) of about 2000. These spectra were collected as the partial fluorescence yield (PFY). The PFY spectra are formed using a post processing method to remove background and fit the emission peaks detected on the SGM's silicon drift detectors. The nitrogen K-edge emission measurements were carried out at Beamline 8.0.1 of the Advanced Light Source [48], with a monochromator resolving power of about 4000 and spectrometer resolving power of about 800. Beamline 8.0.1 uses Rowland circle spectrometer with an area sensitive multichannel plate detector. The emission and absorption measurements at the silicon L-edge were conducted at the REIXS (Resonant Elastic and Inelastic X-ray Scattering) beamline at the Canadian Light Source [49]. This beamline has a high-resolution X-ray spectrometer in the Rowland circle geometry and a high-resolution multichannel plate detector for the detection of emission spectra. The spectrometer resolving power is about 2000. The absorption spectra from this beamline were collected using the total electron yield (TEY).

The low temperature, optical emission spectra of SMS have been published elsewhere. [9] The thermal quenching data shown here are produced by integration over the Eu^{2+} emission band at each temperature. The thermal quenching data for SLA were produced similarly and have been published elsewhere. [8]

Calculations

The WIEN2k software package was used to perform the DFT calculations. A full potential and linearized-augmented-planewaves with local orbitals (LAPW + lo) are used to self-consistently solve the Kohn-Sham equations [9]. For the majority of calculations the generalized gradient approximation of Perdew, Burke and Ernzerhof (GGA-PBE) is used for the exchange and correlation energies [22, 112]. Calculations were also performed using the local density approximation (LDA) and modified Becke-Johnson (LDA-mBJ) potential to predict the band gap and band structure of SMS [92]. Improved band gap predictions with this potential stem from a more accurate modelling of the exact exchange-correlation potential. This calculation was also used for the calculated RXES spectrum, which is created by considering contributions to the partial density of states (pDOS) from only those k-points within the specified energy window. To model the effect of the core holes in the final states of the system during the X-ray absorption measurements, core hole calculations with 2x1x1 supercells, making 288 atoms per supercell, were performed [93,94]. The ground state calculation is sufficient for describing the XES spectra and the DOS.

5.9 Acknowledgements

Research described in this paper was performed at the Canadian Light Source, which is funded by the Canada Foundation for Innovation, the Natural Sciences and Engineering Research Council of Canada, the National Research Council Canada, the Canadian Institutes of Health Research, the Government of Saskatchewan, Western Economic Diversification Canada, and the University of Saskatchewan. The Advanced Light Source is supported by the Director, Office of Science, Office of Basic Energy Sciences, of the U.S. Department of Energy under Contract No. DE-AC02-05CH11231. We would also like to acknowledge the support of the Natural Sciences and Engineering Research Council of Canada (NSERC) and the Canada Research Chair program. The authors also acknowledge Compute Canada. The calculations presented in this work were performed on the Grex high-performance computing cluster, which is part of the Westgrid network (www.westgrid.ca) and Compute Canada Calcul Canada (www.computecanada.ca).

Chapter 6

α-V_2O_5 and ζ-V_2O_5

6.1 Introduction

The preceding studies of nitrides help in finding a deep understanding of what structural properties of phosphors are needed to engender narrow, efficient emissions in the red-spectral region. A quick summary of the necessary characteristics can be made: cuboidal coordination is helpful for the strong negative push it gives the d_{z^2} and $d_{x^2-y^2}$ states, down and away from the conduction band; polarizable ligands are useful in driving the red shift of the emissions; similarity in the DOS of the non-equivalent N sites leads to minimal deviations from the ideal CFS shown in Figure 1.3; a large band gap is needed to comfortably house the Eu^{2+} states. The preceding work does not discuss the Eu states directly however, but rather they are addressed indirectly. There is an open question as to whether DFT will be useful in predicting properties related to the (quasi-)localized Eu 4f and 5d states. To this end it is interesting to visit examples of compounds that are the archetypes for having properties strongly dependent on the varying localization of their states: the transition metal oxides. In particular it will be seen that studies of V_2O_5 compounds can shed considerable light on the subject.

In this vein the following study of α-V_2O_5, the thermal sink of the V_2O_5 system, and ζ-V_2O_5 is an interesting first step. Published in *Phys. Chem. Chem. Phys.*, [147] the effects of ligand polarizability and quasi-itinerant d-states are analyzed with the usual application of soft x-ray spectroscopy and DFT. Focusing on how ligand coordination and bond distances affect properties, the structure-property relationships in these materials are outlined. As per usual, the band gap and other key material properties are measured or analyzed with the aid of calculations. My contributions range from data collection, to the processing and analysis of the data, to writing the manuscript. In this manuscript the post-processing method described in Section 2.2 is applied for the first time in the work presented here. As well, the necessity of accounting for the effects of self-absorption on the O K-edge emission spectral shape are discussed.

6.2 The Publication

Contrasting 1D Tunnel-Structured and 2D Layered Polymorphs of V_2O_5: Relating Crystal Structure and Bonding to Band Gaps and Electronic Structure

Thomas M. Tolhurst[1], Brett Leedahl[1], Justin L. Andrews[2], P. M. Marley[2], Sarbajit Banerjee[2], Alexander Moewes[1*]

1 Department of Physics and Engineering Physics, University of Saskatchewan, 116 Science Place, Saskatoon Saskatchewan S7N 5E2 , Canada. E-mail: alex.moewes@usask.ca.

2 Department of Chemistry, Texas A&M University College Station, TX 77843.

6.3 Abstract

New V_2O_5 polymorphs have risen to prominence as a result of their open framework structures, cation intercalation properties, tunable electronic structures, and wide range of applications. The application of these materials and the design of new, useful polymorphs requires understanding their defining structure-property relationships. We present a characterization of the band gap and electronic structure of nanowires of the novel ζ-phase and the orthorhombic α-phase of V_2O_5 using x-ray spectroscopy and density functional theory calculations. The band gap is found to decrease from 1.90 ± 0.20 eV in the α-phase to 1.50 ± 0.20 eV in the ζ-phase, accompanied by the loss of the α-phase's characteristic split-off d_{xy} band in the ζ-phase. States of d_{xy} origin continue to dominate the conduction band edge in the new polymorph but the inequivalence of the vanadium atoms and the increased local symmetry of [VO_6] octahedra results in these states overlapping with the rest of the V 3d conduction band. ζ-V_2O_5 exhibits anisotropic conductivity along the b direction, defining a 1D tunnel, in contrast to α-V_2O_5 where the anisotropic conductivity is along the *ab* layers. We explain the structural origins of the differences in electronic properties that exist between the α- and ζ-phase.

6.4 Introduction

Vanadium oxides exhibit an array of interesting and useful properties including metal-insulator transitions and electron correlation effects. [16, 148–151] Layered structures like orthorhombic α-V_2O_5 are a natural choice as hosts for cation intercalation, which leads to interesting charge ordering and potential application in Li-ion batteries. [17, 150, 152, 153] However, despite its potential, bulk α-V_2O_5, which is the thermodynamic sink of the V_xO_y system, exhibits poor intercalation kinetics and irreversible lithiation, which stand to limit its usefulness for energy storage, making new phases and nanostructures of interest. [40, 155] V_2O_5 nanowires have also been shown to be useful in high-sensitivity photodetectors. [157, 158]

Nanostructuring of cathode materials, including α-V_2O_5 has been explored in several studies as a means to mitigate limitations of bulk materials such as slow diffusion kinetics, [17, 154, 159] but the irreversible lithiation is still an issue. Ultimately new polymorphs of V_2O_5 are required that show similar accessibility of multiple redox states as α-V_2O_5, but have substantially reduced diffusion barriers for the migration of Li-ions and do not undergo a series of phase transformations upon the insertion/extraction of Li-ions. [18, 164] Recently, a novel, metastable phase of ζ-V_2O_5, has been reported in nanowire form and shows great promise as a stable host for the intercalation of Li and Mg ions. [18] This new polymorph opens up the possibility of controlling the charge ordering of the network, and makes ζ-V_2O_5 a prime candidate for applications in the next generation of Li- and multivalent- ion cathode materials. [18]

In order to assess the utility of new phases a few key material properties, such as the band gap must be determined. Additionally, the interplay between structure and electronic properties must be understood in order to inform the search for new, useful V_2O_5 polymorphs and the tailored design of vanadium pentoxide bronzes. In particular, the relative energy positioning of O 2p and V 3d states is of critical importance for determining the electrical conductivity of oxide cathode materials and their proclivity for the stabilization of small polarons upon ion intercalation. This study uses a combination of x-ray absorption spectroscopy (XAS) and emission spectroscopy (XES), as well as density functional theory (DFT) calculations to contrast the electronic structure of the α-V_2O_5 and novel ζ-V_2O_5

nanowires. Our measurements and calculations show a pronounced difference in the band gap in moving from α-V_2O_5 to ζ-V_2O_5. In addition to providing accurate estimates of the band gap of each of these phases, we utilize band structure calculations to elucidate the root causes of the differences between them.

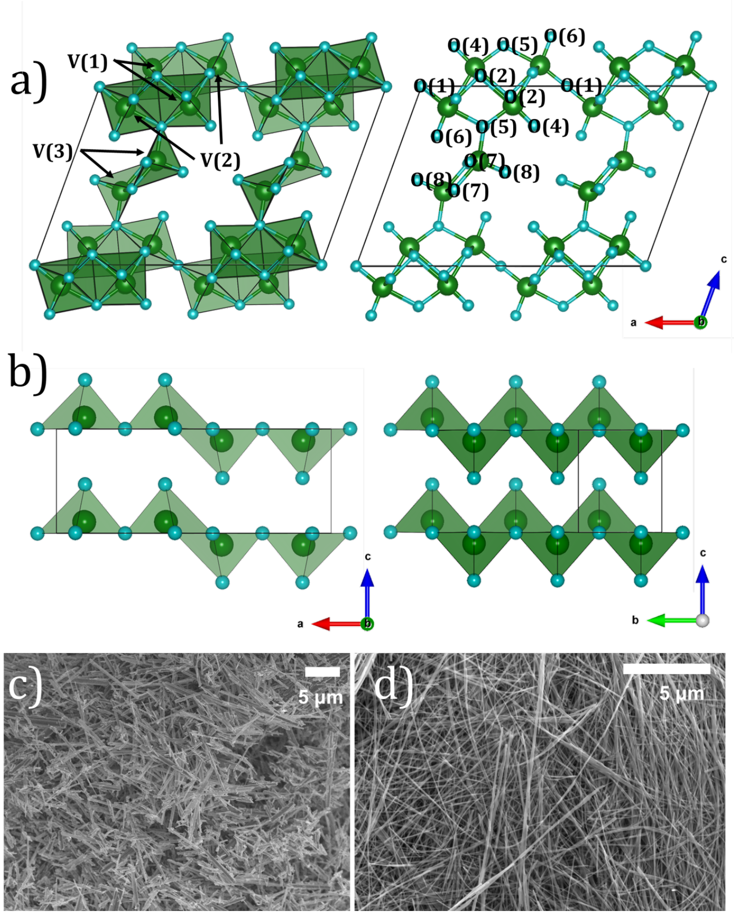

Figure 6.1: a) Crystal structure of bulk ζ-V_2O_5 with inequivalent atomic sites labelled. b) Alternate views of the V-O polyhedra of bulk α-V_2O_5. c) SEM image of the ζ-V_2O_5 nanowires. d) SEM image of the α-V_2O_5 nanowires.

6.5 Structure

The crystal structures of both ζ-V_2O_5 and α-V_2O_5 are shown in Figure 6.1, along with scanning electron microscope (SEM) images of the nano-wires used in this study. The α-V_2O_5 nano-wires are synthesized by the hydrothermal reduction of bulk V_2O_5 to $V_3O_7{\cdot}H_2O$ nanowires and subsequent oxidation to V_2O_5 in air at 573 K. [160] The ζ-V_2O_5 synthesis proceeds through the hydrothermal reaction of silver acetate and V_2O_5 to form the quasi-1D β-$Ag_xV_2O_5$ bronze, followed by the leaching of the Ag ions from the tunnels by a hydrothermal treatment of the resulting nanowires with HCl. [18] A full description of their crystal structures and synthesis has been given elsewhere. [17, 18, 155] The ζ-phase has thus far only been stabilized for materials with nanoscale dimensions and the crystal structure derived from Rietveld refinements to diffraction data are used to model X-ray absorption and emission spectra. The crystal structure of α-V_2O_5 can be seen in several previous studies. [16, 17, 165] Lastly, we have used the bulk crystal structures to model our experimental results, a choice that is justified when considering previous studies on the scale at which confinement effects become relevant. [161–163]

6.6 Results and Discussion

6.6.1 O K-edge and Band Gap

The x-ray emission and absorption measurements probe the occupied and unoccupied density of states of a material, respectively. By combining the measurements on a common energy scale, the band gap of a material can be estimated. The x-ray absorption measurement monitors the cross section for excitation of core electrons into unoccupied states, whereas the x-ray emission measurement records the spectrum of x-rays emitted as electrons from the occupied states decay to fill the core holes. The core state participating in these processes determines the absorption edge, which here will be the O K-edge and V L-edge, involving 1s and 2p core states, respectively. The absorption measurements presented here have been calibrated using the O K-edge absorption of bismuth germanate (BGO)($Bi_4Ge_3O_{12}$), with its first prominent peak taken to lie at 532.7 eV. The emission spectra have been calibrated using the emission spectrum of BGO, with prominent peaks at 517.9 eV and 526.0 eV.

Due to the small energetic separation of the O K-edge and V L-edge, it is typical for the absorption spectra from both edges to be presented as one continuous spectrum, whether collected using total fluorescence (TFY) or electron yield (TEY), as can be seen in most earlier works. [18, 155] However, if an energy-discriminating detector is used to detect the fluorescence, the two spectra can be separated using the partial fluorescence yield (PFY).

The fluorescence detector used in this study was a silicon drift detector (SDD) with an energy resolution of about 100 eV. At this low resolution only a single fluorescence peak is detected, which contains the O K-edge and V L-edge emissions. The nominal separation of these two emission lines is about 15 eV. However, the two spectra can still be separated by making use of two aspects of the SDD: due to the low energy resolution the emission lines from all elements will have about the same FWHM and the energy of an emission line is a constant throughout the measurement. These constraints allow the fitting of two Gaussian peaks, with only three free parameters, to the combined O K - V L emission peak at each step in the absorption measurement. This process is summarized in Figure 6.2, and the resulting separated spectra will be used for most of the analysis presented herein. It is important to note that without this separation, the O K-edge could not be used to determine the band gaps of the materials.

The O K-edge emission and absorption spectra for ζ-V_2O_5 and α-V_2O_5 are shown in Figure 6.3, alongside calculated spectra. Regions of interest have been labelled with upper case Latin letters. There is excellent agreement between the measured-separated and calculated O K-edge absorption spectra. Further, the measured emission spectra are in good agreement with, though slightly sharper than, previous O K-edge XES measurements on α-V_2O_5. [166,167] For both polymorphs the excited state (core hole) calculation provides the best match to the experimental absorption spectrum. The calculation captures the increase in the t_{2g}/e_g peak height ratio (see labelling in Figure 6.3) in passing from α-V_2O_5 to ζ-V_2O_5, which is also observed experimentally in XAS measurements. Although this ratio will be skewed by saturation effects to a degree, the trend will be accurately captured. This ratio has been tied to the magnitude of the metal-insulator transition in other V_xO_y compounds, due to its dependence on the strength of π bonds in the material. [168] The implication is that the π bonding strength is greater in the ζ-phase. This is particularly interesting as it suggests an overall greater degree of covalency in ζ-V_2O_5 , which is known to improve ion transport. [169]

The agreement between the calculated and measured emission spectra is excellent. There is an interesting exception in region **B** of both spectra. As will be discussed further below, the peak heights in this region are associated with the π bond strengths between the various

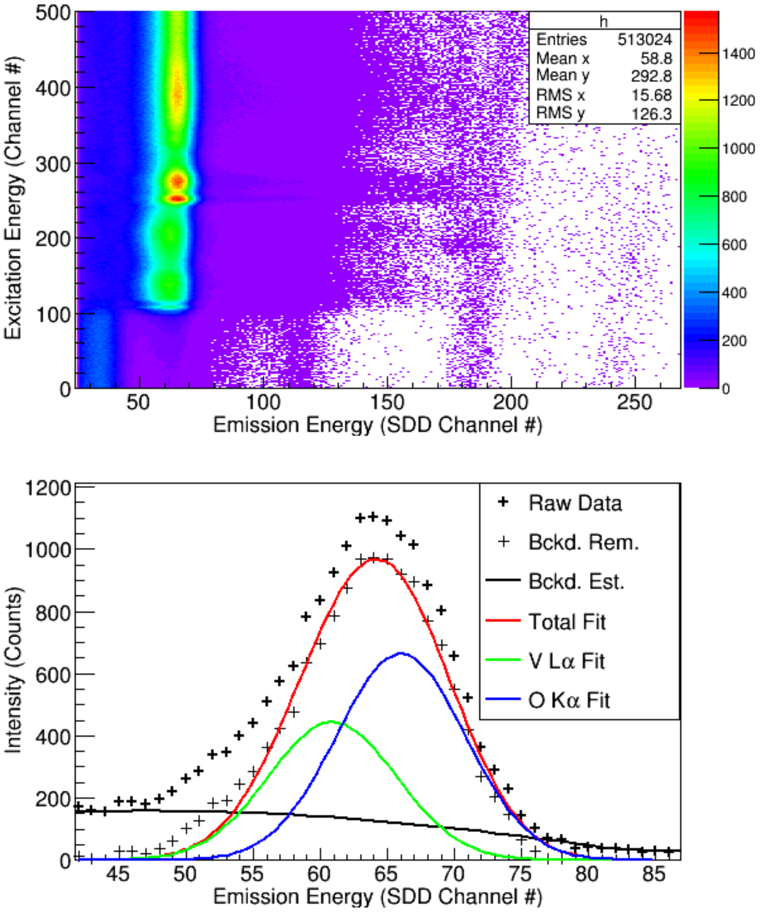

Figure 6.2: Separation of the PFY contributions of the V Lα and O Kα lines in a measurement on α-V_2O_5. The upper panel shows a contour plot of the excitation energy vs the emission energy. A vertical cut of the graph gives a PFY spectrum, a horizontal cut gives an emission spectrum like that shown in the lower panel. The lower panel shows the removal of the background and fitting of the emission peaks for a single SDD emission spectrum.

O and V sites. That the calculation shows excess intensity in this region indicates that the π bonding strength may be slightly overestimated in the calculation. Nonetheless, the π bonding strength in the ζ-phase is still predicted by the calculations to exceed that in the α-phase. It is clear as well that the experimental spectra are in complete accord with this result of the calculations. There is therefore very strong support for increased π bonding strength in moving from the α- to ζ-phase. The otherwise excellent agreement in the XES and XAS spectra shows that the calculations are largely representative of the systems. One is therefore justified in using the results of the calculations to gain further insights into the structure-property relationships in these materials. A decrease in the π bond strength will not affect regions **A** or **C** substantially, which are associated with σ and non-bonding orbitals respectively.

A previous study explored the effect of introducing a Hubbard U parameter into their DFT calculations for α-V_2O_5 , which would be one possible avenue for changing the bond strengths and increasing electron-correlation-induced localization effects in the calculation. [165] The authors' work still shows an excess in the DOS in the region associated with V-O π bonds, in addition to a band gap that is several tenths of an eV larger than most experimental values. We conclude that these systems are best represented using the simple GGA potential used here. One final point to consider is the unique way that self-absorption –the effect of the sample absorbing photons that it previously emitted– will affect the O K-edge emission spectra in any V_xO_y compound. As will be seen in the discussion of the V L absorption edge below, the maximum of the V L_2-edge absorption occurs precisely in region **B** and varies by 25% between this region and the outer edges of the O K-edge emission spectra. The effect is that the presence of the V atoms will selectively diminish the height of features in region **B** in comparison to other parts of the O K-edge emission spectra. Therefore, the minor discrepancy between theory and experiment in region **B** can further be attributed to self-absorption effects resulting from the overlap of the O K-edge emission features and the V L_2 absorption maxima in this region.

The band gap of these systems can now be estimated using the second derivatives of the x-ray emission and absorption spectra, which are shown in the lower panel of Figure 6.3. [93] For the α-V_2O_5 the separation of the XES and XAS spectra was found to be 1.09 ± 0.20 eV. For ζ-V_2O_5 a separation of 0.96 ± 0.20 eV was found. These measurements must be corrected for the effect of the core holes on the XAS spectra. The calculated spectra give shifts of 0.81 eV and 0.54 eV for the α and ζ phases, respectively. The final band gap estimation for α-V_2O_5 is therefore 1.90 ± 0.20 eV, and that for ζ-V_2O_5 is 1.50 ± 0.20 eV, indicating a clear diminution of the bandgap for the new polymorph.

DFT calculations using the generalized gradient approximation (GGA) give band gaps of 1.84 eV and 1.33 eV for the α- and ζ- phases, respectively. Although the agreement between the calculation and experiment is already quite good, it is worth noting that when using

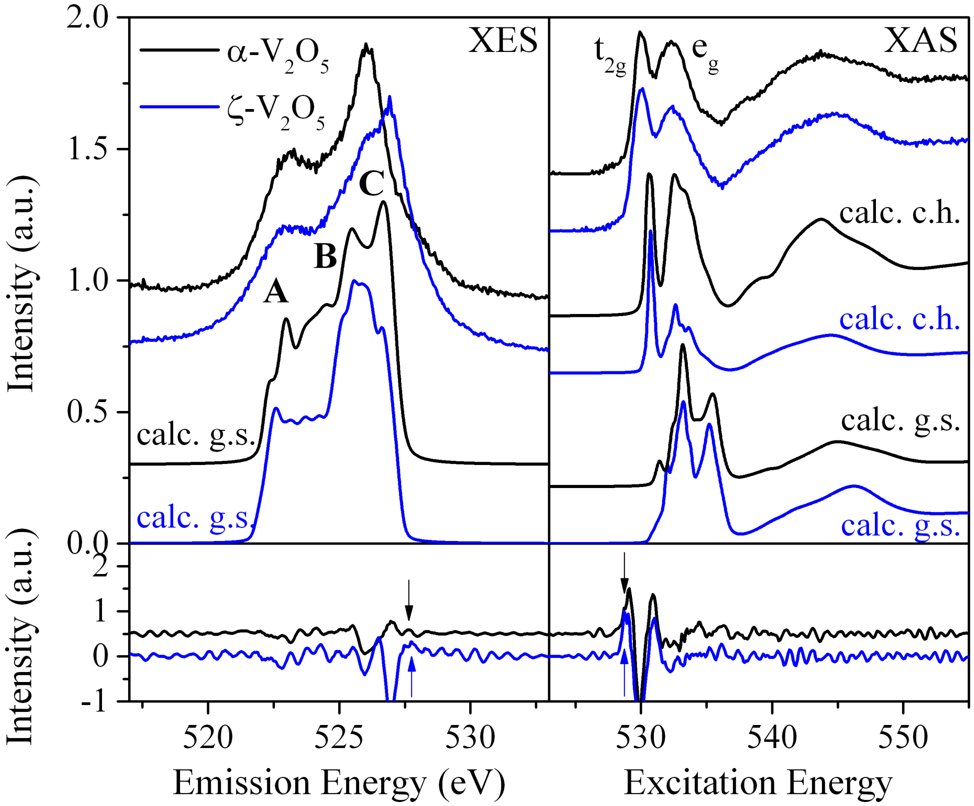

Figure 6.3: Oxygen K-edge emission spectra (left panel) and absorption (right panel) of α-V_2O_5 and ζ-V_2O_5 nanowires. Calculated spectra are shown below the experimental spectra. The lower panel shows the second derivatives of the measured spectra, which are used to determine the band gaps. Arrows indicate the peaks used for that determination.

the Modified Becke-Johnson exchange correlation functional, which is often seen to improve band gap estimates in semiconductors, a band gap of 2.78 eV is obtained for α-V_2O_5, which greatly overestimates the experimental values. Past studies of α-V_2O_5 have reported indirect band gaps from 2.1 eV to 2.35 eV and a direct gap of 2.4 eV. [170–172] Calculated band gaps of 1.74 eV to 2.2 eV using the local density approximation have been reported. [16,173] Cluster model calculations have suggested a band gap of 2.5 eV. [173] For the ζ-phase, a band gap of 1.1 eV using the GGA-PBE in the QUANTUM ESPRESSO package has been reported. [18] Our measurements are in agreement with the indirect band gaps measured previously for α-V_2O_5. They also agree with our calculated band gaps for both systems. We conclude that the GGA gives not only an accurate representation of the DOS of the systems, but also provides a reasonable estimate of the band gap. As a final note, the band gaps for these systems is very close to what is expected from the atomic term energies of the O p and V d states, which are 14.13 eV and 12.55 eV, respectively. [12] This indicates bonding that is predominantly ionic. It is now worth contrasting the crystal and electronic structure of these two phases in order to determine where the band gap difference originates.

6.6.2 Density of States

There are several interesting, telling features in the density of states of ζ- and α-V_2O_5, which are shown in Figure 6.4. The valence band (VB) is separated into two distinct bands, a lower-energy O s-band and a higher energy O p-band. This is the result that is expected for predominantly ionic bonding. [12] Looking in more detail, there are three regions of interest in the upper VB, labelled **A**, **B** and **C** in the figure (**A'**, **B'** and **C'** for α-V_2O_5), corresponding to those in the x-ray emission spectra above in Figure 6.3. These can be associated with the V-O σ bonds, V-O π bonds and non-bonding O p states respectively, based on the degree of energy level splitting that is expected with each type of bond. The dominance of O p-states in the upper VB and V d-states in the lower conduction band (CB) suggests that both of these materials are CT-type insulators, which has been confirmed elsewhere for α-V_2O_5. [173]

Also of interest are the regions **D**, **E**, and **F** in the CB, which can be associated with the t_{2g} (**D**, **E**) and e_g (**F**) states (**D'**, **E'** and **F'** for α-V_2O_5). Of particular interest is region **D**, which is derived from the d_{xy} states in both systems. [174] These are the states that most strongly influence the band gap and conduction properties of these systems. It is immediately clear that it is the d_{xy} states associated with the V2 site that form the bottom of the CB in the ζ-phase, whereas the d_{xy} states associated with the V1 and V3 sites take on a very similar structure to one another and are located at a higher energy than those of the d_{xy} states of the V2 site, or α-V_2O_5. It can also be seen that the d_{xy} states in the ζ-phase are no longer split off from the rest of the CB in the same sense as in α-V_2O_5. [174] However, the lowest d_{xy} bands are still distinct from the rest of the CB, despite overlapping energetically. The relative energy positioning of the CB edge states and the band gap are the two primary differences between the ζ- and α-polymorphs and can be readily understood by considering their band structures and orbital characters.

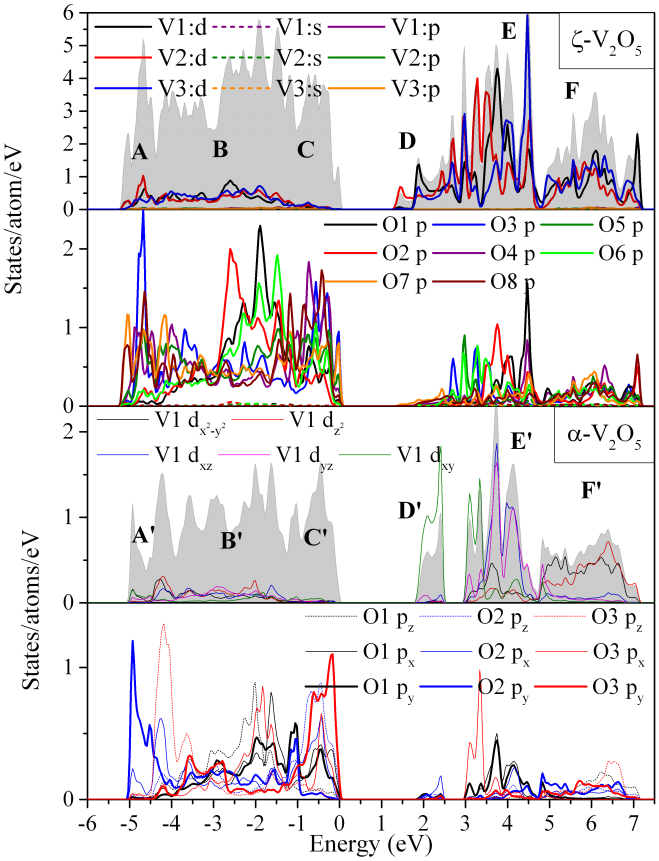

Figure 6.4: Top: DOS of ζ-V_2O_5 showing contributions from inequivalent sites. Bottom: DOS of α-V_2O_5 showing contributions from inequivalent sites and different m. Total DOS are shown as the shaded, grey curves and are scaled to facilitate comparison.

6.6.3 Band Structure

The band structures for α-V_2O_5 and ζ-V_2O_5 are shown in Figure 6.5. The coordinates for the high symmetry points in the first Brillouin zone for both systems have been described and tabulated elsewhere. [175] A reduced display of the α-V_2O_5 structure is given, as it has been discussed previously, having been calculated with several different functionals, [16] which are in good agreement with the results presented here. We focus on those directions in the first Brillouin zone where the VB maximum (T) and CB minimum (Γ) are found. The characteristic split-off band, due to the d_{xy} states, is centered about 2 eV above the VB maximum. A more complete picture of the band structure of ζ-V_2O_5 is given, along with the band characters emphasizing the d_{xy} states of inequivalent V sites. The CB minimum and VB maximum of the ζ-phase are found at the M and F1 points, respectively, giving it an indirect band gap. The comparison of the band structures of the two phases clarifies the origin of the difference in their band gaps, as well as the origin of the energetic overlap of the d_{xy} band with the other t_{2g} bands in the ζ-phase.

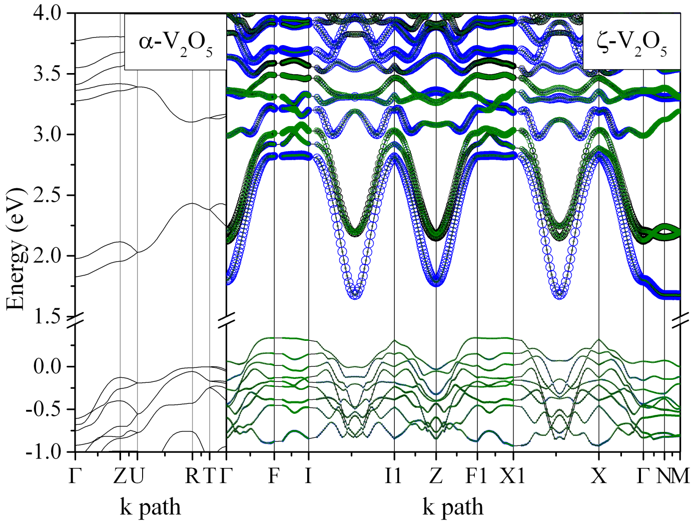

Figure 6.5: Left: band structure of α-V_2O_5. Right: band structure of ζ-V_2O_5, highlighting the d_{xy} character of the bands. The size of the circles indicates the relative contribution of a particular type atom and orbital to the band. The V1 d_{xy}, V2 d_{xy} and V3 d_{xy} are given in black, blue and green respectively.

The differences in the band structure of the ζ-phase with respect to the α-phase are as follows: the VB maximum is located at a slightly higher energy, the lowest d_{xy} states that constitute the edge of the CB are slightly lower in energy, and the d_{xz}/d_{yz} states are also at a slightly lower energy. These characteristics lead to a pronounced reduction of the band gap. Furthermore, there exist additional d_{xy} bands due to the inequivalent V1 and V3 sites, which fill in the gap between the lowest d_{xy} and other bands, and there is a slight increase in the dispersion of the d_{xy} bands. These traits lead to a reduced band gap and the disappearance of the gap between the d_{xy} and d_{xz}/d_{yz} states, when passing from the α- to ζ-phase.

First, the reason for the mixing of the V1 and V3 d_{xy} bands and the distinctiveness of the V2 d_{xy} bands can be understood readily when considering the orientation and coordination of these inequivalent sites in the unit cell (see Figure 6.1). The d_{xy} states of both the V1 and V3 sites, lie in the bc-plane. This allows for the mixing of their respective d_{xy} states throughout this plane, mediated by π bonds with their neighbouring O_c sites. The d_{xy} orbitals of the V2 site are oriented perpendicular to the bc-plane, making mixing with neighbouring V2 sites the primary possibility. This will lead to extended states along the b-axis, particularly in the b[101]-plane. The b-axis is the long axis of the nanowires. It is natural to expect the d_{xy} states associated with the V1 and V3 sites to be at a slightly higher energy by noting that their average V-O_c separation (~ 1.91 Å) is slightly smaller than those of V2 (~ 1.93 Å), leading to increased bond-antibond splitting and ultimately a higher energy for the d_{xy} states.

The increase in the dispersion of the d_{xy} bands can be at least partially explained by the theoretical results of a previous work exploring the effects of displacing the V atoms in the VO_6 octahedra on the α-V_2O_5 band structure. [16] It was found that the band dispersion increased as the degree of distortion of the octahedra decreased. The authors found that small displacements lead to large increases in the dispersion of the bands. The degree of distortion of the VO_6 octahedra does decrease marginally in passing from the α- to the ζ-phase, resulting in an increase in band dispersion for the ζ-phase.

The source of the increase in the energy of the VB in the ζ-phase can be determined by considering the DOS in Figure 6.4 and the preceding discussion on the π bonding between the O_c p - V d_{xy} states. From the DOS it can be seen that the uppermost states of the VB are formed by a very distinct peak, to which the major contributors are the O3, O5 and O7 sites. These sites are all involved in π bonding with the V d_{xy} states. Just as there is a reduction in bond-antibond splitting in moving from the V1/3 sites to the V2 site as a result of the increase in the mean V-O_c separation, the same trend is seen in moving from the ζ- to the α-phase (~ 1.89 Å). This implies greater splitting in the latter case, and a lower energy for the upper edge of the VB. Note also that this implies that the contribution of O3 to this uppermost VB peak in the ζ-phase should be largest, which is seen to be the case in Figure 6.4.

The slight shifts in the energy of the t_{2g} bands, their modest increase in dispersion and the separation of the d_{xy} bands of the V1/3 and V2 sites explain all of the major differences in the band structure of the α- and ζ-phase of V_2O_5. As a last point, the band structure predicts that the conductivity will be quite direction-dependent, being maximal in the bc- and b[101]-planes and lower along the a-axis. This is reflected in the dramatic variations in the dispersion of the bands along different directions of the first Brillouin zone, as can be seen in Figure 6.5. Highly anisotropic conductivity is also well known in layered α-V_2O_5. [155] The analysis can be taken a step further by noting that the d_{xy} states of the V2 site reside at lower energy, ~ 0.5 eV, than those of the V1 and V3 sites. This implies that the V2 sites, which form tunnels along the b-axis, will be the principle contributors to the conductivity. Further, it follows that upon intercalation of cations into the material, the V2 d_{xy} states will be filled first. This will lead to the reduction of the V2 sites, which has been seen to be the source of conductivity in V_2O_5 bronzes. [176]

To close the discussion of the band structures of these materials, we should look at the differences between the direct and indirect gaps that are predicted for the ζ- and α-phase. The predicted difference between the direct and indirect gaps for α-V_2O_5 is 0.25 eV, which agrees very well with the measured differences found previously. [170, 172] The same difference in ζ-V_2O_5 is predicted to be 0.28 eV. This should manifest itself in a difference between the measured band gap reported here and future optical measurements, which due to the negligible momentum of optical photons tend to measure the direct gap.

6.6.4 Electron Density

We have found that the dominant conduction pathways and band gap in α-V_2O_5 and ζ-V_2O_5 are determined by the V d_{xy} - O_c p π bonds. A particular spatial distribution of states is implied by the preceding discussion, making a brief study of the electron density of ζ-V_2O_5 of interest. The electron densities along several cuts of its unit cell are shown in Figure 6.6.

In Figure 6.6 a) the VB electron density is shown and can be seen to be greatest around the O atoms, where it is quite localized and spherically symmetric, indicating that the bonding is predominantly ionic. However, it is clear that some states are shared between the O and V sites, particularly between the V and O_v sites. In Figure 6.6 b) the lowest energy CB states are shown (region **D** of Figure 6.4) largely engaged in forming π bonds with the closest O atoms (O_v) in the ac-plane. In Figure 6.6 c) and d) the lower CB electron density is shown in the local xy-plane of V3 and V2, where it can be seen that the overlap of the V

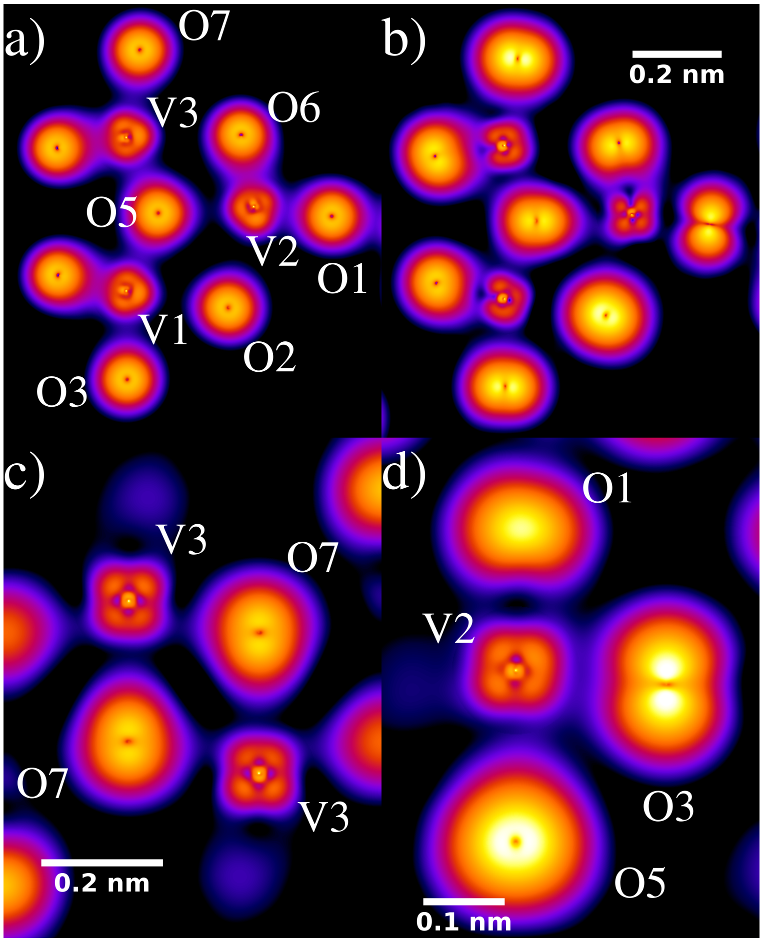

Figure 6.6: The electron density of ζ-V_2O_5 along several cuts of its unit cell, with high densities shown in white and progressing to black for very low densities. a) The valence electron density in the ac-plane (regions **A**, **B**, **C** of Figure 6.4) b) The density of the lowest unoccupied states (region **D** of Figure 6.4) for the same cut as in a). c) The lower CB density along the V3-O7 chains, roughly in the bc-plane. d) The lower CB density along the V2-O3 chains, roughly in the a[101]-plane.

d_{xy} states and the O_c p-states will lead to an extended network of states, corroborating the results of the band structure calculations.

6.6.5 Atomic Charges and Critical Points

The discussion of bonding between atoms can be made more quantitative through a topological analysis based on Bader's atoms in molecules theory. [177] By determining zero charge-density flux ($\vec{\nabla}\rho \cdot \vec{n} = 0$) surfaces, atomic basins can be assigned wherein the charge can be integrated and ionicities determined. Furthermore, the critical points, where $\nabla\rho = 0$ can be determined and used to measure the degree of covalency of a bond through the ratio of the principal curvatures–eigenvalues of the Hessian matrix–at those points. [177, 178]. For the case at hand it will be of interest to consider the ratio of the $h1$ and $h3$ eigenvalues, $|h1|/h3$, where $|h1|/h3 \ll 1$ implies ionic interactions and increases with increasing covalent bond strength. [177, 178] Table 7.3 summarizes the integrated charges in the atomic basins of the nonequivalent V atoms and their coordinating O atoms. The O atoms are labelled generally as O_v, O_c and O_b to facilitate comparison of the α-V_2O_5 and ζ-V_2O_5 phases. There is a marked decrease in the charge of the V atoms in moving from α-V_2O_5 to ζ-V_2O_5 , which is in keeping with our previous remarks and the increase in covalency in moving from α-V_2O_5 to ζ-V_2O_5 . This coincides with the loss of electrons from the O_v sites, although the charge of the O_v coordinating with V2 changes little. This can be directly linked to the relative changes in the V-O bond lengths, which also account for the variations in charge at the other sites. A strong similarity in atomic charges between the lone V site of α-V_2O_5 and the V2 site of ζ-V_2O_5 can be seen, which parallels their generally similar V-O bond lengths. The evaluation of the critical points of these systems leads to similar conclusions. All of the critical points referred to lie on the lines connecting the V and O atoms, making their characteristics relevant to the V-O σ bonds. The $|h1|/h3$ values of the α-V_2O_5 and the V2 site of ζ-V_2O_5 match well, implying similarity in bonding between their respective V and O sites. The critical points between the V-O_v, V-O_c and V-O_b sites give eigenvalue ratios of approximately 1.0, 0.2 and 4.0 respectively. Showing that the V-O_c bond is the most ionic, or weakened with respect to the π-bond strength. In keeping with the results seen from the band structure calculations, the V1 and V3 sites of ζ-V_2O_5 show similar atomic charges and eigenvalue ratios. With their respective ratios being approximately 2.0, 0.2 and 1.0, where the trends in covalency conform to expectations from bond lengths and atomic charges. It is clear that there is an increase in covalency in moving from the α-V_2O_5 to the ζ-V_2O_5 system, which is manifest in several characteristics from the greater dispersion seen in its band structure to the greater overall π-bonding strength.

Atomic Charges				
central atom	V	O_v	O_c	O_b
α-V_2O_5 V1	2.2156	-0.6969	-1.0476	-0.9243
ζ-V_2O_5 V1	2.2080	-0.6083	-1.1047	-1.0447
ζ-V_2O_5 V2	2.1954	-0.6840	-1.0447	-0.9253
ζ-V_2O_5 V3	2.1965	-0.5832	-1.0598	-1.0340

Table 6.1: Integrated charges in the atomic basins of the nonequivalent V and coordinating O atoms in α-V_2O_5 and ζ-V_2O_5 .

6.6.6 V L-edge - RIXS

There are a few additional properties that should be addressed for the ζ- and α-V_2O_5 nanowires, such as the d-d transition–higher energy rearrangements of the d-electrons–and charge transfer (CT)–electrons hopping from the O p band to the metal d states that cause charge fluctuations on the V atoms between the initial and final states–energies, as well as the charge state of the V atoms. These can be addressed with V L-edge XAS and RIXS measurements, [124] which are shown in Figure 6.7 and Figure 6.8. They were analyzed with both DFT and Anderson impurity model (SIAM) calculations. [50, 179]

From the separation of the PFY spectra discussed above, we obtained the isolated V L-edge absorption spectra shown in Figure 6.7. They are shown alongside emission spectra, which were excited at 525 eV, and DFT calculated spectra. As with the O K-edge spectra, the agreement obtained is excellent. A result somewhere between the ground state and full core hole calculations would give the best match to the experimental absorption spectra, suggesting a slight overestimation of the core hole effect at this absorption edge. The ground state calculations reproduce the fluorescence portion of the emission spectra very well. This again confirms that the calculations have properly modelled the DOS of the systems. Comparison to the density of states shows that the strong emissions at 510 eV are associated with the V d-states in the VB, whereas the weaker peak at 497 eV is due to V d and s states hybridized with the O s states. The higher energy features of the emission spectra are not reproduced by the DFT calculations. This is because they are due to inelastic scattering where energy is transferred into d-d and CT excitations. To model the d-d and CT contributions to the spectra, SIAM calculations must be used.

The RIXS measurements and the measured total electron yield (TEY) spectra for the

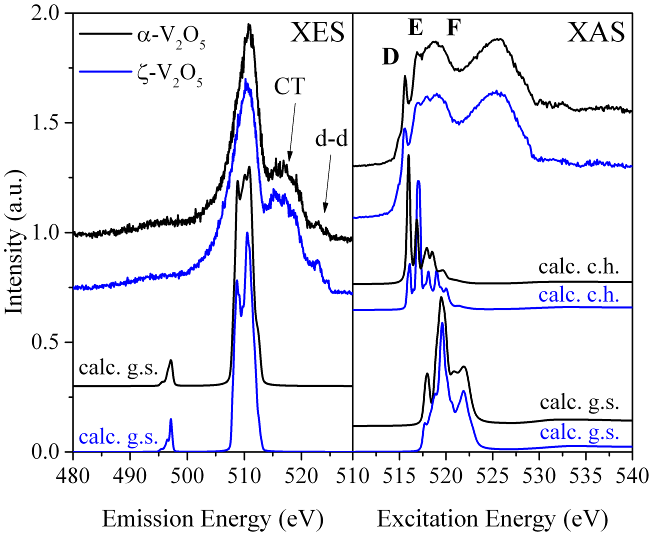

Figure 6.7: Vanadium L-edge spectra and DFT calculations for the α and ζ- phase. Prominent features are labelled with upper case Latin letters.

samples are shown for ζ-V_2O_5 in Figure 6.8, accompanied by the spectra from our SIAM calculations. The corresponding results for α-V_2O_5 are effectively identical and have therefore been omitted. The general features of the TEY of the α-V_2O_5 nanowires match well with what has been seen previously for α-V_2O_5. [166,167] The RIXS excitation energies are shown as color-coded arrows along the TEY spectra. It can be seen that there is excellent agreement between the calculated and RIXS spectra and the experimental spectra. This agreement is obtained by considering the presence of both V^{4+} and V^{5+}. The mixed charge state leads to both CT excitations at around a 6.0 eV energy loss and d-d excitations at about 1.2 eV energy loss. The mean oxidation state of the V atoms in the ζ-phase was found to be about 4.5+. These results are in good agreement with a CT energy of 6-7 eV found for the O 2p-CB transition in α-V_2O_5 previously. [166, 167] The authors do not report the presence of d-d transitions, citing the nominal d^0 configuration of V in α-V_2O_5. Although obscured by the resolution of the spectra, peaks in the appropriate energy range do seem to be present in one of these studies, [170] while the notable covalency between O and V atoms in α-V_2O_5 assures a mixture of V^{4+} and V^{5+} will be present. This is well supported by a previous cluster model calculation on α-V_2O_5, which emphasized the strong role of covalent bonding in this system, giving the $3d^1\underline{L}$ state a 47% contribution to the ground state. [173] The effectiveness of our calculations in modelling the RIXS spectra of ζ-V_2O_5 is highlighted by the agreement between the fine structure of the calculation and the measurement, shown in the inset in Figure 6.8. To emphasize the details of the measured spectrum a maximum entropy deconvolution was performed and is shown in red in the figure. Also in the figure is the deconvolved O K-edge emission spectrum, shown in blue, whose fine structure matches that of the CT peak. This is the expected result, as they both reflect the VB DOS of the O sites. Further, one notes that there is a difference in intensity between the peaks of the deconvolved spectra in region **B**. So while the peak locations are energetically in the same place in our two experimentally determined DOS, the peak height ratios differ because the O XES spectrum is affected by the reabsorption of photons by the V atoms in the sample. That is, the O emission spectrum has its peak in region **B** dampened by the V atoms. Thus, we have shown that the O DOS can be reliably extracted from the CT excitations in the V emission spectra.

6.7 Conclusions

Topochemical leaching has recently enabled the stabilization of a new tunnel-structured polymorph of V_2O_5. Through x-ray spectroscopy measurements the band gaps of novel ζ-V_2O_5 and orthorhombic α-V_2O_5 nanowires have been determined to be 1.50±0.20 eV and 1.90±0.20 eV, respectively. DFT calculations using the bulk crystal structure and GGA exchange correlation potential give band gaps of 1.33 eV and 1.84 eV respectively. The mBJ potential was found to overestimate the band gap of α-V_2O_5, giving 2.78 eV, well outside the range of most experimental results. A decrease in the band gap and the disappearance of the well-known split-off d_{xy} band is seen in passing from α-V_2O_5 to the ζ-phase. Specifically, this pronounced modulation of band structure results from the following effects: (a) the appearance of multiple d_{xy} bands associated with the non-equivalent V sites in the ζ-phase; (b) the slight increase in dispersion of the d_{xy} bands as a result of the slight increase in octahedral symmetry of the VO_6 polyhedra; (c) the changes in π bonding strength due to varying V-O_c distances. RIXS measurements show CT and d-d energies of 6.0 eV and 1.2 eV for both phases, and the accompanying SIAM calculations confirm a strong presence of V^{4+} in these nominally d^0 compounds, likely due to the notable covalency present in both structures. The

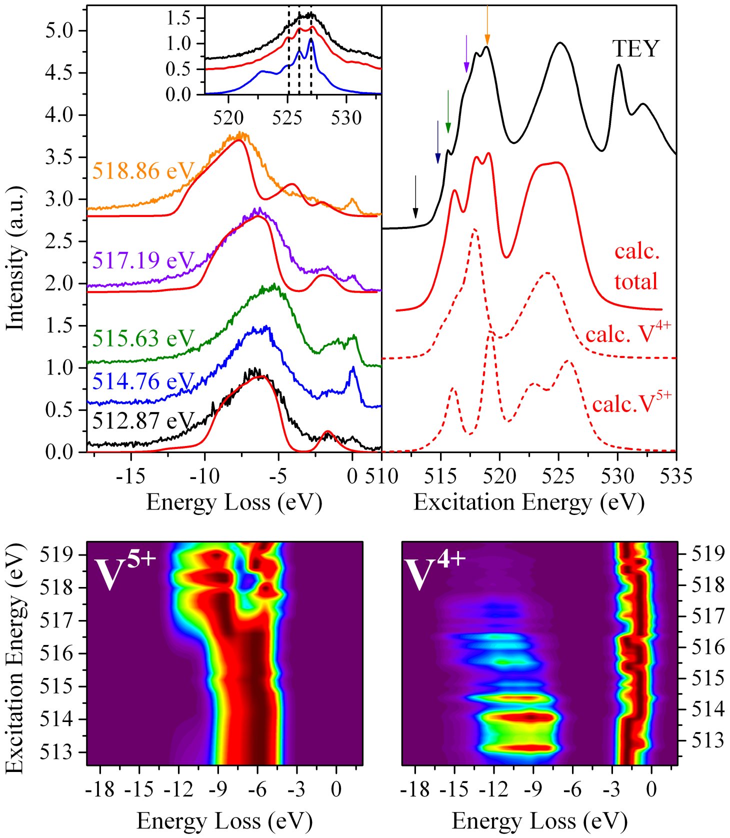

Figure 6.8: Vanadium L-edge spectra and SIAM calculations for ζ-V_2O_5. Calculated spectra are shown in red. Separate calculated absorption spectra for the V^{4+} and V^{5+} contributions are shown as dashed lines, with the additive spectrum indicated as a solid, red line. The inset shows the match between the calculated CT contribution to the RIXS spectra and the maximum entropy deconvolution of a measured RIXS spectrum. The lower panels show calculated RIXS contour plots for the V^{4+} and V^{5+} contributions. Horizontal slices are individual RIXS spectra, while the sum of the two plots gives the emission we see experimentally.

band gap and open structure of ζ-V_2O_5 and α-V_2O_5 nanowires, make them ideal for several frontier electronics and battery applications, highlighting their place in the expanding library of V_2O_5 polymorphs. The trends described here should be seen across the expanding gamut of V_2O_5 polymorphs, and should serve to inform the design of new compounds as well as their application. In particular, the reduced bandgap, continuum of d_{xy} states, and greater covalency suggest a means for mitigating small polaron localization, which can be an impediment to the diffusion of cations and is particularly severe for multivalent cations.

Experimental

For the x-ray spectroscopy measurements the samples were randomly oriented on carbon tape. As a result we do not anticipate the polarization dependence in the x-ray spectra seen for oriented nanowire arrays. [18, 155] Measurements were carried out under a high vacuum of 10^{-7} Torr or better. Absorption measurements at the O K-edge and V L-edge were conducted at the Spherical Grating Monochromator (SGM) Beamline at the Canadian Light Source. [46, 47] The beamline's monochromator resolving power ($E/\Delta E$) is about 5000 at the absorption edges considered here. The spectra were collected as the partial fluorescence yield (PFY), collected using silicon drift detectors (SDDs), and total electron yield (TEY). Post-processing was done to remove the background and fit the emission peaks detected on the SDDs. The oxygen K-edge and vanadium L-edge emission measurements were conducted at Beamline 8.0.1 of the Advanced Light Source [48]. The beamline has a monochromator resolving power of about 4000 and spectrometer resolving power of about 800. It has a Rowland circle spectrometer with an area sensitive multichannel plate detector.

Calculations

DFT calculations were performed using the WIEN2k software package, which uses a full potential and linearized-augmented-planewaves with local orbitals (LAPW + lo) to self-consistently solve the Kohn-Sham equations. [112] For the majority of calculations the generalized gradient approximation of Perdew, Burke and Ernzerhof (GGA-PBE) was used for the exchange and correlation energies. [112] Calculations were also performed using the modified Becke-Johnson (mBJ) potential for an alternate prediction of the band gaps. [92] Core hole calculations with a 1x3x3 supercell for α-V_2O_5 and a 1x1x3 supercell for ζ-V_2O_5 were performed in order to model the effect of the core holes in the final states of the systems during the x-ray absorption measurements. [93, 94] The ground state calculations are the most appropriate for describing the XES spectra and the DOS. The SIAM calculations in this work were performed with the code produced by Cowan, Butler, and Thole. [179, 180] The parameters used in the SIAM calculations are given in Table 6.2. The nonzero Ds and Dt values imply distortions from ideal octahedral symmetry in these systems. The similarity of the ζ-V_2O_5 and α-V_2O_5 spectra imply the distortion is similar in both cases.

SIAM Calculation Parameters for ζ-V_2O_5												
State	10Dq	Ds	Dt	Δ	U_{dd}	U_{cd}	V_{b1g}	V_{a1g}	V_{b2g}	V_{eg}	W	κ
V5+	3.5	-0.05	0.1	6	6	8	2.3	2.0	0.9	1.2	5.5	0.75
V4+	1.7	-0.1	0.1	9	6	8	2.3	2.0	0.9	1.2	7.0	0.85

Table 6.2: SIAM calculation parameters for the RIXS and XAS spectra of ζ-V_2O_5 . The parameters given are as follows: U_{dd} is the Coulomb repulsion between 3d electrons, U_{cd} is the core hole potential acting on 3d electrons, V_x's are the hopping integrals (hybridization strength for an electron in the given symmetry), W is the ligand band width, κ scales the intra-atomic electron-electron interactions. All units are eV except κ.

6.8 Acknowledgements

We would like to acknowledge the support of the Natural Sciences and Engineering Research Council of Canada (NSERC) and the Canada Research Chair program. Research described in this paper was performed at the Canadian Light Source, which is funded by the Canada Foundation for Innovation, the Natural Sciences and Engineering Research Council of Canada, the National Research Council Canada, the Canadian Institutes of Health Research, the Government of Saskatchewan, Western Economic Diversification Canada, and the University of Saskatchewan. The Advanced Light Source is supported by the Director, Office of Science, Office of Basic Energy Sciences, of the U.S. Department of Energy under Contract No. DE-AC02-05CH11231. The authors also acknowledge Compute Canada. The calculations presented in this work were performed on the Grex high-performance computing cluster, which is part of the Westgrid network (www.westgrid.ca) and Compute Canada Calcul Canada (www.computecanada.ca). JLA, PMM, and SB gratefully acknowledge the National Science Foundation for support of this work under DMR 1504702.

Chapter 7

Structural Variations on δ-$Sr_xV_2O_5$ and δ-$K_xV_2O_5$: Structural Control of the Hubbard Bands

7.1 Introduction

The electronic structures, including the experimentally determined band gaps, of α-V_2O_5 and ζ-V_2O_5 were seen to be well described by the DFT calculations in the preceding work. As well, the a semi-quantitative topological analysis of the electron densities were seen to be useful for understanding material properties. Materials based on the layered α-V_2O_5 structure with intercalated cations have gained considerable attention for their diverse properties. [151] These $M_xV_2O_5$ (M = Sr, K, Cu, Ag,...) bronzes exhibit narrow band gaps, electronic correlations, charge ordering, metal-insulator transitions and even superconductivity. [151] They are also systems wanting characterization, and the following manuscript contributes to this end, with its determination of band gaps, and explanation of structure-property relationships governing important properties of $M_xV_2O_5$ bronzes.

This manuscript has been submitted to *Chem. Eur J.*. My contributions are the same as for the preceding manuscript. Though more directly addressed in a subsequent contribution, the Hubbard bands of δ-$Sr_xV_2O_5$ and δ-$K_xV_2O_5$ are experimentally observed, and seen to dissipate with the exfoliation of the compound. The effects of exfoliation and type of cation on the band gap and other material properties form the core of the discussion in this work.

7.2 The Manuscript

Structure-induced switching of the band gap, charge order and correlation strength in ternary vanadium oxide bronzes

Thomas M. Tolhurst[a], Justin L. Andrews[b], Brett Leedahl[a], Peter M. Marley[b], Sarbajit Banerjee[b], Alexander Moewes[a*]

[a]Department of Physics and Engineering Physics, University of Saskatchewan, 116 Science Place, Saskatoon Saskatchewan S7N 5E2, Canada. E-mail: alex.moewes@usask.ca

[b] Department of Chemistry, Texas A&M University, College Station, TX 77843, USA

[*] corresponding author

7.3 Abstract

Recently, V_2O_5 nanowires have been synthesized as several different polymorphs, and as correlated bronzes with cations intercalated between the layers of edge- and corner- sharing VO_6 octahedra. Unlike extended crystals, which tend to be plagued by substantial local variations in stoichiometry, nanowires of correlated bronzes exhibit precise charge ordering, thereby giving rise to pronounced electron correlation effects. These developments have greatly broadened the scope of research, and promise applications in several frontier electronic devices that make use of novel computing vectors. Here we present a study of δ-$Sr_xV_2O_5$, expanded δ-$Sr_xV_2O_5$, exfoliated δ-$Sr_xV_2O_5$ and δ-$K_xV_2O_5$ using a combination of synchrotron soft x-ray spectroscopy and density functional theory calculations. We experimentally determine the band gaps of each system, and discuss their calculated electronic structures from the perspective of the measured spectra. Band gaps ranging from 0.66 ± 0.20 eV to 2.32 ± 0.20 eV are found, and linked to the underlying structure of each material. This demonstrates that the band gap of V_2O_5 can be tuned across a large portion of the range of greatest interest for device applications. The potential for metal-insulator transitions, tuneable electron correlations and charge ordering in these systems is discussed within the framework of our measurements and calculations, while highlighting the structure-property relationships that underpin them.

7.4 Introduction

Ternary vanadium oxide bronzes exhibit many unique structural and electronic properties. [18, 151, 181] Their layered and tunnel structures facilitate the intercalation of a variety of cations, making them candidates for the next generation of Li- and multivalent-ion battery cathodes. [18, 150, 152] At the same time, this can lead to the creation of many unique V_2O_5 bronzes ($M_xV_2O_5$, M = Ca, Sr, K, Pb...), which exhibit multiple charge-ordered states, electronic correlation effects and colossal metal to insulator transitions. [15, 154, 159, 176, 183–186] As such, these materials are of interest from the perspective of fundamental materials science, as well as for their potential applications at the frontiers of electronic device engineering, such as neuromorphic circuitry, Mott field-effect transistors, and electrochromic devices. [187–190]

The electronic phase diagrams of $M_xV_2O_5$ bronzes (where M is an intercalated cation and x is its stoichiometry) are highly sensitive to the type and concentration of cation, temperature and applied voltage, and are closely linked to the crystal structure. [15, 154, 159, 176, 183] This leads to several methods for tuning their electronic properties through alteration of the precise pattern of charge ordering, the overlap of the V d-states and the band gap, which ultimately control the conductivity.

Using a combination of soft x-ray absorption (XAS) and emission (XES) spectroscopy and density functional theory calculations we study the suite of bronzes δ-$Sr_xV_2O_5$, δ-$K_xV_2O_5$, expanded δ-$Sr_xV_2O_5$ (exp-$Sr_xV_2O_5$) and exfoliated δ-$Sr_xV_2O_5$ (exf-$Sr_xV_2O_5$). δ-$Sr_xV_2O_5$ exhibits charge ordering, while δ-$K_xV_2O_5$ is known to exhibit a colossal temperature-induced metal to insulator transition (MIT), as well as a voltage-induced MIT at low temperatures. [15,159] Here focus is given to the evolution of their band gaps and electronic structures as a function of the crystal structure, in order to elucidate the underlying structure-property relationships. We provide experimental and calculated band gaps for all four materials, which is arguably the most critical property for device applications. At the same time the density functional theory calculations, in conjunction with the crystal structure of each material, offer valuable information on changes in bond formation and charge ordering motifs. This in turn gives insight into on the underlying dynamics of the electronic structure and an understanding of the MIT and correlation strengths in each material. [154, 159]

7.5 Crystal Structure

7.5.1 Synthesis

δ-$Sr_xV_2O_5$ platelets with micron-sized dimensions and δ-$K_xV_2O_5$ nanowires were prepared by facile hydrothermal syntheses. [15, 191] In both cases, the use of a 50% excess of Sr and K sources, respectively as well as extended reaction times ensured the formation of large, single crystalline domains with near-maximum site occupancies. In the case of δ-$Sr_xV_2O_5$, Sr cation ordering was observed, as evidenced by the appearance of superlattice reflections in powder diffraction patterns, due to complete occupancy of the Sr crystallographic sites. A detailed explanation of the solution-phase expansion and exfoliation of exp-$Sr_xV_2O_5$ and exf-$Sr_xV_2O_5$ along with morphological characterization will be reported in detail in another contribution. [191] The as-prepared microbeams of δ-$Sr_xV_2O_5$ were treated with stoichiometric amounts of dilute hydrochloric acid, in order to selectively protonate non-adjacent layers of the material and expand the layers to form exp-$Sr_xV_2O_5$. The material was subsequently treated with a surfactant, tetrabutylammonium hydroxide, followed by stirring in order to apply shear forces and fully exfoliate the sheets. For both δ-$K_xV_2O_5$, and δ-$Sr_xV_2O_5$ the K and Sr contents, x, values are ca. 0.50, the crystallographically permitted maximum as deduced from refined site occupancies and energy dispersive X-ray spectra. On protonation of this structure, approximately half of the Sr atoms are replaced by H_3O^+, leading to x of about. 0.25. Upon complete exfoliation, this stoichiometry is expected to remain the same, although energy dispersive X-ray spectroscopy indicates slightly diminished Sr content (<0.25) when moving from exp- to exf-$Sr_xV_2O_5$.

7.5.2 Structure Optimization Using Density Functional Theory

Starting from crystal structures derived from x-ray diffraction measurements, structural relaxations were carried out on all systems. [192, 193] The relaxation of the structures proceeds through the iterative displacement of atoms in the unit cell until the forces on each atom are reduced below 2.0 mRy/Bohr. [192, 193] The principal effect of the force minimization in all systems was the settling of the intercalated cations deeper into the planes of VO_6 octahedra, as depicted in Figure 7.1. This naturally leads to shifts in the bond distances and angles of the VO_6 octahedra, and inevitably, variations in electronic structure. In general a decrease in the degree of distortion of the VO_6 octahedra is seen. Some specific structural changes will be quickly noted for the sake of their relevance to the following analysis. Our labelling conventions are outlined in Figure 7.1; select O sites will be referred to as O_v (vanadyl), O_b (bridging) or O_c (chain) as in previous works. [16, 147]

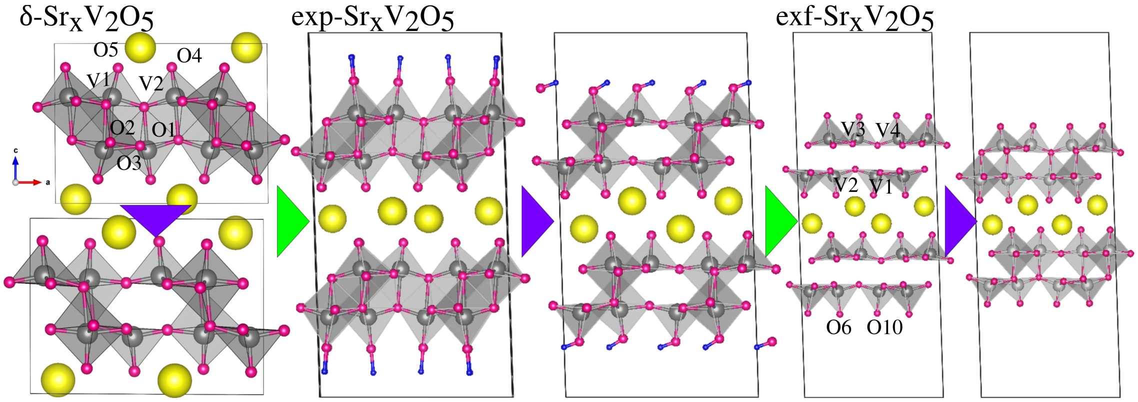

Figure 7.1: Experimentally determined and relaxed structures of δ-$Sr_xV_2O_5$ (left), exp-$Sr_xV_2O_5$ (center) and exf-$Sr_xV_2O_5$ (right). The case of δ-$K_xV_2O_5$ is similar to that of δ-$Sr_xV_2O_5$. with potassium ions intercalated between condensed V_4O_{10} layers. Arrows link the experimental and relaxed structures of each material (violet), as well as show the structural progression from δ-$Sr_xV_2O_5$ to exf-$Sr_xV_2O_5$ (green). Atoms are labelled for reference, all have Wyckoff position 2a. Only bonds with length ≤ 2.5 Å are shown. The color scheme of the atoms is such that Sr, V, O and H are colored yellow, grey, magenta and blue, respectively.

In δ-$Sr_xV_2O_5$ structural relaxation leads to the lengthening of the V-O_v bonds, by about 0.1 Å, all while maintaining similar V-$O_{c/b}$ bond lengths. The network of V-$O_{c/b}$ bonds form the primary conduction paths in each material by mediating the V-V interactions. [194] The long, apical V2-O1 and V1-O2 bonds are respectively lengthened and compressed, interchanging their previous relative lengths. The compression of the V1-O2 bond to 2.33 Å makes for a more ideal octahedron, while the extension of the other pushes it closer towards a local square pyramidal structure. Overall the least change is seen in the V-$O_{c/b}$ separations in δ-$Sr_xV_2O_5$, a trend which holds across the other systems.

In δ-$K_xV_2O_5$ the relaxation effects are essentially the same as in δ-$Sr_xV_2O_5$, although the changes in the longest V-O bonds are less pronounced. These more modest structural changes are expected from the lower charge on the K^+ ions, which thus polarizes the anionic framework to a lesser degree than the doubly ionized Sr^{2+}. [195] This is also in keeping with what is expected from the ionic radii of these two cations, with the larger K^+ settling less readily into the spaces between O_v atoms. There are only slight differences in the distortions experienced by the octahdra in δ-$Sr_xV_2O_5$ and δ-$K_xV_2O_5$. However, the electronic structures of V_2O_5 systems are strongly affected by distortions of the VO_6 octahedra, with slight reductions in distortion leading to large reductions in the band gap deriving from relatively subtle perturbations of V-V overlaps and alteration of electron correlation reminiscent of the canonical metal-insulator transition material VO_2. [16, 194, 196–198]

The situation of exf-$Sr_xV_2O_5$ becomes more interesting as a result of the absence of Sr ions in every other layer of the structure, leading to different relaxation effects in the octahedra adjacent to, and non-adjacent to, the Sr ions. The Sr ions are still drawn deeper into the layers of adjacent VO_6 octahedra, simultaneously drawing the layers on either side of the Sr ions together. This effect is seen in Figure 7.1. In the cation-adjacent layer there is a lengthening of the V-O_v bonds and a slight diminution of the longest, apical V-O bonds, thereby yielding a less distorted octahedron. At the non-adjacent sites the V-O_v bonds are compressed at both V3 and V4. The long V-O bond of the former is lengthened, whereas the latter's is compressed, effectively interchanging the relative lengths of these bonds as seen in the un-relaxed structure.

In exp-$Sr_xV_2O_5$ the results are similar to the exf-$Sr_xV_2O_5$ case, with the main difference being slight differences in the long, apical V-O bond lengths. The mean Sr-O distances are about the same. The interesting effect that makes this sample unique is that of the H-atoms on the system, which like the other intercalcants are drawn into the interstitial space between the VO_6 octahedra. Consequently, the V-O_v separation is not only maintained but is similar to that of the cation-adjacent sites. This creates a situation not unlike δ-$Sr_xV_2O_5$, where all octahedra coordinate with some cation, foreshadowing a similarity in electronic structure.

The often dramatic changes in these systems over the course of structural relaxation, interchange of intercalants, or exfoliation imply similarly radical changes in electronic structure. [16] It is clear that there is potential in these systems for MITs and other changes in electronic properties that could be induced by structural strain, temperature and cation concentration. Changes of this kind have been seen in other studies and bronzes and derive from alterations in the coupling of half-filled V 3d states. [15,151] To summarize the effects of structural relaxation: when present intercalants are drawn deeper into layers of octahedra, if intercalants are removed from between layers the nearest V-O_v bonds compress and acquire greater vanadyl character, there are minimal changes seen in the bond lengths along the conducting planes.

7.6 X-ray Spectra and Measured Band Gaps

7.6.1 Preliminaries

Soft x-ray emission and absorption spectra at the V L-edge and O K-edge were collected for all samples. These measurements probe the occupied and unoccupied partial density of states (pDOS) respectively. When put on a common energy scale they can be used not only to assess the bonding in a material, but can be used to determine the band gap. [93] The ligand K-edge, O in this case, is typically an effective probe of the band gap. This is because its states will tend to form the upper edge of the valence band (VB), and will be present at the bottom edge of the conduction band (CB) as a result of hybridization of ligand's orbital with others in the material.

Vanadium oxide compounds provide an interesting experimental challenge in this regard, due to the proximity of the V L-edge and O K-edge onset energies. The two spectra overlap and the onset of the O K-edge is obscured, which unless resolved cannot be used to determine the band gap. The spectra can however be separated if an energy-discriminating detector is used to render partial fluorescence yield (PFY) absorption spectra. As these show the absorption cross sections of separate atomic species, the O K-edge onset can be determined. The close proximity of the V L-edge and O K-edge is naturally mirrored in their emission energies, making the collection of quality PFY spectra dependent on the energy resolution of the detector that is used. In this study we have used silicon drift detectors (SDDs), which can accommodate comparatively high count rates, while offering moderate energy resolution on the order of 100 eV. This is not sufficient to resolve the V L and O K emissions, but PFY spectra can still be obtained by exploiting a few known detector and material characteristics. [147] Using the methods of this previous work, PFY spectra were extracted and are shown in Figure 7.2. In the figure the total absorption, in the form of the total electron yield (TEY), and the PFY spectra for all four samples are shown. The total fluorescence yield (TFY) can essentially be obtained by adding together the V L- on O K-edge PFY spectra in the figure. It is important to note that the TEY is a surface sensitive technique, probing the first few nanometers of a material, allowing the identification of differences between the bulk and surface electronic structures of a material. [30] With the thus obtained O K-edge PFY spectra, band gaps can be determined for all of the samples.

Finally, prior to discussing the x-ray emission and absorption measurements in the next section, the unique influence of self-absorption effects in VO systems should be briefly considered. The O K-edge emissions will be self-absorbed in a non-uniform fashion by the V atoms, due to their direct energetic overlap with the rapidly varying V L_2-edge. This will lead to a distortion in the shape of the collected x-ray emission spectra, which would otherwise mirror the VB pDOS. As well, there is the opportunity for this same overlap to influence the shape of spectral features of the O K-edge PFY spectra. In the near-edge region there is the possibility of rapid changes in the spectrum of photons emitted from the sample as a result of the excitation of non-equivalent O sites, or the resonant excitation of other degrees of freedom. [33, 35, 53] These spectra will suffer different percentages of absorption as a function of their spectral shape, influencing the number of x-rays collected by the SDD and the resulting peak heights in the PFY spectra. This absorption of O K-edge x-rays by V atoms will lead to either emission of V L-edge x-rays, potentially creating peaks in the V L-edge PFY, or will more likely lead to Auger electron emission. [30] Although the PFY spectra will not record absorption events that end in Auger emission, the TEY spectra will.

7.6.2 O K-edge

The O K-edge emission and absorption measurements for all samples are shown in Figure 7.3, alongside calculated spectra. The agreement between the measured and calculated spectra is excellent in general, though there are a few areas of apparent disagreement. Calculated XAS spectra for the excited states of δ-$K_xV_2O_5$ and δ-$Sr_xV_2O_5$ are shown, but given the good agreement already obtained with the ground state calculations, full excited state spectra

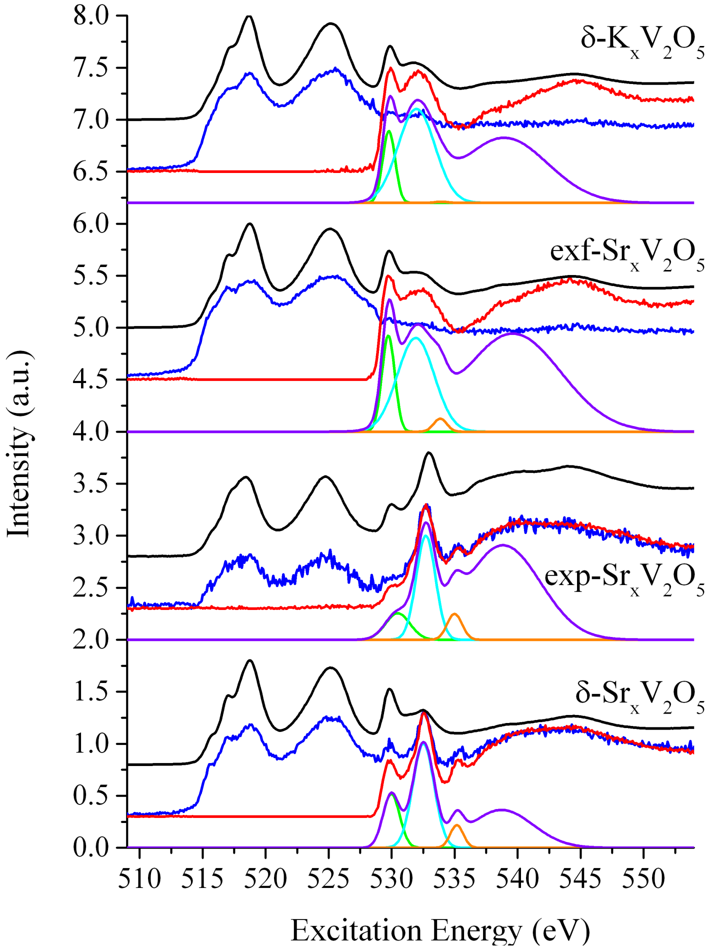

Figure 7.2: Separation of the combined V-O emissions from all samples into distinct V L-edge (blue) and O K-edge (red) PFY spectra. The fitting procedure used is described elsewhere. [147] The TEY sepctra for each sample are show in black, offset above the relevant PFY spectra. Least squares fits of Gaussian peaks to each O K-edge spectrum. The resulting functions are shown individually, along with their sum in violet. The curves have been scaled to facilitate comparison.

were not calculated for the other samples. Prominent features in the spectra are labelled with upper case Latin letters to facilitate comparison.

There are a few well defined peaks in the emission and absorption spectra in the Figure that are common to most the spectra of most of the samples, labelled **A** through **G**. We can assign these to bands of the following character: **A**/**F**/**G** will be due largely to O p - V d σ-bonds, **B**/**E** to O p - V d π-bonds, **C** to O p non-bodning states, **D** to an occupied lower Hubbard band where present. [16, 147]

There are three regions where there is apparent disagreement between the measured and calculated spectra. First in the broad region from **A** to **C** it can be seen that although the locations of peaks are in accord, the corresponding peak heights in the experimental spectra are noticeably smaller. This is simply due to self absorption of the O K-edge emissions by the V L_2-edge, which can bee seen in Figure 7.2 to absorb strongly in this region. Next, peak **E** is somewhat stronger in all calculated spectra. Two reasons can be found immediately: the core hole calculations can be seen to lessen the relative intensity of this feature with respect to the ground state, and there is a general tendency for DFT to overestimate the strength of π bonds, which are the principle contributors to this region of the absorption spectra. [199] There is also a rather prominent difference between measured and calculated spectra in region **D** of the δ-$Sr_xV_2O_5$ and δ-$K_xV_2O_5$ samples. Put simply, the experimentally observed peak is absent from the calculation. As will be discussed below, this peak in the spectra is due to the formation of a lower Hubbard band in these systems, which are known to exhibit electronic correlations not captured in the DFT calculations presented here. [151] Conductivity controlled by a lower and upper Hubbard band has already been proposed previously for δ-$K_xV_2O_5$ but this represents the first direct experimental observation of Mott-Hubbard behavior in these materials. [15] A shift of spectral weight from the CB to the upper VB in the formation of this band can also partly explain the reduction of peak **E** seen in the experimental spectra. For all aspects outside of the Hubbard bands, the good agreement between the experiment and calculations validates the use of the DFT calculation for further studying these materials.

The band gaps of the materials can be determined by taking the separation of the VB and CB onset as determined by the second derivatives of the XES and XAS spectra, respectively. This process is summarized in Figure 7.3. [93] It is also generally important to consider the effect of the core hole created in the x-ray absorption process on the CB onset, as well as the different binding energies of non-equivalent sites. [200] This is because the XAS spectra are indicative of the final state of the system in the absorption process, which contains a core hole. The CB onset is typically shifted to lower energies in this excited state, but a correction for this effect can be derived from DFT calculations. It should be noted that the core hole shift itself is generally less important in transition metal oxides. [93] The

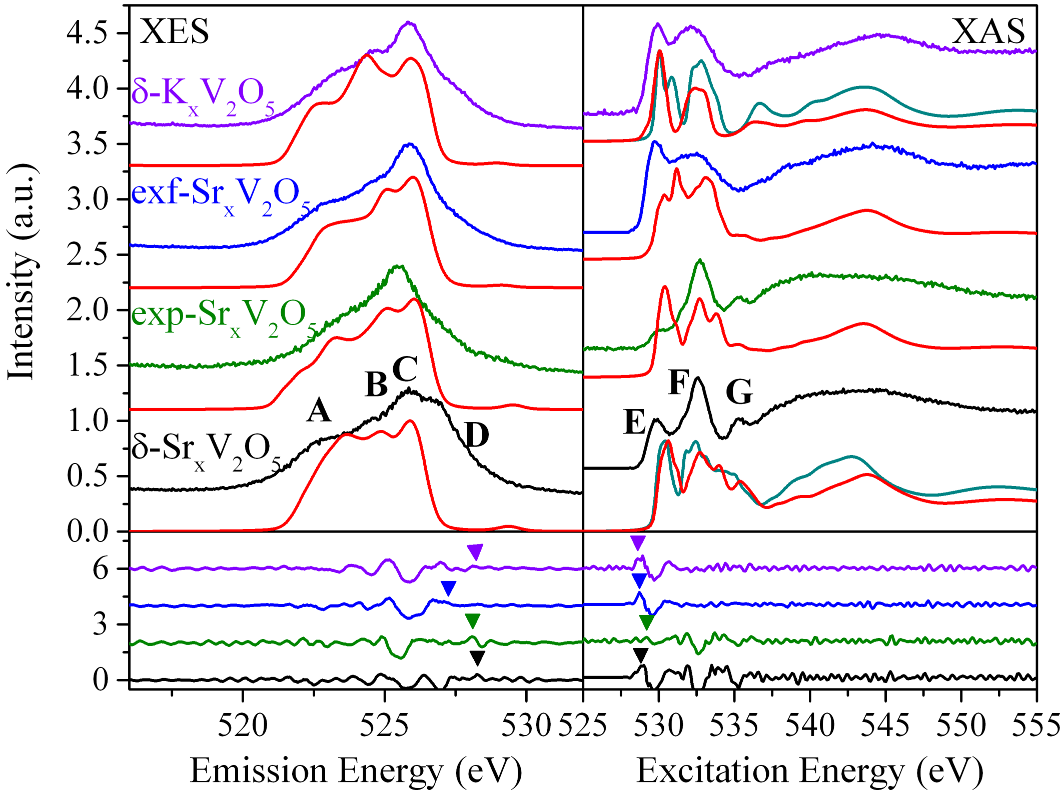

Figure 7.3: X-ray emission (left) and absorption (right) spectra for the full set of samples. Calculated spectra for the ground (red) and excited states (cyan) of each system are set just below the corresponding experimental spectra. Second derivatives of all spectra are given in the lower panels, with peaks used for determining band gaps indicated with color-coded arrows.

measured separation of the x-ray spectra, the core hole corrections and the calculated band gaps for all systems are given in Table 7.1.

It can be seen that there is good agreement between the measured and calculated band gaps in cases where no Hubbard bands are present. Notably, using the second to leading peaks in the second derivatives of the XES spectra of δ-Sr$_x$V$_2$O$_5$ and δ-K$_x$V$_2$O$_5$ leads to a separation of the O p- and V d-states of 1.88 ± 0.20 eV and 1.72 ± 0.20 eV, respectively, much more analogous to the calculated bandgaps. It is the presence of the Hubbard bands that leads to a smaller band gap in these systems. Despite the good agreement between the measured and calculated spectra of exf-Sr$_x$V$_2$O$_5$, there is some disagreement in the measured

Measured and calculated band gaps (eV)				
sample	spectral separation	c.h. correction	measured gap	calculated gap
δ-$Sr_xV_2O_5$	0.54 ± 0.20	0.53	1.07 ± 0.20	2.07
δ-$K_xV_2O_5$	0.38 ± 0.20	0.28	0.66 ± 0.20	1.91
exp-$Sr_xV_2O_5$	1.10 ± 0.20	0.86	1.96 ± 0.20	2.21
exf-$Sr_xV_2O_5$	1.47 ± 0.20	0.85	2.32 ± 0.20	1.50

Table 7.1: Measured and calculated band gaps for each material in this study. The core hole (c.h.) corrections are derived from DFT calculations for each system.

and calculated band gaps. This difference can be explained through a brief study of the calculated density of states of this and the other systems, which will be done in the next section. This all adds to support the accuracy of the DFT calculations presented here for describing the DOS of the itinerant electrons in these systems. No significant change in the calculated band gap of exf-$Sr_xV_2O_5$ is seen as a function of interlayer spacing. No confinement effects are expected for the nanowires given the > 100 nm lateral dimensions, [147] justifying the use of the bulk crystal structures in the DFT calculations of δ-$Sr_xV_2O_5$ and δ-$K_xV_2O_5$.

The comparison of the O K-edge TEY and PFY spectra, as shown in Figure 7.2 should also be made quickly. In most cases the two match, implying a general similarity between the structure of the surface and bulk of the samples. One expects complete agreement in the case of exf-$Sr_xV_2O_5$, where the material itself is only a few atomic layers thick, as is indeed observed here corroborating the successful exfoliation of this compound to structures that span only a few unit cells in thickness. However, the TEY and PFY spectra of δ-$Sr_xV_2O_5$ do not match, implying the outer few nanometers of the wires are rather more similar to α-V_2O_5 than δ-$Sr_xV_2O_5$. [147] It has been discussed elsewhere that there is a tendency for defects to migrate to the surface of the nanowires during synthesis, [154] which may account for this difference. It may also simply reflect the influence of ambient conditions on the wire, resulting in surface reconstruction to orthorhombic V_2O_5, which represents the thermodynamic sink in this system.

7.7 Density of States - Explaining the Band Gaps

The calculated DOS of all systems are shown in Figure 7.4 and Figure 7.5. The important trends in the DOS follow from the comparison of δ-$Sr_xV_2O_5$ to δ-$K_xV_2O_5$, as well as looking at the transition from δ-$Sr_xV_2O_5$, through exp-$Sr_xV_2O_5$ to exf-$Sr_xV_2O_5$. The DOS of δ-$Sr_xV_2O_5$ and δ-$K_xV_2O_5$ are quite similar, as might be expected from their similar crystal structures, where the most notable difference is the interchange of Sr and K ions. It is little surprise that one of the greatest differences in the DOS of these systems is the structure associated with the cation d-states. The Sr d-states form a relatively localized peak at an energy just above that of the V d-states, whereas the K d-states show no overlap with V d-states. This peak is clearly present in the measured XAS spectra, giving a clear indication of the interaction of the Sr intercalant with the adjacent O sites. The two intercalating species thus provide an interesting contrast in that the K-ions interact with the V_2O_5 through more ionic interactions, whereas the interactions of Sr-ions with the V_2O_5 lattice show greater covalent character. When comparing the DOS of the exf-$Sr_xV_2O_5$ and exp-$Sr_xV_2O_5$ samples it can be seen that only those O sites coordinating with the Sr sites show O-Sr hybridization. On this front the broad band of K d-states seen in the DOS is also manifest in the shape of the measured XAS spectrum of δ-$K_xV_2O_5$. It should also be noted that the O_v sites contribute strongly in regions **B**, **C**, and **E**, where their V-O π bonds contribute strongly. Overall the structure of the calculated DOS is realized to a high degree of accuracy in the measured x-ray spectra. The slightly smaller band gap of δ-$K_xV_2O_5$ suggests weaker overlap between the V d_{xy}-states and the O_c p-states, which is corroborated by the increased weight of the O_c p-states at the upper edge of the VB in δ-$K_xV_2O_5$. This will also be related to the more ionic nature of the interaction of the K-intercalants with the host lattice.

Greater changes are seen when comparing δ-$Sr_xV_2O_5$ to exp-$Sr_xV_2O_5$ and exf-$Sr_xV_2O_5$. The greatest difference is seen in the latter two systems, where there is a stark contrast between the DOS of those sites that are adjacent to the intercalant ions, and those that are not. For convenience these will be referred to as the adjacent and non-adjacent sites, respectively. In addition to the presence or absence of Sr-O hybrid states there is a dramatic difference in the positioning of the V d-states. Due to the large differences in bond lengths between these two planes of VO_6 octahedra, the CFS and degree of covalency experienced by the V atoms is quite different. This leads to a strong breaking of the effective degeneracy of the low-lying V d-states that is seen in δ-$Sr_xV_2O_5$. This inevitably leads to stronger charge ordering, which is found quite generally in V_2O_5 bronzes, although the precise pattern is not always clear. [154,159] In other words, adjacent and non-adjacent V sites take on electronically very distinct characters resulting in charge modulation across the 2D layers.

An interesting addition to the discussion of the potential for MITs in exf-$Sr_xV_2O_5$ comes from considering the DOS of the experimentally determined, unrelaxed structure, which is shown in the lower panel of Figure 7.5. The striking difference is that even in this DFT calculation, inter-gap states are formed at the non-adjacent sites. Inter-gap states have been seen elsewhere in DFT calculations for β-$Pb_xV_2O_5$ nanowires. [159] This suggests a general instability in the electronic structure of this system. It is clear that slight distortions of this material can lead to considerable changes in the VB onset, thus changing the band gap. Comparing the DOS of exf-$Sr_xV_2O_5$ to the other systems shows increased prominence of non-bonding O p-states at the upper edge of the VB, which can be expected from the increased V-O_c distances in the non-adjacent layer. These states also begin to have a sharper structure to the peaks, which is indicative of confinement effects, which should be expected in the exfoliated layers. [169] The onset of confinement effects also contributes a partial explanation the discrepancy between the calculated and measured band gap of exf-$Sr_xV_2O_5$.

7.8 Band Structures - Energetic Splitting, Band Gaps and Charge Ordering

Some additional information can be obtained from the band structures of each material, which are shown in Figure 7.6. The coordinates of the selected k-paths are outlined elsewhere. [175] The band gap is indirect in all cases, leading to the usual potential for a disparity between the indirect band gap and measured optical gap. [147] There is little difference between δ-$Sr_xV_2O_5$ and δ-$K_xV_2O_5$, aside from a modest splitting of the bands in δ-$Sr_xV_2O_5$, which is due to the greater difference in V-O bond lengths between its nonequivalent V sites. In both systems the nonequivalent sites contribute equally to the lowest CB bands. However, the nonequivalent sites of exf-$Sr_xV_2O_5$ do not contribute equally to the low-lying conduction bands. As with the DOS above this implies a distinct charge ordering between the layers of VO_6 octahedra with further loss of degeneracy as compared to the charge ordered δ-$Sr_xV_2O_5$ structure before intercalation. The trend in calculated band gaps is further supported here, where a general similarity between δ-$Sr_xV_2O_5$, δ-$K_xV_2O_5$, and exp-$Sr_xV_2O_5$ follows from

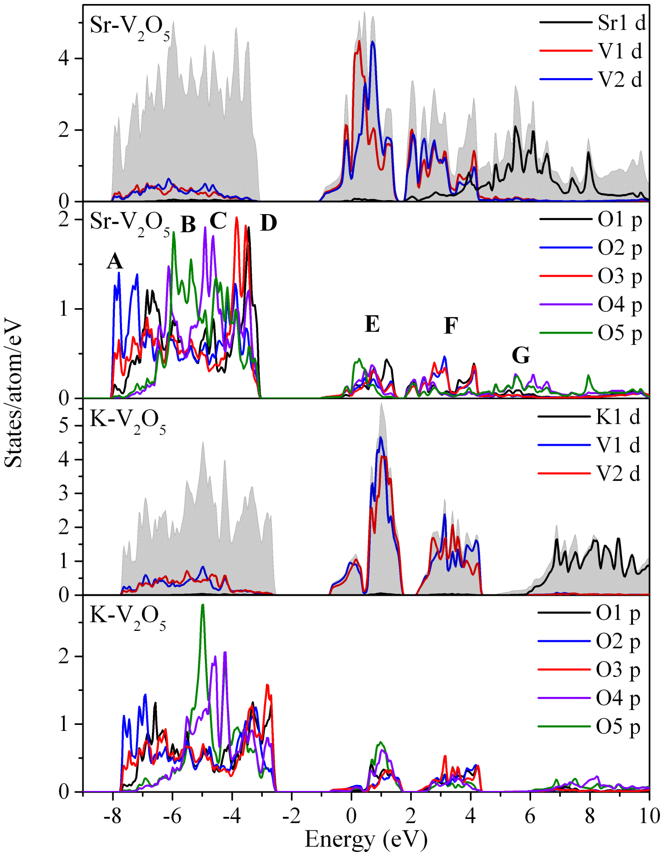

Figure 7.4: Calculated density of states for all nonequivalent sites of δ-Sr$_x$V$_2$O$_5$ (top) and δ-K$_x$V$_2$O$_5$ (bottom). Prominent peaks corresponding to the measured x-ray spectra are labelled with upper case Latin letters. The total densities are shaded and scaled to facilitate comparison.

the generally similar V-O distances. In exf-Sr$_x$V$_2$O$_5$ the increased ionicity implied by the increased prominence of nonbonding O 2p states at the upper edge of the VB, in conjunciton with the larger mean V-O$_c$ distance suggest smaller splitting of states derived from bonding and anti-bonding interactions, leading to a smaller calculated band gap. The GGA-PBE exchange correlation potential used here will not accurately capture the correlation effects in the exfoliated layers, which ultimately underpin the much larger measured band gap for this system.

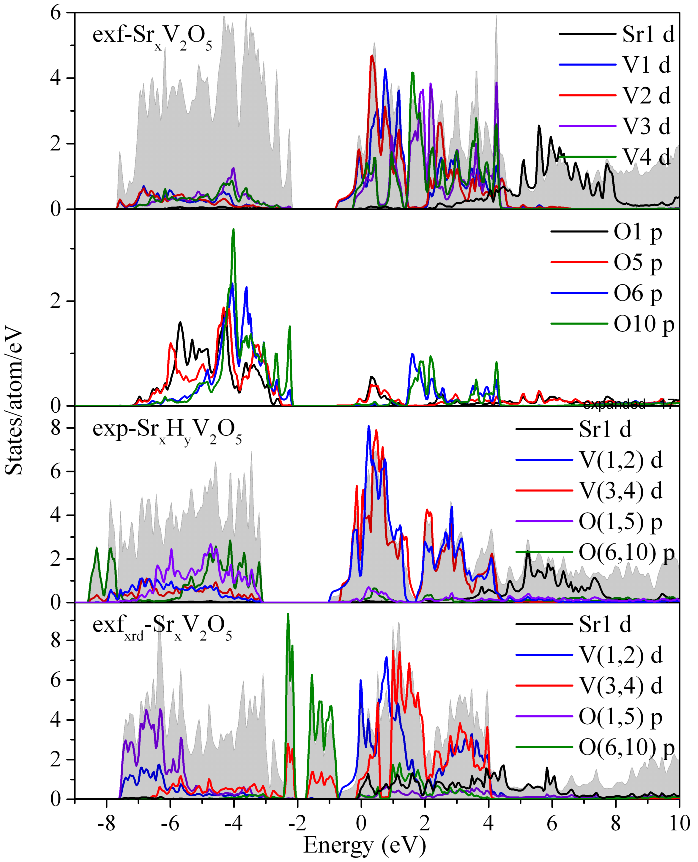

Figure 7.5: Calculated density of states for select nonequivalent sites in exf-Sr$_x$V$_2$O$_5$ (top panels), exp-Sr$_x$V$_2$O$_5$ as well as the exf-Sr$_x$V$_2$O$_5$ (bottom) structure derived from XRD measurements. Only the DOS of the O$_v$ sites are shown, those of the O$_c$ sites are largely similar to δ-Sr$_x$V$_2$O$_5$ in Figure 7.4.

7.9 Peak Areas and the MIT

With the O K-edge spectra separated from the V L-edge spectra, it is possible to use fits to the leading peaks in the O spectra to semi-quantitatively gauge several properties of these materials. O K-edge XAS spectra have been used previously to assess the potential for MITs in vanadium oxides, although it was done using combined V L - O K spectra. [201] By using separated spectra some systematic error is avoided. In the cited, earlier work, which studies the MIT in VO$_2$, only the t$_{2g}$ and e$_g$ peaks are studied. A third peak, labelled **G** in the figures here, is assigned to the Sr d - O p hybrid states that are clearly seen in the calculated DOS in Figures 7.4 and 7.5. The fits to the peak areas are shown in Figure 7.2 and the

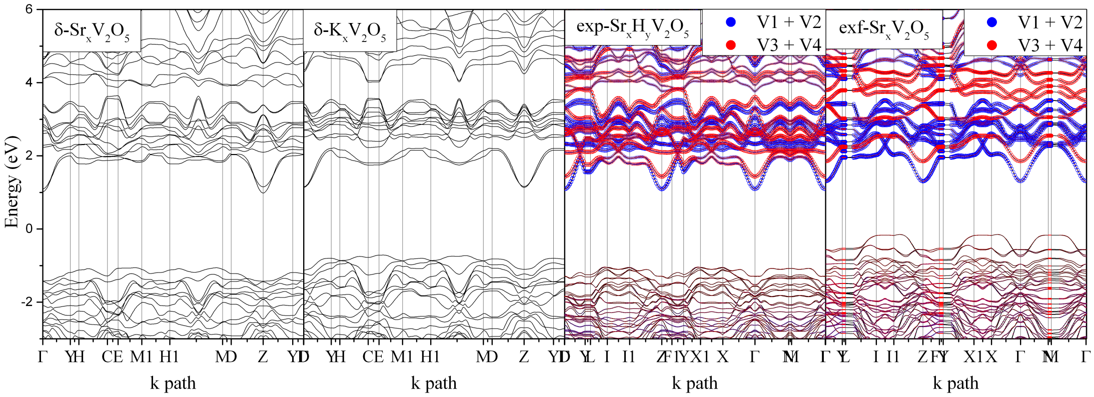

Figure 7.6: Calculated and structures for each system in this study. Character plots are given for exp-Sr$_x$V$_2$O$_5$ and exf-Sr$_x$V$_2$O$_5$, showing the varying contributions of d-states from the ion-adjacent (V1+V2) and nonadjactent (V3+V4) layers. No such splitting is seen in δ-Sr$_x$V$_2$O$_5$ or δ-K$_x$V$_2$O$_5$. The thickness of lines in the color plots indicates the relative contribution of those states (here V d-states) to that coordinate in the band structure.

resulting areas are tabulated in Table 7.2. Although the earlier work used a skewed peak shape, better agreement was found in this case using simple Gaussian distributions.

The link between peak **G** and the Sr ions can now be further established, going beyond the agreement in energetic position of the relevant states in the calculated DOS. This spectral feature is only present in those systems where Sr is present. It should be expected to scale in intensity with the Sr concentration in general. The fact that its relative intensity to **F** does not change between δ-Sr$_x$V$_2$O$_5$ and exp-Sr$_x$V$_2$O$_5$, is not a contradiction to this. The DOS show that those O$_v$ sites coordinating with H atoms also have a peak in their DOS in roughly the same region. Therefore, with all O$_v$ coordinating with cations, the ratio of **G** to **F** should be the same, as observed. It is also noteworthy that the position for peak **G** in the exf-Sr$_x$V$_2$O$_5$ is supported to be at a slightly lower energy than in the other systems. This is exactly the redistribution of spectral weight that is predicted by the DOS calculations. The decrease in the area of peak **G** measured in exf-Sr$_x$V$_2$O$_5$ suggests a relatively low concentration of Sr, which is indeed verified by energy dispersive X-ray spectroscopy experiments. The elimination of alternate layers of cations as schematically illustrated in Figure 1 halves the number of Sr-O interactions.

In previous works looking at MITs in VO compounds, the relative heights of the t$_{2g}$ and

e_g peaks are taken to be indicative of the relative prominence of π and σ bonds in the lattice, respectively. [201] The calculated DOS presented here are also in accord with this idea. The same peak assignments will be kept here. It is natural to assign increased π bonding to the potential for the MIT, as the overlap of the low-lying V d_{xy} states, which are responsible for conduction, overlap in a way that is mediated by π bonds with their coordinating O sites in the ab-plane. This is a standard situation in transition metal (TM) oxides and is strongly related to the TM-O bond lengths along the conduction pathways. [148, 201] The trend holds quite well in moving from δ-$Sr_xV_2O_5$ to δ-$K_xV_2O_5$, where a slight decrease in the t_{2g}/e_g ratio couples with the slight decrease in the overlap of O p- and V d-states noted above. There is however a cautionary point that becomes apparent when comparing to exp-$Sr_xV_2O_5$ and exf-$Sr_xV_2O_5$. The trend seems intact when looking at exp-$Sr_xV_2O_5$, where an increase in the mean V-O_c bond length is matched by a decrease in the area of the t_{2g} peak. The mean V-O_c bond length decreases in exf-$Sr_xV_2O_5$, but there is little change in the relative area of the t_{2g} peak. This underscores the fact that in V_2O_5 compounds there are π bonds that exist outside of the ab-plane, such as the very strong V-O_v π bonds in exf-$Sr_xV_2O_5$. This would suggest that perhaps an MIT is unlikely in exf-$Sr_xV_2O_5$. However, its instability is evident from the dramatic changes seen between the DOS of the experimental and relaxed structures presented here. The posibility of structure-induced MIT seems possible despite the experimental structure having V-V distances greater than the proposed maximum acceptable separation for conduction of 2.94 Å. [151, 201] The relaxed structure has a mean V-V separation below this benchmark for only the layer adjacent to the Sr ions. It is also seen elsewhere that the π/σ ratio varies from wire to wire, [182] implying that the results given here are indicative of an average over many individual wires.

O K-edge peak areas				
—	δ-$Sr_xV_2O_5$	δ-$K_xV_2O_5$	exp-$Sr_xV_2O_5$	exf-$Sr_xV_2O_5$
A1	1.84 (0.46)	0.95 (0.26)	3.37 (0.32)	0.85 (0.32)
A2	4.01 (1.00)	3.70 (1.00)	10.41 (1.00)	2.63 (1.00)
A3	0.68 (0.17)	0.02 (0.01)	2.01 (0.19)	0.12 (0.05)

Table 7.2: Peak areas from the fitting Gaussian distributions to the O K-edge PFY spectra, as shown in Figure 7.2. Areas relative to the e_g peak are given in brackets. Spectra were normalized to the absorption maxima of the V L_2-edge for each sample, making the peak areas dimensionless.

7.10 Atomic Charges

Given the importance of charge ordering and covalency in controlling the MIT in these materials, it is worth considering the atomic charges associated with their noneqivalent sites in a semi-quantitative way. This can be done through a topological analysis based on Bader's "atoms in molecules" theory. [177] Atomic charges are determined by integrating the charge density, ρ, within the volume enclosed by zero charge density flux surfaces, where $\overrightarrow{\nabla}\rho \cdot \hat{n} = 0$. The resulting atomic charges for the nonequivalent V, O_v and Sr/K sites are given in Table 7.3. These charges can be understood in large part by considering the changes in the crystal structure in passing from one system to another. As the V-O_c distances change little between systems, it is most important to consider the O_v sites.

Comparing δ-$Sr_xV_2O_5$ and δ-$K_xV_2O_5$ the immediate, obvious difference is the change in charge on the intercalcant cation site. Looking at the difference between the nominal and determined charge, it is strongly suggested that more charge is transferred to the VO lattice with the Sr intercalant, implying a greater charge density and a greater spectral intensity of the lower Hubbard band, should it form. This is perfectly in keeping with the observed XES spectra, where a substantially weaker peak from the lower Hubbard band is seen in δ-$K_xV_2O_5$, when compared to δ-$Sr_xV_2O_5$. The other notable structural difference between these systems is that the V-O_v bonds are a full 0.1 Å shorter in δ-$K_xV_2O_5$. It can be expected that as the V-O_v distance decreases the covalency of the bond will also increase, moving charge from the rather isolated O_v site onto the $VO_{c/b}$ mesh. This is indeed seen for the O sites, however the greater positive charge on the V sites of δ-$K_xV_2O_5$ can be explained by the competing effect of charge transfer from the intercalant cation just mentioned. The structural differences between δ-$Sr_xV_2O_5$ and δ-$K_xV_2O_5$ lead to a higher electron density at the V sites of δ-$Sr_xV_2O_5$, leading to a greater spectral intensity of the peak from the lower Hubbard band seen experimentally.

Passing from δ-$Sr_xV_2O_5$ to exf-$Sr_xV_2O_5$, the lower Hubbard band disappears. As mentioned above the main structural change is the effective compression of the nearby layers of VO_6 octahedra along the c-axis, leading to stronger Sr-O and V-O_v bonds. The V-O_v separation is only decreased in exf-$Sr_xV_2O_5$ at those sites which do not coordinate with Sr ions. At these O_v sites there is a substantial reduction in electron density, suggesting comparatively covalent bonds. There is at the same time a comparatively positive charge on the non-adjacent V sites. These points in combination with the amount of positive charge on the Sr ions, and higher electron density on the ion-adjacent sites despite an overall lower Sr concentration, suggest a migration of charge away from the vacuum between VO layers. There is competition between the effects of charge transfer from the Sr ions, covalency and charge migration. Higher covalency of V-O bonds will lead to a reduction of the Hubbard U, via reduction of the Racah parameter, or nephelauxetic effect, [129, 199] giving a mechanism for the obseved absence of a lower Hubbard band in exf-$Sr_xV_2O_5$, in addition to the differences in charge transfer from the intercalants. There is a clear charge ordering effect whereby those sites in the ion-adjacent layer have a lower charge, while within a layer the charge is quite similar for nonequivalent sites. This suggests a collection of charge in the ion-adjacent VO layer, with an active drive for the transfer of charge to the ion-adjacent layer. The results in Table 7.3 therefore give a semi-quantitative estimate of the charge ordering motif of exf-$Sr_xV_2O_5$, δ-$Sr_xV_2O_5$ and δ-$K_xV_2O_5$.

Lastly, it is worth comparing the experimental exf-$Sr_xV_2O_5$ structure to the relaxed structure. There is a lower positive charge on the Sr ion, and higher electron density at the ion-adjacent O_v sites. The principle, and rather dramatic, difference is the disipation of the charge ordering seen in the relaxed structure. All V sites now have a similar charge. The increased spacing between layers of octahedra may be inhibiting the transfer of charge between layers, leaving a slightly higher electron density on the ion non-adjacent layer. In effect the large fluctuations in the V-O_v and interlayer spacing that can be brought about by strains on the system can act as switching mechanisms between different charge order regimes. Alternatively, the injection/depletion of charge such as through electrostatic modulation using a gate electrode could potentially enforce or disrupt charge ordering bringing about a large modulation of conductivity enabling the use of these materials as Mott field-effect transistors. The variations in covalency in these systems has additional importance beyond those points already discussed. Lattice covalency will affect the polaron mass, which strongly affects conductivity and is therefore critical for any device applicaitons. [147, 189, 190]

Bader AIM analysis					
—	V1	V2	O_v1	O_v2	Sr/K
δ-$Sr_xV_2O_5$	2.008	2.033	-1.168	-1.134	1.591
δ-$K_xV_2O_5$	2.108	2.133	-0.906	-0.919	0.851
exf-$Sr_xV_2O_{5adj}$	2.090	2.066	-1.103	-1.140	1.604
exf-$Sr_xV_2O_5$	2.136	2.128	-0.607	-0.611	-
exf-$Sr_xV_2O_{5xrd,adj}$	2.075	2.057	-1.180	-1.139	1.514
exf-$Sr_xV_2O_{5xrd}$	2.075	2.064	-0.556	-0.544	-

Table 7.3: Total atomic charges as determined by topological AIM analysis. [177] The charges represent the total integrated charge within zero charge flux density curves around the site. The ion-adjacent and non-adjacent layers are treated separately in exp-$Sr_xV_2O_5$ and exf-$Sr_xV_2O_5$, and are denoted with subscripts.

7.11 V L-edge and RIXS

The discussion of the oxidation states of the V sites in each system naturally leads to a discussion of the resonant inelastic x-ray scattering measurements. The oxidation states of the TM sites play a strong role in determining the spectral shape and possible transitions. [30] In the case of V_2O_5 systems, the nominal d^0 configuration would lead to the observation of energy loss features in the spectra due to CT only. [166] However it is clear that the V sites must have a mixed oxidation state, [147, 173] leading to the presence of V^{4+} states and the observation of d-d transitions in the RIXS process. The measured RIXS spectra and V L-edge absorption spectra are shown in Figure 7.7, along with single impurity Anderson model (SIAM) calculations. [179, 180]

It can be seen that the calculated XAS spectra require a mixture of V^{4+} and V^{5+} to match the experiment in all cases, leading to a combination of CT and d-d excitation features in the RIXS spectra, which similarly match the experiment. The relative prominence of these states is similar in δ-$Sr_xV_2O_5$ and δ-$K_xV_2O_5$, while there is an increase in the presence of V^{4+} in exp-$Sr_xV_2O_5$ and exf-$Sr_xV_2O_5$, in agreement with the above analysis. The d-d and CT energies for δ-$Sr_xV_2O_5$, δ-$K_xV_2O_5$, exp-$Sr_xV_2O_5$ and exf-$Sr_xV_2O_5$ are as follows: 0.78 and 5.81 eV, 1.28 and 5.61 eV, 1.61 and 7.77 eV, 0.94 and 5.77 eV, respectively. These transition energies are consistent with what has been seen in other, uncorrelated V_2O_5 systems. [147]

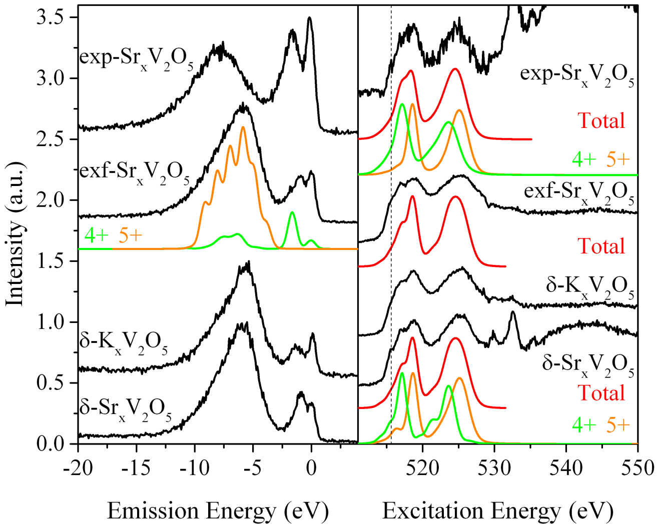

Figure 7.7: V L-edge XAS (right) and RIXS (left) spectra, the RIXS spectra shown were excited at 515.63 eV. Calculated SIAM spectra are shown below the relevant measured spectra. Total calculated spectra are in red, while the individual contributions from other oxidation states are given separately.

7.12 Conclusions

Measurements and calculations of several fundamental material properties have been presented for δ-Sr$_x$V$_2$O$_5$, δ-K$_x$V$_2$O$_5$, exp-Sr$_x$V$_2$O$_5$ and exf-Sr$_x$V$_2$O$_5$. In addition, the structure-property relationships that underpin these properties have been discussed, providing an understanding of how they change with subtle structural alterations. Band gaps ranging from 0.66 ± 0.20 eV to 2.32 ± 0.20 eV have been found, covering an extremely useful range for device applications. In addition the charge ordering pattern in these materials has been outlined, with emphasis on its sensitivity to structural changes. The pattern differs from material to material, but is also seen to be dependent on the strain applied to any single system and the separation between the layers. A distinct increase in lattice covalency is seen passing from δ-Sr$_x$V$_2$O$_5$ to exf-Sr$_x$V$_2$O$_5$, leading to shifts in the charge ordering, as well as the disappearance of the lower Hubbard band of δ-Sr$_x$V$_2$O$_5$, in part through the nephelauxetic effect. This, in conjunction with confinement effects, leads to a band gap change of over an eV. In addition, the changes in the t$_{2g}$ to e$_g$ ratio across the systems show that although it can be used to measure the potential of an MIT to occur, the broader structural changes must be considered. It is clear that vanadium oxide bronzes offer unique and tuneable electronic properties, emphasizing their importance at the forefront of research in materials science and for frontier device applications.

7.13 Experimental

All x-ray measurements were conducted under a vacuum of 10^{-7} Torr or better. The samples were mounted with a random orientation on carbon tape on copper plates. This implies that no polarization-dependent effects should be seen, as in oriented nanowire arrays. [155] The XAS measurements were conducted at the Spherical Grating Monochromator (SGM) beamline at the Canadian Light Source in Saskatoon, Canada. [111] The monochromator at SGM has a resolving power of about 5000. Spectra were collected as both TEY and PFY. The latter were collected using high count rate silicon drift detectors. All of the emission measurements were acquired at Beamline 8.0.1 of the Advanced Light Source in Berkeley, USA. This beamline's monochromator has a resolving power of about 4000, while the beamline spectrometer resolving power of about 800. The spectrometer is in the Rowland Circle configuration and uses a multichannel plate detector. The spectra were calibrated using the emission and absorption spectra of bismuth germanate (BGO). The prominent peaks in the BGO emission spectra were taken to lie at 517.9 and 526.0 eV, while the dominant XAS spectral peak was taken to be at 532.7 eV.

7.14 Calculations

The Density Functional Theory (DFT) calculations presented here were performed with the WIEN2K package, which uses a full potential with linearized-augmented-planewaves and local orbitals (LAPW + lo) to solve the Kohn-Sham equations. [192] In all cases the generalized gradient approximation of Perdew, Burke and Ernzerhof (GGA-PBE) was used to model the exchange correlation energies. [192] Core hole calculations were used to model the excited states of the systems. [93, 94] The core hole calculations used supercells of dimension 1x1x3 for δ-$Sr_xV_2O_5$ and δ-$K_xV_2O_5$. Smaller cells were used for the exp-$Sr_xV_2O_5$ and exf-$Sr_xV_2O_5$ structures, and only for a limited set of the nonequivalent sites in order to limit the computation time consumed for the full analysis. In all cases the k-mesh was scaled down in the supercell calculations to account for the increased unit cell size. The k-mesh sizes were selected by increasing the mesh size until the total system energy had converged to 10^{-5} Ry. The SIAM calculations presented here use the code of Cowan, Butler and Thole. [179, 180]

7.15 Acknowledgements

Research described in this paper was performed at the Canadian Light Source, which is funded by the Canada Foundation for Innovation, the Natural Sciences and Engineering Research Council of Canada, the National Research Council Canada, the Canadian Institutes of Health Research, the Government of Saskatchewan, Western Economic Diversification Canada, and the University of Saskatchewan. The Advanced Light Source is supported by the Director, Office of Science, Office of Basic Energy Sciences, of the U.S. Department of Energy under Contract No. DE-AC02- 05CH11231. We would like to acknowledge the support of the Natural Sciences and Engineering Research Council of Canada (NSERC) and the Canada Research Chair program. We also acknowledge the support of Compute Canada. The calculations presented in this work were performed on the Grex high-performance computing cluster, part of the Westgrid network (www.westgrid.ca) and Compute Canada Calcul Canada (www.computecanada.ca). JLA, PMM, and SB gratefully acknowledge the National Science Foundation for support of this work under DMR 1504702.

Chapter 8

The Hubbard Bands in δ-$Sr_xV_2O_5$

This chapter focuses on my contribution to a manuscript that has recently been submitted to *Chem. Mater.*, entitled ‘Intercalation-Induced Dimensional Reduction and Thickness-Modulated Electronic Structure of a Layered Ternary Vanadium Oxide’ by Justin L. Andrews, Luis R. De Jesus, Thomas M. Tolhurst, Peter Marley, Alexander Moewes and Sarbajit Banerjee. The manuscript focuses on the synthesis and other properties of δ-$Sr_xV_2O_5$ and its exfoliated counterparts. My contribution is that of x-ray spectroscopy measurements, DFT calculations, data processing and analysis. This is the first case where we presented the observed presence of the lower Hubbard band in these systems, their band gaps, and the observation of interaction of the intercalant, Sr, with the VO lattice. This chapter will feature a figure from, and discussion based on, my contribution to this manuscript.

Following the analysis of V_2O_5 bronzes in the preceding chapter, an explanation for the presence of the Hubbard band in δ-$Sr_xV_2O_5$, as well as its disappearance with expansion (leading to the sample labled exp-$Sr_xV_2O_5$) and exfoliation(leading to the sample labled exf-$Sr_xV_2O_5$), as seen in Figure 8.1 can be arrived at rather quickly. It can be seen that the agreement between the calculated spectra for the relaxed δ-$Sr_xV_2O_5$ structure and the experiment is excellent, outside of the region where the Hubbard band is present, especially once the attenuation from the V L_2-edge is considered. The same can be said of the spectra for the other systems. It can therefore be expected that at least in these bronzes, the Hubbard bands can be considered separately from the itinerant electrons in the system, which are modelled well by the DFT calculations.

The intercalation of Sr into the V_2O_5 framework introduces electrons to the otherwise

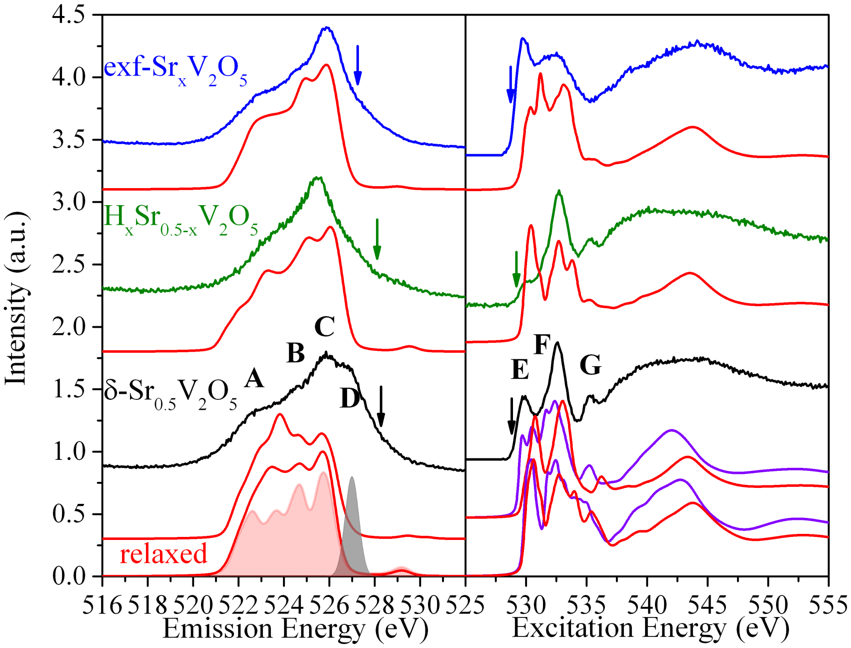

Figure 8.1: Measured and calculated O K-edge XES and XAS spectra for δ-$Sr_xV_2O_5$, exp-$Sr_xV_2O_5$ and exf-$Sr_xV_2O_5$. Band edges determined with the second derivatives of the spectra, are marked with colour-coded arrows. Calculated ground state spectra using relaxed crystal structures are shown for all samples. For δ-$Sr_xV_2O_5$ spectra are also shown for the XRD-derived structure, as well as core hole calculations in violet. An attenuated, calculated emission spectrum derived with Equation 9.1 is shown as a shaded, red curve. A Gaussian peak indicating the location of the lower Hubbard band is added to the figure as a filled grey curve.

unoccupied V d-states. Although this would generally make the system metallic, the increased e-e interaction strength at the semi-localized V d-states lead to the formation of an upper and lower Hubbard band, making the system a narrow-gap insulator, as reported above. Upon expansion, the Hubbard band is seen to disappear, leading to an increase in the band gap, furthered by the introduction of confinement effects in the exfoliated V_2O_5 layers. This exfoliation-induced band gap widening is seen in dramatic style in the following study of ϵ-V_2O_5.

Chapter 9

A New, Expanded V_2O_5 polymorph: ϵ-V_2O_5

9.1 Introduction

It has been seen that dimensional reduction of V_2O_5 bronzes leads to an increase in the band gap through multiple mechanisms. There is a band gap increase with respect to the ambient-stable α-V_2O_5 when it is modified to exf-$Sr_xV_2O_5$. However, the latter material still contains intercalated Sr cations, and it would be interesting to see the effects of exfoliation on a VO-only compound. This is explored in the following contribution, which details the electronic structure of ϵ-V_2O_5. In addition to its intriguing, wide band gap, ϵ-V_2O_5 also shows a rich RIXS spectrum, showing this functional material may also be an interesting system for quasi-particle studies.

My contribution ranges from data collection, to the processing and analysis of data, to writing the manuscript. This study emphasizes that there is a tremendously wide range of phenomena to be studied and functional properties to be uncovered in V_2O_5 compounds. Not only that, but the interplay of itinerant and localized d-electrons in these systems portend the variations in properties that are likely to be seen in lanthanide-based phosphors. Their 5d states are inevitably distributed further from the nucleus than 3d electrons, but a key lesson from these studies of VO compounds is that this is not enough for the states to be itinerant, local coordination geometry is paramount. This manuscript will be submitted for publication in March, 2017.

9.2 The Manuscript

Electronic structure of ϵ-V_2O_5: how increasing interlayer spacing expands the band gap

T.Tolhurst[1], B. Leedahl[1], J. L. Andrews[2], S. Banerjee[2], A. Moewes[1]

1 Department of Physics and Engineering Physics, University of Saskatchewan, 116 Science Place, Saskatoon Saskatchewan S7N 5E2 , Canada. E-mail: alex.moewes@usask.ca.

2 Department of Chemistry, Texas A&M University College Station, TX 77843.

9.3 Abstract

Dimensional reduction has shown itself to be an effective means of modifying the electronic structure of materials. Layered compounds are particularly amenable to this treatment, and given its unique properties, α-V_2O_5 is an outstanding candidate. This is a study of the electronic structure, including an accurate determination of the band gap, of ϵ-V_2O_5. This new polymorph of V_2O_5 has an increased interlayer separation that is found to lead to a dramatic increase in the band gap, through the introduction of confinement effects into the system. The band gap is measured to be 3.27 ± 0.20 eV, an increase of over 1 eV from α-V_2O_5. Further, the distortions brought on by the exfoliation process lead to a complex RIXS spectrum, showing a rich series of d-d excitations, as well as orbital excitations manifest in a 0.86 eV orbiton.

9.4 Introduction

Vanadium oxides have found themselves at the forefront of research into novel compounds for battery and device applications. The open, layered structure of α-V_2O_5 makes it a natural candidate cathode material for Li-ion batteries, however the lithiation of bulk α-V_2O_5 is irreversible. [17, 18] This has driven the search for new polymorphs that retain α-V_2O_5's open structure, while also exhibiting reversible lithiation. [18, 147] At the same time there is interest in engineering the band gaps of these materials, while also inducing other changes in their electronic structure. The radical changes that can be effected to the α-V_2O_5 electronic structure are exemplified in the strongly correlated V_2O_5 bronzes that have been recently reported. [15, 154, 159, 176, 183] Of course, correlation effects are well known for other VO stoichiometries. [202, 203] Recently, structural modification through exfoliation of the layered α-V_2O_5 structure has been reported, opening a new frontier for tuning the VO electronic structure. [191]

Here we present a soft x-ray spectroscopy and density functional theory-based study of ϵ-V_2O_5, a new phase of V_2O_5 with an increased interlayer separation mediated by intercalated H_2O molecules. We address the question of how the interlayer spacing affects the band gap, as well as the potential induction of correlation effects using x-ray absorption and emission spectroscopy (XAS and XES).

9.5 Synthesis and Structure

The synthesis of this material will be reported in greater depth elsewhere. This polymorph consists of V_2O_5 layers supported by interstitial, non-coordinating water molecules. The analysis herein uses an approximate structure derived from XRD as a starting point. The direct structure solution is not possible as a result of a large degree of preferred orientation and disorder between layers. The approximate structure is given in Figure 9.1, along with one derived from a DFT-based force minimization. The principal difference between the structures is a shortening of the V-O_v bonds and a further increase in the interlayer spacing. The result is that the V coordination is much closer to a square pyramidal configuration, rather than octahedral.

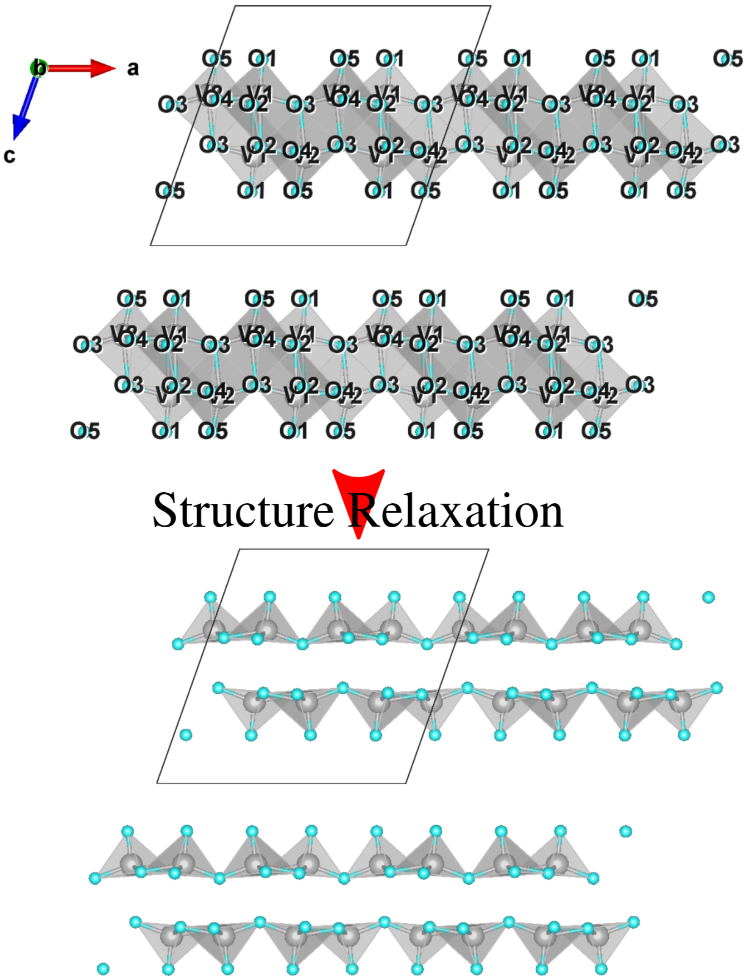

Figure 9.1: The approximate (top) and relaxed (bottom) structures of ϵ-V_2O_5. Non-equivalent sites are labelled and will also be generally referred to as O_c, O_b and O_v as in other works. [16] Only bonds less than or equal to 2.5 Å in length are shown.

9.6 Oxygen K-edge

A set of x-ray emission spectroscopy (XES) spectra with a corresponding x-ray absorption spectroscopy (XAS) spectrum collected from the as-prepared ϵ-V_2O_5 sample is shown in Figure. 9.2. There are a considerable number of features to discuss in the spectra. As a result it is worth breaking up the discussion into several parts. First and foremost is the absorption spectrum, collected as the partial fluorescence yield (PFY), and the normal x-ray emission spectrum (NXES). The latter is obtained by exciting high above the absorption energy threshold in order to give a spectrum with no resonant effects, which will be proportional to the occupied density of states (DOS) of the material. [30] Spectra calculated using density functional theory (DFT) are shown alongside the measured spectra in the figure. These spectra should correspond to the measured NXES and XAS spectra. These spectra will be the focus of the first few sections of this work, the other emission spectra seen in the figure are resonant emission spectra and will be discussed afterwards.

The measured and calculated absorption spectra match each other very well. The best agreement is seen between the experimental spectrum and the calculation using the relaxed structure. The disagreement at peak **G** and the subsequent two peaks is only apparent. These are peaks are due to the interstitial water that is thought to be present in the material. Taken together these features correspond exceptionally well to the known absorption spectrum of water. [204–206] Noting that no similar spectral features were found in the α-V_2O_5 reference spectra measured concurrently, the presence of water in the structure of ϵ-V_2O_5 is confirmed.

There is again very good agreement between the calculated NXES and the measurement. Some spectral contribution from the interstitial water must again be expected. However, this is not the source of apparent disagreement in this case. Here the disagreement stems from the effect of sample self-absorption. In VO compounds this effect is dramatic as a result of the overlap of the O K-edge emissions with the V L_2-edge. [147] A correction can be applied to the calculated spectra using the following fundamental parameters equation

$$I_{det,i}(E) = A' \frac{I_{calc}(E)}{\mu_{M,I_0} \csc\theta + \mu_{M,i}(E) \csc\phi} \tag{9.1}$$

where A' is an arbitrary constant, μ_{M,I_0} is the mass absorption coefficient of the matrix for the incident radiation, $\mu_{M,i}(E)$ is the key functional term representing the mass absorption coefficient of the matrix for the O K-edge emissions. The mass absorption coefficients were determined using calculated V L-edge spectra and tabulated elemental mass absorption values. [27] The incident and outgoing x-ray angles are given by θ and ϕ, respectively. The adjusted, calculated spectra, $I_{det,i}(E)$, are shown in Figure 9.2. It is seen that the agreement between the measured and calculated spectra is excellent, especially in the case of the calculation based on the relaxed structure.

The calculated spectra have been seen to match the experiment very well and the DFT calculations for the relaxed structure can be taken to form a good description of the material.

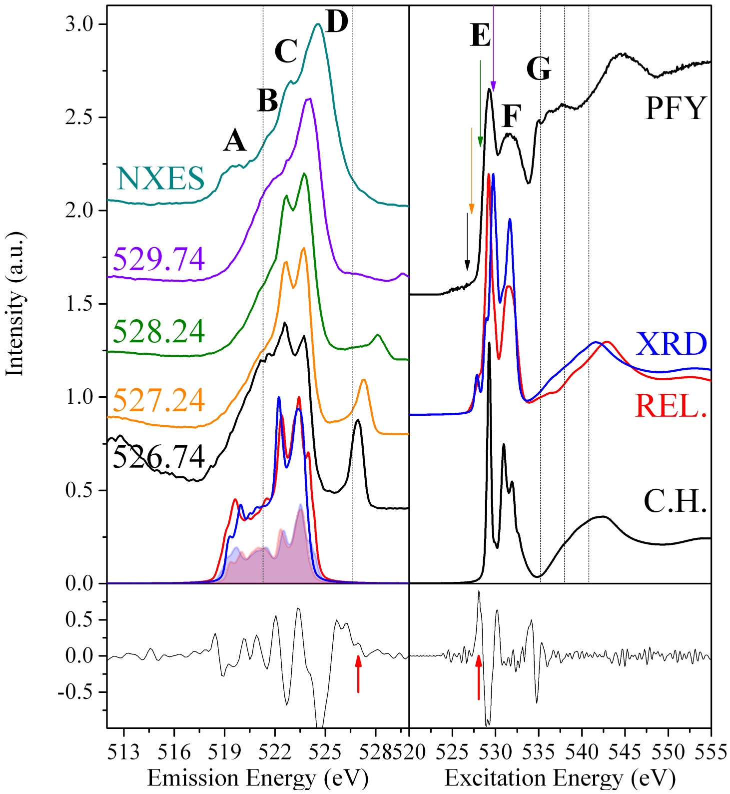

Figure 9.2: Upper panels show measured and calculated XES and XAS spectra for ϵ-V_2O_5. Calculations are shown for the XRD-derived (blue) and relaxed (red) structures, as well as calculated emission spectra that have had a fundamental parameters calculation applied to predict the attenuation of the spectrum that is expected from self-absorption (shaded curves). The lower panels show the second derivatives of the measured NXES and XAS spectra, with arrows indicating peaks used for determining the locations of the band edges. The vertical dashed lines indicate averaged literature values for major peaks in the x-ray spectra of liquid water. [204–207] The resonant emission spectra are color-coded to match the arrows marking their excitation energies on the XAS spectrum.

In conjunction with the measurements, the calculations can then be used to determine an experimental band gap for ϵ-V_2O_5. The second derivatives of the experimental XAS and NXES spectra give an accurate measure of the onset of the occupied and unoccupied density of states. [93] Since the XAS spectrum is indicative of the excited state of the system in general, it is necessary to apply a core hole correction to the separation of states obtained from the spectra. [93, 94] Using these methods the experimental band gap for ϵ-V_2O_5 is determined to be 3.27 ± 0.20 eV. The VB onset of the emission spectrum excited at 529.74 eV was used to avoid contributions from the interstitial water. The calculated band gap, using the generalized gradient approximation (GGA) for the exchange-correlation potential, for this system is 2.08 eV when the relaxed structure is used, and 1.38 eV for the approximate structure. It is interesting to compare this to a similar study of α-V_2O_5, which gives a calculated gap using the same DFT functional of 1.84 eV, in agreement with the experimental value. [147] In the same study, using a modified Becke-Johnson (mBJ) potenital, which uses a modified atomic exchange energy, a calculated gap of 2.78 eV was obtained. The structural similarity in the neighbourhood of the V atoms suggests the ϵ-V_2O_5 and α-V_2O_5 electronic structures should be similar, which is supported by the similarity of their XAS spectra. This is also supported by the DFT results, where similar band gaps where obtained. However the mBJ calculation of α-V_2O_5 better approximates the observed gap in ϵ-V_2O_5. The conclusion here is that the increased band gap of ϵ-V_2O_5 is due to confinement effects brought on by exfoliation of the layer of an α-V_2O_5-like structure. This result is consistent with the band gap modification seen from confinement effects in, for example, nanowires. [208] This analysis so far ignores any effect of the states associated with the interstitial water in ϵ-V_2O_5.

The large band gap measured here seems at odds with the dark body color of the as prepared sample. It is important to realize that the band gap reported here is the separation of the occupied and unoccupied states in the VO layers only. Optical measurements can not discriminate in this way. Comparing the x-ray photo-emission literature for H_2O and α-V_2O_5 suggests that the former has an O K-edge binding energy that is about 8.5 eV stronger than the latter. [209, 210] This implies that the LUMO of H_2O lies about 1.65 eV below the CB of the VO-only portion of the material. The gap of the composite system would then be $\approx$ 0.73 eV, leading to a black body color.

9.7 DOS

With the agreement between the measured and calculated spectra, and given the dependence of the x-ray spectra on the density of states of a material, it is natural to use the DOS to develop greater insight into the material's properties. The calculated DOS for the relaxed and unrelaxed structures are shown in Figure 9.3. The DOS of ϵ-V_2O_5 are very similar to those of α-V_2O_5 (not shown). [147] Despite the presence of two nonequivalent V sites in ϵ-V_2O_5 the well-know split-off d_{xy} band of α-V_2O_5 is preserved, in contrast to the ζ-V_2O_5

polymorph. [147] The DOS of the unrelaxed ϵ-V_2O_5 structure show dramatically different contributions from nonequivalent V sites to different energetic regions, while there is an almost erratic structure to the V-O π-bonding features in the VB. This contrasts rather strongly the DOS of the relaxed structure, which shows near equality of the DOS of V_1 and V_2 throughout and well defined VB structure. This is again suggestive that the relaxed structure better approximates the equilibrium structure of the material.

As is typical the VB DOS is dominated by O p-states, with characteristic peaks due to σ- and π-bond formation. [147] Strong σ-bonds are seen between the V-O_c and V-O_b sites, while strong π-bonds are seen for the V-O_v interaction. Importantly, another shared feature with α-V_2O_5, is the contribution of weak π bonds between the V d_{xy}-O_c p-states, which is also corroborated by their coincidence in the lower CB. These represent the principal conduction pathway in α-V_2O_5, and the case of ϵ-V_2O_5 is evidently the same.

Some finer detail can be seen if the calculated band structure of the material is considered. It is shown in Figure 9.3 and the isolated nature of the low-lying d_{xy} band can be clearly seen. The overal features resulting from the relaxed and unrelaxed structures are quite similar. The contributions of the nonequivalent sites are shifted with respect to one another in the latter case, leading to broadening of the bands. Their contributions to the material's electronic structure are truly unique, and suggest the possibility of charge ordering in distorted structures. The VB maxima and CB minima for the unrelaxed structure are respectively found at the M and L points, while they are at the Γ and Z-F1 in the relaxed structure. The similarity of the band structure contributions from the nonequivalent sites in the relaxed structure is also interesting when compared to α-V_2O_5, which has a single V site. These results further emphasize the well known result that the electronic structure of VO systems is very sensitive to the relative positions of the V atoms and their ligands. [16]

9.8 Topological Analysis of The Electron Density

To better understand the changes in charge distribution between different polymorhphs of a compound, it is often useful to conduct a topological analysis based on Bader's atoms in molecules theory. [177] Here the comparison will be made between the relaxed and unrelaxed structures, as well as the atomic charges of α-V_2O_5 and ζ-V_2O_5 from the literature. [147]

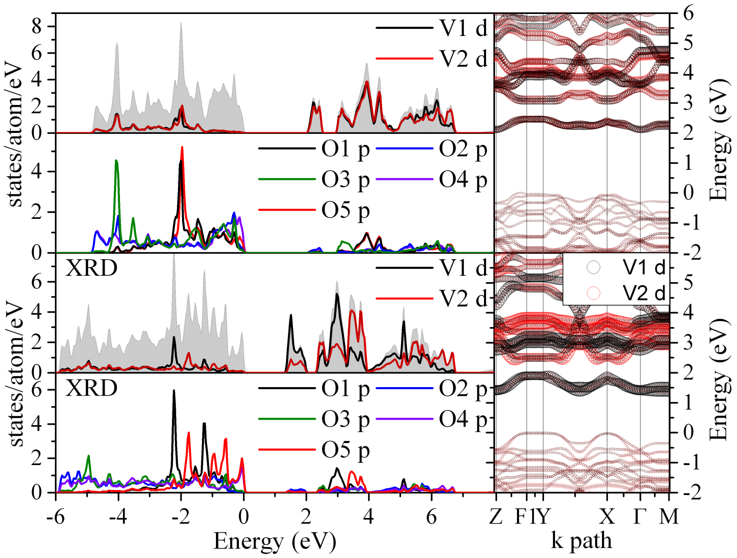

Figure 9.3: Calculated DOS and band structures for the XRD (bottom) and relaxed structures (top). Relevant DOS for the nonequivalent sites are colour coded for each structure, with the scaled, total DOS shown as a grey, shaded curve. In the band structures the contributions from the nonequivalent V sites are colour coded to emphasize the electronic structural change upon relaxation. The labeling of O sites is such that O1/O5 are O_v sites, O2/4 are O_c sites and O3 is an O_b site.

The atomic charge of the O_c and O_b sites are very similar to those of α-V_2O_5 and ζ-V_2O_5, reinforcing the result that there is little change along the conducting planes of these materials. The largest differences are seen in the charges at V and O_v sites. The V sites of the relaxed and unrelaxed ϵ-V_2O_5 structures have similar charges, that are each lower than that in α-V_2O_5. It is also significant that the O_v sites of ϵ-V_2O_5 have lower, that is to say more positive, charges than any similar site in the other polymorphs, with the exception of the V_3 site of ζ-V_2O_5. This site is highly isolated and thus has a strong V-O_v bond, suggesting a similar, and intuitively reasonable, situation in ϵ-V_2O_5. Looking at the charge difference between the two ϵ-V_2O_5 structures being considered here it can be seen that the O_v sites have rather different charges in the unrelaxed structure, and become similar upon relaxation. It can be concluded that the higher electron density at the V sites in ϵ-V_2O_5 is due to the reduced V-O_v distance. This is consequential, because in conjunction with the similarity of the charges of the O sites in the conduction plane, it implies the V-O_v bond is a principle means for switching between oxidation states of the V sites, as well as being influential in determining the extent of nephelauxetic effect and crystal field splitting for the V d-states. These phenomena are of interest as they play a role in the charge ordering of these materials, as well as the strength of correlation effects. Here an increased electron density at the V sites is suggested to be brought about be the covalency of the V-O_v bond.

Bader's AIM atomic charges				
structure	V	O_v	O_c	O_b
oct1	2.173	-0.600	-1.090	-1.062/-0.994
oct2	2.180	-0.600	-1.062	-0.994/-1.090
oct1XRD	2.176	-0.563	-1.099	-1.048/-1.020
oct2XRD	2.167	-0.613	-1.048	-1.020/-1.099
dif	-0.003	-0.037	0.009	-0.014/0.026
dif	0.013	0.013	-0.014	0.026/0.009

Table 9.1: Bader's AIM analysis of ϵ-V_2O_5. The table is organized in terms of the ocatahedra associated with V1 and V2. The atomic charges for the nonequivalent sites of the relaxed and unrelaxed structures are given. The differences in charge between the analogous sites in the two structures are given in the lower two rows. Multiple charges are given where there is more than one O site filling a particular role.

9.9 Resonant Emission

Resonant x-ray emission spectroscopy (RXES) is a rich source of information on many material properties. [30] The RXES spectra collected on ϵ-V_2O_5 are shown in Figure 9.2, with the excitation energies indicated with color-coded arrows on the XAS spectrum. There are two principal phenomena that are observable: variations in the spectral shape of the constant-energy fluorescence portion of the spectra (peaks **A** to **D**) as a result of nonequivalent site excitation, as well as peaks at constant energy loss below the elastic peaks due to resonant inelastic x-ray scattering (RIXS). To distinguish the two, the former alone will be referred to as RXES and the latter as RIXS.

RXES occurs as a result of preferential excitation of, and therefore emission from, nonequivalent atomic sites in the lattice as a results of the variations in binding energy and local unoccupied DOS. It should be possible to model this portion of the spectra using the DFT calculations already discussed by forming the appropriate linear combination of emission spectra from the nonequivalent O sites. If agreement is seen between experiment and calculation here, then it provides further support for the accuracy of the DFT calculations and structures on which they are based. The importance of correcting for the sample self-absorption can be appreciated, as without having accounted for it, it would be difficult to assess the match of experiment and theory. Calculated RXES spectra for several models are shown in Figure 9.4, which correspond to the measured spectra. Using the broadened XAS spectra from the nonequivalent O sites for the approximate, relaxed and core hole calculations, weights for combining emission spectra were determined. The weights of the emission spectra are given by the overlap of a 0.2 eV FWHM Gaussian with the XAS spectra, and the resulting RXES spectra are shown in the left panel of the figure. A contour plot can be generated for each case, and those using the ground state XAS are shown in the bottom of the figure. Ideally the analogs of the experimental spectra should be found within this contour plot. It can be seen that only the relaxed structure offers the necessary spectral shapes. The agreement is in fact quite good, though there could be debate about whether the ground state or core hole calculation offers the best set of spectral weights. The ground state offers better agreement for the low excitation energy spectra, while the core hole XAS gives better agreement for the higher energy excitations. The conclusion to be drawn is that the XES spectral shapes represent the experiment very well, but that the excited state during measurement is best represented by a spectrum somewhere between the ground and excited state calculations presented here. This leads to the usual conclusion that the full core hole overestimates the effect in the experiment. Therefore, the measured band gap presented here represents an upper limit for the ϵ-V_2O_5 band gap.

9.10 Resonant Inelastic Scattering

The experimental RIXS spectra are shown in Figure 9.5, alongside the measured TEY absorption spectrum. The emission spectra from the O K-edge are simply those in Figure 9.2, magnified several times to focus on the region near the elastic peak, and placed on an energy loss scale. Excitation energies for both the V L-edge and O K-edge are shown in the figure. Anderson impurity model (SIAM) calculations for the V L-edge emissions are shown as magenta curves sitting in coincidence with the experimental spectra.

The energy loss features at the V L-edge are generally due to intra-site excitations, [35] which here are d-d excitations. This is a clear experimental deviation from the nominal d^0

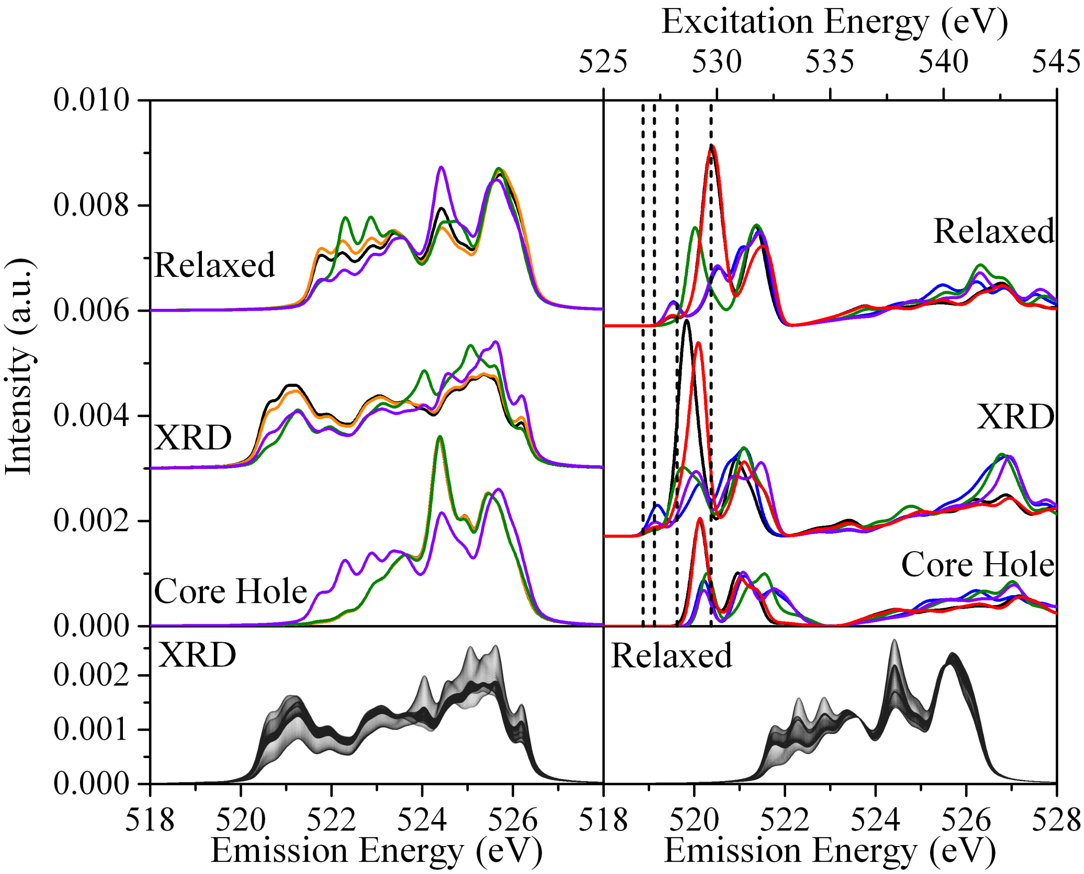

Figure 9.4: Calculated O K-edge RXES spectra. Right: overlap of a Gaussian profile, representing the incident x-ray beam, with the calculated absorption spectra of the nonquivalent O sites. Left: linear combinations of emission spectra from the nonequivalent O sites weighted at each RXES excitation energy (dashed lines) by the values of the respective overlap functions in the right panel. RXES are colour coded to match the measured spectra. Bottom: left and right panels show the full range of possible RXES spectra, when exciting up to 535 eV, from the XRD and relaxed structures, respectively.

configuration of V_2O_5. This is not unusual, it is well known that V_2O_5 is best described as having a considerable d^1 contribution. [35, 147] It can be seen that the energy loss features at this edge are well described by the d-d portion of the SIAM calculation. This is a particularly rich spectrum of d-d excitations when compared to those of α-V_2O_5 or ζ-V_2O_5, which typically show a single energy loss peak. This stems from the high degree of distortion of the VO_6 octahedra in ϵ-V_2O_5. This is in keeping with the structure relaxation results, which suggest that the geometry changes from roughly octahedral to distorted square pyramidal.

It is also interesting to consider energy losses at the O K-edge, which are becoming appreciated for their ability to give information on inter-atomic excitations. [35–38] Comparing these spectra to the V L-edge, it can be seen that most of the energy loss features coincide with the d-d excitations seen at that edge. However there is a weak energy loss feature at -0.86 eV in the all of the O K-edge RIXS. That this peak does not appear at the metal edge suggests that it is due to an inter-atomic excitation, that is to say orbitons or magnons. [35]

Double orbital excitations have been seen in YVO_3, [38] and that the next greatest energy loss in the O K-edge RIXS occurs at -1.59 eV is quite suggestive. However this peak clearly already matches a d-d excitation energy, effectively ruling out a double orbital excitation. This assignment also fits better with the expected energy scale for these excitations. [37, 211, 212] This still leaves the lowest energy loss unaccounted for and given its absence in the V L-edge spectra it can be assigned to a single orbital excitation.

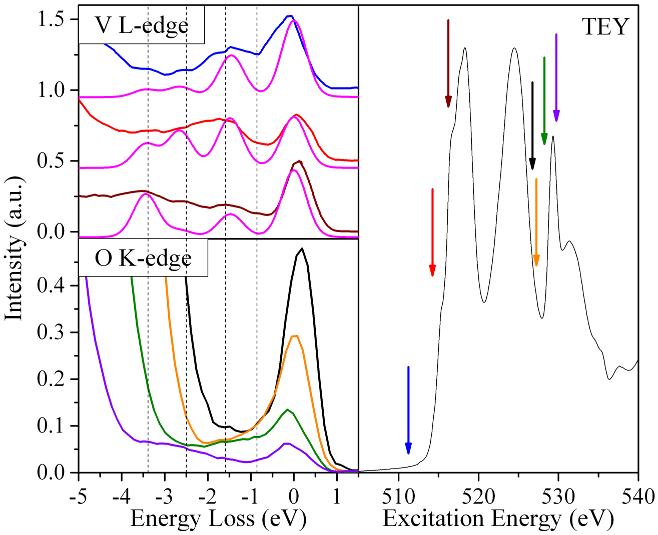

Figure 9.5: Measured RIXS spectra at the V L-edge and O K-edge, with the measured TEY at the right of the figure. Excitation energies are marked on the TEY with colour-coded arrows to match the emission spectra in the left panel. SIAM calculations for the d-d excitations are shown in magenta for the V L-edge spectra. Vertical lines mark energy loss features resolved at either edge.

To make the discussion of the low-energy loss peak more precise, deconvolution of the RIXS spectra was conducted with a sum of Gaussian distributions. As a first order attempt, only those peak energies known from the V L-edge were fixed and all other parameters were allowed to vary. Proceding in this way gave positions of the low energy peak ranging from 0.3

to 0.5 eV, with variation in the standard deviation from 0.3 to 0.6 eV. Although this is not a satisfying result, one important effect was accounted for, the same peak width was obtained for the elastic peak in all spectra. The data is therefore best described by considering the presence of a peak around 0.5 eV energy loss. The fit to the data is improved dramatically by making the reasonable constraint that all RIXS peaks have the same width. Fitting the data in this way gave the results shown in Figure 9.6. The fits are remarkably good, all with $\chi^2 < 0.004$. The peak widths of about 0.3 eV match the elastic peak width from the earlier fitting attempt. The low-energy loss peak is found to sit at about 0.8 eV for the three lowest excitation energies, but change sharply to 0.5 eV for the highest excitation energy. This last effect suggests that different quasiparticles are involved, such as phonons. [33]

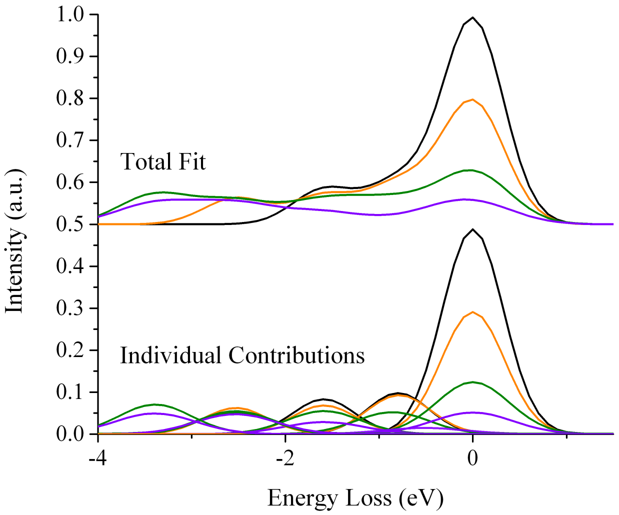

Figure 9.6: Results of fitting a series of constrained Gaussian distributions to the O K-edge RIXS data in Figure 9.5. The fit results are color coded to correspond to the experimental spectra.

9.11 Conclusions

A band gap of 3.27 ± 0.20 eV was found for ϵ-V_2O_5, a substantial increase from that of α-V_2O_5. This shows the effectiveness of dimensional reduction for modulating the band gap of V_2O_5 systems. Although other effects such as reduction of the V-O_v bond length lead to an increased nephelauxetic effect, and crystal field splitting, the driving force in the expansion of the band gap here is supported to be an increase in the strength of exchange-correlation interactions. Additional increase in the band gap can be expected from the increased O p-V d_{xy} overlap in the conduction plane. The sensitivity of VO systems to structural distortion is clearly visible in the DFT calculations presented here. Suggesting an additional mechanism for modifying their electronic structures. A particularly rich d-d excitation spectrum is seen at the V L-edge, supporting that the VO_6 octahedra are highly distorted, and a mixed oxidation state for the V sites. This is also supported by the DFT calculations. O K-edge RIXS show not only the d-d excitations, but also a 0.86 eV orbiton. The presence of interstitial water in ϵ-V_2O_5 has also been confirmed, and is seen to have a significant impact on its optical band gap. The electronic structure of ϵ-V_2O_5 has not only been outlined, but its ability to be modified through chemical or physical means is clear. In addition to this it hosts an unusually rich series of elementary excitations, earning it a place of interest for application and fundamental science.

9.12 Experimental

The x-ray absorption spectroscopy measurements presented here were collected at the spherical grating monochromator beamline at the Canadian Light Source, in Saskatoon, Saskatchewan, Canada. [111] The monochromator resolving power is about 5000 at the energies used here. The TEY absorption was recorded using the current flow needed to neutralize the sample during the measurement. The PFY measurements were collected by measuring the emitted fluorescence intensity using silicon drift detectors. The V L-edge and O K-edge spectra were deconvoluted using a post-processing method described elsewhere. [147] The x-ray emission measurements were conducted at the Advanced Light Source in Berkeley, California, USA. [48] The resolving power of the monochromator is about 4000. The spectrometer is in the Rowland Circle configuration and has a resolving power of about 1000. The powder samples were prepared by simple adhesion to carbon or copper tape before transfer to the vacuum chambers used for the measurements. Measurements were conducted in a vacuum of 10^{-6} Torr or better. Energy calibration was carried out by aligning the most intense peak of the MgO absorption spectrum to 546.5 eV. Emission spectra were calibrated using the elastic scattering peaks recorded with the spectra.

9.13 Calculations

The density functional theory calculations presented here were obtained with the WIEN2k software package. [112] It uses linearized augmented plane waves and augmented plane waves with local orbitals (LAPW and APW + lo) to solve the Kohn-Sham equations. The resulting Eigenvalue spectrum is used to determine the band structure, density of states and other material properties. The generalized gradient approximation of Perdew, Burke and Ernzerhof (GGA-PBE) was used to model the exchange correlation energies. [112] A 19x5x19 k-mesh was used for the ground state calculations, which was determined by increasing the mesh size until the total energy of the unit cell was found to be consistent to 10^{-5} Ry. The core hole calculations, which are necessary to model the excited state of ϵ-V_2O_5, [93, 94], used a 1x1x3 supercell, and appropriately scaled k-mesh. The SIAM calculations used for the V L-edge used the code of Cowan, Butler and Thole. [179, 180] The parameters resulting from this calculation are: $10dq = 2.65$, $ds = -0.32$, $dt = 0.1$, $du = -0.05$, $dv = -0.05$, $\beta = 0.65$.

Chapter 10

Coming Full Circle: Comparing CLMS and BLSA to SLA

10.1 Introduction

This thesis will close with a few studies of new phosphors that can be compared with SLA and SMS, both confirming assertions made earlier and pushing the understanding of luminescence properties further. First, a study of the electronic structure of $Li_2Ca_2[Mg_2Si_2N_6]:Eu^{2+}$ (CLMS) and $Ba[Li_2(Al_2Si_2)N_6]:Eu^{2+}$ (BLSA) focusing on the band gap and its origin is pursued, in the same spirit as the earlier works. A second manuscript looking in finer detail at their luminescence properties, based on RIXS measurements and informed by the preceding studies of VO-compounds, follows as the last manuscript herein.

My contribution ranges from data collection, to the processing and analysis of the data, as well as writing the manuscript. Synthesis, as in all cases in this thesis, is carried out by the coauthors of the publication. The case of CLMS and BLSA is curious, as although they are structurally and compositionally similar to SMS, they do not suffer from the same debilitatingly small band gap. At the same time their luminescence centres lack the elegant high symmetry of those in SMS.

10.2 The Manuscript

The band gap of CLMS and BLSA determined with soft x-ray spectroscopy and density functional theory

T. M. Tolhurst[1], P. Strobel[2], W. Schnick[2], A. Moewes[1]

1 Department of Physics and Engineering Physics, University of Saskatchewan, 116 Science Place Saskatoon, Saskatchewan S7N 5E2, 1-306-966-6431, alex.moewes@usask.ca

2 Department of Chemistry, University of Munich (LMU), Butenandtstrasse 5-13, 81377 Munich, Germany.

Abstract

We present a detailed characterization of luminescent materials $Li_2Ca_2[Mg_2Si_2N_6]$:Eu^{2+} and $Ba[Li_2(Al_2Si_2)N_6]$:Eu^{2+} using soft x-ray spectroscopy and density functional theory calculations. The band gap of $Li_2Ca_2[Mg_2Si_2N_6]$:Eu^{2+} is determined to be 4.84±0.20 eV, while that of $Ba[Li_2(Al_2Si_2)N_6]$:Eu^{2+} is determined to be 4.82±0.20 eV. The origin of the band gaps is discussed in the context of the calculated DOS of each material, and compared to benchmark materials SLA and SMS. Critically, the elements determining the band gaps are identified using the calculated density of states, as well as experimental resonant x-ray emission measurements. This allows for predictive power when these materials are used as the base of solid solution series, or for engineering luminescent materials more generally.

10.3 Introduction

Lighting is a leading consumer of energy globally, following only transportation and building temperature control. Solid state lighting, the phosphor converted light emitting diode (pc-LED) in particular, is poised to reduce energy consumption in the lighting sector by 40% within the next decade and half. [2] In order to achieve or even exceed this goal, several advances are wanting. Improvements to device architecture are important, [1] but there are also considerable gains to be made in both phosphor efficiency and the luminous efficacy of the devices. [2] The former is accessible through improved quantum efficiency of the phosphors, but the latter requires narrow, red emitting phosphors.

The discovery of the highly efficient red emitter $M_2Si_5N_8$ (M = Ca, Sr, Ba, Eu), and its demonstration as an LED phosphor were milestones in the field. [7,213] The recent discovery of narrow emitting $Sr[LiAl_3N_4]:Eu^{2+}$ (SLA) and $Sr[Mg_3SiN_4]:Eu^{2+}$ (SMS) has made ultra-high color rendering pc-LEDs realizable. [8, 9] There are still improvements that can be made, and efficient phosphors emitting in different regions of the visible spectrum are highly desirable.

This is a study of two new phosphors: narrow green-emitting $Ba[Li_2(Al_2Si_2)N_6]:Eu^{2+}$ (BLSA) and narrow red-emitting $Li_2Ca_2[Mg_2Si_2N_6]:Eu^{2+}$ (CLMS). [10, 11, 214] Each emit in highly useful regions of the visible spectrum and show promising quantum efficiencies. Accurate measurements of their band gaps, arguably one of the most important material characteristics, are made through the use of soft x-ray spectroscopy. The density functional theory calculations for each phosphor are presented and used to explain the origins of their band gaps, while relating them to other important, benchmark phosphors. The comparison between phosphors is used to form an understanding of the structure-property relationships that underpin the useful properties of CLMS and BLSA. This understanding can guide the search for the next generation of efficient, narrow-emitting phosphors.

10.4 Synthesis and Structure Models

The powder samples of BLSA and CLMS where synthesized in sealed tantalum ampules through a modified solid-state metathesis reaction. [10, 11] Full synthesis details and characterization of crystal structures are described elsewhere. [10, 11] Crystal structures derived from single crystal x-ray diffraction (XRD) are the primary input to the density functional theory (DFT) calculations presented here. Due to the statistical occupation of the Si/Al sites in BLSA, half of the sites in the unit cell were assigned to each for the DFT calculations. Both samples in this study are doped with Eu, which leads to $4f^7 \rightarrow 5d^1 4f^6$ emissions in each sample in the red (CLMS) and green (BLSA) spectral regions.

10.5 Nitrogen K-edge and the Band Gap

Soft x-ray emission and absorption measurements for each sample were conducted at the N K-edge and are shown in Figures 10.1 and 10.2. The x-ray absorption spectroscopy (XAS) measurements were collected as partial fluorescence yield (PFY). The x-ray emission spectroscopy (XES) measurements can be divided into two types, based on the excitation energy that was used. Those spectra excited near the onset of the XAS will contain resonant effects and are referred to here as RXES (resonant x-ray emission spectroscopy) spectra. They will be discussed in a subsequent section. The spectrum collected with an excitation energy of 427.89 eV, which is well above the absorption edge, should contain no resonant effects and represents a normal x-ray emission spectroscopy (NXES) spectrum. Both the XAS and the NXES have intensities that to first order are proportional to the density of states of the material. [30] Calculated spectra are shown alongside the measurements. A calculation for the ground state (g.s.) of each system is given, as is an excited state (c.h.) calculation that includes a N 1s hole and an electron added to the conduction band. The former is sufficient for describing the XES spectra, whereas an excited state calculation with a core hole is generally needed to properly describe the XAS spectra. [93–95] The band gaps and other properties of CLMS and BLSA can now be discussed in turn.

It can be seen that there is excellent agreement between the measured and calculated spectra of CLMS in Figure 10.1. There is a small region of apparent disagreement in the XAS around 401 eV. However this is simply due to absorption from N_2 gas that results from small amounts of radiation damage to the sample. As discussed elsewhere for similar phosphors, this is of no consequence to the results of interest here. [131] Outside of the narrow region of N_2 absorption the calculations and experiment match exceptionally well. It is also clear that

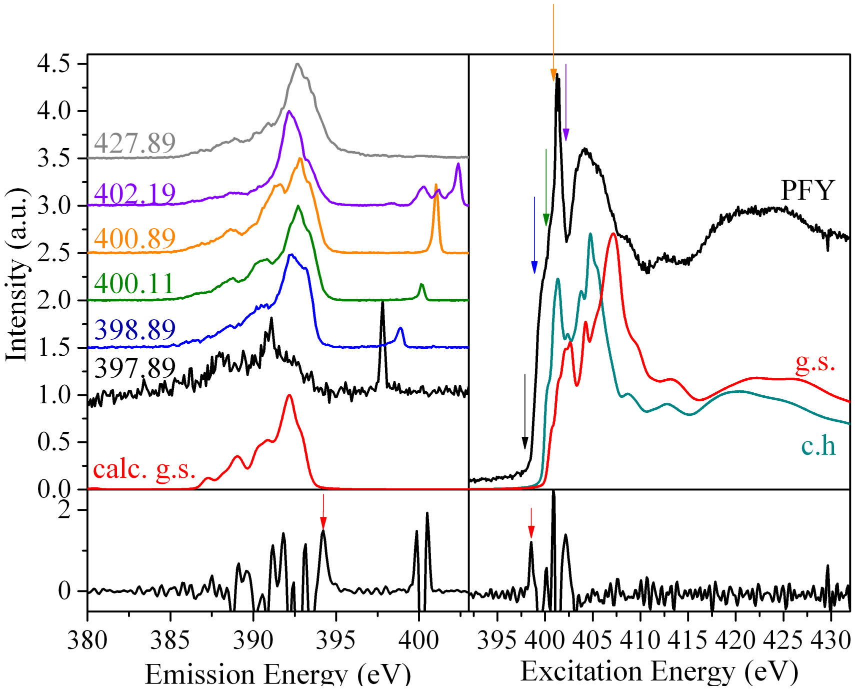

Figure 10.1: X-ray emission and absorption spectra of CLMS. The XES (left) and XAS (right) are shown alongside DFT calculations, while the second derivatives of the 400.11 eV RXES spectrum and the XAS spectrum are shown in the lower panels. The calculated ground state (g.s.) and excited state (c.h.) spectra are shown as red and cyan curves, respectively.

the core hole calculation provides the best match to the XAS data. The proportionality of the x-ray spectra to the density of states, along with a successful model of the excited state, allows for a determination of the band gap. To determine the valence and conduction band onsets, the second derivatives of the XES and XAS spectra are taken, respectively. The band onsets are taken to be the first peaks above the noise level at the upper edge of the XES and lower edge of the XAS spectra, as indicated with red arrows in Figure 10.2. Applying a DFT-derived correction for the effect of the core hole (the calculated energy difference between the CB onset in the ground and excited states) and nonequivalent site splitting to the band separation provides an accurate band gap measurement. In this way the band gap of CLMS is found to be 4.84 ± 0.20 eV. It should be noted that in order to avoid influence of N_2 emissions in the determined valence band onset, the second derivative of the XES spectrum excited at 400.11 eV has been used, as no N_2 will be excited at this energy. The contributions of N_2 to spectra excited at higher energies is evident. [134] The calculated band gap for this system is 3.04 eV. This underestimation is typical, and can be improved upon by using the modified Becke-Johnson (mBJ) exchange-correlation potential. [92] In this case a band gap of 4.15 eV results, in much better agreement with experiment.

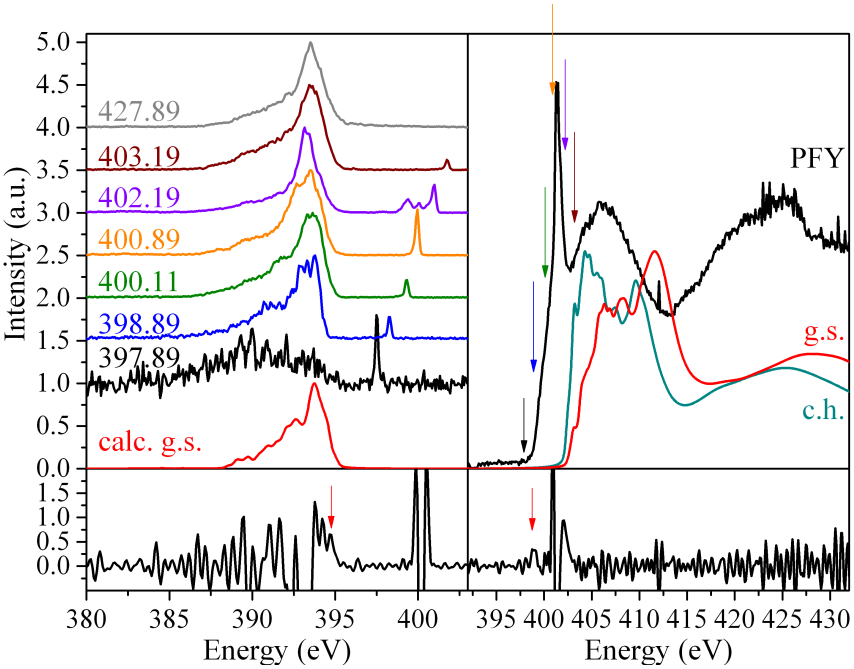

Figure 10.2: X-ray emission and absorption spectra of BLSA. The XES (left) and XAS (right) are shown alongside DFT calculations, while the second derivatives of the 400.11 eV RXES spectrum and the XAS spectrum are shown in the lower panels.

Comparing the measured and calculated spectra for BLSA in Figure 10.2, it can be seen that there is again excellent agreement. The core hole effect is somewhat overestimated, and leads to the usual conclusion that the band gap given here will represent an upper limit. Using the same methodology as above the band gap of BLSA is found to be 4.82 ± 0.20 eV. The calculated band gap using the GGA potential is found to be 3.26 eV, and the band gap resulting from use of the mBJ potential is 4.43 eV. Given that the mBJ potential is expected to be accurate to within about 10%, the agreement here is good. The experiment and calculations suggest that the band gaps of CLMS and BLSA are the same, with that of BLSA perhaps being larger by a few tenths of an eV.

10.6 Density of States and Band Structure

Given the good agreement between the experimental and calculated spectra, it is worth while to look at the DOS of each system in order to try to develop and deeper understanding of their electronic structures. In particular why these materials, despite having different composition and crystal structures, have similar band gaps? Further, why CLMS has a relatively large band gap when compared to the compositionally similar phosphor SLA? The band gap of the latter is detrimental to the efficiency of its $4f^7 \rightarrow 5d^1 4f^6$ emissions when doped with Eu^{2+}. [131] In this case both CLMS and BLSA have band gaps similar to the ultra-efficient phosphor SLA, which has an elemental composition similar to BLSA. [108] The similarity, and subtle differences, of all of these compounds make their comparison very informative.

The density of states of CLMS and BLSA are shown in Figure 10.3. The DOS of CLMS can be considered first. Gross features of the DOS are quite similar to SLA and SLA. [108, 131] The N p-states dominate the upper VB. There is a strong presence of Si p-states in the middle VB, and s-states towards the lower VB. The Si p-states are also strong in the middle of the CB. These features are characteristic of strong N p - Si sp^3 hybridization, as seen in SMS. There is comparatively little presence of the Mg states, which is do due it being largely ionized. The lower CB is dominated by the Ca d-states. It is common for the alkaline earth ion d-states to contribute heavily to the lower CB. [108, 131]

There is again tremendous similarity between the gross features of the DOS of BLSA and the other systems being discussed. There is evidence for strong interaction between N p-states and sp^3-hybridized Si states. Similar to CLMS, the Ba d-states are dominant in the lower CB. There is a noticeable presence of the Li states near the non-bonding N p-states at the upper edge of the VB, as well as higher in the CB. This implies relatively weak orbital overlap and that the Li is largely ionized. The Al states show the same general structure as the Si states. However, their intensity is lower than the Si states, which is to be expected from the lower electronegativity of Al. It can be concluded that the Al states are also modelled well by sp^3 hybrids, though their bonding with N is slightly more ionic.

Ignoring the alkaline earth cations for the moment, all other cations are tetrahedrally coordinated by N atoms. The DOS support the intuitive notion that in moving along the

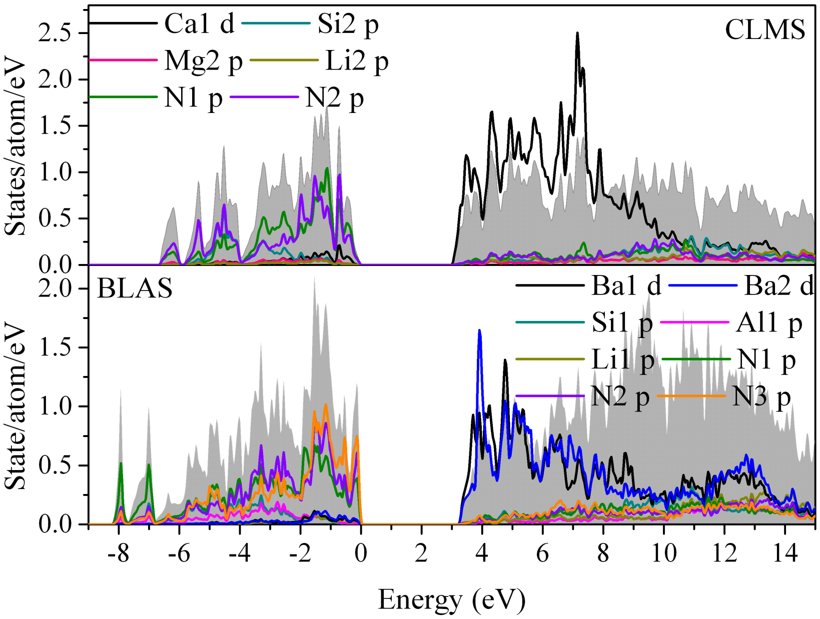

Figure 10.3: Calculated density of states for CLMS (top) and BLSA (bottom). The structures derived from XRD where used for both.

sequence Si → Al → Mg → Li, the bonds become more ionic, and the approximation of local sp^3 hybrid orbitals becomes less appropriate for describing the DOS. The strong bonding between Si, Al and N leads to sp^3 hybridization of the Si and Al, but also leads to Si and Al playing a prominent role in determining the orbital character at the N sites. Careful analysis of the relative intensity of non-bonding N p-states for the nonequivalent sites, and contributions to different regions of the VB and CB support this readily. [53] The influence of the Mg and Li will be secondary.

A few final points are worth noting. The splitting into individual bands of the states in the lower VB of BLSA suggests that the covalency of the CLMS lattice is somewhat higher than in BLSA. [12] This is supported by the red optical emissions for CLMS. [138] The analysis of SLA and SMS in the literature would suggest that the band gap of CLMS should be much smaller than that of BLSA. It has been found that the band gap of SMS is small as a result of the small energetic separation of the Mg s- and N p-states. [131] The band gap of CLMS is about 1 eV greater than that of SMS, despite containing Mg. The central problem in need of explanation here is whether Mg still limits the band gap of CLMS, and if so, why it is greater than in SMS. There are two phenomena that offer an explanation, both related to the N-Mg separation in the two materials; it is much smaller in CLMS. This is quite natural, as one generally expects a reduction in bond lengths if smaller alkaline earth metals are used, here Ca as opposed to Sr. [90] The reduction of the N-Mg bond length will increase the bond-antibond splitting, which in general varies at the square of the bond length. [12] As well, the increasing covalency of the N-Mg bond will drive the hybridization of the Mg s and p states, leading to orbitals that more closely resemble sp^3 hybrids. This also increases the energy of the unoccupied Mg states. These two effects in concert can account for the band gap increase seen in CLMS, when compared to SMS. Given the comparatively high energy of Ca d-states, one still expects the CB minimum to be determined by the Mg states, though the presence of the emptied Li s-states should be born in mind. [108, 131] From the analysis of SLA in the literature, [108, 131] it can be expected that BLSA should have band gap about the size of SLA, which is seen. At the same time, one would also expect that the CB minimum will be determined by the Ba d-states. The DOS are suggestive of this, but it is worthwhile to view the band structures of these materials in order to get a more detailed view of their electronic structures.

10.7 Band Structures

The calculated band structures of CLMS and BLSA are shown in Figure 10.4. The low-lying conduction bands of both materials are largely composed of the alkaline earth d-states, with one exception in CLMS. The lowest-lying conduction band is of predominantly s-character. This is in keeping with the idea that the tetrahedral cation sites, Mg and Li will determine the CB minimum in this material. Thus BLSA is a type I material like SLA, and CLMS a type II material, like SMS. [139] It is also interesting to note the curvature of the bands at the VB and CB edges of CLMS. The low lying s-band of CLMS has a high curvature and therefore a relatively low electron effective mass, [12] on which the mobility depends. On the other hand relatively low particle mobilities can be expected at the VB maxima of CLMS. This is to be expected with the VB maxima determined by the non-bonding N p-states. Both have indirect band gaps, which should be conducive to a high quantum efficiency for the Eu^{2+} emission, due to the comparatively low radiative efficiency of the host. The VB maxima of CLMS and BLSA are at the I and $M - \Gamma$ points, respectively. Likewise the CB minima are respectively at Γ and $\Gamma - Z$.

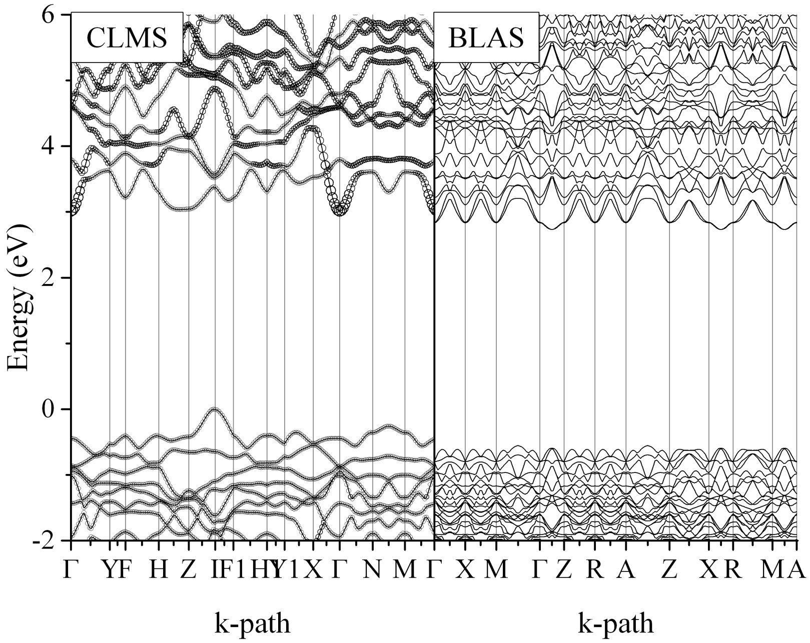

Figure 10.4: Calculated band structure of CLMS (left) and BLAS (right). The s-character states are plotted for CLMS, where the thickness of the lines in the plot indicates the relative contribution of the s-states to the total DOS at each point.

10.8 RXES

There are two main phenomena leading to the variations in spectral shape of the RXES spectra in Figures 10.1 and 10.2: resonant inelastic x-ray scattering (RIXS), as well as non-equivalent site excitation. The former manifests itself as peaks at some energy loss below the elastic scattering peaks, which results from the creation of, or scattering from, quasiparticles. The low energy RIXS excitations present in the spectra will be discussed in another contribution. The latter shows up as changes in the shape of the constant-energy fluorescence spectrum, which is proportional to the DOS of the states involved. It is the changes in the shape of this constant energy portion of the spectra that are of interest here. It can be seen in the above figures that there is little change in spectral shape for most spectra excited above 398 eV, implying all nonequivalent N-sites are excited in rough proportion to their concentrations, as with the NXES spectrum. There is an obvious change in shape for the lowest-energy excitation at 397.89 eV. The spectral shape is clearer in CLMS, and so it will be the point of focus. In Figure 10.5 this spectrum is shown alongside several models.

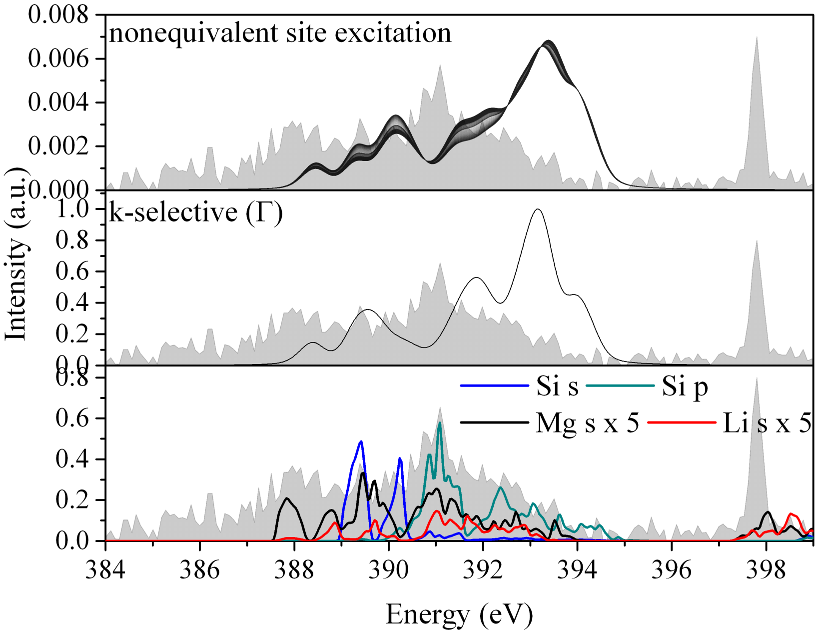

Figure 10.5: Top: calculated RXES spectra for excitations over the first 8 eV of the CB, which form a contour plot. The spectra are derived by weighting the contributions from nonequivalent N sites by their relative absorption intensities at each incident x-ray energy. Middle: spectra due only to those states near the Γ point. Bottom: select calculated DOS of CLMS. The RXES spectrum excited at 397.89 eV is shown as the shaded grey curve in each panel.

The calculated spectra for nonequivalent site excitation are shown in the upper panel of the figure, and show little variation in spectral shape, in keeping with the experimental spectra in earlier figures. Clearly nonequivalent site excitation does not describe the spectrum. Another possibility is k-conserving RIXS, [33] that leads to emission from only those states with the same crystal momentum as the state to which the core electron was excited. A calculation for this type of emission, assuming excitation at the Γ point, is shown in the central pane of the figure. Again this offers little explanation of the spectral shape. An explanation offers itself if the DOS of the tetrahedral cation s-states are compared to the spectrum. It would seem that the spectral shape is directly proportional to the s-state density of Mg, and perhaps Li. Keeping in mind that the DOS calculations suggest the CB minimum of CLMS is associated with the same states, this RXES excitation is clearly the result of excitation to the $(|N\ p> + |Mg/Li\ s>)^*$ and de-excitation from the $|N\ p> + |Mg/Li\ s>$ states. This strongly reinforces that the CB minimum of CLMS is determined by the Mg s-, and Li s-states. Based on this and the preceding discussion of the DOS and band structures, the energy level diagram in Figure 10.6 has been constructed. It is based on atomic term energies and is simply qualitative, but summarizes the energetic ordering of states for CLMS and BLSA in a useful manner. [12] The utility of such a diagram is rooted in the linear combinations of atomic orbitals model of electronic structure, as well as the general importance of nearest neighbour bonds in forming electronic structures in solids. [12, 91, 102, 103]

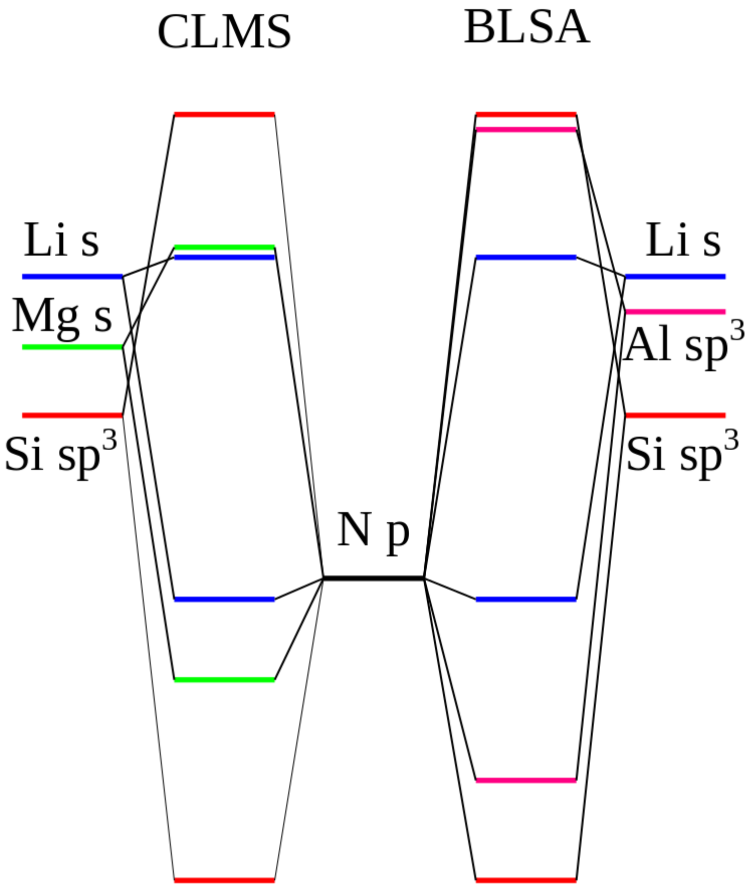

Figure 10.6: Energy level diagram for CLMS and BLSA based on tabulated term energies and the orbital mixing described above. [12]

10.9 Conclusions

The band gaps of CLMS and BLSA have been found to be 4.84±0.20 eV and 4.82±0.20 eV, respectively. They therefore have the large band gaps that are a prerequisite for efficient emissions from the Eu dopant. The DOS of the nonequivalent N sites show some variation in intensity with energy, which suggest they will have the narrow emissions that are desirable in the next generation of LED-phosphors. CLMS has been determined by RXES measurements and DFT calculations to be a Type II material, while BLSA is a Type I material. Importantly this designation predicts their properties under doping and use as the base of solid-solution series for tuning optical properties. Finally, it has been clarified that CLMS has a large band gap when compared to SMS because of its decreased N-Mg separation that drives orbital hybridization at the Mg site, and increased bond-antibond splitting. It is clear that both of these materials have high potential for use as phosphors, or as the conceptual parents of phosphors, in the next generations of high-efficiency phosphors for solid state lighting.

10.10 Experimental

The x-ray absorption measurements were collected at the spherical monochromator grating beamline at the Canadian Light Source in Saskatoon, Saskatchewan, Canada. [111] The absorption intensity was measured as the partial fluorescence yield (PFY), determined by post-processing the emission spectra collected using Si drift detectors. The beamline monochromator has a resolving power of about 5000 at the N K-edge. The x-ray emission spectroscopy (XES) measurements were collected at Beamline 8.0.1.1 of the Advanced Light Source in Berkeley, California, USA. [48] The beamline monochromator has a resolving power of about 5000. The emission spectrometer is in the Rowland Circle configuration and has a resolving power of about 1000. Samples were prepared for measurement under Ar or N_2 atmospheres to avoid hydrolysis of CLMS, which is mildly hygroscopic. The powder samples were pressed into clean In foil, prior to transfer to the vacuum chambers used for the measurements. All measurements were conducted under a vacuum of 10^{-6} Torr or better.

10.11 Calculations

The density functional theory calculations presented here used the WIEN2k software package. [112] This package uses linearized augmented plane waves (LAPW) and augmented plane waves with local orbitals (APW+lo) to solve the Kohn-Sham equations. The generalized gradient approximation of Perdew, Burke and Ernzerhof (GGA-PBE) was used throughout to model the exchange-correlation energies. Additional calculations using the modified Becke-Johnson (mBJ) potential were conducted, in order to obtain accurate estimates of the band gap. [92] The k-mesh for each sample was determined by increasing the mesh size until the total energy of the unit cell converged to 10^{-5} Ry. Core hole calculations used 2x1x1 supercells, with an appropriately scaled k-mesh.

Chapter 11

New Phenomena in phosphors SLA, BLSA, and CLMS

11.1 Introduction

Having outlined the basic electronic structure of CLMS and BLSA in the last chapter, the finer details of their luminescence properties are now considered using both RIXS and the, rather underutilized, XEOL technique. These experimental techniques allow direct access to the inter-band states that are the source of the luminescence properties of RE-doped phosphors. In this they are quite unique. Most methods for determining the location of RE-states in the band gaps of luminescent materials are empirical. [45] Direct measurements of these states are the sorely needed precursor to more accurate models of the energetic positioning of the RE 5d and 4f states in phosphors. In turn these lead to the understanding that is needed to predict key phosphor properties, such as emission colour, efficiency and thermal quenching behaviour.

My contribution ranges from data collection, to the processing and analysis of the data, as well as writing the manuscript. Synthesis, as in all cases in this thesis, is carried out by the coauthors of the publication. In its demonstration of the effectiveness of RIXS and XEOL for understanding RE state energies, it is seen that a very complete picture, going beyond the description of band gaps and itinerant electrons, can be obtained with x-ray spectroscopy.

11.2 The Manuscript

Optical transitions in $Li_2Ca_2[Mg_2Si_2N_6]$:Eu^{2+}, $Ba[Li_2(Al_2Si_2)N_6]$:Eu^{2+} and $Sr[LiAl_3N_4]$:Eu^{2+} with resonant inelastic x-ray scattering and x-ray excited optical luminescence

T.Tolhurst[1], P. Strobel[2], P. Pust[2], P. J. Schmidt[3], W. Schnick[2], A. Moewes[1]

1 Department of Physics and Engineering Physics, University of Saskatchewan, 116 Science Place Saskatoon, Saskatchewan S7N 5E2, 1-306-966-6431, alex.moewes@usask.ca

2 Department of Chemistry, University of Munich (LMU), Butenandtstrasse 5-13, 81377 Munich, Germany.

3 Lumileds Development Center Aachen, Lumileds Germany GmbH, Philipsstrasse 8, 52068 Aachen, Germany.

Abstract

Effective empirical models have been produced for predicting the properties of rare-earth-doped phosphors for phosphor-converted light emitting diodes. This study presents direct measurements of rare-earth energy levels that are critical to the color and efficiency of LED-phosphors. The 5d-conduction band separation as determined by resonant inelastic x-ray scattering is presented for $Li_2Ca_2[Mg_2Si_2N_6]$:Eu^{2+}, $Ba[Li_2(Al_2Si_2)N_6]$:Eu^{2+} and $Sr[LiAl_3N_4]$:Eu^{2+}. The band to band and 4f to valence band transitions are also observed in the x-ray excited optical luminescence spectra of $Sr[LiAl_3N_4]$:Eu^{2+}, giving a comprehensive, experimental picture of the rare-earth energy levels. These techniques are widely applicable and the resulting experimentally determined energy levels form the base that is needed for a detailed discussion of the structure-property relationships underpinning phosphor color and efficiency.

11.3 Introduction

Phosphor-converted light emitting diodes are positioned to significantly reduce global energy consumption. At the same time, they stand to become the dominant commercial lighting technology in the near future. [2,5] It is little surprise that the synthesis and characterization of LED-phosphors has become a vibrant research domain, and that many advances have been made in understanding the useful properties of phosphors. Rare-earth-doped materials have received particular favour for their tuneable and, often times, efficient emissions throughout the visible spectrum. [5,139,215] The structure-property relationships that lead to efficient emissions and stable compounds are complex, but must be understood in order to discover and engineer new, desirable phosphors. It has long been understood that the band gap plays a significant role in the efficiency of phosphors. [9,108,131,139] However, the problem is multidimensional and has been pursued aggressively, albeit empirically, in many earlier works. [45] There is therefore a relatively strong empirical framework in place for predicting the energetic positions of the rare-earth 4f and 5d states in a general way in the band gaps of phosphors. It is the interplay of the locations of band edges and the rare-earth ion states that leads to the manifold luminescence properties in these compounds. Direct measurements of these state energies are lacking, as only some are accessible through optical spectroscopy. X-ray spectroscopy techniques allow the measurement of state energies that are often not accessible with optical techniques, and therefore are a powerful compliment to optical studies.

This is a study of next-generation phosphors $Sr[LiAl_3N_4]:Eu^{2+}$ (SLA), $Li_2Ca_2[Mg_2Si_2N_6]:Eu^{2+}$ (CLMS) and $Ba[Li_2(Al_2Si_2)N_6]:Eu^{2+}$ (BLSA). [8,10,11,214] using resonant inelastic x-ray scattering (RIXS) and x-ray excited optical luminescence (XEOL). [35,39] Both allow the measurement of transitions that are often inaccessible to optical spectroscopy. [35] The 5d-conduction band (CB) separation in each sample is measured using RIXS, while other states are probed with XEOL. The latter has allowed confirmation of previously reported band gaps of SLA, as well as the measurement of additional inter-gap states, which match well with what is expected from excited Eu 4f levels. The direct measurement of these rare-earth energy levels on a case-by-case basis levels provides the foundation needed for a detailed discussion of the structure property relationships that lead to exceptional phosphor performance.

11.4 RIXS at the Nitrogen K-edge

The resonant x-ray emission spectroscopy (RXES) and corresponding x-ray absorption spectroscopy (XAS) spectra collected at the N K-edge for CLMS, BLSA and SLA are shown in Figure 11.1. Only low excitation energy, resonant x-ray emission spectra are shown. Emission spectra collected with higher excitation energies will be presented and discussed in a separate contribution. The principle character of the XAS spectra that is relevant here is that they are roughly proportional to the unoccupied partial DOS. [30] At the N K-edge, the XAS spectra are proportional to the unoccupied density of p-character states. This analysis focuses largely on the RXES spectra, referring to the XAS spectra only when needed. There are two main effects noticeable in the RXES spectra. First there are the variations in spectral shape that result from the excitation of nonequivalent N sites in each sample. [53] This is the strongest contribution to the spectra. Here the focus will be entirely on the second observable phenomenon, which is more subtle: the RIXS. [35] This process appears as subsidiary peaks at energies just below the elastic scattering peak. They represent energy losses of the incident x-rays to low-energy (optical) excitations in the sample. [35] In Figure 11.2 this portion of the spectra is shown on an energy loss scale, where the excitation energy has been subtracted from the abscissa in Figure 11.1, moving the elastic peaks to an energy loss of 0 eV. The energy loss in RIXS spectra is due to the excitation of electrons and other quasiparticles in a crystal. [35] Typical energy losses range from < 0.1 eV for phonons, to ~ 0.1 eV for orbital excitations, to ~ 1.0 eV for crystal field excitations and > 1.0 eV for charge transfer excitations. [35] Many of these are accessible to optical spectroscopy, though some are more effectively studied with RIXS, due to the selection rules involved.

Excitations using at least two different incident x-ray energies are shown for each sample, one at the CB onset and one at a slightly higher energy. For SLA, data were also collected for an undoped sample, one spectrum is shown in Figure 11.2. Unless explicitly stated otherwise, the Eu^{2+}-doped samples are those to which the discussion refers. The region of the XAS spectra that contains the lowest excitation energies for each sample is marked with solid vertical lines in Figure 11.1. Exact excitation energies are indicated in the space directly above each RXES spectrum. The data for CLMS and BLSA were collected under the same

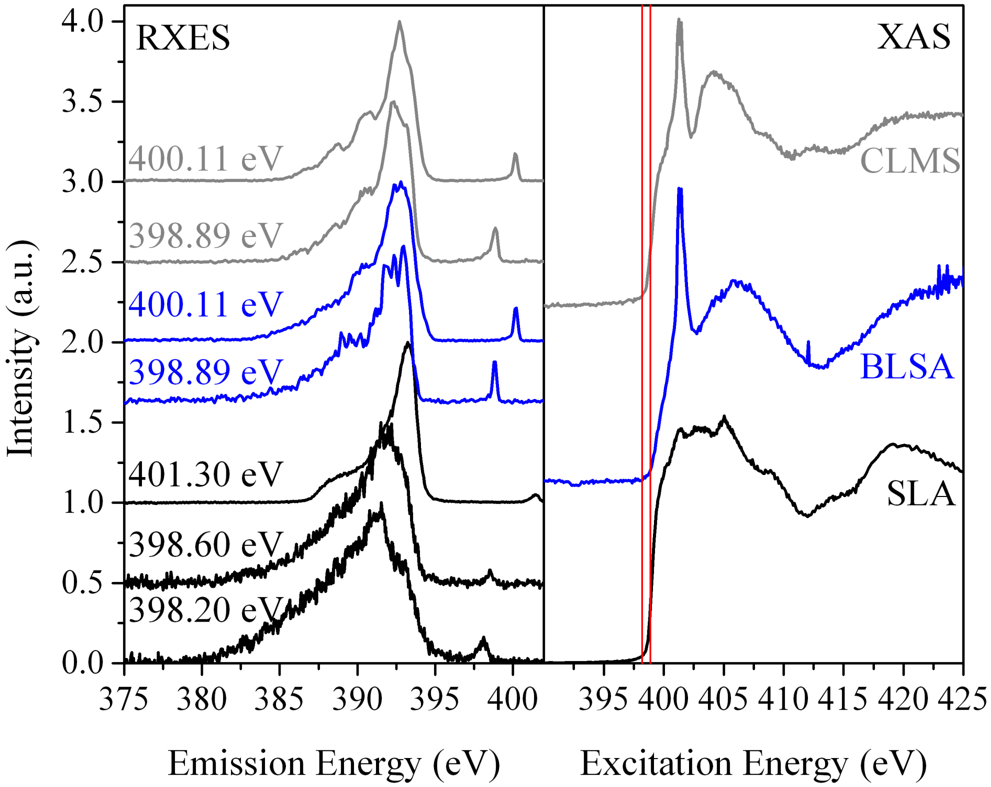

Figure 11.1: Absorption (right) and resonant x-ray emission spectra (left) at the N K-edge for CLMS (grey), BLSA (blue) and SLA (black). The 398.20 eV and 398.89 eV excitations are marked on the absorption spectra as red, vertical lines.

beamline conditions in rapid succession. On a separate occasion the data for SLA, including the undoped sample, were collected under the same beamline conditions in rapid succession.

To make the identification of peak locations and widths as precise as possible, they have been fit with a sum of two Gaussian distributions, with centers E_0 and standard deviations σ, as seen in Figure 11.2. The elastic peak and RIXS peaks will be referred to with subscripts 1 and 2, respectively. The parameters were allowed to vary freely during the fitting procedure to minimize any bias in the results. The fit results and uncertainties derived from the fitting are given in Table 11.1. As opposed to quoting the E_0 values for each peak and sample, the energy loss of the RIXS feature, $\Delta E_{RIXS} = E_{0,1} - E_{0,2}$, is given for each sample. For comparison, the ΔE_{TQ} values derived from the thermal quenching (TQ) data on each sample are also given in the table. The TQ data and the fit of a typical Arrhenius curve to the

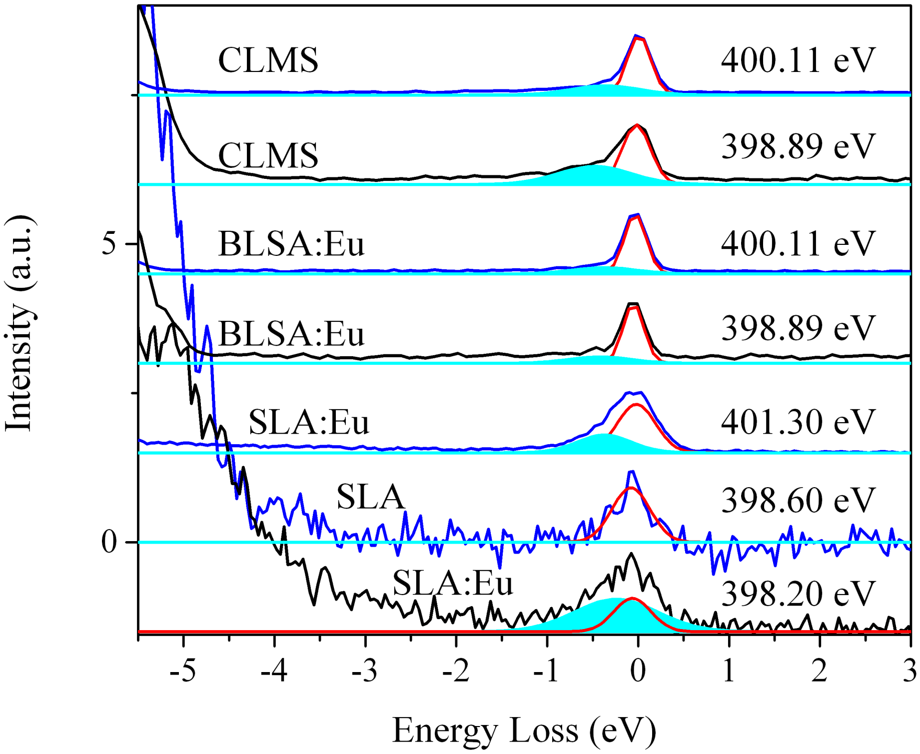

Figure 11.2: Comparison of the RIXS spectra of all samples on an energy loss scale. The ordering is the same as in Figure 11.1, with the excitation energy marked above each spectrum. The peaks from a least squares fit of two Gaussians to the RIXS are shown as a red (elastic) and cyan (loss feature) curves.

data, [139] which was used to obtain the ΔE_{TQ} values in the table, are shown in Figure 11.3.

First, it is critical to note that the fits to the data give the same elastic peak widths for all data collected under the same beamline conditions. This is necessary for the logical consistency of the results and supports the accuracy of the fitting. This also immediately suggests that any other breadth to the peaks must be due to inelastic scattering, which will be captured by the second Gaussian peak included in each fit. With this consistent result for the elastic peaks, the inelastic peaks can be considered.

Inelastic peaks are seen in all spectra except for the low energy excitation of undoped SLA. At the same time, the energy losses seen for the high energy excitations are about the same in each sample, while those for the low energy excitations vary considerably. The energy

Guassian Deconvolution Results				
Sample	σ_1	σ_2	ΔE_{RIXS}	ΔE_{TQ}
$\text{CLMS}_{398.89eV}$	0.155	0.400	0.46 ± 0.03	0.49 ± 0.03
$\text{CLMS}_{400.11eV}$	0.129	0.375	0.370	
$\text{BLSA}_{398.89eV}$	0.115	0.347	0.37 ± 0.03	0.253 ± 0.008
$\text{BLSA}_{400.11eV}$	0.120	0.355	0.338	
$\text{SLA}_{398.20eV}$	0.205	0.464	0.2 ± 0.1	0.291 ± 0.009
$\text{SLA'}_{398.60eV}$	0.210	0.0	n.a.	
$\text{SLA}_{401.30eV}$	0.211	0.302	0.353	

Table 11.1: Comparison of the standard deviations (σ_1 the elastic peak, σ_2 the inelastic peak) and peak separations from the fits shown in Figure 11.2. The 5d-CB separations derived from least squares fits to TQ data for each sample are shown in the far right column for comparison. The TQ data for SLA has been reported previously. [8, 108] The undoped SLA sample is denoted as SLA'.

losses seen for the high and low energy excitation in each sample are thus also different in general.

RIXS measurements at ligand edges tend to emphasize inter-site excitations, such as magnons or orbitons, between metal sites in a crystal. [35, 38] It has also been used to measure the location of defect states in the band gaps of metal oxides, [217] which could be enabled by the same superexchange process that makes ligands RIXS sensitive to inter-site excitations. [35] In the cases at hand all N atoms coordinate with alkaline earth metal ions, or the rare-earth dopants that occupy some of those same sites. Due to the low dopant concentrations it is also likely that most N atoms will coordinate with at most one rare-earth ion. When combined with previous results showing that the CB minimum in many phosphors, including SLA, consists largely of alkaline earth metal d-states, [108, 131] it is seen that the RE 5d to CB transition is effectively a RE 5d → M nd (M=Ca (n=3), Sr (n=4), Ba (n=5)) transition. It can therefore be proposed that the energy loss in the low excitation energy RIXS spectra is due to the 5d-CB transition in each material, which is analogous to an orbital excitation. This also agrees well with previous work using O K-edge RIXS to study intra-gap states in WO_3, where the defect-associated energy loss was strongest when exciting at the band edge, and the intensity of the peak also scaled with the defect concentration. [217] The defect concentrations in this WO_3 study were similar to those of the RE dopants here. One would also expect the peak intensity in the case at hand to scale with the degree of N-RE orbital overlap, and thus the RE-ligand distance. The relative peak intensities in Figure 11.2

decrease from CLMS to SLA to BLSA, in accord with the RE-ligand distances.

Further support is provided by looking at the effect of increasing the excitation energies slightly, as well as by comparing to the data for the undoped SLA sample. First, the low energy excitation for undoped SLA shows no energy loss feature, and an elastic peak with a width that corresponds to that determined from the fits for the other samples. The only difference between the doped and undoped SLA should be the Eu^{2+} dopant, correlating the energy loss feature for low energy excitations to the doping with Eu. The 401.30 eV excitation of SLA and undoped SLA (not shown) is then interesting to consider. The spectra, including the energy loss peak location and width, are identical. The energy loss at higher excitation energies therefore cannot be due to the Eu dopant. Combining this with the observation above that a different energy loss is seen for all samples between the low and high energy excitations, and that the high energy excitations show similar energy loss for all samples, suggests another mechanism is responsible for the energy loss in the latter cases. The energy loss for the low energy excitation varies sample to sample, as would be expected for the 5d-CB separation. The constancy of the energy loss at excitation energies increasingly above the CB minimum is well explained by losses to phonons. It is known that the phonon density rises rapidly over the first few tenths of an eV above the CB minimum and quickly dominates the RIXS spectrum at ligand edges. [33] This explains the quenching of the 5d-CB energy loss peak with increasing excitation energy, the differences between SLA and undoped SLA, as well as the differences between samples. Combining this with the good match between the energy loss of the low excitation energy spectra and what is ideally the 5d-CB separation derived from the TQ data, provides strong support that these RIXS measurements have indeed recorded the 5d-CB separation in SLA, CLMS and BLSA.

11.5 XEOL

XEOL has proven to be a tremendously useful tool for understanding the electronic structure, presence of defects and luminescence properties of solids. [40, 41] The basic experimental technique is to collect an XAS measurement as above, while also recording the optical photon spectra emitted from the sample at every step in the raster scan. [39] XEOL provides an opportunity to observe luminescence not usually seen in optical excitations due to the high

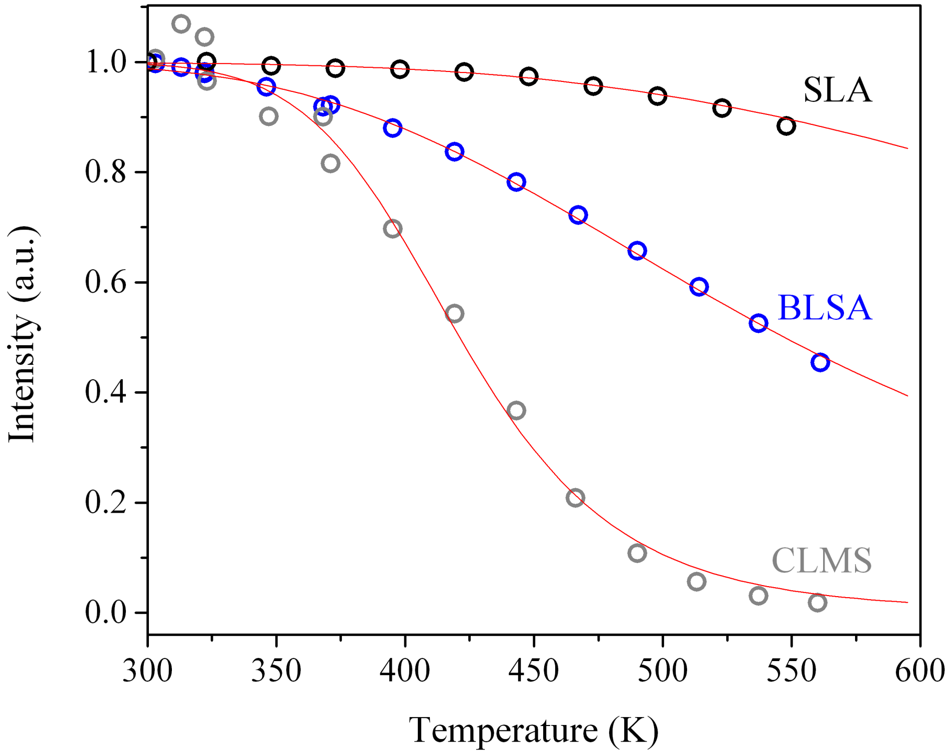

Figure 11.3: Fits of standard Arrhenius-type curves to the thermal quenching data of CLMS, BLSA and SLA. The activation energies are given in Table 11.1.

electron-hole density that is introduced into the system during measurement. Combining this with the potential for site-specific information inherent in XAS, makes XEOL a formidable technique. [39]

XEOL spectra excited at the Eu $M_{4,5}$-edge for all the samples being considered here are given in Figure 11.4. The spectra are divided into regions **A**, **B**, and **C** for ease of discussion. Region **A** is due to the $5d^1 4f^6 \rightarrow 4f^n$transition, in agreement with the literature. [8–10] However, the peaks in regions **B** and **C** are not observed in the optical spectroscopy data in the literature, which are usually excited with blue light.

The emission peak in **C** is only seen in the undoped SLA sample. Given its energetic location and shape it can be assigned to the CB-valence band (VB) transition in the sample. [8, 108] This should only be observed in a high quality sample with few relevant intra-gap defect states. It can be concluded that the defect concentration in the undoped sample is low, and that the Eu states will represent the only relevant intra-gap states in SLA. Note that this peak is absent in all doped samples, indicating that the Eu states become the preferred pathway for electron-hole recombination whenever present, which is an ideal characteristic for an LED-phosphor.

The emission feature in **B** is only seen in SLA, which based on the results for the undoped sample, should be attributed to Eu states. Given their energetic position it is reasonable to assign the peak to $4f^7 \rightarrow VB(\underline{L})$ transitions. This would constitute a metal to ligand charge transfer (MLCT). The broad peak is fit well by two Gaussians, and will therefore be treated as representing two nearby emission peaks. The peaks are located at 3.184 ± 0.001 eV (standard deviation 0.218 eV or 25.8 nm) and 2.781 ± 0.001 eV (standard deviation 0.199 eV or 23.4 nm). These are in keeping with the expectations for the energetic locations and widths of charge transfer peaks involving 4f states in materials doped with rare-earth ions. [139]

To assign the peaks in **B** to particular 4f states, the oxidation state of the Eu must be addressed, since it determines the relevant state energies. [139, 218] It can be inferred from the band structure of SLA that the hole mobility in the VB of SLA will be lower than the electron mobility in the CB. This gives rise to the sequence of possible transitions shown in Figure 11.4. With the initial trapping of an electron by the Eu 5d state, a MLCT of the form $Eu^{1+} + \underline{L} \rightarrow Eu^{2+} + \gamma$ will occur. Where the γ is that giving rise to one of the peaks in region **B**. The two lowest energy $4f^6$ states of Eu^{2+} that could lie in the band gap are the $^6P_{7/2}$ and $^6I_{7/2}$. The transitions in the diagram are labelled to match the observed peaks in the optical emission spectra.

Measurements were also conducted at the Eu $N_{2,3}$-edge for all samples, though not shown in the figure, the same emission peaks appear in each case. There is however, an interesting difference that is seen at the two edges for SLA: the ratio of peak intensities in regions A and B is different. Denoting the emission intensity Λ, one finds at the $M_{4,5}$-edge that $\Lambda_B/\Lambda_A = 0.51 \pm 0.04$, while at the $N_{2,3}$-edge it is found that $\Lambda_B/\Lambda_A = 0.90 \pm 0.23$. Assuming the source of the peaks is electron-hole recombination in the sequence shown in Figure 11.4, one expects that $\Lambda_B/\Lambda_A = 1$. The principle difference in the edges as far as the

XEOL measurements are concerned is the excitation energy itself and whether other atoms in the material can be excited, as well as the character of states to which the core electron is excited. At the low energy N_{23}-edge, only Eu has a substantial cross section for absorbing the incident x-rays, leading to a situation like that shown in the figure, where every absorbed x-ray leads to an electron in the CB and a hole in VB. At the $M_{4,5}$-edge, the other elements in the sample have a substantial photoabsorption cross section for the incident x-rays, leading to high energy photoelectrons that could directly excite the Eu 4f electrons into 5d states, as well as create electron-hole pairs. As a last detail of the observed emission processes, the branching ratio of the charge transfer transitions from the two different 4f states can be determined. Using the notation in Figure 11.4, one has $\Lambda_P/\Lambda_I = 0.73 \pm 0.06$ at the $M_{4,5}$-edge and $\Lambda_P/\Lambda_I = 0.59 \pm 0.15$ at the $N_{2,3}$-edge, which agree within the bounds of experimental uncertainty.

11.6 Conclusions

The 5d-CB energetic separation in a suite of next-generation LED-phosphors has been determined through direct measurement. This is a dramatic step forward in a field that often relies on empirical models to predict the location of rare-earth states in the CB of a material. The separations measured through RIXS for SLA, CLMS and BLSA are 0.2 ± 0.1 eV, 0.46 ± 0.03 eV and 0.37 ± 0.03 eV, respectively. The optical band-to-band transitions were observed directly in undoped SLA, confirming previous band gap measurements. At the same time, the doped SLA sample showed metal to ligand charge transfer features that are not usually seen in optical measurements. This thorough determination of dopant energy levels in the band gaps of these materials gives the needed experimental basis for a deeper understanding of the structure-property relationships that are critical for tailoring the luminescence properties of individual phosphors.

11.7 Experimental

The x-ray absorption spectroscopy measurements were conducted at the Spherical Grating Monochromator (SGM) Beamline at the Canadian Light Source, in Saskatoon, Canada.

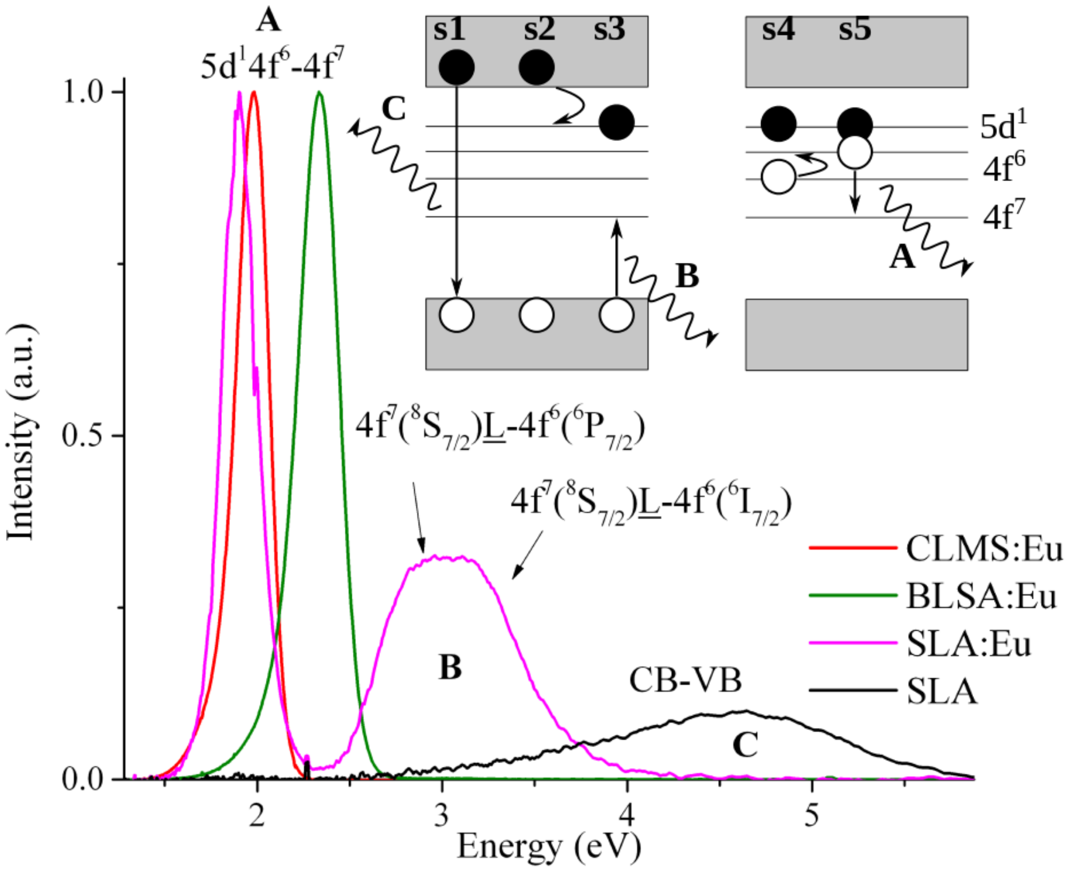

Figure 11.4: XEOL data for all three samples, including doped and undoped SLA. Spectra regions are labelled as A, B and C, with the corresponding transitions indicated. The diagram in the upper right shows the sequence of transitions expected to follow x-ray absorptions and also lead to the transitions observed. Path s1 is a simple CB-VB transition, as seen in the undoped SLA sample. Paths s2 to s5 are the sequence facilitating electron-hole recombination in the doped samples. Straight arrows denote optical transitions, while curved arrows indicate non-radiative transitions.

[111] The x-ray emission measurements were conducted at Beamline 8.0.1.1 of the Advanced Light Source in Berkeley, USA. [48] The SGM beamline has a monomchromator resolving power of about 5000 at the N K-edge, while the PFY spectra were collected using an array of silicon drift detectors. Beamline 8.0.1.1 has a monochromator resolving power of 5000, and a Rowland circle x-ray spectrometer for collecting the emission measurements. The spectrometer resolving power is about 800 at the N K-edge. The powder samples were prepared for measurement under N_2 or Ar atmospheres. Once pressed into clean wafers of In foil, the samples were transferred to the vacuum chambers used for the measurements.

Chapter 12

Conclusions and Perspectives

> Pursue science because it is knowledge, because it broadens our horizons. There is so much more to be discovered.
>
> –Gerhard Herzberg

No matter how far one pushes the horizon of understanding, there is always more to learn one step beyond. This work has evolved from studying larger scale details of the electronic structure of solids and has ended looking into finer details of RIXS spectra. This is the point where the DFT calculations that were the work horse for interpreting experimental results become much less applicable and new calculation approaches are needed. This thesis will close looking at some of the still-frayed ends of the thread of inquiry that has been woven throughout the preceding pages.

12.1 XEOL of SMS

In addition to the XEOL data presented in Chapter 11, which looked at SLA, CLMS and BLSA, data were also collected on several doped samples of SMS. Although in most cases, only the usual $4f^{n-1}d^1 \rightarrow 4f^n$ emissions were seen, in a high-quality sample measured concurrently with an SLA sample showing MLCT transitions, a transition in the same energy range was seen from SMS. The SMS XEOL spectrum is shown in Figure 12.1, alongside all of the spectra shown in Chapter 11. Highlighted in blue, the SMS spectrum shows a single peak in the region that was attributed to MLCT transitions in SLA. Where there were two nearly Gaussian peaks in SLA, only a single, skewed peak is seen in SMS.

In principle, the spectrum of Eu 4f states should be the same in SLA and SMS, due to the atomic nature of those states. It initially seems a little mysterious as to why only one peak would appear in SMS. Moreover, it calls into question whether the emissions in this region of the optical spectrum can be attributed to Eu 4f to VB transitions at all. However, a solution is presented by the same energy band diagram used for analyzing the electron hole recombination process in SLA in the preceding chapter. The same set of energy levels should be present in SMS, but there is a significant difference between SLA and SMS that needs to be considered. It is the large difference in their band gaps that was seen at the very beginning of the studies presented here. The 4f levels responsible for the MLCT transition in SLA, which should be at the same energy relative to the VB in SMS, will overlap strongly with the CB of SMS. Thus the peak seen at about 3 eV in SMS is the CB-VB transition seen in undoped SLA. Indeed, their spectral shape is the same. This provides additional confirmation of the band gaps of SLA and SMS, as well as the MLCT mechanism proposed to describe the $\approx$ 3 eV optical emissions in the XEOL of SLA.

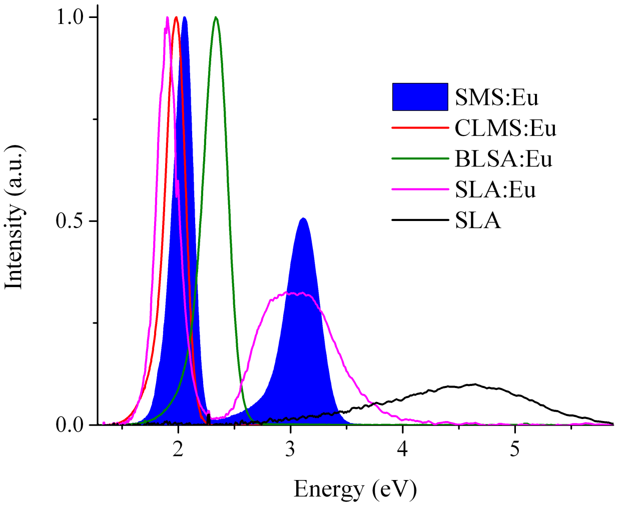

Figure 12.1: XEOL measurements presented in the previous chapter, with a XEOL spectrum of SMS added as a shaded, blue curve.

12.2 Quasiparticles in VO Compounds

More data has been collected for the preceding suite of V_2O_5 compounds than what has been analyzed in detail in earlier chapters. Ligand K-edge RIXS measurements on all compounds were recently collected, and are shown in Figure 12.2. All exhibit RIXS energy loss features as were seen above for ϵ-V_2O_5. This is an interesting result, as it suggests that not only are such features ubiquitous in these compounds at ligand edges, but that in addition to being functional materials for their band gaps and other properties, they are excellent candidates for studying quasiparticle states at a time when RIXS measurement resolutions are every increasing. [35] This is especially so, as to study fine spectral features samples with few defects are desirable, and V_2O_5 nanowires generally exhibit very low defect concentrations due to self-purification. [151]

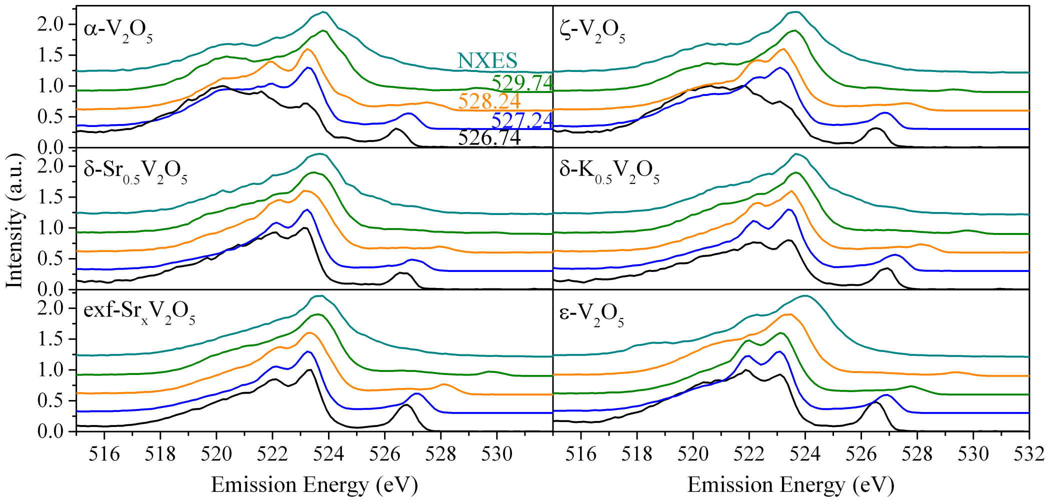

Figure 12.2: RXES measurements at the O K-edge on the suite of V_2O_5 compounds studied in this thesis. The excitation energies are as above for ϵ-V_2O_5. There are clear RIXS features for all samples.

12.3 Perspectives

12.3.1 Survey of Measured and Calculated Band Gaps

It is interesting at this point to leverage the relatively large sample of band gap measurements and calculations that have been made here to see if any trends exist. There are always the general expectations that the GGA or LDA calculations will underestimate the band gap, that the mBJ will be more accurate, [92] and that there should be general agreement between the x-ray measured band gaps and optical measurements, though the latter should generally be somewhat larger than the former. In Figure 12.3 the calculated band gaps for all samples presented here are plotted against the x-ray spectroscopy based band gaps. Data have been included for the series of phosphors $M_2Si_5N_8$ (M=Ca,Sr,Ba), which are an extremely important group for pc-LEDs, representing one of the first breakthrough red LED-phosphors. [7, 213]

There is a clear trend that can be seen. Although the slopes of the best fit lines for the GGA and mBJ calculations are about the same, being 0.49 ± 0.06 and 0.5 ± 0.1, respectively, the intercepts of the dependent axis are very nearly 1 eV apart. In both cases the slope falls short of the ideal of unit slope, by a rather large margin. It is clear that the main effect of the mBJ calculation is to shift the band gaps for all materials about 1 eV higher in energy, without changing how they vary as a function of the measured band gap. Of course the possibility of bias due to the lack of mBJ calculations for small band gap samples needs to be kept in mind.

The linearity and sub-unity slopes of the fits to the data necessitate that there will be a particular range over which the GGA and mBJ will each produce results that agree with experiments. Evidently, at least for the compounds studied here, the GGA is accurate for band gaps around 2 eV and the mBJ for band gaps around 4 eV. The slope measured here for the GGA matches well with that seen in previous publications, while that for the mBJ is still below unity. [92] This highlights that while the mBJ may produce more accurate band gaps for many compounds, it does contain empirically derived parameters and may not always give accurate results. Accurate band gaps can be expected from combining calculations with multiple experimental techniques.

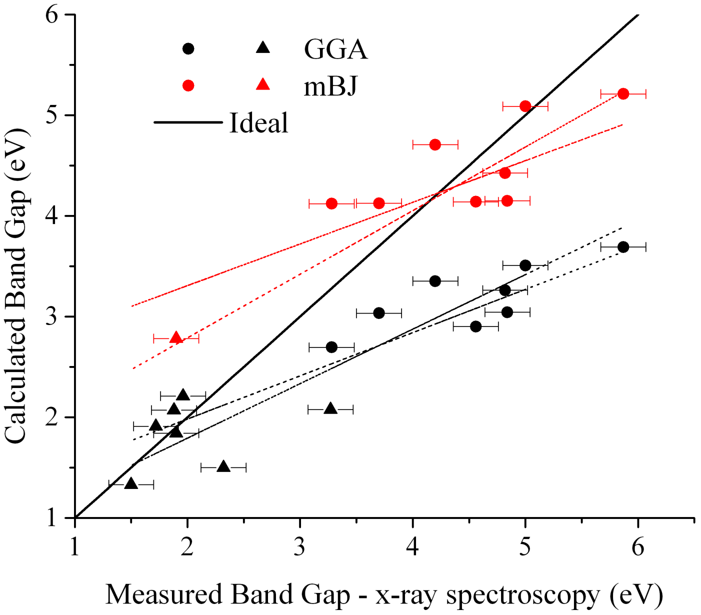

Figure 12.3: Compilation of band gap calculations using the GGA and mBJ functionals, compared to the measurements from the studies presented herein. Band gaps pertaining to vanadium oxides are shows as triangles, while circles denote the band gaps of nitrides. Best fit lines for each group are shown as broken lines.

On this front it is interesting to note that the band gaps included here for $M_2Si_5N_8$, in comparison to the optical band gaps in the literature, [219] where the optical band gap of $Ca_2Si_5N_8$ is given as 5.0 eV, while those of $Sr_2Si_5N_8$ and $Ba_2Si_5N_8$ are pinned at 4.9 eV. The x-ray spectroscopy measurements and calculations do suggest a rather different scenario. Calculated gaps using the GGA potential for M = Ca, Sr and Ba are 3.51 eV, 3.35 eV and 3.03 eV, respectively. The GGA calculation predicts a 0.5 eV variation across these systems, which in light of the analysis in Figure 12.3, should amount to an actual difference of about 1 eV. The gaps measured through x-ray spectroscopy for M = Ca, Sr and Ba are 5.00 ± 0.20 eV, 4.21 ± 0.20 eV and 3.70 ± 0.20 eV, in strong disagreement with the optical gaps, but in accord with the trend in Figure 12.3. It is well worth noting that all of the data for these samples were collected in rapid succession, and calibrated in the same manner simultaneously. Additionally, the results should be considered in light of the preceding analysis in this thesis. One expects the Si states to be sp^3 hybridized, and to form strong covalent bonds with the N sites, leading to large bond-antibond splitting. The gap between these states should be much greater than 5 eV, and will be similar in all samples, bearing in mind the effects of bond distance, which will decrease with increasing alkaline earth cation size. It follows directly that these will be type I materials, [139] where the band gap is determined by the alkaline earth ion 3d states. Looking back at SLA, which contains Sr and was determined to be a type I material, its band gap was found to be 4.14 ± 0.20 eV, in excellent agreement with $Sr_2Si_5N_8$, and the type I material designations.

12.3.2 Closing Remarks

The studies of rare earth doped phosphors herein have been quite broad in scope. Although many aspects were linked together in the preceding analysis it is well worth taking one last moment to try and precipitate those parts that are still disparate. The band gaps of SLA, SMS, CLMS and BLSA have all been determined and explained satisfactorily. They are all quite similar to one another, but with very different luminescecnce properties. The detail that is perhaps quite underaddressed is the dynamics of the Eu 4f and 5d states in these systems, which may elude accurate description with DFT calculations.

To draw a few final conclusions about these systems, their local coordination and electronic structure can be considered. The local coordination of the alkaline earth sites in each system is shown in Figure 12.4. The coordination of SLA and SMS is a nearly perfect cubic coordination, which leads to the $5d_{z^2}$ and $5d_{x^2-y^2}$ being lowered as deep as possible into the band gap, as shown in Figure 1.3. By contrast the cubic coordination polyhedron is strongly distorted in BLSA, and is closer to trigonal antiprismatic in CLMS. Looking at the splitting of states in Figure 1.3 it is clear why cubic coordination is usually associated with narrow, efficient emission from rare earth doped phosphors. [8,9]

Finally, there is a critical lesson from the preceding studies of V_2O_5 for studies of these systems. The rare earth 5d states will be prone to being itinerant. On the one hand this may suggest some hope for DFT studies of these states, but on the other it warns against complacently treating the Eu centres as isolated systems when the 5d is of interest. There are two strong possibilities to consider: the rare earth 5d states involved in luminescence may be hybridized with surrounding N p-states, or there could be direct overlap of Eu 5d states with d-states of nearby metal sites. The first case will facilitate superexchange transfer of electrons between metal sites. The latter will encourage the formation of d-character bands lying near the CB minimum. In both cases the effect will be enhanced as the alkaline earth ions in the lattice decrease in radius, leading to decreases in bond lengths. Where the low band gap of SMS may inhibit its emitting efficiently at high temperatures, enhanced transition probabilities stemming from increased orbital overlap may achieve the same thing in CLMS, or BLSA. Interestingly, the alkaline earth ions in many of these materials form long chains, spaced by N atoms, which would readily allow overlap of 5d states on nearby metal sites. Evidently SLA represents an ideal that is hard to replicate, but what makes it an ideal is becoming quite clear.

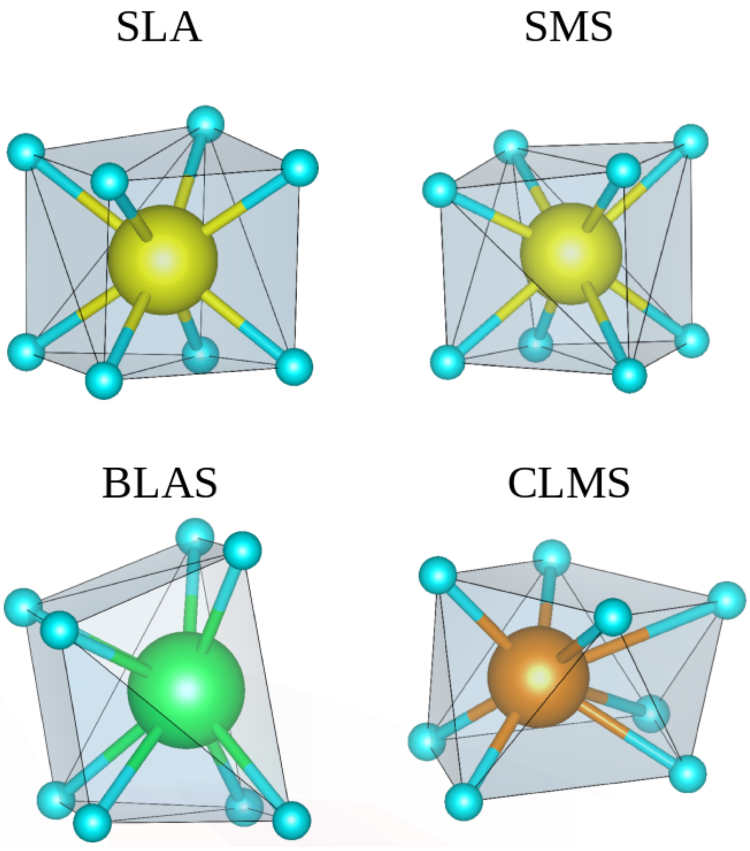

Figure 12.4: Local coordination environments of the alkaline earth ions in SLA, SMS, CLMS and BLSA. Nitrogen atoms are shown in cyan. The associated crystal fields are shown in Figure 1.3.

X-ray spectroscopy has an eminent ability to provide measurements of many key material properties, from band gaps, to impurity bands, to isolated defect states, to quasiparticles. For example, where one might be able to obtain direct measurements of the rare earth 5d-CB separation with infra red pump-probe measurements, the transition is often dipole forbidden. The RIXS transitions are often allowed and therefore yield higher peak intensities and data that are more easily analyzed. There is a tremendous amount of x-ray spectroscopic work that would still be valuable on rare earth phosphors and vanadium oxides. However, the need to go beyond DFT calculations for more detailed theoretical interpretations is clear. Where Anderson impurity model calculations are effective at metal absorption edges, calculations for RIXS at ligand edges, as well as optical spectra are less accessible. There is clearly a lot of room for experiment and theory to further one another, while characterizing important properties of the advanced materials that are contributing to the progress of global society.

Appendices

Appendix A

Copyright Information

This apendix contains details of the copyright information pertaining to previously published articles, whose text or figures have been reproduced in the text of this thesis. Text that is quoted from copyright agreements with the respective journals is given in italics.

A.1 Copyright Agreements for Reproduced Articles

A.1.1 Wiley-VCH

The articles in Chapters 4 and 5 (references [108], [131]) were originally published in *Advanced Optical Materials*, while the article in Chapter 3 (reference [53]) was originally published in *Chemistry - A European Journal.* These journals are published by Wiley-VCH Verlag GmbH & Co. KGaA (hereafter Wiley), and are here reproduced with permission. It is further noted that in Wiley's copyright transfer agreement, which was signed by the authors for each article, contains the following clause:

3. Final Published Version. *Wiley-VCH hereby licenses back to the Contributor the following rights with respect to the final published version of the Contribution:*

b. Re-use in other publications. *The right to re-use the final Contribution or parts thereof for any publication authored or edited by the Contributor (excluding journal articles) where such re-used material constitutes less than half of the total material in such publication. In such case, any modifications should be accurately noted.*

As first author of each paper I qualify as a Contributor, and the manuscripts qualify as authored publications. The aforementioned chapters constitute less than half of this thesis, making reproduction of these articles acceptable without further written permission from

Wiley.

A.1.2 The Royal Society of Chemistry

The article in Chapter 6 (reference [147]) was originally published in *Physical Chemistry Chemical Physics*, an international journal for the publication of work in physical chemistry, chemical physics and biophysical chemistry. It is published by the Royal Society of Chemistry. Here, the article is reproduced by permission of the PCCP Owner Societies. The full paper is available at http://pubs.rsc.org/-/content/articlehtml/2016/cp/c6cp02096h.

Bibliography

[1] A. Kitai, Luminescent Materials and Applications, 2008 John Wiley & Sons Ltd, England.

[2] P. Pust, P. J. Schmidt, W. Schnick, *Nat. Mater.*, 2015, 14, 454.

[3] C. Ronda, Luminescence: From Theory to Applications, 2008 WILEY-VCH, Germany.

[4] United States Energy Information Administration (EIA) - FAQ, http://www.eia.gov/tools/faqs/faq.cfm?id=99&t=3, accessed February 1, 2017.

[5] S. Ye, F. Xiao, Y. X. Pan, Y. Y. Ma, Q. Y. Zhang, *Mater. Sci. Eng., R*, 2010, 71, 1.

[6] G. BLSAse, B.C. Grabmaier, Luminescent Materials, 1994, Springer-Verlag Berline Heidelberg, Germany.

[7] R. Mueller-Mach, G. Meuller, M. R. Krames, H. A. Höppe, F. Stadler, W. Schnick, T. Jeustel, P. Schmidt, *Phys. Stat. Sol.*, 2005, 202, 1727.

[8] P. Pust, V. Weiler, C. Hecht, A. Tücks, A. S. Wochnik, A.-K. Henß, D. Wiechert, C. Scheu, P. J. Schmidt, W. Schnick, *Nat. Mater.*, 2014, 13, 891.

[9] S. Schmiechen, H. Schneider, P. Wagatha, C. Hecht, P. J. Schmidt, W. Schnick, *Chem. Mater.*, 2014, 26, 2712.

[10] P. Strobel, S. Schmiechen, M. Siegert, A. Tücks, P. J. Schmidt, W. Schnick, *Chem. Mater.*, 2015, 27, 6109.

[11] S. Schmiechen, F. Nietschke, W. Schnick, *Eur. J. Inorg. Chem.*, 2015, 1592.

[12] W. A. Harrison, Electronic Structure and the Properties of Solids, 1980 W. H. Freeman and Company, USA.

[13] J. L. Schnapf, T. W. Kraft, D. A. Baylor, *Nature*, 1987, 325, 439.

[14] B. M. Karnakov, V. P. Krianov, WKB Approximation in Atomic Physics, 2013 Springer-Verlag Berlin Heidelberg.

[15] C. J. Patridge, T.-L. Wu, C. Jaye, B. Ravel, E. S. Takeuchi, D. A. Fischer, G. Sambandamurthy, S. Banerjee, *Nano Lett.*, 2010, 10, 2448.

[16] V. Eyert, K.-H. Höck, *Phys. Rev. B*, 1998, 20, 57.

[17] J. M. Velazquez, S. Banerjee, *Small*, 2009, 5, 1025

[18] P. M. Marley, T. A. Abtew, K. E. Farley, G. A. Horrocks, R. V. Dennis, P. Zhang, S. Banerjee, *Chem. Sci.*, 2015, 6, 1712.

[19] L. D. Landau, E. M. Lifshitz, Statistical Physics, 3rd edition Part1, 1980 Elsevier Ltd., UK.

[20] C. J. Ballhausen, Introduction to Ligand Field Theory, McGraw-Hill Book Company, Inc., 1962, USA.

[21] R. H. Landau, Quantum Mechanics II, 2nd eddition, 1996 John Wiley & Sons, Inc., USA.

[22] S. Cottenier, Density Functional Theory and the family of (L)APW-methods: a step-by-step introduction, 2002-2013 (2nd edition), ISBN 978-90-807215-1-7 (freely available at http://www.wien2k.at/reg_user/textbooks).

[23] K. Schwarz, *J. Solid State Chem.*, 2003, 176, 319.

[24] J. P. Perdew, K. Burke, M. Ernzerhof, *Phys. Rev. B*, 1996, 77, 3865.

[25] J. Zaanen, G. A. Sawatzky, J. W. Allen, *Phys. Rev. Lett.*, 1985, 55, 418.

[26] B. Beckhoff, B. Kanngießer, N. Langhoff, R. Wedell, H. Wolff, Handbook of Practical X-ray Fluorescence Analysis, Springer-Verlag, 2006, Germany.

[27] B.L. Henke, E.M. Gullikson, and J.C. Davis. X-ray interactions: photoabsorption, scattering, transmission, and reflection at E=50-30000 eV, Z=1-92, Atomic Data and Nuclear Data Tables Vol. 54 (no.2), 181-342 (July 1993).

[28] A. J. Achkar, T. Z. Regier, H. Wadati, Y.-J. Kim, H. Zhang, D. G. Hawthorn, *Phys. Rev. B*, 2011, 83, 129901.

[29] W. Heitler, The Quantum Theory of Radiation, Clarendon Press, 1936, England.

[30] F. de Groot, A. Kotani, Core Level Spectroscopy of Solids, Taylor & Francis Group, 2008, USA.

[31] J. J. Sakurai, Advanced Quantum Mechanics, Addison-Wesley Publishing Company Inc., 1967, USA.

[32] R. J. Green, T. Z. Regier, B. Leedahl, J. A. McLeod, X. H. Xu, G. S. Chang, E. Z. Kurmaev, A. Moewes, *Phys. Rev. Lett.*, 2015, 115, 167401.

[33] S. Eisebitt, W. Eberhardt, *J. Electron Spectrosc. Relat. Phenom.*, 2000, 110-111, 335.

[34] Y. Ma, N. Wassdahl, P. Skytt, J. Guo, J. Nordgren, P. D. Johnson, J-E. Rubensson, T. BOske, W. Eberhardt, S. D. Kevan, *Phys. Rev. Lett.*, 1992, 69, 2598.

[35] L. J. P. Ament, M. van Veenendaal, T. P. Devereaux, J. P. Hill, J. van den Brink, *Rev. Mod. Phys.*, 2011, 83, 705.

[36] L.-C. Duda, T. Schmitt, M. Magnuson, J. Forsberg, A. Olsson, J. Nordgren, *Phys. Rev. Lett.*, 2006, 96, 067402.

[37] M. Moretti Sala, M. Rossi, S. Boseggia, J. Akimitsu, N. B. Brookes, M. Isobe, M. Isobe, M. Minola, H. Okabe, H. M. Rønnow, L. Simonelli, D. F. McMorrow, G. Monaco, *Phys. Rev. B*, 2014, 89, 121101.

[38] E. Benckiser, L. Fels, G. Ghiringhelli, M. Moretti Sala, T. Schmitt, J. Schlappa, V. N. Strocov, N. Mufti, G. R. Blake, A. A. Nugroho, T. T. M. Palstra, M. W. Haverkort, K. Wohlfeld, M. Grüninger, *Phys. Rev. B.*, 2013, 88, 205115.

[39] M. J. Ward, J. G. Smith, T. Z. Regier, T. K. Sham, *J. Phys.: Conf. Ser.*, 2013, 425, 132009.

[40] D. Wang, J. Yang, X. Li, J. Wang, R. Li, M. Cai, T. K. Sham, X. Sun. *Cryst. Growth Des.*, 2012, 12, 397.

[41] Z. Wang, C. L. Liu, T. K. Sham, *J. Chem. Phys.*, 2013, 138, 084706.

[42] W. M. Yen, S. Shionoya, H. Yamamoto, Fundamentals of Phosphors, Taylor & Francis Group, 2007, USA.

[43] P. Dorenbos, *J. Phys.: Condens. Matter*, 2003, 15, 575.

[44] P. Dorenbos, *Phys. Rev. B*, 2002, 65, 235110.

[45] P. Dorenbos, *ECS J. Solid State Sci. Technol.*, 2013, 2, 3001.

[46] T. Regier, J. Krochak, T. K. Sham, Y. F. Hu, J. Thompson, R. I. R. Blyth, *Nucl. Instrum. Methods Phys. Res., Sect. A*, 2007, 582, 93.

[47] T. Regier, J. Paulsen, G. Wright, I. Coulthard, K. Tan, T. K. Sham, R. I. R. Blyth, *AIP Conf. Proc.*, 2007, 879, 473.

[48] J. J. Jia, T. A. Callcott, J. Yurkas, A. W. Ellis, F. J. Himpsel, M. G. Samant, J. Stöhr, D. L. Ederer, J. A. Carlisle, E. A. Hudson, L. J. Terminello, D. K. Shuh, R. C. C. Perera, *Rev. Sci. Instrum.*, 1995, 66, 1394.

[49] M. Boots, D. Muir, A. Moewes, *J. Synchrotron Radiat.*, 2013, 20, 272.

[50] R. J. Green, Transition Metal Impurities in Semiconductors: Induced Magnetism and Band Gap Engineering, 2013 Ph.D. thesis at the University of Saskatchewan.

[51] M. Morháč, J. Kliman, V. Matoušek, M. Veselský I. Turzo, *Nucl. Instrum. Methods Phys. Res., Sect. A*, 1997, 401, 113.

[52] I. Antcheva et al., *Comput. Phys. Commun.*, 2009, 180, 2499.

[53] T. M. Tolhurst, C. Braun, T. D. Boyko, W. Schnick, A. Moewes, *Chem. Eur. J.*, 2016, 22, 10475.

[54] A. Stock, H. Gruneberg, *Ber. Dtsch. Chem. Ges.*, 1907, 40, 2573.

[55] S. Horstmann, E. Irran, W. Schnick, *Z. Anorg. Allg. Chem.*, 1998, 624, 620.

[56] S. Horstmann, E. Irran, W. Schnick, *Angew. Chem. Int. Ed. Engl.*, 1997, 36, 1873.

[57] S. Horstmann, E. Irran, W. Schnick, *Angew. Chem. Int. Ed. Engl.*, 1997, 36, 1992.

[58] E. O. Huffman, G. Tarbutton, G. V. Elmore, A. J. Smith, M. G. Rountree, *J. Am. Chem. Soc.*, 1957, 79, 1765.

[59] W. Schnick, J. Lücke, F. Krumeich, *Chem. Mater.*, 1996, 8, 281.

[60] H. Gu, Y. Gu, Z. Li, Y. Ying, Y. Qian, *J. Mater. Res.*, 2011, 18, 2359.

[61] K. Senevirathne, C. S. Day, M. D. Gross, A. Lachgar, N. A. W. Holzwarth, *Solid State Ionics*, 2013, 233, 95.

[62] W. Schnick, J. Lücke, *Solid State Ionics*, 1990, 38, 271.

[63] W. Schnick, J. Z. Lücke, *Anorg. Allg. Chem.*, 1990, 588, 19.

[64] W. Schnick, J. Lücke, *J. Solid State Chem.*, 1990, 87, 101.

[65] F. J. Pucher, F. Hummel, W. Schnick, *Eur. J. Inorg. Chem.*, 2015, 1886.

[66] D. Baumann, R. Niklaus, W. Schnick, *Angew. Chem. Int. Ed.*, 2015, 54, 4388.

[67] D. Baumann, W. Schnick, *Eur. J. Inorg. Chem.*, 2015, 617.

[68] A. Marchuk, W. Schnick, *Angew. Chem.*, 2015, 127, 2413.

[69] A. Marchuk, S. Wendl, N. Imamovic, F. Tambornino, D. Wiechert, P. J. Schmidt, W. Schnick, *Chem. Mater.*, 2015, 27, 6432.

[70] A. Marchuk, F. J. Pucher, F. W. Karau, W. Schnick, *Angew. Chem Int. Ed.*, 2014, 53, 2469-.

[71] D. Baumann, W. Schnick, *Inorg. Chem.*, 2014, 53, 7977.

[72] A. Marchuk, L. Neudert, O. Oeckler, W. Schnick, *Eur. J. Inorg. Chem.*, 2014, 21, 3427.

[73] S. J. Sedlmaier, E. Mugnaioli, O. Oeckler, U. Kolb, W. Schnick, *Chem. - A Eur. J.*, 2011, 17, 11258.

[74] W. Schnick, *Angew. Chem Int. Ed. Eng.*, 1993, 32, 806.

[75] S. Vepřek, J. Roos, *J. Phys. Chem. Solids.*, 1976, 37, 554.

[76] S. Vepřek, Z. Iqbal, J. Brunner, M. Schrli, *Philos. Mag. Part B.*, 2006, 43, 527.

[77] Y. H. Jeong, T. Sugano, S.-K. Jo, B.-H. Lee, *IEEE Electron Device Lett.*, 1995, 16, 109.

[78] Y. H. Jeong, G. T. Kim, S. T. Kim, *J. Appl. Phys.*, 1991, 69, 6699.

[79] A. Astito, A. Foucaran, G. Bastide, M. Rouzeyre, J. L. Leclercq, J. Durand, *J. Appl. Phys.*, 1991, 70, 2584.

[80] S. Vepřek, Z. Iqbal, J. Brunner, M. Schärli, *Philos. Mag. B*, 1981, 43, 527.

[81] K. Landskron, H. Huppertz, J. Senker, W. Schnick, *Z. Anorg. Allg. Chem.*, 2002, 628, 1465.

[82] K. Landskron, H. Huppertz, J. Senker, W. Schnick, *Angew. Chem. Int. Ed.*, 2001, 40, 2643.

[83] P. Kroll, W. Schnick, *Chem. Eur. J.*, 2002, 8, 3530.

[84] M. Bykov, E. Bykova, V. Dyadkin, D. Baumann, W. Schnick, L. Dubrovinsky, N. Dubrovinskaia, *Acta Crystallogr. Sect. E Crystallogr. Commun.*, 2015, 71, 1325.

[85] F. Xia, H. Wang, Y. Jia, *Nat. Commun.*, 2014, 5, 4458.

[86] N. M. Latiff, W. Z. Teo, Z. Sofer, A. C. Fisher, M. Pumera, *Chem. Eur. J.*, 2015, 21, 13991.

[87] C. Heindl, E. V. Peresypkina, D. Lüdeker, G. Brunklaus, A. V. Virovets, M. Scheer, *Chem. Eur. J.*, 2016, 22, 2599.

[88] S. Ma, C. He, L. Sun, H. Lin, Y. Li, K. Zhang, *Phys. Chem. Chem. Phys.*, 2015, 17, 32009.

[89] C.-Y. Pu, X.-T. Ye, H.-L. Jiang, F.-W. Zhang, Z.-W. Lu, J.-B. He, D.-W. Zhou, *Chinese Phys. B*, 2015, 24, 036301.

[90] F. J. Pucher, A. Marchuk, P. J. Schmidt, D. Wiechert, W. Schnick, *Chem. Eur. J.*, 2015, 21, 6443.

[91] G. L. W. Hart, A. Zunger, *Phys. Rev. B*, 2000, 62, 13522.

[92] F. Tran, P. Blaha, *Phys. Rev. Lett.*, 2009, 102, 226401.

[93] E. Z. Kurmaev, R. G. Wilks, A. Moewes, L. Finkelstein, S. Shamin, J. Kunes, *Phys. Rev. B*, 2008, 77, 165127.

[94] G. D. Mahan, *Phys. Rev. B*, 1980, 21, 1421.

[95] U. von Barth, G. Grossman, *Solid State Commun.*, 1979, 32, 645.

[96] T. D. Boyko, R. J. Green, R. Dronskowski, *A. Moewes, J. Phys. Chem. C*, 2013, 117, 12754.

[97] P. Kroll, R. Riedel, R. Hoffmann, *Phys. Rev. B*, 1999, 60, 3126.

[98] W. Olovsson, C. Goransson, T. Marten, I. Abrikosov, *Phys. Stat. Sol.*, 2006, 243, 2447.

[99] J. L. Leclercq, J. Durand, L. Cot, R. Berjoan, C. Dupuy, *Appl. Surf. Sci.*, 1992, 52, 289.

[100] Y. Hirota, O. Mikami, *Thin Solid Films*, 1988, 162, 41.

[101] H. Gu, Y. Gu, Z. Li, Y. Ying, *J. Mater. Res.*, 2003, 18, 2359.

[102] D. Weaire, M. F. Thorpe, *Phys. Rev. B*, 1971, 4, 2508.

[103] R. P. Gupta, *Phys. Rev. B*, 1985, 32, 8278.

[104] N. W. Johnson, P. Vogt, A. Resta, P. De Padova, I. Perez, D. Muir, E. Z. Kurmaev, G. Le Lay, A. Moewes, *Adv. Funct. Mater.*, 2014, 24, 5253.

[105] W. F. Tsai, C. Y. Huang, T. R. Chang, H. Lin, H. T. Jeng, A. Bansil, *Nat. Commun.*, 2013, 4, 1500.

[106] H. L. Poh Z. Sofer, M. Nováček, M. Pumera, *Chem. Eur. J.*, 2014, 20, 4284.

[107] S. Md. Pratik, A. Nijamudheen, A. Datta, *Chem. Eur. J.*, 2015, 21, 18454.

[108] T. M. Tolhurst, T. D. Boyko, P. Pust, N. W. Johnson, W. Schnick, A. Moewes, *Adv. Opt. Mater.*, 2015, 3, 546.

[109] P. Pust , V. Weiler, C. Hecht, A. Tücks, A. S. Wochnik, A. Henß, D. Wiechert, C. Scheu, P. J. Schmidt , W. Schnick, *Nat. Mater.*, 2014, 13, 891.

[110] F. Karau, PhD-thesis, University of Munich (LMU), 2007.

[111] T. Regier, J. Krochak, T. K. Sham, Y. F. Hu, J. Thompson, R. I. R. Blyth, Nucl. Instrum. Methods *Phys. Res., Sect. A*, 2007, 582, 93.

[112] K. Schwarz, P. Blaha, *Comput. Mater. Sci.*, 2003, 28, 259.

[113] Y. Q. Li, N. Hirosaki, H. Yamamoto, Nitride Phosphors and Solid-State Lighting, Boca Raton, FL: Taylor & Francis, 2011.

[114] W. B. Im, N. George, J. Kurzman, S. Brinkley, A. Mikhailovsky, J. Hu, B. Chmelka, F. Bradley S. P. Denbaars, R. Seshadri, *Adv. Mater.*, 2011, 23, 2300.

[115] C. C. Lin, R.-S. Liu, *J. Phys. Chem. Lett.*, 2011, 2, 1268.

[116] H. Yang, S. W. Kim, J. Y. Han, S. Lee, D. Y. Jeon, *Adv. Mater.*, 2008, 20, 2696.

[117] R. Mueller-Mach, G. Mueller, M.R. Krames, H.A. Hoppe, F. Stadler, W. Schnick, T. Juestel, P. Schmidt, *Phys. Status Solidi A*, 2005, 202, 1727.

[118] X. Wang, X. Yan, W. Li, K. Sun, *Adv. Mater.*, 2012, 24,2742.

[119] P. Pust, A. Wochnik, E. Baumann, P.J. Schmidt, D. Wiechert, C. Scheu, W. Schnick *Chem. Mater.*, 2014, 26, 3544.

[120] M. R. Krames, G. O. Mueller, R. B. Mueller-Mach, H. Bechtel, P. J. Schmidt, PCT Int. Appl. WO 2010131133, A1, 2010.

[121] K. Kuriyama, Y. Kaneko, K. Kushida. *J. Cryst. Growth*, 2005, 275, 395.

[122] M. Mikami, H. Watanabe, K. Uheda, S. Shimooka, Y. Shimomura, T. Kurushima, N. Kijima, *IOP Conf. Ser.: Meter. Sci. Eng.*, 2009, 1, doi:10.1088/1757-8981/1/1/012002.

[123] Y.Q. Li, N. Hirosaki, R.J. Xie, T. Takeka, M. Mitomo *J. Solid State Chem.*, 2009, 182, 301.

[124] A. Kotani, S. Shin, *Rev. Mod. Phys.*, 2001, 73, 203.

[125] C. J. Duan, X. J. Wang, W. M. Otten, A. C. A. Delsing, J. T. Zhao, H. T. Hintzen, *Chem. Mater.*, 2008, 20, 1597.

[126] M. Dadsetani, S. Namjoo, H. Hejati. *J. Electron. Mater.*, 2010, 39, 1186.

[127] C. Braun, M. Seibald, S. L. Börger, O. Oeckler, T. D. Boyko, A. Moewes, G. Miehe, A. Tücks, W. Schnick, *Chem. - Eur. J.*, 2010, 16, 9646.

[128] P. Dorenbos, *Phys. Rev. B*, 2001, 64, 125117.

[129] C. Housecroft, A. Sharpe, Inorganic Chemistry, Second Edition. Pearson Education Limited, 2005.

[130] U. von Barth, G. Grossman, *Solid State Commun.*, 1979, 32, 645.

[131] T. M. Tolhurst, S. Schmiechen, P. Pust, P. J. Schmidt, W. Schnick, A. Moewes, *Adv. Opt. Mater.*, 2016, 4, 584.

[132] C. C. Lin, R. S. Liu, *J. Phys. Chem. Lett.*, 2011, 2, 1268.

[133] C. T. Chen, Y. Ma, F. Sette, *Phys. Rev. A*, 1989, 40, 6737.

[134] J. Nordgren, P. Glans, K. Gunnelin, J. Guo, P. Skytt, C. Såthe, N. Wassdahl, *Appl. Phys. A: Mater. Sci. Process.*, 1997, 65, 97.

[135] C. Braun, S. L. Börger, T. D. Boyko, G. Miehe, H. Ehrenberg, P. Höhn, A. Moewes, W. Schnick, *J. Am. Chem. Soc.*, 2011, 133, 4307.

[136] T. de Boer, T. D. Boyko, C. Braun, W. Schnick, A. Moewes, *Phys. Status Solidi RRL*, 2015, 9, 250.

[137] P. Dorenbos, *J. Phys.: Condens. Matter*, 2003, 15, 2645.

[138] P. Dorenbos, *J. Lumin.*, 2003, 104, 239.

[139] P. Dorenbos, *J. Phys.: Condens. Matter*, 2005, 17, 8103.aphy of SLA

[140] D. C. Rodriguez Burbano, S. K. Sharma, P. Dorenbos, B. Viana, J. A. Capobianco *Adv. Opt. Mater.*, 2015, 3, 551.

[141] Y. Chen, Y. Li, J. Wang, M. Wu, C. Wang, *J. Phys. Chem. C*, 2014, 118, 12494.

[142] K. Inoue, N. Hirosaki, R. Xie, T. Takeda, *J. Phys. Chem. C*, 2009, 113, 9392.

[143] L. Wang, ; H. M. Noh, B. K. Moon, S. H. Park, K. H. Kim, J. Shi, J. H. Jeong, *J. Phys. Chem. C*, 2015, 119, 15517.

[144] W. Lv, Y. Jia, Q. Zhao, M. Jiao, B. Shao, W. Lü, H. You. Crystal Structure and Luminescnce Properties of $Ca_8Mg_3Al_2Si_7O_{28}$:Eu^{2+} for WLEDs *Adv. Opt. Mater.*, 2014, 2, 183-188.

[145] N. Yamashita, O. Harada, K. Nakamura, *Jpn. J. Appl. Phys.*, 1995, 34, 5539.

[146] S. Schmiechen, P. Strobel, C. Hecht, T. Reith, M. Siegert, P. J. Schmidt, P. Huppertz, W. Schnick, *Chem. Mater.*, 2015, 27, 1780.

[147] T. M. Tolhurst, B. Leedahl, J. L. Andrews, P. M. Marley, S. Banerjee, A. Moewes, *Phys. Chem. Chem. Phys.*, 2016, 18, 15798.

[148] M. Imada, A. Fujimori, Y. Tokura, *Rev. Mod. Phys.*, 1998, 70, 1039.

[149] Z. Yang, C. Ko, S. Ramanathan, *Annu. Rev. Mater. Res.*, 2011, 41, 337.

[150] N. A. Chernova, M. Roppolo, A. C. Dillon, M. S. Whittingham, *J. Mater. Chem.*, 2009, 19, 2526.

[151] P. M. Marley, G. A. Horrocks, K. E. Pelcher, S. Banerjee, *Chem. Commun.*, 2015, 51, 5181.

[152] M. S. Whittingham, *Chem. Rev.*, 2004, 104, 4271.

[153] M. Winter, O. B. Jurgen, M. E. Spahr, P. Novak, *Adv. Mater.*, 1998, 10, 725.

[154] P. M. Marley, S. Banerjee, *Inorganic Chemistry*, 2012, 51, 5264.

[155] J. M. Velazquez, C. Jaye, D. A. Fischer, S. Banerjee, *J. Phys. Chem.*, 2009, 113, 7639.

[156] Y. Wang, K. Takahashi, K. Lee, G. Cao, *Adv. Funt. Mater.*, 2006, 16, 1133.

[157] T. Zhai, L. Li, X. Wang, X. Fang, Y. Bando, D. Golberg, *Adv. Funct. Mater.*, 2010, 20, 4233.

[158] T. Zhai, H. Liu, H. Li, X. Fang, M. Liao, L. Li, H. Zhou, Y. Koide Y. Bando, D. Golberg, *Adv. Mater.*, 2010, 22, 2552.

[159] P. M. Marley, A. A. Stabile, C. P. Kwan, S. Singh, P. Zhang, G. Sambandamurthy, S. Banerjee, *Adv. Funct. Mater.*, 2013, 23, 153.

[160] G. A. Horrocks, M. F. Likely, J. M. Velazquez, S. J. Banerjee, *Mater. Chem. A*, 2013, 1, 15265.

[161] M. Nolan, S. O'Callaghan, G. Fagas, J. C. Greer, T. Frauenheim, *Nano Lett.*, 2007, 7, 34.

[162] H. Peng, J. Li, *J. Phys. Chem. C*, 2008, 112, 20241.

[163] O. Demichel, V. Calvo, P. Noé, B. Salem, P.-F. Fazzini, N. Pauc, F. Oehler, P. Gentile, N. Magnea, *Phys. Rev. B*, 2011, 83, 245443.

[164] V. P. Filonenko, M. Sundberg, P. -E. Werner, I. P. Zibrov, *Acta Crystallogr., Sect. B: Struct. Sci.*, 2004, 60, 375.

[165] S. Laubach, P. C. Schmidt, A. Thißen, F. J. Fernandez-Madrigal, Q. H. Wu, W. Jaegermann, M. Klemm, S. Horn, *Phys. Chem. Chem. Phys.*, 2007, 9, 2564.

[166] S. Shin, M. Fujisawa, H. Ishii, Y. Harada, M. Watanabe, M. M. Grush T. A. Callcott, R. C. C. Perera, E. Z. Kurmaev, A. Moewes, R. Winarski, S. Stadler, D. L. Ederer, *J. Electron Spectrosc. Relat. Phenom.*, 1998, 92, 197.

[167] O. Y. Khyzhun, T. Strunskus, W. Grünert, C. Wöll, *J. Electron Spectrosc. Relat. Phenom.*, 2005, 149, 45.

[168] C. J. Patridge, T. L. Wu, G. Sambandamurthy, S. Banerjee, *Chem. Commun.*, 2011, 47, 4484.

[169] C. Kittel, Introduction to Solid State Physics, 8th edn., 2005 John Wiley & Sons, USA.

[170] G. A. Khan, C. A. Hogarth, *Journal of Materials Science*, 1991, 26, 412.

[171] C. V. Ramana, B. S. Naidu, O. M. Hussain, R. Pinto, *J. Phys. D: Appl. Phys.*, 2001, 34, L35.

[172] Z. S. El Mandouh, M. S. Selim, *Thin Solid Films*, 2000, 371, 259.

[173] R. J. O. Mossanek, A. Mocellin, M. Abbate, B. G. Searle, P. T. Fonseca, E. Morikawa, *Phys. Rev. B*, 2008, 77, 075118.

[174] D. Maganas, M. Roemelt, M. Hävecker, A. Trunschke, A. Knop-Gericke, R. Schlögl, F. Neese *Phys. Chem. Chem. Phys.*, 2013, 15, 7260.

[175] W. Setyawan, S. Curtarolo *Comput. Mater. Sci.*, 2010, 49, 299.

[176] C. J. Patridge, C. Jaye, H. Zhang, A. C. Marschilok, D. A. Fischer, E. S. Takeuchi, S. Banerjee, *Inorg. Chem.*, 2009, 48, 3145.

[177] R. F. W. Bader, *Atoms in molecules : a quantum theory*, Oxford Press, USA., 1990.

[178] R. Laskowski, P. Blaha, K. Schwarz, *Phys. Rev. B*, 2003, 67, 075102.

[179] G. van der Laan, B. T. Thole, G. A. Sawatzky, M. Verdaguer, *Phys. Rev. B*, 1988, 37, 6587.

[180] R. J. Green, D. A. Zatsepin, D. J. St. Onge, E. Z. Kurmaev, N. V. Gavrilov, A. F. Zatsepin, A. Moewes, *J. Appl. Phys.*, 2014, 115, 103708.

[181] L. R. De Jesus, G. A. Horrocks, Y. Liang, A. Parija, C. Jaye, L. Wangoh, J. Wang, D. A. Fischer, L. F.J. Piper, D. Prendergast, S. Banerjee, *Nat. Commun.*, 2016, 7, 12022.

[182] C. J. Patridge, T.-L. Wu, G. Samabandamurthy, S. Banerjee, *Chem. Commun.*, 2011, 47, 4484.

[183] P. M. Marley, S. Singh, T. A. Abtew, C. Jaye, D. A. Fischer, P. Zhang, G. Sambandamurthy, S. Banerjee, *J. Phys. Chem. C*, 2014, 118, 21235.

[184] T. Yamauchi, Y. Ueda, *Phys. Rev. B*, 2008, 77, 104529/104521.

[185] T. Yamauchi, Y. Ueda, N. Mori, *Phys. Rev. Lett.*, 2002, 89, 057002/057001.

[186] J.-I. Yamaura, T. Yamauchi, M. Isobe, H. Yamada, Y. Ueda, *J. Phys. Soc. Jpn.*, 2004, 4, 914.

[187] Y. Lu, L. Liu, D. Mandler, P. S. Lee, *J. Mater. Chem. C*, 2013, 1, 7380.

[188] W. Kang, C. Yan, X. Wang, C. Y. Foo, A. W. M. Tan, K. J. Z. Chee, P. S. Lee, *J. Mater. Chem. C*, 2014, 2, 4727.

[189] C. Glynn, D. Thompson, J. Paez, G. Collins, E. Benavente, V. Lavayen, N. Yutronic, J. D. Holmes, G. Gonzalez, C. O'Dwyer, *J. Mater. Chem. C*, 2013, 1, 567.

[190] Z. Tong, H. Yang, L. Na, H. Qu, X. Zhang, J. Zhao, Y. Li, *J. Mater. Chem. C*, 2015, 3, 3159.

[191] J. L. Andrews, L. R. De Jesus, T. M. Tolhurst, P. Marley, A. Moewes, S. Banerjee, submitted to *Chem. Mater.*

[192] K. Schwarz, P. Blaha, *Comput. Mater. Sci.*, 2003, 28, 259.

[193] K. Schwarz, *Journal of Solid State Chemistry*, 2003, 176, 319.

[194] J. B. Goodenough, *J. Solid State Chem.*, 1970, 1, 349.

[195] H. D. Yoo, I. Shterenberg, Y. Gofer, G. Gershinsky, N. Pour, D. Aurbach, *Energ Environ Sci*, 2013, 6, 2265.

[196] J. M. Booth, P. S. Casey, *Phys. Rev. Lett.*, 2009, 086402/1.

[197] A. Cavalleri, T. Dekorsky, H. H. W. Chong, J. C. Kieffer, W.Schoenlein, *Phys. Rev. B*, 2004, 70, 161102/161101.

[198] W. H. Brito, M. C. O. Aguiar, K. Haule, G. Kotliar, *Phys. Rev. Lett.*, 2016, 117, 1.

[199] H. T. Dang, X. Ai, A. J. Millis, C. A. Marianetti, *Phys. Rev. B*, 2014, 90, 125114.

[200] T. D. Boyko, E. Bailey, A. Moewes, P. F. McMillan, *Phys. Rev. B.*, 2010, 81, 155207.

[201] D. Ruzmetov, S. D. Senanayake, V. Narayanamurti, S. Ramanathan, *Phys. Rev. B*, 2008, 77, 195442.

[202] D. Ruzmetov, S. D. Senanayake, V. Narayanamurti, S. Ramanathan, *Phys. Rev. B*, 2008, 77, 195442.

[203] A. A. Stabile, S. K. Singh, T. -L. Wu, L. Whittaker, S. Banerjee, G. Sambandamurthy, *Appl. Phys. Lett.*, 2015, 107, 013503.

[204] H. Fukui, S. Huotari, D. Andrault. T. Kawamoto, *J. Chem. Phys.*, 2007, 127, 134502.

[205] J. S. Tse, D. M. Shaw, D. D. Klung, S. Patchovskii, G. Vankó G. Monaco, M. Krisch, *Phys. Rev. Lett.*, 2008, 100, 095502.

[206] S. Schrek, P. Wernet, *J. Chem. Phys.*, 2016, 145, 104502.

[207] T. Tokushima *Chem. Phys. Lett.*, 2008, 460, 387.

[208] M. Nolan, S. O'Callaghan, G. Fagas, J. C. Greer and T. Frauenheim, *Nano Lett.*, 2007, 7, 34.

[209] B. Winter, E. F. Aziz, U. Hergenhahn, M. Faubel, I. V. Hertel, *J. Chem. Phys.*, 2007, 126, 124504.

[210] Q.-H. Wu, A. Thissen, W. Jaegermann, M. Liu *Appl. Surf. Sci.*, 2004, 236, 473.

[211] C.G. Fatuzzo, M. Dantz, S. Fatale, P. Olalde-Velasco, N. E. Shaike, B. Dalla Piazza, S. Toth, J. Pelliciari, R. Fittipaldi, A. Vecchione, N. Kikugawa, J. S. Brooks, H. M. Rønnow, M. Grioni, Ch. Rüegg, T. Schmitt, J. Chang, *Phys. Rev. B*, 2015, 91, 155104.

[212] X. Liu, M. P. Dean, J. Liu, S. G. Chiuzbăian, N. Jaouen, A. Nicolaou, W. G. Yin, C. R. Serrao, R. Ramesh, H. Ding, J. P. Hill, *J. Phys. Condens. Matter*, 2015, 27, 202202.

[213] H. Huppertz, W. Schnick, *Acta. Cryst.*, 1997, 53, 1751.

[214] P. Strobel, V. Weiler, C. Hecht, P. J. Schmidt, W. Schnick, *Chem. Mater.*, 2017, 29, 1377.

[215] M. Zeuner, S. Pagano, W. Schnick, *Angew. Chem. Int. Ed.*, 2011, 50, 7754.

[216] L. J. P. Ament, M. van Veenendal, T. P. Devereaux, J. P. Hill J. van den Brink *Rev. Mod. Phys.*, 2011, 83, 705.

[217] M. B. Johansson, P. T. Kristiansen, L. Duda, G. A. Niklasson L. Österlund *J. Phy. Condens. Matter*, 2016, 29, 475802.

[218] G. H. Dieke, H. M. Crosswhite, *Appl. Opt.*, 1963, 2, 675.

[219] O. M. ten Kate, Z. Zhang, P. Dorenbos, H. T. Hintzen, E. van der Kolk, *J. Solid State Chem.*, 2013, 197, 209.